

**Study of X-ray Absorption Spectroscopy of Heavy Elements
and Transient Chemical Species**

ASAKURA, Hiroyuki

2014

Preface

The discovery of X-ray reported by Prof. Röntgen in 1895 has astonished scientists all over the world and brought in versatile applications of this fascinating light into analytical science, such as X-ray diffraction, X-ray scattering, X-ray absorption and other X-ray related phenomena of materials. On X-ray absorption, Maurice de Broglie first reported X-ray absorption edges, which were proved to be the K-edge of Ag and Br in the photographic emulsion in 1913 and a number of scientists concurrently have been devoting their efforts to the fundamental and applied science on the X-ray absorption spectroscopy. As a result, the basic knowledge on the X-ray absorption spectrum of almost every element in the periodic table has been accumulated and applied to understand chemistry and physics of various materials such as catalysts, dielectric materials, dopants in semiconductors, cathode materials for lithium ion battery or many other practical materials or devices in these days.

The X-ray absorption (XAS) spectrum is usually divided into two regions, X-ray absorption near edge structure (XANES), which is an abrupt increase of absorption (absorption edge) in XAS spectrum, and extended X-ray absorption fine structure (EXAFS), which is a fine oscillation observed above the absorption edge. In 1971, Sayers, Stern and Lytle proposed the EXAFS equation and widely accepted quantitative interpretation procedure of EXAFS oscillation in relation with the local structure of surroundings of an X-ray absorbing atom. On the other hand, the XANES region has not been understood well because of the complexity of the multiple scattering process of the photoelectron ejected from an X-ray absorbing atom. However, in these two decades, an amazing progress on both of experimental and theoretical approaches (*e.g.* multiple scattering theory and density functional theory) to XANES spectroscopy raised themselves to another quantitative analytical tool for research on the local structure or electronic states of an X-ray absorbing atom.

From the point of view of experimental technique, the emergence of synchrotron radiation facilities is a milestone in the history of X-ray absorption spectroscopy. The broad spectrum of X-ray radiated from synchrotron facilities (from a few keV to more than 100 keV in some facilities) enabled us to measure high quality X-ray absorption spectrum in very short time compared to the measurement in laboratories with X-ray tubes. It also enables time-resolved X-ray absorption spectrum measurement, which is essential for *in situ* studies (*e.g.* applying X-ray absorption

spectroscopy into catalysts at their working condition) by so-called quick scanning mode or dispersive mode with bending crystals.

On these backgrounds, XANES spectra of so-called 3d transition metal elements or precious metal elements such as Ru, Rh, Pd, Ag, Ir, Pt, or Au have been extensively studied for their importance in various materials, but fundamental study on those of the other elements such as early 4d, 5d metal elements or lanthanide elements is relatively scarce. On the other hand, enormous application of time-resolved XAS measurement on solid materials such as heterogeneous catalysts have accumulated for a long period, but those on dispersion system or homogeneous system are still not so common.

From these perspectives, the author has studied fundamental and applied issues of X-ray absorption spectroscopy on heavy elements and transient chemical species. One is a relationship between characteristic features of the XANES spectra of heavy elements (Nb, Mo, Ta, W, Re) and their local structures and the author extended the insights to a rarely discussed field of XANES spectroscopy of various lanthanide elements. The other is reaction processes of Rh metal nanoparticle formation, and an organometallic catalytic cycle of a Ni complex catalyst. The author believes these studies give a small but significant advance in the field of X-ray absorption spectroscopy.

The researches in this thesis have been performed at Department of Molecular Engineering, Graduate School of Engineering, Kyoto University from 2007 to 2012, and Synchrotron Radiation Research Center, Nagoya University from 2012 to 2014 under the supervision of Professor Tsunehiro Tanaka.

The author wants to express his sincerest gratitude to Professor Tsunehiro Tanaka for the fruitful discussion, insightful suggestion and generosity throughout this study. The author is greatly indebted to Professor Tetsuya Shishido at Tokyo Metropolitan University for his instructive discussion, advices and continuous encouragement. The author makes his gratitude to Professor Kentaro Teramura for his precise comments, and helpful supports. The author would like to demonstrate his gratitude to Professor Yutaka Hitomi at Doshisha University for his support during the first year in Professor Tanaka's lab.

The author also makes grateful acknowledgements to Professor Ning Yan at National University of Singapore, Dr. Siyu Yao and Professor Yuan Kou at Peking University and Professor Shingo Fuchi at Aoyama Gakuin University for our collaboration works. The author shows deep gratitude to Dr. Seiji Yamazoe at University of Tokyo, Dr. Junya Ohyama at Nagoya University, and Dr. Shinya Furukawa at Tokyo Institute of Technology, Professor Tomoko Yoshida at Nagoya University, Professor Hisao Yoshida at Kyoto University, Professor Sakae Takenaka at Kyushu University, Professor Hirofumi Aritani at Saitama Institute of Technology, Professor Takashi Yamamoto at Tokushima University, Professor emeritus Okamoto Atsuhiko at Aichi Synchrotron Center for their continuous encouragement. The author is grateful to Professor Atsushi Satsuma at Nagoya University for his aid in the X-ray diffraction measurements. The author would like to thank Messrs. Akira Yamamoto, Shoji Iguchi, Jun-ichi Hirota, Zheng Wang and Dr. Lidan Deng for fruitful discussion. Many thanks must be dedicated to Messrs. Yasuhiro Higuchi, Hideo Tsuneoka and Dr. Tomoyuki Kitano, who joined Professor Tanaka's lab in the same year, for their discussion and advices. The author would like to express his sincerest gratitude to Professor Masao Tabuchi, Professor Yoshikazu Takeda and Professor Yoshinobu Baba for their insightful advice, encouragement and generosity. The author also would like to thank the staffs in synchrotron radiation facilities, Mr. Kazuo Kato, Dr. Kiyofumi Nitta, Professor Tomoya Uruga, Professor Hajime Tanida at SPring-8 and Dr. Hiroaki Nitani, Mr. Yasuhiro Niwa at Photon Factory, KEK, and Mr. Hiroyuki Morimoto at AichiSR and all the other staffs at SPring-8, Photon Factory, Saga Light Source, UVSOR, and Aichi Synchrotron Center.

Two financial supports, Grant-in-Aid for JSPS Fellows from Japan Society for the Promotion of Science, and Adaptable and Seamless Technology transfer Program through target driven R&D from Japan Science and Technology Agency must be acknowledged.

Finally, the author would like to thank his parents, Mr. Mitsuhiko Asakura and Mrs. Michiko Asakura, for their constant assistance, understanding and generosity.

ASAKURA, Hiroyuki

Nagoya,

December, 2014

CONTENTS

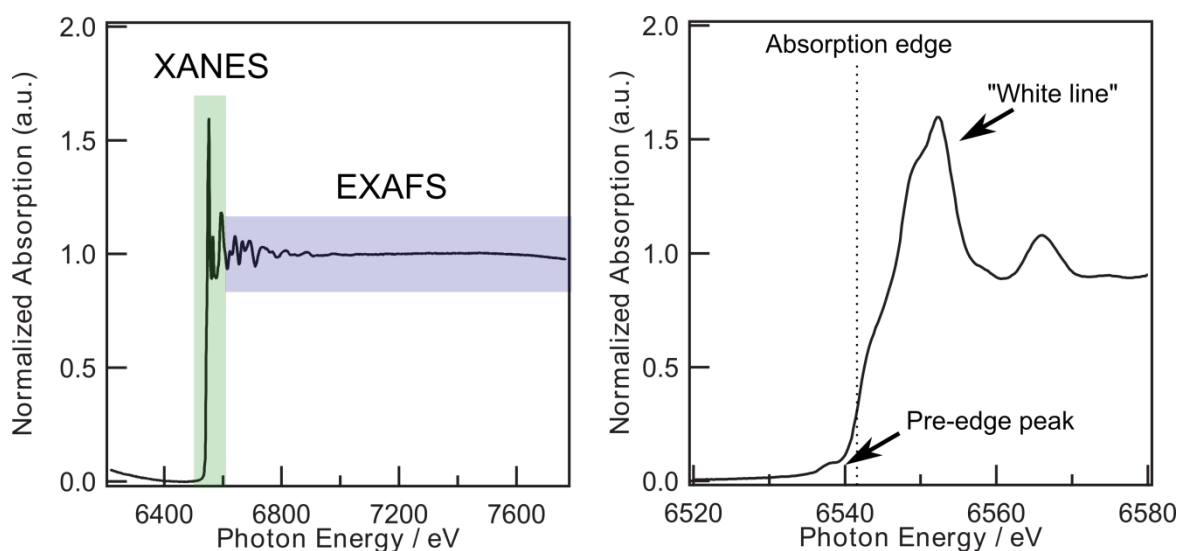
Preface

General Introduction	—————	1
Chapter 1	Structural Analysis of Group V, VI, VII Metal Compounds by XAFS and DFT Calculation	18
Chapter 2	La L ₁ and L ₃ -Edge XANES spectra of Lanthanum Complex Oxides: Experimental and Theoretical Approach to Local Structure	47
Chapter 3	Local Structure and L ₁ and L ₃ -edge XANES spectra of Early Lanthanide Elements in Their Complex Oxides	76
Chapter 4	Local Structure and L ₁ and L ₃ -edge XANES spectra of Late Lanthanide Elements in Their Complex Oxides	101
Chapter 5	In Situ Time-Resolved DXAFS Study of Rh Nanoparticle Formation Mechanism in Ethylene Glycol at Elevated Temperature	121
Chapter 6	Insights into the Formation Mechanism of Rhodium Nanocubes	141
Chapter 7	In Situ Time-Resolved XAFS Study of the Reaction Mechanism of Bromobenzene Homocoupling Mediated by [Ni(cod)(bpy)]	170
Summary	—————	184
List of Publication	—————	187

General Introduction

X-ray Absorption Fine Structure

X-ray absorption fine structure (XAFS) is a fine structure observed in an X-ray absorption spectrum around the absorption edge, which is an abrupt increase of X-ray absorption caused by an interaction between a core electron of an element and an incident X-ray. Thus, XAFS spectrum has element selectivity and exhibits several different absorption edges related to core electrons at the 1s, 2s, 2p or higher levels (*i.e.* K (1s), L₁ (2s), L₂ (2p_{1/2}) or L₃ (2p_{3/2}) edges). The term “XAFS” is used for the fine structure or the X-ray absorption spectrum around the absorption edge itself.



Mn K-edge XAFS spectrum (left) and XANES spectrum (right) of MnO

The XAFS spectrum is usually divided into two regions, X-ray absorption near edge structure (XANES), which is a fine structure around the absorption edge (within about 50 eV from the absorption threshold), and extended X-ray absorption fine structure (EXAFS), which is a fine oscillation observed above the absorption edge (above the XANES region typically up to 1.0 keV from the absorption edge) as illustrated in the graph above (left).

EXAFS derives from the interference between the outgoing photoelectron waves ejected from a core level of an X-ray absorbing atom and the incoming photoelectron waves scattered by the electrons of the neighboring atoms. Thus, the oscillation has information of the character of the surrounding atoms (scattering atom) such as the number of the scattering atoms, the atomic distance

between the X-ray absorbing atom and the scattering atoms, the static and dynamic atomic displacement property (so-called Debye-Waller factor) of the scattering atoms, and the characteristic scattering properties of the neighboring atoms, backscattering factor and phase shift factor, which influence on the scattered photoelectron waves. In addition, the EXAFS oscillation is also affected by the mean free path of the photoelectron, which is the mean travelling length of the photoelectron before inelastic scattering or core electron refilling by X-ray fluorescence process, for example. The formalism is summarized in the EXAFS equation below.^{1,2}

$$\chi(k) = \sum_j \frac{N_j}{kR_j^2} F_j(k) \sin\left(2kR_j + \delta_j(k)\right) \exp(-2k^2\sigma_j^2) \exp\left(-\frac{2R_j}{\lambda(k)}\right)$$

where k is the wavenumber of the photoelectron, N_j is the number of the neighboring atom j , R_j is the atomic distance to the neighboring atom j , $F_j(k)$ and $\delta_j(k)$ are backscattering factor and phase shift factor of the neighboring atom j , σ_j^2 is the atomic displacement parameter of the neighboring atom j , and the $\lambda(k)$ is the mean free path of the photoelectron. This equation represents two essential properties of XAFS. One is the $\lambda(k)$ and R_j^{-2} terms indicate the XAFS oscillation is induced only by the atoms in very short range usually within 5 Å. The other is XAFS oscillation is a sum of sine curves corresponding to each scatterer. This led early XAFS experts to perform Fourier transform on the EXAFS to obtain pseudo radial distribution function for the better and comprehensible interpretation of EXAFS oscillation toward the local structure analysis.³ If one could obtain an EXAFS spectrum experimentally, it became possible to extract physical parameters using curve fitting analysis with the EXAFS equation above. The important point is the estimation of the $F_j(k)$ and $\delta_j(k)$ terms. These parameters can be determined by curve fitting analysis on the standard EXAFS spectra of structurally well-known compounds. However, this strategy is not applicable to the complicated system whose multiple scattering processes (the photoelectron ejected from an X-ray absorbing atom is scattered by two or more neighboring atoms) have significant contribution to the EXAFS oscillation, for example. Then, theoretical simulation codes such as FEFF are used to obtain $F_j(k)$ and $\delta_j(k)$ for further curve fitting process in these days.

XANES reflects a complicated multiple scattering processes of the low energy photoelectron having a relatively long mean free path ejected from an X-ray absorbing atom and the neighboring

atoms, which is the electronic transition from core level to unoccupied states induced by X-ray absorption. XANES region have three main features, the absorption edge energy, the white line, and the pre-edge peak. The absorption edge is interpreted into the starting point of the electronic transition of the core electron to the continuum state, which means the photoelectron gets out of the potential of the X-ray absorbing atom with a finite kinetic energy. It is not easy to determine the absorption edge energy experimentally because of the overlapping absorption phenomena of the electronic transition to several different unoccupied states or complicated multiple scattering effect derived from the large scattering factors $F_j(k)$ for low kinetic energy photoelectron. From the practical point of view of experimental data manipulation, the absorption edge is determined by the first inflection point from the absorption threshold in many cases and it shifts toward higher energy as the oxidation state of the X-ray absorbing atom increases because of the relation between the absorption edge and the binding energy of the core electron. The “white line” usually means an intense peak above the absorption edge, which exhibits significantly larger absorption coefficients than the EXAFS region. This term comes from X-ray absorption experiments in early days taken with photographic plates as X-ray detector. The absorption edge appears as white bands on the plate developed in negative because strong X-ray absorption at the absorption edge of some samples prevent the plate from X-ray exposure. The white line is typically observed in L_3 -edge measurement of metal atoms with many unoccupied d states. In some cases, the first intense peak above the absorption edge of transition metal K-edge XANES spectra of their oxides are also referred to as white line. The pre-edge peak is one or more peaks observed below the absorption edge. The origin is the electronic transition to unoccupied states having p character for the K or L_1 -edge XANES spectra because only the electric dipole transition from $1s$ or $2s$ states to p states is allowed. The p character is usually introduced into the unoccupied states related to the pre-edge region via p - d hybridization induced by specific coordination environment. For example, an X-ray absorbing atom in a tetrahedral coordination environment gets much stronger p - d hybridization effect than that in an octahedral like environment. Several examples of the interpretation of absorption edge shift, pre-edge peak, or other characteristic features of XANES spectra are discussed in the following section.

Brief History of X-ray Absorption Spectroscopy

The discovery of X-ray reported by Prof. Röntgen in 1895⁴ has astonished scientists in the world and opened a brand new vast fertile field of X-ray diffraction, X-ray scattering, X-ray absorption, and other X-ray related phenomena of materials. Although there are brilliant literatures on the history of the X-ray absorption spectroscopy,^{5, 6} I would like to overview a brief history of X-ray Absorption Fine Structure (XAFS).

In 1913, Maurice de Broglie first reported X-ray absorption edges, which were proved to be the K-edge of Ag and Br in the photographic emulsion⁷, when he scanned a photographic plate with an incident X-ray monochromated by a single crystal mounted on a rotatable cylinder barometer with an angular velocity of about 2 degree per hour. In 1920, Fricke first observed the fine structure of K-edge X-ray absorption spectra of Al, P, S, Sc, Ti, and V,⁸ which is called X-ray absorption near edge structure (XANES) today and Kossel proposed the first theory on the X-ray absorption based on the transition of electrons to higher unoccupied orbitals of the X-ray absorbing atom,⁹ which is similar to the present theory on XANES spectra. In 1931 and 1932, Kronig explained the extended X-ray absorption fine structure observed beyond a few hundred eV above the absorption edge,^{10, 11} which cannot be explained in the Kossel's theory. The Kronig theory based on long range order (LRO) of the well-ordered crystal successfully explained the fine structure of the experimental extended X-ray absorption spectra, the "Kronig structure". However, the X-ray absorption spectra of As, Se, Br, Zn, Hg, Xe, and Kr in solid, vapor or solution form reported by Hanawalt¹² inspired Kronig to also develop a theory based on short range order (SRO) for each molecule.¹³ The SRO theory have been developed by Petersen,^{14, 15} Hartree,¹⁶ Hayashi, Sawada,¹⁷ Shiraiwa,¹⁸ Kostarev, Kozlenkov and many other scientists successively, simultaneously or separately as described in the Lytle's essay.⁵ The breakthrough of the modern EXAFS theory was done by Sayer, Stern, and Lytle to provide clear pictures of Fourier transform of EXAFS spectra of crystalline Ge and amorphous Ge to demonstrate that the short range order theory is appropriate for the interpretation of EXAFS³. The theory on X-ray absorption near edge structure (XANES) theory has been also developing. Based on the multiple scattering theory,¹⁹ Rehr *et al.* have developed a sophisticate X-ray absorption simulation code, FEFF²⁰⁻²² named from effective backscattering amplitude, f_{eff} , which realizes

quantitative analysis on EXAFS spectra and at least qualitative analysis on XANES spectra. Other theoretical calculation packages based on density functional theory (DFT), configuration interaction (CI) method have been also successfully applied to analysis on XANES spectra. For example, Wien2k, a program package calculating electronic structure of solids based on the full potential (linearized) augmented plane-wave and local orbitals method, or ORCA, another program package based on DFT, molecular orbital theory, and sophisticated CI or coupled cluster methods can semi-quantitatively predict the experimental data and provide crucial information for the interpretation of origin and change in XANES spectra.

X-ray Absorption Near Edge Structure and Local Structure

After the publication of one of the most important paper for the interpretation of EXAFS spectrum via Fourier transform by Sayers, Stern, and Lytle,³ enormous amount of application of X-ray spectroscopy have been performed in almost every scientific fields such as physics, chemistry, biology, or earth science. On the other hand, X-ray absorption near edge structure (XANES) has been also attracting scientists in various fields.

In 1960, Van Nordstrand reported several examples of XANES spectroscopy of four 3d transition metal elements, Mn, Co, Cr, and Ti for the study of solid catalysts²³. Even though the X-ray absorption spectrometer was simply made from a commercial X-ray diffractometer by putting a quartz single crystal onto the goniometer as a single crystal monochromator, the quality of the spectra of the samples in the XANES region are impressively good enough to explain the well-known spectral features such as pre-edge peaks, absorption edge shift. For example, he showed a figure of distinct types of X-ray absorption spectra of Mn in various chemical states and associated the absence of the pre-edge peak of the K-edge XANES spectrum of $\text{MnCl}_2 \cdot 4\text{H}_2\text{O}$ with a single octahedral coordination sphere of Mn, and the presence of an intense pre-edge peak of that of KMnO_4 with the tetrahedral manganese ions. He also pointed out XANES spectra are not determined or influenced by the long range crystallinity from the identity of spectra of aqueous solution and those of corresponding crystalline hydrate salts, referring to the reports from Beeman, Bearden²⁴ and Böke.²⁵ Furthermore, the effect of valence state to XANES spectra is also discussed on the shifts of the principal peak of XANES spectra of $\text{Mn}(\text{acac})_3$ and $\text{Mn}(\text{C}_2\text{H}_3\text{O}_2)_3 \cdot 3\text{H}_2\text{O}$ to higher energies

against that of $\text{Mn}(\text{acac})_2 \cdot 2\text{H}_2\text{O}$ and $\text{Mn}(\text{C}_2\text{H}_3\text{O}_2)_2 \cdot 4\text{H}_2\text{O}$. The XANES spectra of manganese oxides, MnO , Mn_3O_4 , Mn_2O_3 , and MnO_2 , also supported the hypothesis of the dependency of the absorption edge energy on the valence states. He extended the study to Co, Cr and Ti including their catalysts and also found a number of interesting points. For example, in comparison among the XANES spectra of $\text{K}_3[\text{Cr}(\text{NCS})_6]$, $\text{NH}_4[\text{Cr}(\text{NH}_3)_2(\text{SCN})_4]$, $\text{trans-}[\text{Cr}(\text{en})_2(\text{SCN})_2]\text{NCS}$, and $[\text{Cr}(\text{en})_3](\text{NCS})_3$, he associated the second prominent peak observed on that of $\text{K}_3[\text{Cr}(\text{NCS})_6]$ to the Cr-C distances. An application of Mn K-edge XANES spectroscopy on Mn catalysts supported on activated carbon or silica gel clearly demonstrated that the Mn species remains on silica gel as permanganate species, but turned to be reduced to MnO_2 or some other hydrous manganic oxide on active carbon, which cannot be distinguished by X-ray diffraction because of the absence of long range order. On Co catalysts, highly active catalysts had CoO species, but bad catalysts had metallic Co. For Co-Mo on alumina materials which may be catalysts for hydrodesulfurization, the state of Co was found to have a strong interaction with alumina support, not with the coexisting molybdena. He also investigated some titania catalysts and concluded tetrahedral Ti species were important for some catalysis.

Although there are enormous amount of brilliant literature related to XANES spectroscopy, from the viewpoint of focusing on a specific metal element, one can give several seminal papers to this field. Farges *et al.* reported Ti K-edge XANES spectra of various Ti compounds which have different coordination number and local structure, and their mixtures.²⁶ They carefully analyzed the XANES spectra according to the coordination number of O atoms, the pre-edge peak height, position, area, with the aid of theoretical simulation; and discussed on the peak assignment, and quantitative analysis of the pre-edge peak. Their criteria for evaluation of the pre-edge peak at Ti K-edge XANES spectra have been widely accepted. Wong *et al.* measured V K-edge XANES spectra of various V oxides and other compounds such as vanadate compounds, vanadyl compounds, vanadium intermetallics which have a wide range of formal oxidation states, coordination geometries, with various ligands.²⁷ They paid an attention to the energy positions of the rising edge, the pre-edge, the absorption edge, and the second peak above the absorption edge which is assigned to the electric dipole transition from 1s to 4p and found a clear linear relationship against the formal charge of the vanadium oxide samples. They also found a correlation between the pre-edge peak area and the average bond length between V and the adjacent atoms. Westre *et al.* have performed systematic

survey on the pre-edge features at the Fe K-edge XANES spectra of many ferrous and ferric model complexes which have different spin state, oxidation state, geometry or ligands.²⁸ The detailed multiplet analysis by experiments and theoretical simulation based on density functional theory gave a comprehensive view of the origin of the “1s → 3d” pre-edge peaks as both of electric quadrupole and dipole (from 3d-4p mixing) transitions. They also proposed a general trend of 3d-4p mixing of the unoccupied states from DFT calculation on several structural models of Fe complexes. Farges *et al.* also gave great contribution to the interpretation of the Mn,²⁹ Ni³⁰ and other K-edge XANES spectra. For example, on the study of the coordination environment of Ni in Ni silicate glasses, they performed systematic survey on the high resolution Ni K-edge XANES spectra of various Ni compounds with 4, 5, and 6-coordinated Ni species.³⁰ A detailed analysis on the small pre-edge peak by careful background subtraction clarified the correlation among the average Ni-O distances, the pre-edge peak heights and positions. They applied the findings to the determination of the local environment of Ni species in several Ni silicate glasses and found the average coordination number of Ni was about 5 for the glass samples discussed in the literature. On the other hand, Cu, Zn, or Ga K-edge XANES spectra usually exhibit no or very weak pre-edge peaks in any form. However, for example, Nishi *et al.* reported curve fitting analysis on the Ga K-edge XANES spectra of Ga oxides or Ga/SiO₂ catalysts having different local environments.³¹ They analyzed the characteristic two large peaks above the absorption edge at the Ga K-edge XANES spectra by curve fitting analysis with a set of Gaussian and arctangent functions and estimated the contribution of the GaO₄ tetrahedra and GaO₆ octahedra from the extracted peak areas. The XANES analysis results were consistent to a similar analysis on EXAFS oscillation of the same samples.

For the metal elements in the fifth period of the periodic table, Ru, Rh, Pd, or Ag, which are practically or potentially important to industrial use such as catalysts for exhaust gas from factories or vehicles, or organic synthesis, exhibit a bit less characteristic spectra as their K-edge XANES than that of 3d metal elements. However, the shift of the absorption edge observed in these elements is quite informative to track the redox reaction of the metal species used in various catalysts, which is essentially important for chemical reaction. For example, Dohmae *et al.* investigated the reduction speed of Rh species supported on Al₂O₃ with *in situ* time-resolved XAFS.³² The rapid shift of the Rh K-edge absorption edge to lower energy in about 2 minutes after the gas switching from 20% O₂/He

to 3% H₂/He at 523 K was clearly observed by dispersive XAFS technique. The pre-edge feature of Ru K-edge XANES spectra was reported by Miura *et al.* They measured the Ru K-edge XAFS spectra of Ru catalysts effective for C-C coupling reaction of alkyne with acrylates and found the Ru/CeO₂, which exhibits a predominant catalytic activity, only shows a prominent pre-edge peak among other Ru catalysts such as Ru/SiO₂, Ru/Al₂O₃, Ru/TiO₂, Ru/MgO.³³

On the other hand, the XANES spectra of group 4 – 7 elements have been also studied in detail. Kanai *et al.* reported Zr K-edge XANES spectra of ZrO₂, ZrSiO₄, Zr(acac)₄, Zr(OBu^t)₄ and several ZrO₂/SiO₂ catalysts and observed pre-edge peaks on Zr species having tetrahedral coordination sphere.³⁴ Tanaka *et al.* analyzed Nb oxides supported on Al₂O₃ by means of XAFS.³⁵ The Nb K-edge XANES spectrum shows a relatively small but distinct shoulder peak near the absorption edge, which indicates presence of tetrahedral Nb species. They also pointed out two distinct peaks above the absorption edge may represent the two Nb=O bonds in comparison with the similar results of Nb/SiO₂. Aritani *et al.* presented Mo K-edge XANES spectra of various Mo compounds and several MoO₃-MgO binary oxides after high temperature calcination or reduction with hydrogen.³⁶ They found a similar systematic change of the pre-edge peak to that of 3d metal K-edge XANES spectra, that is the Mo species in tetrahedral geometry exhibits larger pre-edge peak than that in octahedral geometry.

There are few papers on Hf L₁-edge XANES spectrum, but Uehara *et al.* used Hf L₁-edge XANES spectra to analyze high-*k* gate dielectric material, Hf(Si)O_x ultrathin films.³⁷ They did not mention in the literature, but observed a clear pre-edge peak at the Hf L₁-edge which might be related to the local structure of Hf in the film. For Ta, W, and Re, Chen *et al.* analyzed local structure of Ta in Ta oxides supported on Al₂O₃, SiO₂, TiO₂, ZrO₂ catalysts by Ta L₁-edge XANES spectra and found almost all of the Ta exists as 6-coordinated Ta species except for Ta₂O₅/SiO₂ which have tetrahedral Ta species in its dehydrated form.³⁸ Yamazoe *et al.* used W L₁ and L₃-edge XAFS spectra to identify the state of W species loaded on TiO₂ catalyst for photo-oxidation of NH₃ by quantitative analysis the pre-edge peak area of W L₁-edge XANES spectra and *ab initio* DFT calculation of W model species in various geometries.³⁹ Oikawa *et al.* utilized Re L₁-edge XANES spectra for structural analysis on a new heterogeneous olefin metathesis catalyst and found the catalytically active Re species has a tetrahedral local structure.⁴⁰

Furthermore, L-edge XAFS spectra of heavier precious metals such as Ir, Pt, and Au also exhibit interesting features. Lytle *et al.* reported L₃-edge XANES spectra of Ir, Pt, and Au metals and their compounds such as oxides and found the peak area of the difference spectra are related to differences in the electronic structure of the X-ray absorbing atoms.⁴¹ They also employed this technique to the highly dispersed metal catalysts such as 1 wt% Pt/Al₂O₃ or 1wt% Ir/Al₂O₃ under He or O₂ and successfully estimated the oxidation state of the metal clusters by means of L₃-edge XANES spectroscopy. Mansour *et al.* proposed a curve fitting procedure on Pt L₂ and L₃-edge XANES spectra for quantitative analysis of the electronic states⁴² and also applied the procedure to Pt/Al₂O₃ and Pt/SiO₂ catalysts.⁴³ Asakura *et al.* found another interesting phenomenon of a drastic change of the Pt L₃-edge XANES spectrum caused by adsorption of H₂ onto Pt nanoparticles, which can be used to quantify the amount of adsorbed H₂.⁴⁴ Thus, L-edge XANES spectra of important heavy precious metals such as Ir, Pt or Au are sensitive to their electronic structure.

In brief, XANES spectra of almost all the elements were investigated by many researchers in the world for the interesting property themselves and practical application to obtain element specific information of the local and electronic structure in various materials, which could be a key to clarify their functions or properties. However, in comparison to the 3d transition metal elements, systematic and comprehensive survey on the L-edge XANES spectra of 4d and 5d transition metal or lanthanide elements are still relatively scarce.

X-ray Absorption Near Edge Structure of Lanthanide Elements

One of the characteristic features of L-edge XANES spectra of lanthanide elements (Ln) is large absorption edge shift depending on the electronic states of the target elements. For example, Tanaka and Baba *et al.* reported *in situ* Yb L₂-edge XANES spectra of Yb introduced into Y-zeolite during decomposition of Yb(II,III) amides species to Yb(II,III) imides, and then Yb(III) nitride by heating and evacuation. A large shift of the absorption edge of Yb²⁺ and Yb³⁺, *ca.* 10 eV, enables a clear quantification of Yb species at different oxidation states.^{45, 46} Yoshida *et al.* evaluated the valence state of the highly dispersed Ce species supported on silica quantitatively by curve fitting analysis on Ce L₃-edge XANES spectra.⁴⁷ Again, a large edge shift dependent on the electronic state of Ce enables them to quantify the oxidation number of Ce supported on silica. Shioi *et al.* used the Eu

L₃-edge XANES spectra to track the change of the oxidation state of the luminescence center of Eu phosphor⁴⁸ and evaluated the sample spectra with linear combination fitting analysis based on that of standard compounds to determine the ratio of the Eu²⁺ and Eu³⁺.

On the other hand, there are less reports on the dependency of Ln L-edge XANES spectra on the local structure of Ln species. Antonio *et al.* measured Er and Lu L₁ and L₃-edge XAFS spectra of Er or Lu incorporated into sodium silicate glasses to determine the local structure of the Er and Lu atoms.⁴⁹ Curve fitting analysis on the L₃-edge EXAFS spectra clarified the relatively small number of coordinated O atoms, 6, but they also used each XANES spectrum and its second derivative to evaluate the local symmetry in the analogy with the W L₃-edge XANES spectra and mentioned on the possibility of 5 or 7 coordinated environment in combination with the presence of the pre-edge peak at the L₁-edge XANES, which indicates some distortion from inversion symmetry. D'Angelo *et al.* reported a series of papers on Ln L-edge EXAFS⁵⁰⁻⁵⁴ and XANES⁵⁵⁻⁵⁷ spectra of their aqueous complexes and illustrated the solvation model of the Ln aqueous or multidentate ligand complexes from La to Lu. They analyzed the XANES spectra in combination with molecular dynamics or elaborated XANES fitting procedure with MXAN,^{58,59} and obtained plausible structural parameters which are consistent to the EXAFS results. They also pointed out the L₃-edge XANES spectra is sensitive to the second shell around the X-ray absorbing atoms.

However, systematic survey on a specific lanthanide element focused on the local environment is relatively scarce. As well known in the K-edge XANES spectra of 3d transition metal elements, the author suppose the L₁ and L₃-edge XANES spectra of lanthanide elements would have an interesting relationship to the local structure of lanthanide elements.

Time-resolved Measurement of X-ray Absorption Fine Structure

The most common XAFS measurement is operated in the so-called step scanning mode, which is realized by a cycle of rotation of a monochromator to change the incident X-ray energy and data acquisition at each energy point for a certain time with X-ray detectors such as ion chamber or solid state detector, and rotation of the monochromator, and so on.

In 1981, a fast XAFS data acquisition technique is proposed by Matsushita *et al.* They obtained wavelength dispersive X-ray by a curved crystal and measured the X-ray intensity distribution

behind the focus in the presence and absence of a specimen at the focusing point to construct XAFS spectrum.⁶⁰ For this technique called dispersive XAFS (DXAFS) at present, they used an X-ray film as the detector, and a XAFS spectrum of Cu foil was obtained in 0.1 seconds at that time. In these days, the DXAFS techniques are realized with position sensitive detectors such as X-ray CCD cameras. Frahm also developed another technique called quick XAFS (QXAFS) in 1988, simply by moving a conventional X-ray monochromator continuously, and obtained typical EXAFS spectra of Fe and Cu foils consistent to that measured in step scanning mode within 10 seconds covering an energy region up to 800 eV.⁶¹ He also pointed out the quick scanning mode is also applicable to XAFS measurement in fluorescent mode. These experimental techniques enable us to track the fast change of the samples and opened enormous application of XAFS spectroscopy to transient chemical reaction. From a few recent examples, Yamamoto *et al.* directly observed redox dynamics of high performance oxygen storage capacitor, CeO₂-ZrO₂, by means of D XAFS technique at the both of Ce L₃-edge and Zr K-edge.⁶² They discussed the diffusion process of oxygen indirectly observed via the redox phenomena of Ce and Zr. Uemura *et al.* investigated the redox behavior of Pt₃Sn or PtSn nanoparticles supported on Al₂O₃ by means of *in situ* time-resolved XAFS.^{63, 64} They found the sensitivity of Pt to oxidation was strongly affected by the amount of coexisting Sn species on the alumina.

The author applied these time-resolved XAFS technique to two interesting applications for the elucidation of the formation mechanism of Rh metal nanoparticles in polyol process and the identification of intermediate species of bromobenzene homocoupling reaction mediated with a Ni complex catalyst.

Needless to say, a number of scientists have been paying attention to fascinating properties of nanoparticles induced by the quantum effect, such as catalytic activity, luminescence, and surface plasmon resonance, and have already established various methods to prepare small, well-structured, and monodisperse nanoparticles. The formation mechanism is also investigated by analyzing the formed nanoparticles with, TEM, SEM, and so forth. However, these techniques are only applicable to the result of the particle formation and cannot provide direct evidence on the formation mechanism of nanoparticles. Then, *in situ* spectroscopy has been applied to the formation mechanism of nanoparticles such as SAXS, XRD, and XAFS. Harada *et al.* used *in situ*

time-resolved SAXS technique to explore the formation process of several metal nanoparticles in various environments. They analyzed the formation of Rh and Pd nanoparticles in aqueous ethanol solution of poly(*N*-vinyl-2-pyrrolidone) (PVP) during photoreduction by *in situ* time-resolved SAXS measurements.⁶⁵ The kinetic analysis based on the SAXS spectra proved the first stage of the Rh nanoparticle formation was autocatalytic nucleation and the second stage was the Ostwald ripening process. On the other hand, in the case of Pd nanoparticles, the reduction finished quickly and the main process of the nanoparticle formation is ascribed to the particle growth step based on the Ostwald ripening. They also reported similar analyses on Ag,⁶⁶ Pt and Au.⁶⁷ Ohyama *et al.* reported *in situ* observation of formation of Rh or Au nanoparticles by means of DXAFS and very fast QXAFS techniques.⁶⁸⁻⁷¹ They revealed photodeposition process of Rh metal nanoparticles on TiO₂ from Rh³⁺ aqueous solution in the presence of methanol as a sacrificial reductant. In combination with ICP analysis for the quantification of remaining Rh cation in the suspension during the photodeposition, they proposed the Rh nanoparticles in a uniform size appear at a constant rate with no apparent growth of the nanoparticles. They also employed millisecond time-resolved QXAFS measurement to clarify the formation mechanism of Au nanoparticles from HAuCl₄ solution in the presence of equimolar dodecanethiol, and revealed some part of Au precursor was reduced to Au⁺ before the nanoparticle formation, the kinetics of the formation mechanism of Au nanoparticles.

Identification of an intermediate complex generated during homogeneous catalytic reaction mediated by an organometallic complex is an important point to demonstrate the reaction mechanism of the catalysis. For that purpose, the most common and essential approach is to isolate the intermediate compound, recrystallize it in a single crystal form, and measure and solve the diffraction patterns. However, both processes of isolation and recrystallization are usually difficult and sometimes impossible. In addition, as the geometric and electronic structure of the dissolved complex could be different from that in solid form, the recrystallized compounds could be different from the true intermediate species because of the absence of the solvation effect. Even though the structural analysis by EXAFS spectroscopy is limited to the first or second shells around the X-ray absorbing atoms, *in situ* time-resolved XAFS measurement could be one solution to shed light on the intermediate species. The main problem of this approach is that the XAFS spectrum has only averaged information of the chemical species during the reaction and one cannot assume each

spectrum consists of a specific species. However, a series of time-resolved spectra can be analyzed in the aid of kinetics and statistics such as reaction rate equation or factor analysis to perform a plausible analysis on the experimental data.

Outline of the Present Thesis

The author found a correlation among the local configuration, the characteristic features observed at K, L₁ or L₃-edge XANES spectra for group 5, 6, 7 metal and lanthanide elements in their complex oxide forms and proposed two interpretation strategies for *in situ* time-resolved XAFS measurements aiming to elucidate the formation mechanism of Rh metal nanoparticles or the intermediate complex in catalytic reaction with organometallic complex.

For the former theme, a systematic survey of K, L₁ and/or L₃-edge XANES spectra of Nb, Mo, Ta, W, Re complex oxides or compounds was performed. The pre-edge peak areas at the Nb or Mo K-edge or Ta, W, Re L₁-edge XANES spectra, and the width of the split white lines at the Nb, Mo, Ta, W, Re L₃-edge XANES spectra depend on the local structure of each element, namely on the coordination number of adjacent O atoms and/or crystallographic distortion of the local environment of the element. DFT calculation on the primitive hydride complex models also supported the experimentally observed dependence of the characteristic features of XANES spectra on the local environments. This result encouraged the author to extend the idea to the XANES study on lanthanide elements.

A systematic survey on the L₁ and L₃-edge XANES spectra of lanthanide elements, La, Pr, Nd, Sm, Eu, Gd, Ho, Er, and Yb in their complex oxide forms, demonstrated the pre-edge peak area at the Ln L₁-edge XANES spectra depends on the change of the local configuration. The group 5, 6, 7 elements usually take 4 to 6 adjacent atoms, which can be classified into tetrahedral, trigonal bipyramidal, or octahedral geometries, but these lanthanide elements usually take 7 to 12 adjacent atoms, which is completely different from the group 5, 6, 7 elements. Thus, a new primitive, but practical indexing methodology for parameterization of the local configuration only from the geometry is introduced for the interpretation of the complicated local configuration. On the Ln L₃-edge XANES spectra, even though the lifetime broadening of these lanthanide elements are a bit smaller than or similar to that of Ta (4.88 eV), W (4.98 eV), and Re (5.04 eV), (La: 3.41 eV, Pr: 3.60

eV, Nd: 3.65 eV, Sm: 3.86 eV, Eu: 3.91 eV, Gd: 4.01 eV, Ho: 4.26 eV, Er: 4.35 eV, Yb: 4.60 eV), the energy resolution in this range from 5.5 keV to 9.0 keV is lower than in the range above 10 keV (Ta L₃-edge) because typical Si crystal plane to monochromate the incoming white X-ray from synchrotron source is Si(111) in the lower range, but Si(311) in the higher energy. This means energy resolution of the lanthanide XANES spectra could be lower than that of Ta, W, Re in practice. This brings a difficulty to use derivative spectra of lanthanide XANES to estimate the energy splitting of the unoccupied states as performed in group 5, 6, 7 elements. It was overcome simply by evaluating the full width at half maximum (fwhm) of the white line of the Ln L₃-edge XANES spectra by curve fitting analysis with one pseudo-Voigt and one arctangent functions. The fwhm values also show correlation with the change of the local structure. The relationship was also supported by DFT calculation and other theoretical simulation based on multiple scattering theory.

On the latter themes, the author tried to clarify the reaction mechanism and the intermediate transient chemical species during Rh nanoparticles formation in the absence and presence of bromide protecting reagents or during homocoupling reaction of bromobenzene into biphenyl with Ni(cod)₂ as a homogeneous catalyst by means of *in situ* time-resolved XAFS technique.

The author investigated the formation mechanism of Rh metal nanoparticles prepared by a typical polyol process by means of *in situ* time-resolved XAFS and ICP-MS techniques. In the reaction condition, the formation process of Rh nanoparticles obeys on a first order kinetics, which indicates Rh nanoparticles appear consecutively in a uniform size without any observable transient chemical species and they do not aggregate with each other. On the other hand, in the presence of quaternary ammonium bromides as structure control reagents, the Rh nanoparticles turned to be cubic form. To clarify the drastic change of the Rh nanoparticles structure, the author also applied *in situ* time-resolved XAFS technique to the Rh nanocube formation process and found a detailed picture of the formation mechanism such as formation of Rh bromide clusters, one of the important transient chemical species in the aid of ICP-MS, XRD, UV/Vis, and TEM.

The main target of the latter experiment, a transient Ni dimer complex previously proposed from the detailed reaction results,⁷² could not be caught at this time, but, spectral deconvolution of a series of EXAFS spectra based on kinetic equations provided an intermediate spectrum, which can be assigned to an intermediate Ni complex generated by oxidative addition of bromobenzene. A curve

fitting analysis on the extracted EXAFS spectrum suggested a possible significant coordination of solvent, which cannot be reached by the structural analysis on the isolated compounds.

References

- (1) Lytle, F. W.; Sayers, D. E.; Stern, E. A., *Phys. Rev. B*, **1975**, *11*, 4825-4835.
- (2) Stern, E. A.; Sayers, D. E.; Lytle, F. W., *Phys. Rev. B*, **1975**, *11*, 4836-4846.
- (3) Sayers, D. E.; Stern, E. A.; Lytle, F. W., *Phys. Rev. Lett.*, **1971**, *27*, 1204-1207.
- (4) Röntgen, W. C., *Science*, **1896**, *3*, 227-231.
- (5) Lytle, F., *J. Synchrotron Rad.*, **1999**, *6*, 123-134.
- (6) Stumm von Bordwehr, R., *Ann. Phys. Fr.*, **1989**, *14*, 377-465.
- (7) de Broglie, M., *C. R. Acad. Sci.*, **1913**, 924-926.
- (8) Fricke, H., *Phys. Rev.*, **1920**, *16*, 202-215.
- (9) Kossel, W., *Z. Physik*, **1920**, *1*, 119-134.
- (10) Kronig, R. d., *Z. Physik*, **1932**, *75*, 191-210.
- (11) Kronig, R. d., *Z. Physik*, **1931**, *70*, 317-323.
- (12) Hanawalt, J. D., *Phys. Rev.*, **1931**, *37*, 715-726.
- (13) Kronig, R. d., *Z. Physik*, **1932**, *75*, 468-475.
- (14) Petersen, H., *Z. Physik*, **1933**, *80*, 258-266.
- (15) Petersen, H., *Z. Physik*, **1932**, *76*, 768-776.
- (16) Hartree, D. R.; de L. Kronig, R.; Petersen, H., *Physica*, **1934**, *1*, 895-924.
- (17) Sawada, M.; Tsutsumi, K.; Shiraiwa, T.; Obashi, M., *J. Phys. Soc. Jpn.*, **1955**, *10*, 464-468.
- (18) Shiraiwa, T.; Ishimura, T.; Sawada, M., *J. Phys. Soc. Jpn.*, **1958**, *13*, 847-859.
- (19) Lee, P. A.; Pendry, J. B., *Phys. Rev. B*, **1975**, *11*, 2795-2811.
- (20) Rehr, J. J.; Kas, J. J.; Vila, F. D.; Prange, M. P.; Jorissen, K., *Physical Chemistry Chemical Physics*, **2010**, *12*, 5503-5513.
- (21) Rehr, J. J.; Kas, J. J.; Prange, M. P.; Sorini, A. P.; Takimoto, Y.; Vila, F., *C. R. Phys.*, **2009**, *10*, 548-559.
- (22) Rehr, J. J.; Albers, R. C., *Rev. Mod. Phys.*, **2000**, *72*, 621-654.
- (23) Nordstrand, R. A. V., The Use of X-Ray K-Absorption Edges in the Study of Catalytically Active Solids. In *Advances in Catalysis*, D.D. Eley, P. W. S.; Paul, B. W., Eds. Academic Press: 1960; Vol. Volume 12, pp 149-187.
- (24) Beeman, W. W.; Bearden, J. A., *Phys. Rev.*, **1942**, *61*, 455-458.
- (25) Böke, K., *Z. Phys. Chem.*, **1957**, *10*, 59-82.
- (26) Farges, F.; Brown, G. E.; Rehr, J. J., *Phys. Rev. B*, **1997**, *56*, 1809-1819.
- (27) Wong, J.; Lytle, F. W.; Messmer, R. P.; Maylotte, D. H., *Phys. Rev. B*, **1984**, *30*, 5596-5610.
- (28) Westre, T. E.; Kennepohl, P.; DeWitt, J. G.; Hedman, B.; Hodgson, K. O.; Solomon, E. I., *J. Am. Chem. Soc.*, **1997**, *119*, 6297-6314.

- (29) Farges, F., *Phys. Rev. B*, **2005**, *71*, 155109.
- (30) Farges, F.; Brown Jr, G. E.; Petit, P. E.; Munoz, M., *Geochim. Cosmochim. Acta*, **2001**, *65*, 1665-1678.
- (31) Nishi, K.; Shimizu, K.; Takamatsu, M.; Yoshida, H.; Satsuma, A.; Tanaka, T.; Yoshida, S.; Hattori, T., *J. Phys. Chem. B*, **1998**, *102*, 10190-10195.
- (32) Dohmae, K.; Nagai, Y.; Tanabe, T.; Suzuki, A.; Inada, Y.; Nomura, M., *Surf. Interface Anal.*, **2008**, *40*, 1751-1754.
- (33) Miura, H.; Shimura, S.; Hosokawa, S.; Yamazoe, S.; Wada, K.; Inoue, M., *Adv. Synth. Catal.*, **2011**, *353*, 2837-2843.
- (34) Kanai, H.; Okumura, Y.; Utani, K.; Hamada, K.; Imamura, S., *Catal. Lett.*, **2001**, *76*, 207-211.
- (35) Tanaka, T.; Yoshida, T.; Yoshida, H.; Aritani, H.; Funabiki, T.; Yoshida, S.; Jehng, J.-M.; Wachs, I. E., *Catal. Today*, **1996**, *28*, 71-78.
- (36) Aritani, H.; Tanaka, T.; Funabiki, T.; Yoshida, S.; Kudo, M.; Hasegawa, S., *J. Phys. Chem.*, **1996**, *100*, 5440-5446.
- (37) Uehara, Y.; Kawase, K.; Tsuchimoto, J. i.; Shibano, T., *J. Electron. Spectrosc. Relat. Phenom.*, **2005**, *148*, 75-79.
- (38) Chen, Y.; Fierro, J. L. G.; Tanaka, T.; Wachs, I. E., *J. Phys. Chem. B*, **2003**, *107*, 5243-5250.
- (39) Yamazoe, S.; Hitomi, Y.; Shishido, T.; Tanaka, T., *J. Phys. Chem. C*, **2008**, *112*, 6869-6879.
- (40) Oikawa, T.; Ookoshi, T.; Tanaka, T.; Yamamoto, T.; Onaka, M., *Microporous Mesoporous Mater.*, **2004**, *74*, 93-103.
- (41) Lytle, F. W.; Wei, P. S. P.; Greigor, R. B.; Via, G. H.; Sinfelt, J. H., *J. Chem. Phys.*, **1979**, *70*, 4849-4855.
- (42) Mansour, A. N.; Cook, J. W.; Sayers, D. E., *J. Phys. Chem.*, **1984**, *88*, 2330-2334.
- (43) Mansour, A. N.; Cook Jr, J. W.; Sayers, D. E.; Emrich, R. J.; Katzer, J. R., *J. Catal.*, **1984**, *89*, 462-469.
- (44) Asakura, K.; Kubota, T.; Chun, W. J.; Iwasawa, Y.; Ohtani, K.; Fujikawa, T., *J. Synchrotron Rad.*, **1999**, *6*, 439-441.
- (45) Tanaka, T.; Hanada, T.; Yoshida, S.; Baba, T.; Ono, Y., *Jpn. J. Appl. Phys.*, **1993**, *32*, 481.
- (46) Baba, T.; Hikita, S.; Koide, R.; Ono, Y.; Hanada, T.; Tanaka, T.; Yoshida, S., *J. Chem. Soc. Faraday Trans.*, **1993**, *89*, 3177-3180.
- (47) Yoshida, H.; Yuliati, L.; Hamajima, T.; Hattori, T., *Mater. Trans.*, **2004**, *45*, 2062-2067.
- (48) Shioi, K.; Hirosaki, N.; Xie, R.-J.; Takeda, T.; Li, Y. Q., *J. Alloy. Compd.*, **2010**, *504*, 579-584.
- (49) Antonio, M. R.; Soderholm, L.; Ellison, A. J. G., *J. Alloy. Compd.*, **1997**, *250*, 536-540.
- (50) Persson, I.; Damian Risberg, E.; D'Angelo, P.; De Panfilis, S.; Sandström, M.; Abbasi, A., *Inorg. Chem.*, **2007**, *46*, 7742-7748.
- (51) D'Angelo, P.; De Panfilis, S.; Filippini, A.; Persson, I., *Chem. Eur. J.*, **2008**, *14*, 3045-3055.

- (52) Persson, I.; D'Angelo, P.; De Panfilis, S.; Sandström, M.; Eriksson, L., *Chem. Eur. J.*, **2008**, *14*, 3056-3066.
- (53) Lundberg, D.; Persson, I.; Eriksson, L.; D'Angelo, P.; De Panfilis, S., *Inorg. Chem.*, **2010**, *49*, 4420-4432.
- (54) D'Angelo, P.; Zitolo, A.; Migliorati, V.; Chillemi, G.; Duvail, M.; Vitorge, P.; Abadie, S.; Spezia, R., *Inorg. Chem.*, **2011**, *50*, 4572-4579.
- (55) D'Angelo, P.; Zitolo, A.; Migliorati, V.; Mancini, G.; Persson, I.; Chillemi, G., *Inorg. Chem.*, **2009**, *48*, 10239-10248.
- (56) D'Angelo, P.; Zitolo, A.; Migliorati, V.; Persson, I., *Chem. Eur. J.*, **2010**, *16*, 684-692.
- (57) D'Angelo, P.; Migliorati, V.; Spezia, R.; De Panfilis, S.; Persson, I.; Zitolo, A., *Phys. Chem. Chem. Phys.*, **2013**, *15*, 8684-8691.
- (58) Benfatto, M.; Della Longa, S.; Natoli, C. R., *J. Synchrotron Rad.*, **2003**, *10*, 51-57.
- (59) Benfatto, M.; Congiu-Castellano, A.; Daniele, A.; Della Longa, S., *J. Synchrotron Rad.*, **2001**, *8*, 267-269.
- (60) Matsushita, T.; Phizackerley, R. P., *Jpn. J. Appl. Phys.*, **1981**, *20*, 2223.
- (61) Frahm, R., *Nucl. Instrum. Methods Phys. Res., Sect. A*, **1988**, *270*, 578-581.
- (62) Yamamoto, T.; Suzuki, A.; Nagai, Y.; Tanabe, T.; Dong, F.; Inada, Y.; Nomura, M.; Tada, M.; Iwasawa, Y., *Angew. Chem. Int. Ed.*, **2007**, *46*, 9253-9256.
- (63) Uemura, Y.; Inada, Y.; Bando, K. K.; Sasaki, T.; Kamiuchi, N.; Eguchi, K.; Yagishita, A.; Nomura, M.; Tada, M.; Iwasawa, Y., *Phys. Chem. Chem. Phys.*, **2011**, *13*, 15833-15844.
- (64) Uemura, Y.; Inada, Y.; Bando, K. K.; Sasaki, T.; Kamiuchi, N.; Eguchi, K.; Yagishita, A.; Nomura, M.; Tada, M.; Iwasawa, Y., *J. Phys. Chem. C*, **2011**, *115*, 5823-5833.
- (65) Harada, M.; Tamura, N.; Takenaka, M., *The Journal of Physical Chemistry C*, **2011**, *115*, 14081-14092.
- (66) Harada, M.; Katagiri, E., *Langmuir*, **2010**, *26*, 17896-17905.
- (67) Harada, M.; Saijo, K.; Sakamoto, N.; Einaga, H., *Colloids Surf., A*, **2009**, *345*, 41-50.
- (68) Ohyama, J.; Teramura, K.; Okuoka, S.; Yamazoe, S.; Kato, K.; Shishido, T.; Tanaka, T., *Langmuir*, **2010**, *26*, 13907-13912.
- (69) Ohyama, J.; Teramura, K.; Higuchi, Y.; Shishido, T.; Hitomi, Y.; Aoki, K.; Funabiki, T.; Kodera, M.; Kato, K.; Tanida, H.; Uruga, T.; Tanaka, T., *Phys. Chem. Chem. Phys.*, **2011**, *13*, 11128-11135.
- (70) Ohyama, J.; Teramura, K.; Higuchi, Y.; Shishido, T.; Hitomi, Y.; Kato, K.; Tanida, H.; Uruga, T.; Tanaka, T., *ChemPhysChem*, **2011**, *12*, 127-131.
- (71) Ohyama, J.; Teramura, K.; Shishido, T.; Hitomi, Y.; Kato, K.; Tanida, H.; Uruga, T.; Tanaka, T., *Chem. Phys. Lett.*, **2011**, *507*, 105-110.
- (72) Yamamoto, T.; Wakabayashi, S.; Osakada, K., *J. Organomet. Chem.*, **1992**, *428*, 223-237.

Chapter 1

Structural Analysis of Group V, VI, VII Metal Compounds

by X-ray Absorption Edge Near Structure

Abstract

The characteristic features of K-, L₁-, and L₃-edges of X-ray Absorption Near Edge Structure (XANES) spectra of group V, VI, and VII elements in their compounds, which have different coordination number, number of d electrons, and the coordination sphere symmetry, have been classified. Two p → d transitions were observed in the second derivatives of the L₃-edge XANES spectra for the group V, VI, and VII compounds. These two transitions can be assigned to split d orbitals. The splitting of the white line depends on the symmetry of coordination sphere because the splitting corresponds to the crystal field splitting of d orbitals. The splitting of d orbitals is correlated with the pre-edge peak area of K or L₁-edge XANES spectra, which are attributed to the electric dipole transition from s to p component of hybridized orbitals. This correlation is supported by DFT calculations of virtual hydride complex models of V, VI, and VII elements, which have four-, five-, or six-coordinated geometries, respectively. Clarifying the correlation between the splitting of the white line and local structure of group V, VI, and VII metal compounds is important to provide structural information about unknown group V, VI, and VII metal sites.

Introduction

X-ray absorption near edge structure (XANES) is a powerful probe of the geometric and electronic structure within a distance of several angstroms around the target atom. The target atom valence is often determined by the position of the K- and/or L₃-edges. The local symmetry is inferred by the pre-edge peak area of K- or L₁-edge XANES spectra, which show “s → d” transitions. The s → d transitions are dipole forbidden transitions for regular octahedral (O_h) site symmetry; however, the dipole transition of s-electron to the p-component of the p-d hybridized orbital, which is formed in the case of a polyhedron where O_h symmetry is distorted, occurs. This indicates the absence of a center of inversion symmetry and the mixing of p and d orbitals. Therefore, central atoms with tetrahedral (T_d) symmetry exhibit large pre-edge peak areas in K- and L₁-edge XANES spectra. Recently, Yamamoto reviewed the characteristics of pre-edge peaks in K-edge XANES spectra of 3d transition metals, from the view points of the selection rule, coordination number, number of d-electrons, and coordination sphere symmetry.¹ The features of pre-edge peaks in K-edge XANES spectra for 4d elements and the L₁-edge for 5d elements are analogous to those for 3d elements, but the pre-edge peak is broadened because of the large natural width of the core level.¹ The main peak observed at the L₃-edge XANES spectrum, so-called white line directly reflects the electronic states of vacant d orbitals of the X-ray absorbing atom. In the case of Mo L₃-edge, the white line exhibits well-resolved two peaks.²⁻⁵ The splitting and area of these two peaks depends on the symmetry at the Mo site because the splitting corresponds to crystal field effects on the d orbitals. The XANES spectra of the W L₃-edge probe the d orbital character as well as those of the Mo L₃-edge because the prominent peak of the W L₃-edge XANES spectrum is the white line caused by the 2p → 5d transition.⁶ Although the features of L₃-edge XANES spectra for 5d elements such as Ta^{7,8} and Re⁹ are analogous with those for W, there is little information about the relationship between the white line splitting and the structure of 5d species. This is because the white line is not distinctly split as the Mo L₃-edge white line, probably because of the wide natural width of the core level. The white line appears to consist of multiple overlapping peaks, which are very likely to correspond to the electron transition from 2p orbitals to the split d orbitals. In this study, the characteristic features have been classified to evaluate the influence of the period and group of each element in group V, VI,

VII on the correlation between the d orbital splitting and pre-edge peak areas of K- or L₁- edge XANES spectra and the coordination chemistry. A theoretical calculation based on density functional theory (DFT) of their simplified model compounds supported the spectral change of each spectrum. The energy gaps of split d orbitals of several models having 4-, 5-, and 6-coordinated 4d and 5d transition metal centers were calculated by means of DFT. The relationship between the d orbital energy gap and the metal center symmetry was classified. The mixing ratio of the vacant p orbital with d orbitals for several models was also evaluated, and the correlation between the hybridization and the d orbital energy gap was classified. The correlation among the width of white line splitting of the L₃-edge XANES spectra and pre-edge peak area of the K- or L₁-edge XANES spectra and the local configuration of group V, VI, VII elements will provide structural information about unknown group V, VI, and VII metal sites.

Experimental Section

Preparation of Reference Samples

Reference samples containing the Nb atom in the form of LiNbO₃, NaNbO₃, and Nb₂O₅ were purchased from Nacalai Tesque Ltd. (Kyoto, Japan). KNbO₃ and YbNbO₄ were synthesized by solid-state reaction. KNbO₃: K₂CO₃ (Nacalai Tesque, 0.384 g, 2.78 mmol) and Nb₂O₅ (Aldrich, St. Louis, MO, USA, 0.669 g, 2.52 mmol) were mixed and ground, followed by heating at 1323 K for 10 h. YbNbO₄: Yb₂O₃ (Kanto chemical, Tokyo, Japan, 0.799 g, 2.03 mmol) and Nb₂O₅ (Aldrich, 0.536 g, 2.02 mmol) were mixed and ground, followed by heating at 1423 K for 24 h.

MgMoO₄, Na₂MoO₄, and MoO₃ were purchased from Nacalai Tesque, and (NH₄)₆Mo₇O₂₄·4H₂O was purchased from the Wako Chemical Co. (Tokyo, Japan). Ba₂NiMoO₆ was synthesized by solid-state reaction. Ba₂NiMoO₆: BaCO₃, NiCO₃ (Wako), and MoO₃ were mixed and ground. The mixture was heated at 1373 K for 20 h, reground, and then calcined at 1423 K for 12 h.

Ta₂O₅ was purchased from Kojundo Kagaku (Tokyo, Japan). YTaO₄, KTaO₃, LiTaO₃, and NaTaO₃ were synthesized by solid state reaction. YTaO₄: Y₂O₃ and Ta₂O₅ were mixed, ground, and calcined. KTaO₃: K₂CO₃ (2.594 g, 18.77 mmol) and Ta₂O₅ (7.886 g, 17.85 mmol) were mixed and ground, followed by heating at 1373 K for 20 h, hydration by stirring in 100 mL of water, and then

finally drying. NaTaO₃: Na₂CO₃ (2.465 g, 23.26 mmol) and Ta₂O₅ (9.789 g, 22.15 mmol) were mixed, ground, and calcined. LiTaO₃: Li₂CO₃ (2.397 g, 32.44 mmol) and Ta₂O₅ (13.637 g, 30.86 mmol) were mixed and ground, followed by heating at 1373 K for 10 h and subsequent hydration.

WO₃ and Na₂WO₄·2H₂O were purchased from Nacalai Tesque. (NH₄)₁₀W₁₂O₄₁·5H₂O was purchased from Wako. H₃PW₁₂O₄₀·13H₂O was kindly supplied by the Nippon Inorganic Color & Chemical Co., Ltd. Cr₂WO₆, Ba₂NiWO₆, and Sc₂W₃O₁₂ were synthesized by solid-state reaction as described in previous literatures.^{10,11} Cr₂WO₆: Cr₂O₃ (Koso Chemical Co., Ltd., Tokyo, Japan) and WO₃ were mixed and ground. The mixture was calcined at 1423 K for 24 h. Ba₂NiWO₆: BaCO₃, NiCO₃ (Wako), and WO₃ were mixed and ground. The mixture was heated at 1373 K for 20 h, reground, and calcined at 1423 K for 12 h. Sc₂W₃O₁₂: Sc₂O₃ (Kanto Chemical Co., Inc.) and WO₃ were mixed, ground, and calcined at 1273 K for 5 h, reground, and then reheated at 1423 K for 24 h.

NaReO₄, NH₄ReO₄, and Re₂O₇ were purchased from Aldrich or Strem. Sr₂NaReO₆, Ba₂LiReO₆, Ba₂NaReO₆, and La₃ReO₈ were synthesized by solid-state reaction as described in previous papers.¹²⁻¹⁵ Ba₂NaReO₆: BaCO₃ (Wako, 394.2 mg), NH₄ReO₄ (Wako, 296.2 mg), and Na₂CO₃ (Wako, 53.4 mg) were mixed and ground. The mixture was heated at 873 K for 1 h and then at 1173 K for 3 h. Ba₂LiReO₆: BaCO₃ (Wako, 397.0 mg), NH₄ReO₄ (Wako, 303.8 mg), and Li₂CO₃ (Wako, 38.2 mg) were mixed and ground. The mixture was heated at 873 K for 1 h and then at 1173 K for 3 h. Sr₂NaReO₆: SrCO₃ (Wako, 184.9 mg), Na₂CO₃ (Wako, 33.8 mg), and NH₄ReO₄ (Wako, 185.4 mg) were mixed and ground. The mixture was heated at 973 K for 1 h and at 1173 K for 4 h. La₃ReO₈: La₂O₃ (Wako, 200.9 mg) and NH₄ReO₄ (Wako, 111.6 mg) were mixed and ground. The mixture was heated at 873 K for 3 h and then at 1173 K for 4 h. Confirmation of the identity of synthesized samples was done by comparison with literature XRD patterns. Re₂O₇/Al₂O₃ (18 wt %) was also prepared by the impregnation method from NH₄ReO₄ and Al₂O₃ (JRC-ALO-8), following calcination at 773 K for 3 h.

XAFS Measurements

Nb and Mo L₃-edge XANES data were recorded at the BL-1A station¹⁶ on the soft X-ray beamline at UVSOR (Institute for Molecular Science, Okazaki, Japan). Spectra of their powder samples were recorded in a total electron yield mode at room temperature, using an InSb(111) double

crystal monochromator. The photon energy was calibrated using the Nb and Mo L₃-edges of Nb and Mo metal samples, respectively, and this energy was set as the standard reference energy. Nb and Mo K-edge and Ta, W, and Re L₁- and L₃-edge XANES data were collected at the BL01B1 beamline at the SPring-8 (Japan Synchrotron Radiation Research Institute, Hyogo, Japan) in transmission mode in air at room temperature. Powder samples were mixed with an appropriate amount of boron nitride and pressed into pellets. Incident X-ray and transmitted fluxes were measured by ion chambers filled with N₂ (50%)/Ar (50%) and Ar (75%)/Kr (25%) for Nb and Mo K-edges and N₂ (85%)/ Ar (15%) and N₂ (50%)/Ar (50%) for Ta, W, and Re L₁- and L₃-edges. A Si(311) double crystal monochromator was used to obtain a monochromatic X-ray beam. Higher harmonic X-rays were removed by changing the glancing angle of the X-ray mirrors. The photon energy was calibrated by each metal. Data reduction was carried out with the REX2000 ver.2.5.9 program¹⁷ (Rigaku, Tokyo, Japan) and Igor Pro ver. 6.06J (Wavemetrics, Lake Oswego, OR, USA).

Theoretical Calculations

The splitting of vacant d orbitals and mixing ratio of p to d orbitals were estimated by DFT calculations with the Gaussian03 program package¹⁸ in the B3LYP/LanL2DZ level and the NBO package.^{19, 20} Metal hydride complex models (vide infra) were used to evaluate the crystal field effect as for the hydride being the nearest anion. As the models of six-, five-, and four-coordinated 4d and 5d transition metal sites, [MH₆]⁻, MH₅, and [MH₄]⁺ (M = Nb and Ta), MH₆, [MH₅]⁺, and [MH₄]²⁺ (M = Mo and W), and [MH₆]⁺, [MH₅]²⁺, and [MH₄]³⁺ (M = Re) were used, respectively. Single point calculations were performed on the different structure models, and the splitting of d orbitals by the crystal field was estimated as the difference of the energies between the averaged upper and lower molecular orbitals. The contribution of p orbitals into d orbitals of the metal center was also calculated, from the atomic orbital contribution to the molecular orbitals using the NBO package. This was done to evaluate the relationship between the p orbital contribution and the pre-edge peak area of K- or L₁-edge XANES spectra, which corresponds to the s → d dipole forbidden transition. The metal hydride models are very simple point charge models compared from actual reference compounds, which have several oxygen bonds. In this study, we focused on the symmetry of the

target atom based on the crystal field theory, and the DFT calculations are just preliminary or elementary analyses.

Results and Discussion

Re L₃-Edge XANES Spectra of Re Complex Oxides

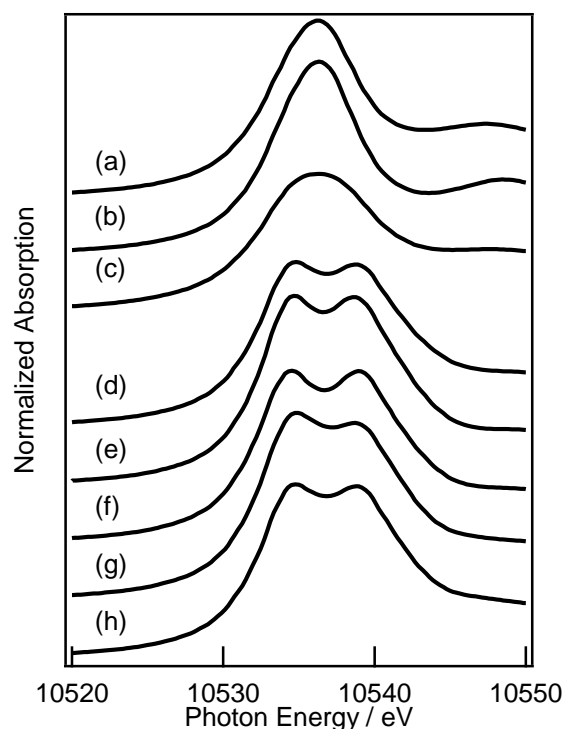


Figure 1. Re L₃-edge XANES spectra of (a) NH₄ReO₄, (b) NaReO₄, (c) Re₂O₇, (d) Sr₄NiRe₂O₁₂, (e) La₃ReO₈, (f) Sr₂NaReO₆, (g) Ba₂NaReO₆, and (h) Ba₂LiReO₆.

Figure 1 shows the Re L₃-edge XANES spectra of reference samples containing the Re⁷⁺ ion. The perovskite compounds Ba₂LiReO₆, Ba₂NaReO₆, and Sr₂NaReO₆ have regular O_h symmetry and exhibit two peaks assignable to electronic transition from the 2p orbitals to vacant 5d orbitals (2p_{3/2} state to 5d_{3/2} or 5d_{5/2} states). On the other hand, L₃-edge XANES spectra of La₃ReO₈ and Sr₄NiRe₂O₁₀, which have a distorted ReO₆ unit symmetry, show a similar white line to Re compounds containing regular octahedral ReO₆ units. Re₂O₇ has both a highly distorted ReO₆ unit and a ReO₄ unit and exhibits a small white line with only one peak. The reason why the white line of Re species of Re₂O₇ is smaller than that of other Re compounds might be ascribed to the result of the convolution of the XANES spectra of each ReO₄ and ReO₆ units. NaReO₄ and NH₄ReO₄ have

complete tetrahedral ReO_4 unit symmetry and exhibit one asymmetrical peak as white line. These differences in white line shape are interpreted to reflect the influence of the splitting of the Re 5d orbitals by the crystal field. The distortion of regular O_h symmetrical units solves the degeneracy of 5d orbitals and results in smaller splitting of the 5d orbitals. Therefore, La_3ReO_8 and $\text{Sr}_4\text{NiRe}_2\text{O}_{10}$ which have distorted O_h symmetry show smaller d orbital splitting. NaReO_4 and NH_4ReO_4 with almost complete tetrahedral ReO_4 unit symmetry have two degeneracy d orbitals as e and t_2 symmetry and much smaller d orbital splitting. Thus, the white line of these compounds shows only one peak with a small shoulder peak at around 10536 eV.

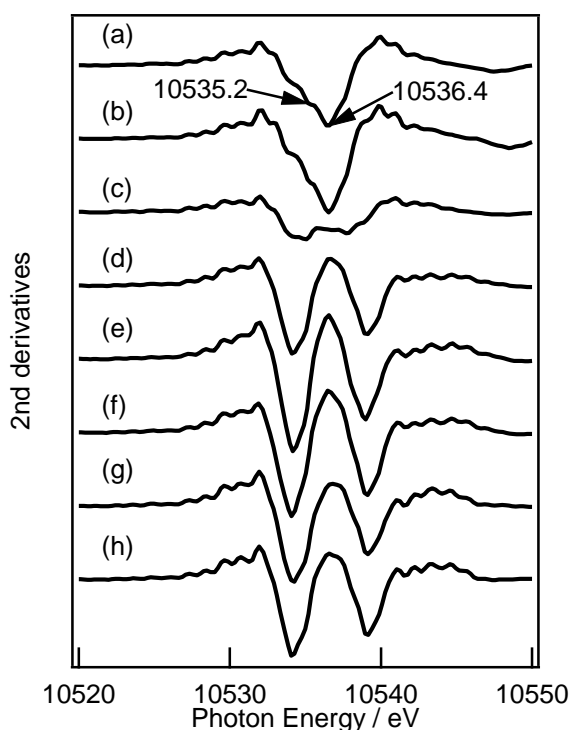


Figure 2. Second derivatives of Re L_3 -edge XANES spectra of (a) NH_4ReO_4 , (b) NaReO_4 , (c) Re_2O_7 , (d) $\text{Sr}_4\text{NiRe}_2\text{O}_{12}$, (e) La_3ReO_8 , (f) $\text{Sr}_2\text{NaReO}_6$, (g) $\text{Ba}_2\text{NaReO}_6$, and (h) $\text{Ba}_2\text{LiReO}_6$.

To clarify the state of vacant d orbitals from the Re L_3 -edge white line, second derivative spectra can be used in an analogous manner to that done for W L_3 -edge XANES spectra.⁶ Second derivatives of the Re L_3 -edge white line make it clearly apparent that the white line consists of two peaks (NaReO_4 and NH_4ReO_4 exhibit a large peak with a shoulder at lower energy), as shown in Figure 2. The difference in d orbital energy can be easily elucidated from the energy gap of the two minima in the second derivative spectra. $\text{Sr}_2\text{NaReO}_6$, $\text{Ba}_2\text{NaReO}_6$, and $\text{Ba}_2\text{LiReO}_6$ with regular O_h ReO_6 unit

symmetry exhibit the largest energy gaps, with values of 5.0, 4.9, and 5.1 eV, respectively. $\text{Sr}_4\text{NiRe}_2\text{O}_{12}$, and La_3ReO_8 , with distorted O_h ReO_6 unit symmetry exhibit slightly smaller energy gaps of 4.6 and 4.8 eV, respectively. Re_2O_7 with both a highly distorted octahedral ReO_6 unit and a tetrahedral ReO_4 unit and NaReO_4 and NH_4ReO_4 with complete tetrahedral ReO_4 unit symmetry show the smallest energy gaps of 2.6, 1.2, and 1.2 eV, respectively. The relationship between their local symmetry and the energy gap of Re L_3 -edge XANES spectra follows a tendency similar to that reported for W compounds.⁶ They reported that W compounds with tetrahedral WO_4 unit symmetry have small energy gaps (1.7 – 1.9 eV), and octahedral WO_6 unit symmetry compounds exhibit large energy gaps (4.8 – 5.6 eV). Distorted octahedral WO_6 unit symmetry compounds exhibit midrange energy gaps (3.0 – 4.0 eV).

Re L_1 -Edge XANES Spectra of Re Complex Oxides

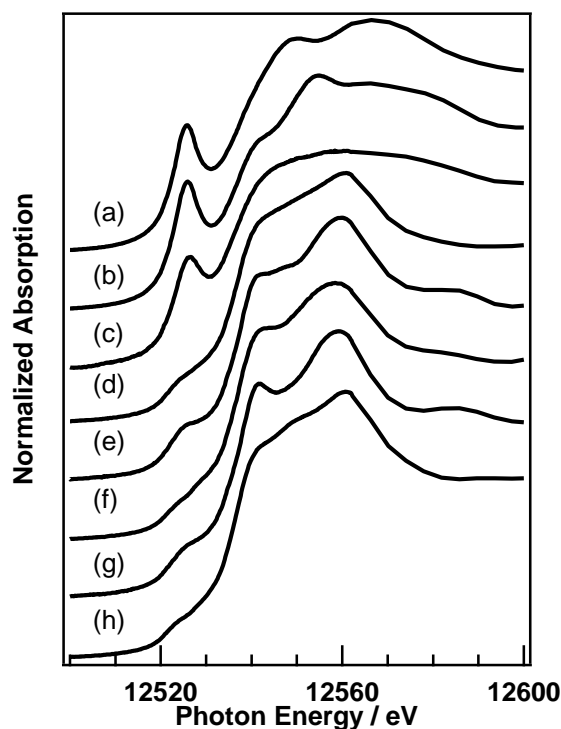


Figure 3. Re L_1 -edge XANES spectra of (a) NH_4ReO_4 , (b) NaReO_4 , (c) Re_2O_7 , (d) $\text{Sr}_4\text{NiRe}_2\text{O}_{12}$, (e) La_3ReO_8 , (f) $\text{Sr}_2\text{NaReO}_6$, (g) $\text{Ba}_2\text{NaReO}_6$, and (h) $\text{Ba}_2\text{LiReO}_6$.

Figure 3 shows the Re L_1 -edge XANES spectra of the reference samples. The L_1 -edge of XANES spectra reflects the electronic state and geometry of the Re species, which are identified by

the X-ray absorption edge position and the pre-edge peak intensity. The pre-edge peak of each Re L_1 -edge XANES spectrum at around 12525 eV can be preliminary attributed to electric transition from the “2s to 5d” orbitals. A less symmetric Re species (*i.e.*, distorted from O_h symmetry) provides a larger pre-edge peak because the forbidden electron transition ($2s \rightarrow 5d$) is allowed by the mixing of Re and ligand p orbitals into vacant d orbitals. Ba_2LiReO_6 , Ba_2NaReO_6 , and Sr_2NaReO_6 all have an octahedral ReO_6 unit and exhibit small pre-edge peaks, while La_3ReO_8 and $Sr_4NiRe_2O_{12}$ have distorted octahedral ReO_6 unit symmetry and exhibit moderate pre-edge peak areas. By contrast, $NaReO_4$ and NH_4ReO_4 with a complete ReO_4 unit and Re_2O_7 with mixed tetrahedral ReO_4 and octahedral ReO_6 units all exhibit large pre-edge peak areas. To quantitatively evaluate the pre-edge peak area, each Re L_1 -edge XANES spectrum was analyzed by a deconvolution method as previously reported by Horsley.²¹ The deconvolution of Re L_1 -edge XANES spectra was performed with three Lorentzian and an arctangent function, which involves electronic transition from the 2s core orbital to unoccupied orbitals including multiple scattering effect and to the vacuum level, respectively.

Deconvolution results are shown in Figure 4. Although the pre-edge peaks of Ba_2LiReO_6 , Ba_2NaReO_6 , Sr_2NaReO_6 , $Sr_4NiRe_2O_{12}$, Re_2O_7 , $NaReO_4$, and NH_4ReO_4 can all be fitted with one Lorentz function, two Lorentz functions were used in the case of La_3ReO_8 . Westre *et al.* reported that the pre-edge features of the Fe K-edge for iron complexes consist of electric dipole and quadrupole transitions.²² The electric quadrupole transition from the s to d orbitals is usually much weaker than the electric dipole transition and that the electric dipole intensity was explained by the mixing of Fe 4p into Fe 3d orbitals. In the present study, it is assumed that Ba_2LiReO_6 , Ba_2NaReO_6 , and Sr_2NaReO_6 also have no (or little) hybridization of the d and p orbitals and that only quadrupole electronic transitions can occur as for the case with Fe complexes. Therefore, the pre-edge peaks of Ba_2LiReO_6 , Ba_2NaReO_6 , and Sr_2NaReO_6 were all assigned to the quadrupole electron transitions from 2s to t_{2g} and e_g of the 5d orbitals. The large pre-edge peaks of $NaReO_4$ and NH_4ReO_4 are predominantly caused by electric dipole transitions. For La_3ReO_8 , $Sr_4NiRe_2O_{12}$, and Re_2O_7 , the deviation in ReO_6 symmetry from O_h would account for the medium pre-edge peak intensity originating from electric dipole transition.

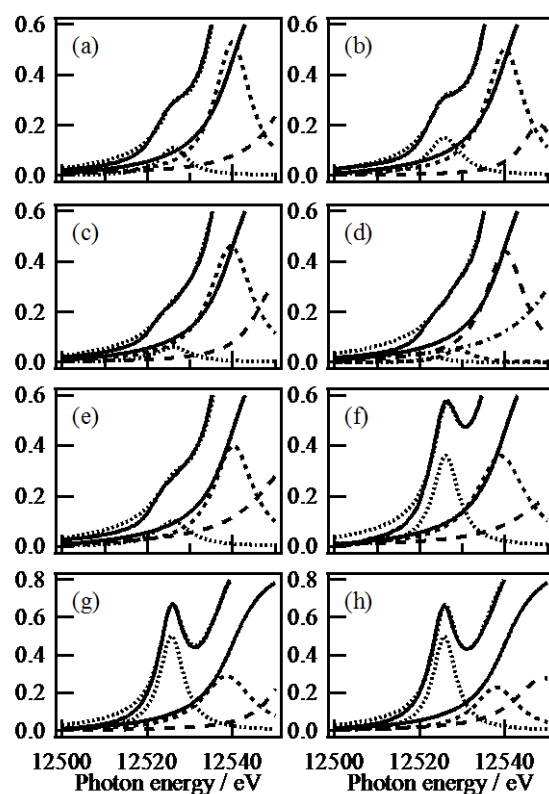


Figure 4. Deconvolution of the pre-edge peak for Re L_1 -edge XANES spectra of (a) Ba_2LiReO_6 , (b) Ba_2NaReO_6 , (c) Sr_2NaReO_6 , (d) La_3ReO_8 , (e) $Sr_4NiRe_2O_{12}$, (f) Re_2O_7 , (g) $NaReO_4$, and (h) NH_4ReO_4 .

Relationship between the splitting width of white line at L_3 -Edge XANES and the pre-edge peak area at L_1 -Edge XANES spectra

The pre-edge peak area of Re L_1 -edge XANES spectra expresses the mixing ratio of the p orbitals of Re and ligands into vacant 5d orbitals, and this mixing ratio depends on the symmetry of the Re species. For example, Oikawa *et al.* estimated the local structure of Re species of Re/Al_2O_3 catalysts from Re L_1 -edge XANES spectra.²³ The splitting width of the two peaks at the Re L_3 -edge reflects the splitting of the 5d orbitals by crystal field. It can be reasonably expected that the combination of pre-edge peak area of Re L_1 -edge XANES spectra and the energy gap between the peaks of the Re L_3 -edge XANES spectra provides more reliable information on the local structure of the Re species.

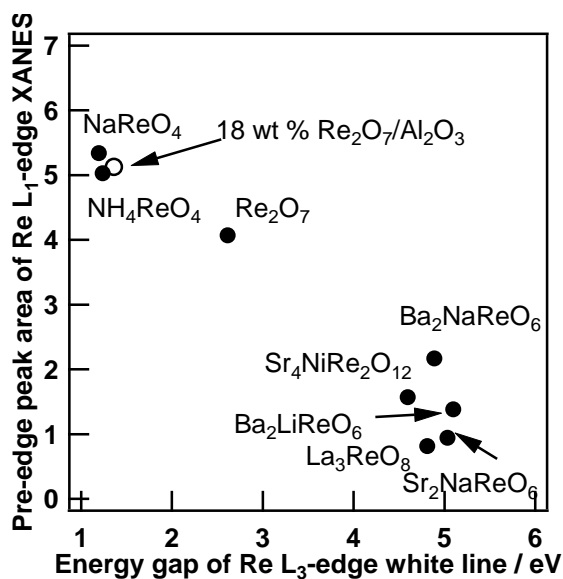


Figure 5. Dependence of the pre-edge peak area of Re L₁-edge XANES spectra on the splitting of white line of Re L₃-edge XANES spectra. Reference samples were Ba₂LiReO₆, Ba₂NaReO₆, Sr₂NaReO₆, La₃ReO₈, Sr₄NiRe₂O₁₂, Re₂O₇, NaReO₄, and NH₄ReO₄ (open circle: 18 wt % Re₂O₇/Al₂O₃).

Figure 5 shows the pre-edge peak area of the Re L₁-edge XANES spectra plotted against the energy gap of the split Re L₃-edge white line of the reference samples. Figure 5 reveals an interesting relationship that the pre-edge peak area has a linear correlation with the energy gap. Octahedral Re species appear on the lower right corner in Figure 5, and distortion from O_h symmetry moves species toward the upper left corner. La₃ReO₈, Sr₄NiRe₂O₁₂, and Re₂O₇ all have a distorted octahedral ReO₆ unit or mixed states and are located between the octahedral ReO₆ species (Ba₂LiReO₆, Ba₂NaReO₆, and Sr₂NaReO₆) and tetrahedral ReO₄ species (NaReO₄ and NH₄ReO₄). Moreover, the Re L₁- and L₃-edge XANES spectra of 18 wt % Re₂O₇/Al₂O₃, which acts as the effective catalyst for olefin metathesis, was measured and analyzed in the same procedure above. As shown in Figure 5, the plot of 18 wt % Re₂O₇/Al₂O₃ is located at the upper left corner. Thus, the Re species in 18 wt % Re₂O₇/Al₂O₃ can be concluded as a tetrahedral species.

Analysis of XANES Spectra for Other Reference Samples (Nb, Mo, Ta, and W)

K- and L₃-edge XANES spectra of Nb reference samples (LiNbO₃, NaNbO₃, KNbO₃, Nb₂O₅, YbNbO₄), Mo reference samples (BaNiMoO₆, (NH₄)₆Mo₇O₂₄·4H₂O, MoO₃, MgMoO₄, Na₂MoO₄), and L₁- and L₃-edge XANES spectra of Ta reference samples (LiTaO₃, NaTaO₃, KTaO₃, Ta₂O₅,

YTaO₄), W reference samples (Ba₂NiWO₆, Cr₂WO₆, (NH₄)₁₀W₁₂O₄₁·5H₂O, WO₃, H₃PW₁₂O₄₀·12H₂O, Na₂WO₄·2H₂O, Sc₂W₃O₁₂) were analyzed in the same way as Re compounds.

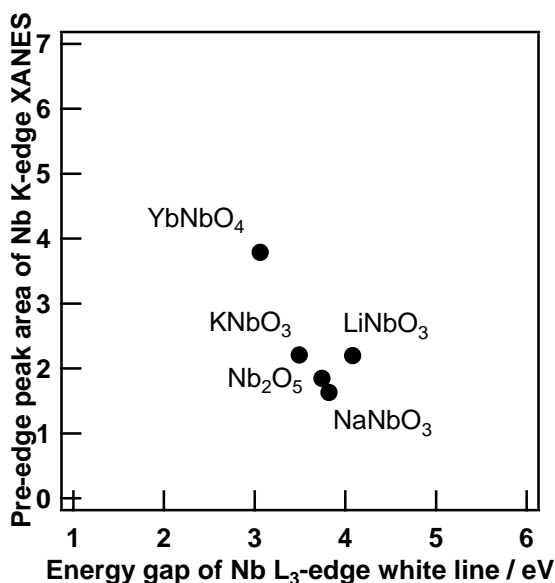


Figure 6. Dependence of the pre-edge peak area for Nb K-edge XANES spectra on the energy gap of the split Nb L₃-edge white line. Reference samples were LiNbO₃, NaNbO₃, KNbO₃, Nb₂O₅, and YbNbO₄.

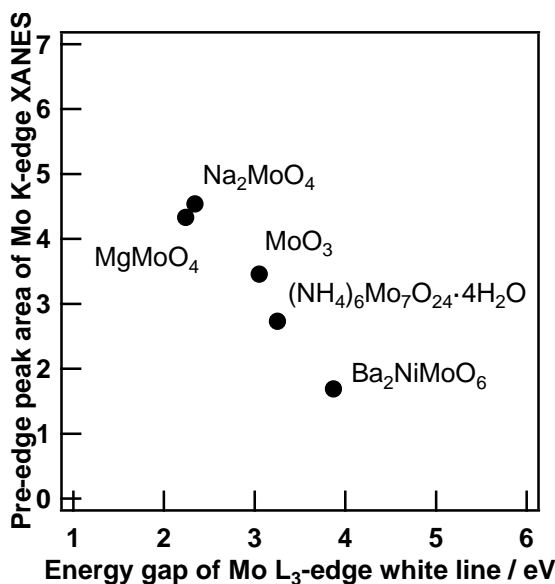


Figure 7. Dependence of pre-edge peak area of Mo K-edge XANES spectra on the energy gap of the split Mo L₃-edge white line. Reference samples were Ba₂NiMoO₆, (NH₄)₆Mo₇O₂₄·4H₂O, MoO₃, MgMoO₄, and Na₂MoO₄.

Figure 6 shows the pre-edge peak area of Nb K-edge XANES spectra plotted against the energy

gap of the split Nb L₃-edge white line. Figure 6 reveals an interesting correlation similar to that of Re compounds shown in Figure 5. Octahedral Nb species including LiNbO₃, NaNbO₃, and KNbO₃ appear in the lower right corner in Figure 6, and distortion from O_h to T_d symmetry shifts toward the upper left corner. Nb₂O₅ has complicated 6- and 7-coordinated NbO₆ and NbO₇ units and is located between distorted octahedral NbO₆ species (LiNbO₃, NaNbO₃, and KNbO₃) in Figure 6. YbNbO₄ has a distorted tetrahedral NbO₄ unit and is located in the upper left corner. For Nb compounds, a relatively small difference of these features was observed. Nb compounds with complete tetrahedral NbO₄ unit symmetry would be expected to be plotted in the upper left corner (approximate 2 eV energy gap and 6 eV pre-edge peak area) in Figure 6. Figure 7 shows the pre-edge peak area of Mo K-edge XANES spectra plotted against the energy gap of the split Mo L₃-edge white line and reveals a much clearer correlation, in that the octahedral Mo species like Ba₂NiMoO₆ appear in the lower right corner, and distortion from O_h symmetry shifts species toward the upper left corner. (NH₄)₆Mo₇O₂₄·4H₂O and MoO₃ are located between the complete octahedral MoO₆ unit species (Ba₂NiMoO₆) and nearly complete tetrahedral MoO₄ unit species (Na₂MoO₄ and MgMoO₄).

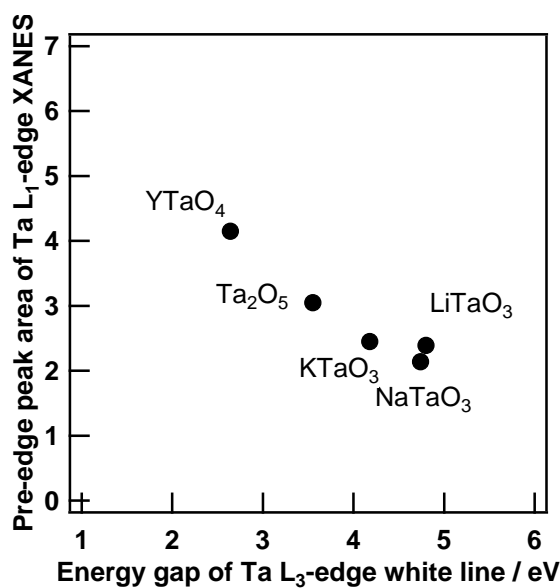


Figure 8. Dependence of pre-edge peak area of Ta L₁-edge XANES spectra on the energy gap of the split Ta L₃-edge white line. Reference samples were LiTaO₃, NaTaO₃, KTaO₃, Ta₂O₅, and YTaO₄.

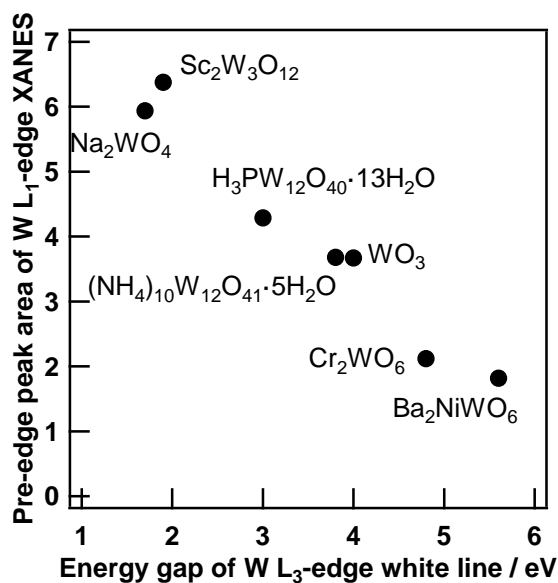


Figure 9. Dependence of the pre-edge peak area of W L₁-edge XANES spectra on the energy gap of the split W L₃-edge white line. Reference samples were Ba₂NiWO₆, Cr₂WO₆, (NH₄)₁₀W₁₂O₄₁·5H₂O, WO₃, H₃PW₁₂O₄₀·12H₂O, Na₂WO₄·2H₂O, and Sc₂W₃O₁₂.

Figure 8 shows the pre-edge peak area of Ta L₁-edge XANES spectra plotted against the energy gap of the split Ta L₃-edge white line, where a clear correlation is again apparent. Distorted octahedral Ta species such as LiTaO₃, NaTaO₃, and KTaO₃ appear on the lower right corner, with distortion from O_h toward T_d symmetry shifting the plot toward the upper left corner. Ta₂O₅ has complicated 6- or 7-coordinated TaO₆ or TaO₇ units and is located between distorted octahedral TaO₆ species (LiNbO₃, NaNbO₃, and KNbO₃) and distorted tetrahedral TaO₄ species (YTaO₄). Figure 9 shows the pre-edge peak area of W L₁-edge XANES spectra plotted against the energy gap of the split W L₃-edge white line and reveals a clear linear correlation. Octahedral W species like Ba₂NiWO₆ appear in the lower right corner, and distortion from O_h symmetry shifts species toward the upper left corner. WO₃, H₃PW₁₂O₄₀·12H₂O, and (NH₄)₁₀W₁₂O₄₁·5H₂O have large distorted octahedral structures and the plots of WO₃ and H₃PW₁₂O₄₀·12H₂O are located between the octahedral WO₆ species (Cr₂WO₆ and Ba₂NiWO₆) and tetrahedral WO₄ species (Na₂WO₄·2H₂O and Sc₂W₃O₁₂). The effects of element group and period on characteristic features of XANES spectra are discussed below.

DFT Calculations

We evaluated the mixing ratio of 6p orbitals into 5d orbitals for all ReH_x ($x = 4, 5,$ and 6) models and investigated the relationship between mixing ratio and the energy gap of split 5d orbitals using the DFT calculations. This calculation was carried out to support the relationship between local structure and electronic state discussed above.

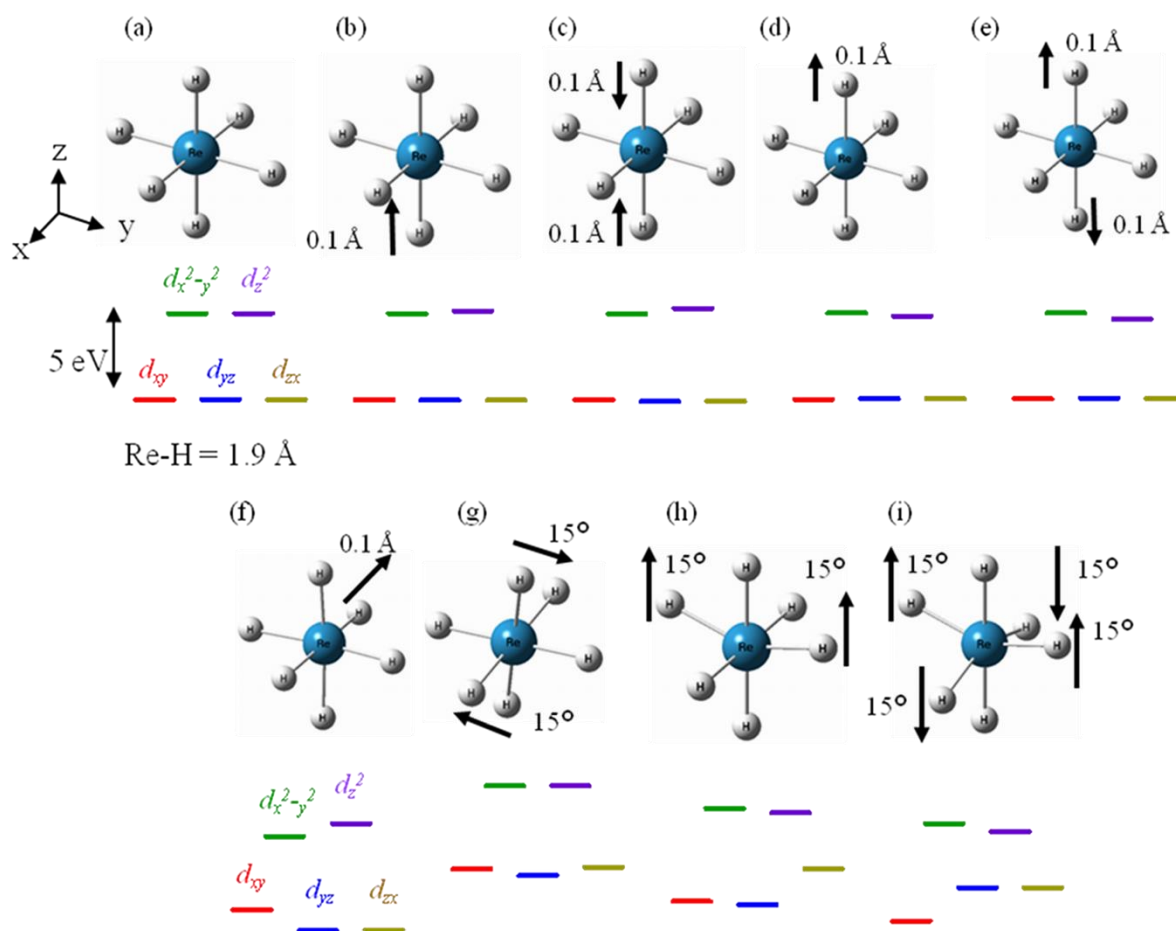


Figure 10. Crystal field splitting of Re^{7+} d orbitals (d^0) in 6-coordination: (a) octahedral structure with a 1.90 Å bond length for Re–H; (b–f) distance(s) between H atom(s) and the central cation are changed by 0.1 Å in the direction(s) marked by the arrow(s); (g–i) H atom(s) are rotated by 15°.

Figure 10 shows several $[\text{ReH}_6]^+$ models and their calculated 5d orbital splitting. A series of $[\text{ReH}_6]^+$ models with various Re–H bond lengths on the z axis are given in Figure 10a–e. The ReH_6 model in Figure 10a has octahedral symmetry (O_h), and all the Re–H lengths are 1.9 Å. The 5d orbitals split into the t_{2g} and e_g states. When one or two H atoms on the z axis are 0.1 Å closer to or

further from the Re atom, a small splitting of the e_g state occurs, as shown in Figure 10b–e. The shortening or elongation of the Re–H bond makes the d_{z^2} orbital unstable or stable, respectively. The average energy gap between the t_{2g} and e_g states shows that the coordination distance of Re–H has a small effect on the 5d splitting. The $[\text{ReH}_4]^+$ model in Figure 10f involves the central Re atom moving 0.1 Å in the yz direction, and this exhibits only a small splitting of the t_{2g} and e_g states. Rotation of two H atoms on the z axis toward the y direction (Figure 10g) results in a similar electronic state to that in Figure 10b–e. However, the energy gap of the t_{2g} and e_g states is smaller than that of the basic octahedral $[\text{ReH}_6]^+$ model. We also performed calculations where H atoms on the x and/or y axis were rotated toward the z axis, shown in Figure 10h,i. Both splitting of the t_{2g} and e_g states and reduction in the energy gap occur because of stability of the d_{z^2} orbital and instability of the d_{yz} and d_{zx} orbitals. These results indicate that Re–H bond length is associated with splitting of the t_{2g} state and that the angular distortion from an octahedral structure affects the energy gap between the split 5d orbitals. In some instances, the splitting of the t_{2g} and e_g states is also affected.

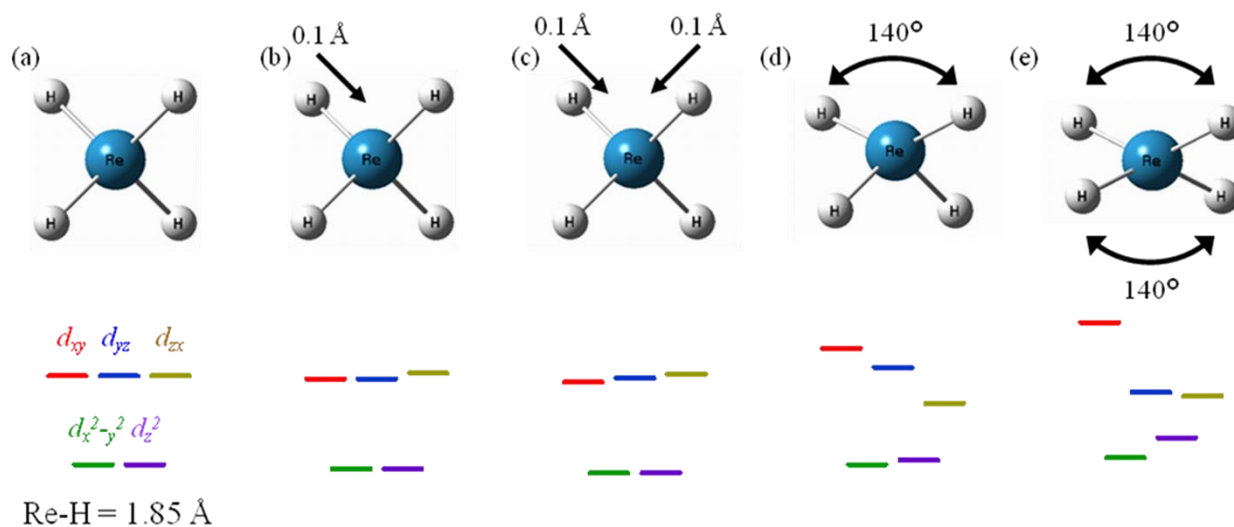


Figure 11. Crystal field splitting of Re^{7+} d orbitals (d^0) in 4-coordination: (a) tetrahedral structure with 1.85 Å bond length for all Re–H; (b–e) distance(s) between the H atom(s) and central cation are changed by 0.1 Å in the direction marked by the arrow(s); (d, e) angle(s) of H–Re–H are changed to 140°.

DFT calculations were also carried out on $[\text{ReH}_4]^{3+}$ models in addition to $[\text{ReH}_6]^+$ models, and the results are shown in Figure 11. The $[\text{ReH}_4]^{3+}$ model in Figure 11a has tetrahedral symmetry, and

all Re–H bond lengths are 1.85 Å. The 5d orbitals of Re consist of doubly degenerate e states and triply degenerate t_2 states. The energy gap of the split 5d orbitals is 3.89 eV and is smaller than the energy gaps for all $[\text{ReH}_6]^+$ models. Shortening one or two Re–H bonds in Figure 11b,c destabilizes the d_{zx} orbital but has little effect on the energy gap between the e and t_2 states. Figure 11d shows the $[\text{ReH}_4]^{3+}$ model in which the angle between the H–Re–H bonds of model (a) is changed from 109.5° to 140.0° , with the two bond lengths remaining 1.85 Å. Increasing this angle results in an unstable d_{xy} orbital and a stable d_{zx} , and therefore the splitting of the t_2 state is spread. The H–Re–H angle has a larger influence on the spreading of the t_2 state than Re–H bond length. The energy level of the stable d_{yz} orbital is almost midway between the e and the other t_2 state. Therefore, the split 5d orbitals consist of e and t_2 states, except that of d_{yz} . In this case, the energy gap of the split 5d orbital is 3.92 eV, and the large angle leads to a large energy gap. Figure 11e also shows that changing the angle between the other H–Re–H bonds from 109.5° to 140.0° makes the d_{xy} orbital unstable, and in contrast the d_{yz} and d_{zx} orbitals both become stable. The 5d orbital energy gap of the $[\text{ReH}_4]^{3+}$ model in Figure 11e is expressed by the difference between the average energies of the four 5d orbitals ($d_{x^2-y^2}$, d_{z^2} , d_{zx} and d_{yz}) and the energy of d_{xy} because the stable d_{zx} and d_{yz} orbitals are close to $d_{x^2-y^2}$ and d_{z^2} . The energy gap is calculated to be 3.40 eV. These results indicate that the energy gap of the split 5d orbitals depends on distortion of the H–Re–H bond angle from tetrahedral symmetry.

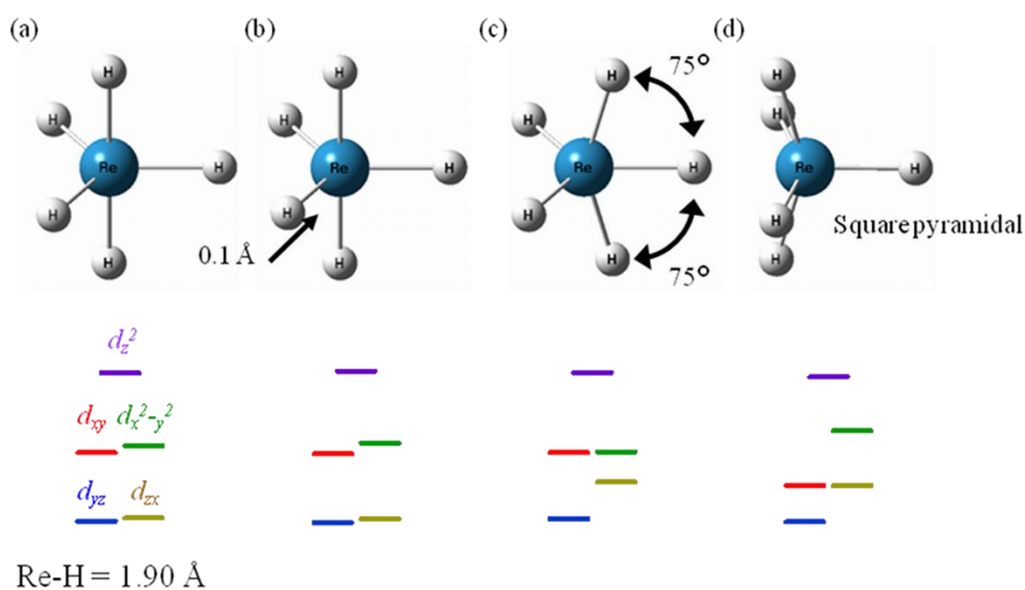


Figure 12. Crystal field splitting Re^{7+} d orbitals (d^0) in 5-coordination: (a) trigonal-bipyramidal structure with 1.90 Å bond length for all Re–H. (b) The distance of H atom to the central cation is changed by 0.1 Å in the direction marked by the arrow. (c) z axis is rotated by 15°. (d) Square-pyramidal structure with 1.90 Å bond lengths for all Re–H.

$[\text{ReH}_5]^{2+}$ models were also calculated using the DFT method, and the results are shown in Figure 12. The 5d states of the $[\text{ReH}_5]^{2+}$ model in Figure 12a, having a trigonal-bipyramidal structure, consist of two stable 5d orbitals (d_{yz} and d_{zx}), slightly unstable 5d orbitals (d_{xy} and $d_{x^2-y^2}$), and an unstable d_{z^2} orbital. The energy gap of the split 5d orbitals is expressed by the difference between the average energy of the four orbitals d_{zx} , d_{yz} , d_{xy} , and $d_{x^2-y^2}$ and the energy of the d_{z^2} orbital because the d_{xy} and $d_{x^2-y^2}$ levels are close to the d_{zx} and d_{yz} levels. The energy gap is 4.62 eV, and this value is between that for tetrahedral $[\text{ReH}_4]^{3+}$ and octahedral $[\text{ReH}_6]^+$ models. Shortening one of the three Re–H bonds on the xy plane by 0.1 Å has hardly any effect on the 5d states, as shown in Figure 12b. On the other hand, distortion of the trigonal-bipyramidal structure by moving two H atoms on the z axis in the x direction (Figure 12c) leads to an unstable d_{zx} orbital and a smaller energy gap (4.29 eV) for the split 5d orbital than that of $[\text{ReH}_5]^{2+}$ (Figure 12a). The $[\text{ReH}_5]^{2+}$ model in Figure 12d, with a square-pyramidal structure, showed different 5d states from those of $[\text{ReH}_5]^{2+}$ in Figure 12a–c. The 5d states in Figure 12d split into d_{xy} , d_{yz} , and d_{zx} orbitals and $d_{x^2-y^2}$ and d_{z^2} orbitals. These can be assumed to t_{2g} and e_g states, respectively. This tendency is similar to that of 6-coordinated $[\text{ReH}_6]^+$. However, the energy gap between the “ t_{2g} ” and “ e_g ” states is smaller than that of the $[\text{ReH}_6]^+$ models. The energy gaps of the 5d states of all $[\text{ReH}_5]^{2+}$ models have values between those of the $[\text{ReH}_4]^{3+}$ and $[\text{ReH}_6]^+$ models. We carried out DFT calculations for models of our reference samples to compare calculated results with experimental ones. Re geometries for the reference samples were obtained from published data.^{12-15, 24, 25}

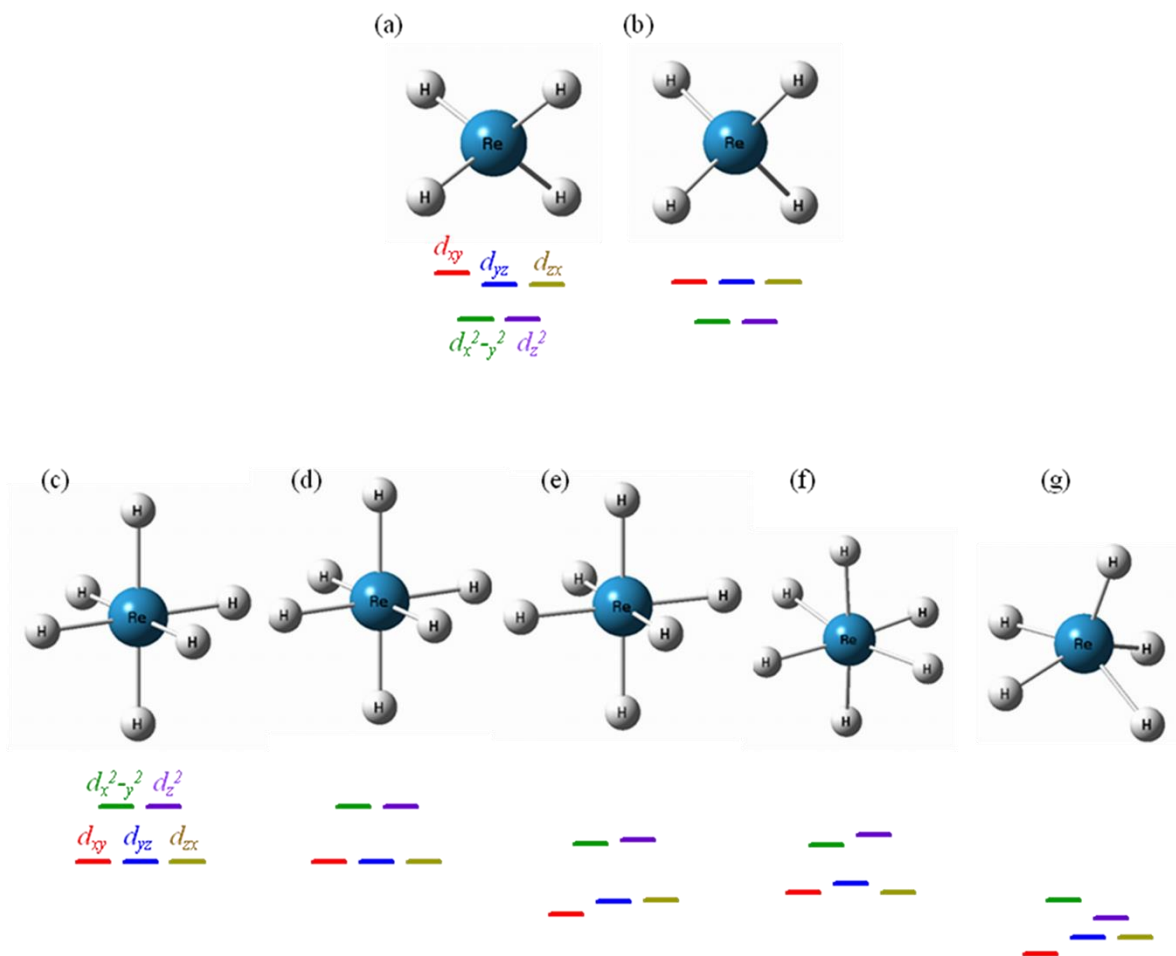


Figure 13. Crystal field splitting of Re^{7+} d orbitals (d^0) in reference samples and ReO_3 : (a) NH_4ReO_4 , (b) NaReO_4 , (c) $\text{Ba}_2\text{NaReO}_6$, (d) $\text{Ba}_2\text{LiReO}_6$, (e) $\text{Sr}_2\text{NaReO}_6$, (f) ReO_3 , (g) $\text{Sr}_4\text{NiRe}_2\text{O}_{12}$.

The calculated 5d states are shown in Figure 13. NH_4ReO_4 has T_d symmetry and exhibits 5d states similar to the $[\text{ReH}_4]^{3+}$ model in Figure 11a. NaReO_4 has C_{2v} symmetry and exhibits 5d states similar to the $[\text{ReH}_4]^{3+}$ model in Figure 11c. The structures of $\text{Ba}_2\text{LiReO}_6$, $\text{Ba}_2\text{NaReO}_6$, and $\text{Sr}_2\text{NaReO}_6$ have O_h symmetry and exhibit 5d states similar to the $[\text{ReH}_6]^+$ models in Figure 10a. ReO_3 is similar to the structure in Figure 10f, so the 5d states are close to those of the $[\text{ReH}_6]^+$ model depicted in Figure 10f. The relationship between the calculated energy gap of the split 5d state and the Re structure of the reference samples is in approximate agreement with the results obtained from the split in the Re L_3 -edge white line. Such agreement indicates that the energy gap of the split 5d states for some Re structures can be estimated from DFT calculations. The pre-edge peak of Re L_1 -edge XANES spectra is caused by the mixing of empty 6p orbitals into vacant 5d orbitals.

Therefore, a correlation between the local structure and pre-edge peak intensity can be deduced from the DFT calculation electronic state. We estimated the p orbital contribution into the vacant molecular orbitals (predominantly the d orbitals for all ReH_x models in Figures 10–13) using the NBO package.

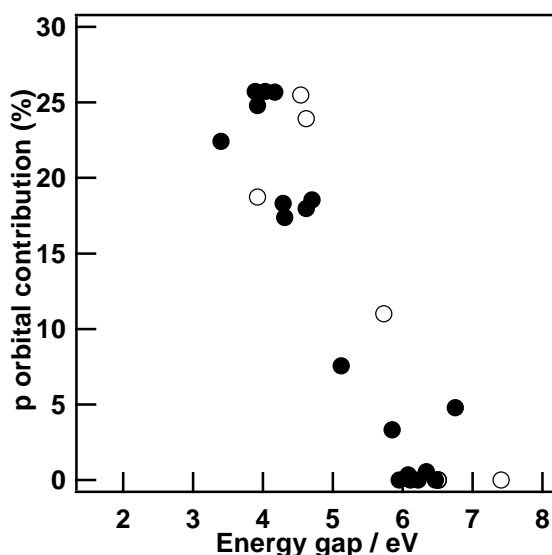


Figure 14. Dependence of the 6p orbital contribution to the energy gap of the split 5d orbital for ReH_x models. (●: ReH_x models; ○: reference sample models).

The mixing ratio of 6p orbitals into 5d orbitals for all ReH_x models is plotted against the energy gap of split 5d states in Figure 14, and the relationship is clearly linear. This observation supports our earlier relationship showing a correlation between the pre-edge peak area and the energy gap of split 5d orbitals, obtained from Re L_1 - and L_3 -edge XANES spectra, respectively. The linear correlation shown in Figure 14 suggests that the structure of Re species can be easily estimated using the pre-edge peak areas of Re L_1 -edge XANES spectra and the energy gap of the split Re L_3 -edge white line. DFT calculation above is based on the crystal field theory, and the metal hydride complex models were chosen to evaluate the unoccupied orbitals derived from the metal p and d orbital mixing induced by hydrides (dealt like point charges). The p orbital of adjacent oxygen atoms, which exist in the reference compounds, may have some influence on the electronic states and the observed XANES spectra. However, for instance, the pre-edge peak intensity of the Mo K-edge XANES spectrum of the $\text{MoO}_2(\text{acac})_2$ complex, which has two Mo=O bonds, is smaller than that of ammonium heptamolybdate (AHM), which has six Mo–O bonds with highly distorted Mo–O

configuration.²⁶ If the 2p orbital of the adjacent oxygen strongly affects the unoccupied orbitals, the pre-edge peak intensity of the Mo K-edge XANES spectrum of MoO₂(acac)₂ should be larger than that of AHM because the electronic transition from Mo 1s to the unoccupied orbital hybridized with the O 2p orbital is allowed. However, the observed characteristics of the XANES spectra are opposite. In addition, for example, George *et al.* discussed the pre-edge intensity of Ti K-edge XANES spectra of several Ti cyclopentadienyl complexes with experimental and theoretical results based on DFT.²⁷ In this paper, there is a clear linear correlation between the Ti 4p orbital contribution to unoccupied orbitals and experimental Ti K-edge pre-edge intensity of each Ti complex. The importance of the mixing of the 4p orbital into the 3d orbital is also reported in the case of Fe complexes with experimental XANES spectra and extended Hückel molecular orbital calculation.²⁸ Therefore, we assumed that the point charge approximation based on the crystal field theory is adequate to evaluate the characteristics of XANES spectra in this study.

Discussion

The characteristics of XANES spectra strongly correlate to the local structure of the target elements. Therefore, we tried to parameterize the distortion from the ideal local structure and elucidate the relationship between the distortion parameters and the local structure of the target element in a semi-quantitative manner. First, we define the distortion parameter of the average distortion in angle from the crystal structure of the reference compounds. The bond length between the target metal and the adjacent oxygen atoms may affect the feature of its XANES spectrum, but as discussed in the DFT calculation section, the effect of the bond length seems to be much smaller than that of the ligand–metal–ligand angle. Thus, the distortion parameters are calculated from the O–M–O angle as expressed by

$$A_{\text{distortion}} = A_i^{\text{ideal}} \pm \frac{\sum_{i=1}^n |A_i^{\text{ideal}} - A_i^{\text{crystal}}|}{n}$$

where n is the number of the geometrically different target elements; $A_{\text{distortion}}$ is a parameterized “distorted angle”; A_i^{ideal} is an angle of the ideal structure, that is, 90° when the target atom has six coordination (*i.e.*, octahedral) and 109.47° when four coordination (*i.e.*, tetrahedral), and A_i^{crystal} is each angle of the O–M–O of reference compounds. On this assumption, we found

the direct relationship between the parameter $A_{\text{distortion}}$ and the energy gap of the L_3 -edge XANES spectra of reference samples.

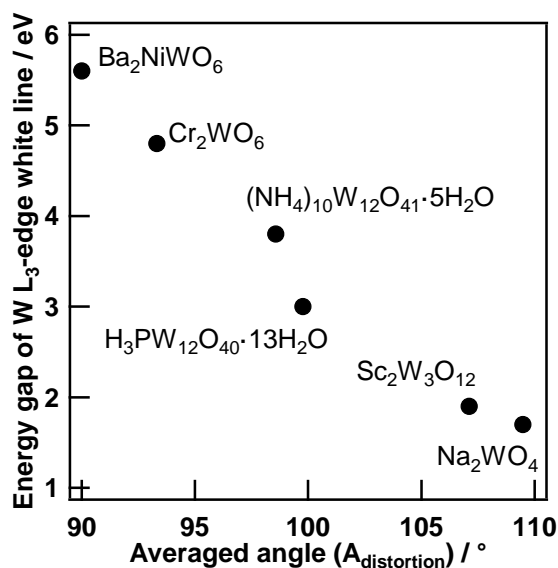


Figure 15. Dependence of the energy gap of the split 5d orbital for W reference samples on the averaged distorted angle.

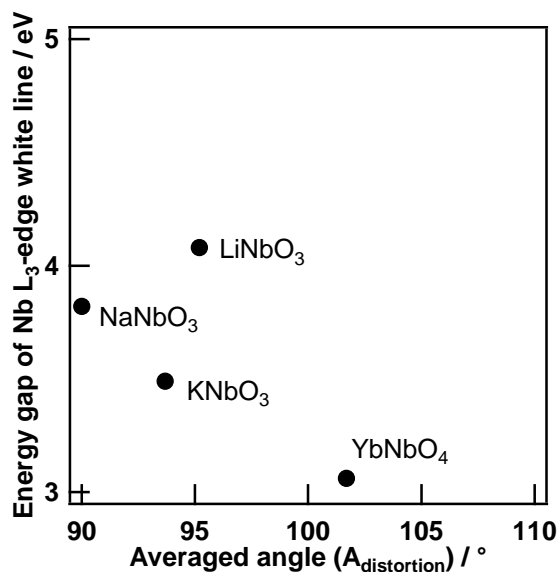


Figure 16. Dependence of the energy gap of the split 4d orbital for Nb reference samples to the averaged distorted angle.

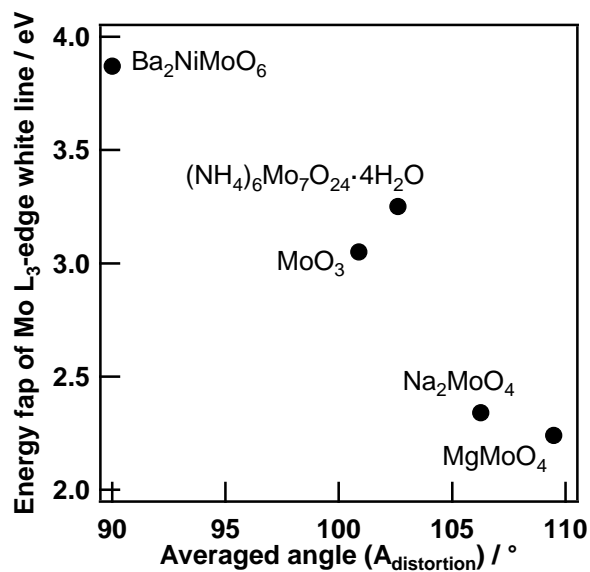


Figure 17. Dependence of the energy gap of split $4d$ orbital for Mo reference samples to the averaged distorted angle.

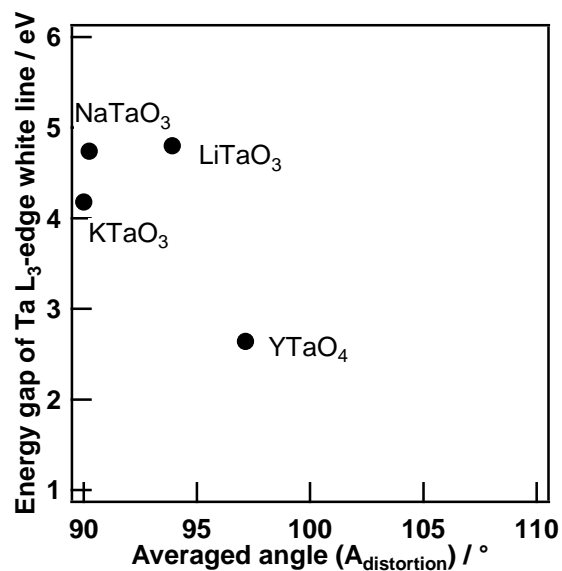


Figure 18. Dependence of the energy gap of split $5d$ orbital for Ta reference samples to the averaged distorted angle.

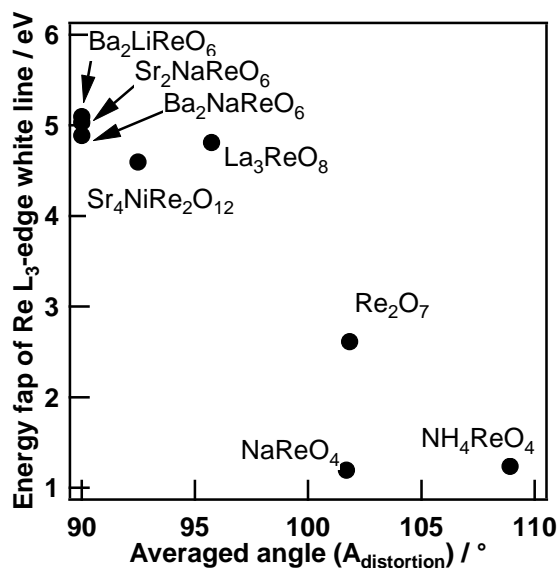


Figure 19. Dependence of the energy gap of split 5d orbital for Re reference samples to the averaged distorted angle.

Figure 15 shows the clear correlation between the physical and electronic parameters of W reference compounds and the corresponding graphs of the other elements (Nb, Mo, Ta, and Re) are summarized in Figure 16–19. At present, we do not have a detailed physical explanation of this relationship, but at least this empirical and semi-quantitative analysis can be used to estimate the degree of the local structure of unknown metal compounds.

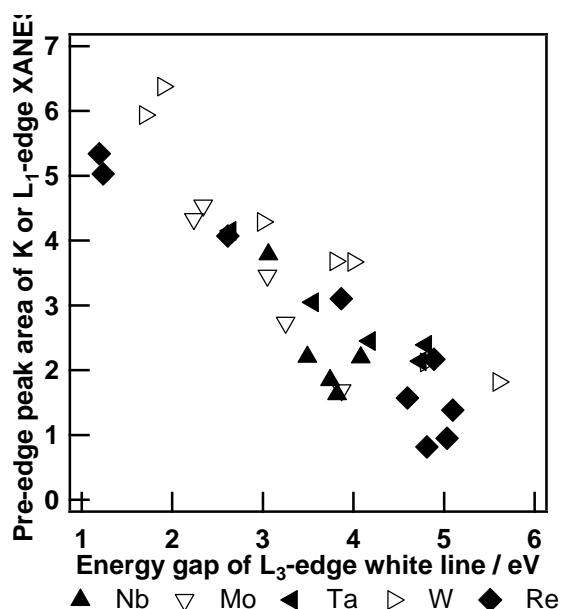


Figure 20. Dependence of pre-edge peak area of K- or L₁-edge XANES spectra on the energy gap of the L₃-edge white line. Reference samples were Nb, Mo, Ta, W, and Re.

Figure 20 shows again correlation trends of reference sample on the splitting of vacant d orbitals and the mixing ratio of p orbitals into d orbitals for Nb, Mo, Ta, W, and Re reference compounds. The correlation between local structure and characteristic shape of the XANES spectrum is a wide phenomenon common to group 5, 6, and 7 elements. We assume that the natural width and effective nuclear charge of each element can qualitatively explain the results.

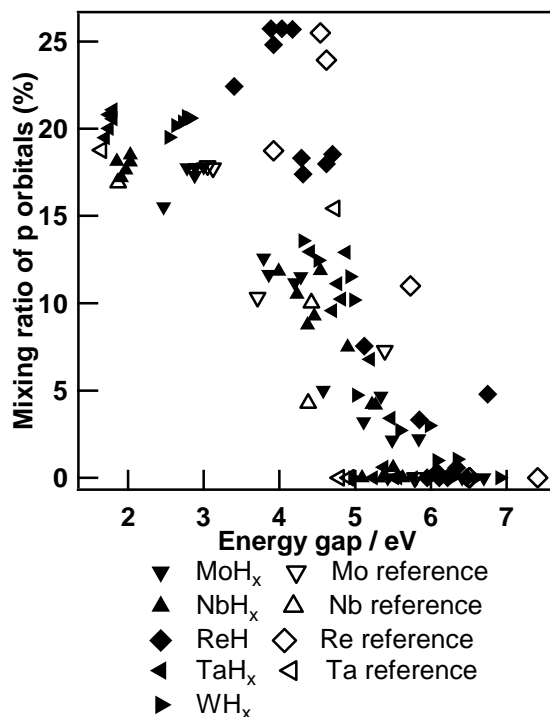


Figure 21. Dependence of 6p orbital contribution to 5d orbitals on the split 5d orbital energy gap for MH_x models (M = Nb, Mo, Ta, W, and Re).

Figure 21 shows the effect of element group or period on the electronic structure of MH_x models simulated by DFT calculation. Figure 21 exhibits a similar correlation between d orbital energy gap and p orbital contribution into d orbital, to the XANES analysis of all the elements presented in Figure 20. This result indicates the characteristic features of K, or L₁, and L₃-edge XANES spectra of the elements at different local configuration can be predicted by DFT calculation.

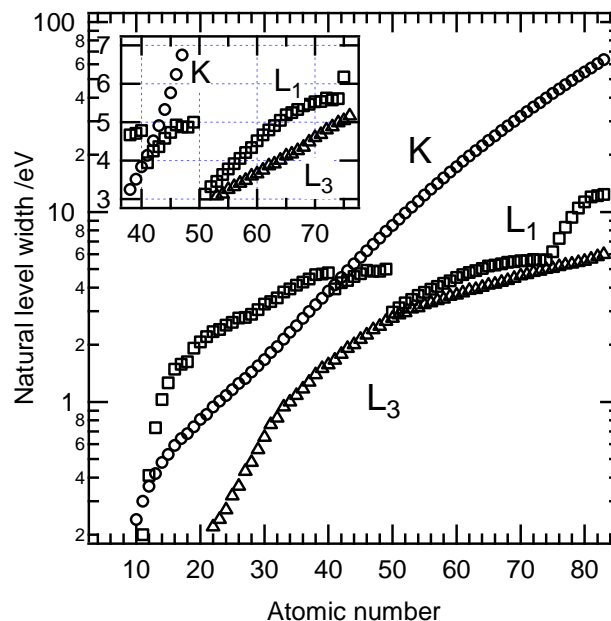


Figure 22. Natural widths for the K-, L_1 -, and L_3 -edges. Inset shows a magnified view including Nb, Mo, Ta, W, and Re. Natural widths are taken from Krause et al.²⁹

Figure 22 shows natural widths for the K-, L_1 -, and L_3 -edges. The natural widths of all elements vary from 0.2 to 60 eV; however, the natural widths of the K-edge of Nb (atomic number 41) and Mo (42) and L_1 -edge of Ta (73), W (74), and Re (75) are 4.14, 4.52, 5.58, 5.61, and 6.18, respectively, and thus are similar to each other. The similarity of W L_1 -edge XANES spectra for WO_4 species and Mo K-edge XANES of MoO_4 species has been pointed out on the basis of their natural level widths. Similar broadening of the pre-edge peak of Nb, Mo K-edge and Ta, W, Re L_1 -edge XANES is expected. Therefore, their pre-edge peak areas are anticipated to exhibit similar values to each other, assuming their local structures are alike.

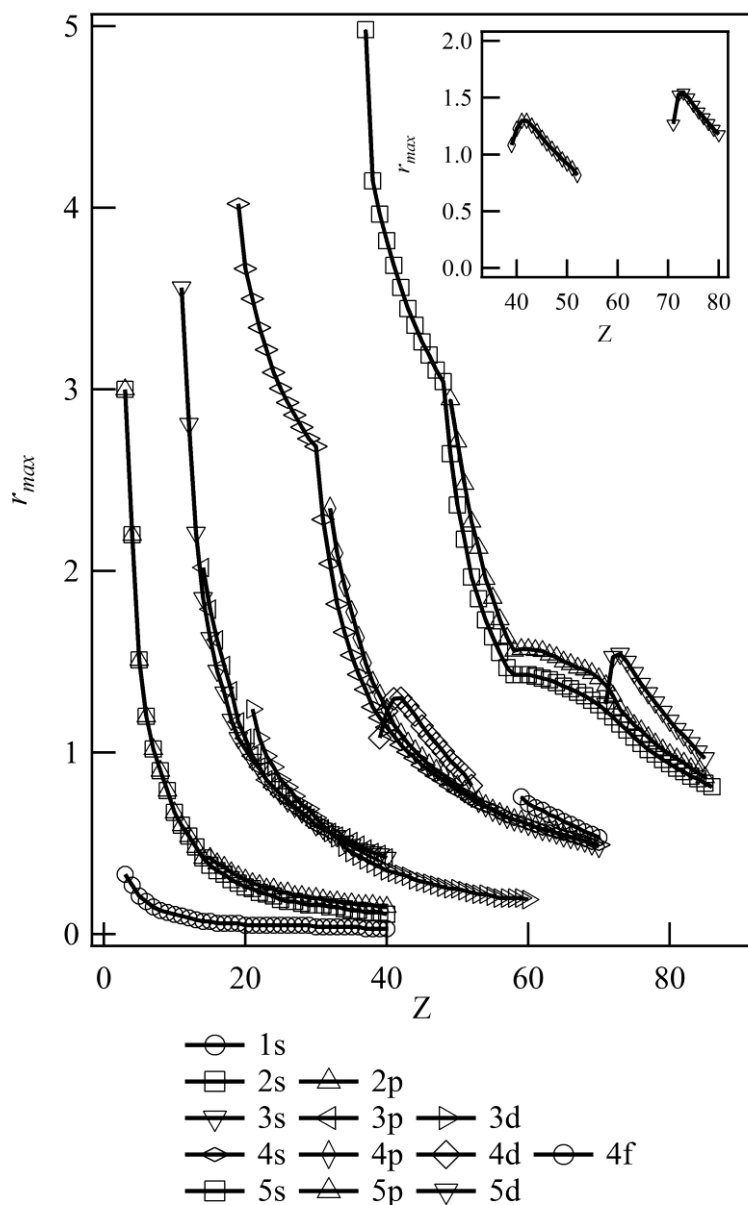


Figure 23. Radii of maximum charge density plotted against atomic number Z (reproduced from Clementi *et al.*, *J. Chem. Phys.*, **1967**, 47, 1300.).^{30, 31}

Figure 23 shows radii of maximum charge density r_{\max} plotted against atomic number. This refers to the radius of each orbital in the minimal-basis-set SCF functions of Slater's expression.^{30, 31} The arbitrary values of r_{\max} for Nb (atomic number 41) and Mo (42) 4d orbitals and for Ta (73), W(74), and Re (75) 5d orbitals are 1.2 – 1.6 and are similar to each other as shown in Figure 23. This means that 4d or 5d virtual orbitals for Nb, Mo, Ta, W, and Re experience a similar effective nuclear charge and exhibit a similar d orbital splitting value. Therefore, each compound containing Nb, Mo, Ta, W, or Re exhibits similar characteristic features on their XANES spectra.

Conclusions

The characteristic features of K-, L₁-, and L₃-edge XANES spectra for group V, VI, and VII elements in their complex oxide form, which have different coordination number, number of d electrons, and coordination sphere symmetry, have been summarized. The pre-edge peak area of K or L₁-edge XANES spectra has a linear correlation to the energy gap of the two white lines of the L₃-edge XANES spectra, depending on their local structure. This relationship can be attributed to the electric dipole transition from s to p component of the unoccupied hybridized orbitals. This correlation is supported by DFT calculations of several group V, VI, and VII structural models. This correlation indicated that careful analysis of XANES spectral details provides structural information about unknown group V, VI, and VII metal sites.

References

- (1) Yamamoto, T., *X-Ray Spectrom.*, **2008**, *37*, 572-584.
- (2) Aritani, H.; Shinohara, S.; Koyama, S.; Otsuki, K.; Kubo, T.; Nakahira, A., *Chem. Lett.*, **2006**, *35*, 416-417.
- (3) Bare, S. R.; Mitchell, G. E.; Maj, J. J.; Vrieland, G. E.; Gland, J. L., *J. Phys. Chem.*, **1993**, *97*, 6048-6053.
- (4) Bare, S. R., *Langmuir*, **1998**, *14*, 1500-1504.
- (5) Aritani, H.; Tanaka, T.; Funabiki, T.; Yoshida, S.; Eda, K.; Sotani, N.; Kudo, M.; Hasegawa, S., *J. Phys. Chem.*, **1996**, *100*, 19495-19501.
- (6) Yamazoe, S.; Hitomi, Y.; Shishido, T.; Tanaka, T., *J. Phys. Chem. C*, **2008**, *112*, 6869-6879.
- (7) Chen, Y.; Fierro, J. L. G.; Tanaka, T.; Wachs, I. E., *J. Phys. Chem. B*, **2003**, *107*, 5243-5250.
- (8) Tanaka, T.; Nojima, H.; Yamamoto, T.; Takenaka, S.; Funabiki, T.; Yoshida, S., *Physical Chemistry Chemical Physics*, **1999**, *1*, 5235-5239.
- (9) Froba, M.; Lochte, K.; Metz, W., *J. Phys. Chem. Solids*, **1996**, *57*, 635-641.
- (10) Jacob, K. T., *J. Mater. Sci.*, **1980**, *15*, 2167-2174.
- (11) Varga, T.; Wilkinson, A. P.; Jupe, A. C.; Lind, C.; Bassett, W. A.; Zha, C. S., *Phys. Rev. B*, **2005**, *72*, 024117.
- (12) Sleight, A. W.; Ward, R., *J. Am. Chem. Soc.*, **1961**, *83*, 1088-1090.
- (13) Baud, G.; Besse, J. P.; Chevalier, R.; Gasperin, M., *J. Solid State Chem.*, **1979**, *29*, 267-272.
- (14) Aneas, M.; Picard, J. P.; Baud, G.; Besse, J. P.; Chevalier, R., *Mater. Chem. Phys.*, **1983**, *8*, 119-123.
- (15) Bharathy, M.; Loye, H. C. Z., *J. Solid State Chem.*, **2008**, *181*, 2789-2795.
- (16) Hiraya, A.; Horigome, T.; Okada, N.; Mizutani, N.; Sakai, K.; Matsudo, O.; Hasumoto, M.;

- Fukui, K.; Watanabe, M., *Rev. Sci. Instrum.*, **1992**, *63*, 1264-1268.
- (17) Taguchi, T.; Ozawa, T.; Yashiro, H., *Physica Scripta*, **2005**, *T115*, 205-206.
- (18) Frisch, M. J.; Trucks, G. W.; Schlegel, H. B.; Scuseria, G. E.; Robb, M. A.; Cheeseman, J. R.; Montgomery, J., J. A.; Vreven, T.; Kudin, K. N.; Burant, J. C.; Millam, J. M.; Iyengar, S. S.; Tomasi, J.; Barone, V.; Mennucci, B.; Cossi, M.; Scalmani, G.; Rega, N.; Petersson, G. A.; Nakatsuji, H.; Hada, M.; Ehara, M.; Toyota, K.; Fukuda, R.; Hasegawa, J.; Ishida, M.; Nakajima, T.; Honda, Y.; Kitao, O.; Nakai, H.; Klene, M.; Li, X.; Knox, J. E.; Hratchian, H. P.; Cross, J. B.; Bakken, V.; Adamo, C.; Jaramillo, J.; Gomperts, R.; Stratmann, R. E.; Yazyev, O.; Austin, A. J.; Cammi, R.; Pomelli, C.; Ochterski, J. W.; Ayala, P. Y.; Morokuma, K.; Voth, G. A.; Salvador, P.; Dannenberg, J. J.; Zakrzewski, V. G.; Dapprich, S.; Daniels, A. D.; Strain, M. C.; Farkas, O.; Malick, D. K.; Rabuck, A. D.; Raghavachari, K.; Foresman, J. B.; Ortiz, J. V.; Cui, Q.; Baboul, A. G.; Clifford, S.; Cioslowski, J.; Stefanov, B. B.; Liu, G.; Liashenko, A.; Piskorz, P.; Komaromi, I.; Martin, R. L.; Fox, D. J.; Keith, T.; Al-Laham, M. A.; Peng, C. Y.; Nanayakkara, A.; Challacombe, M.; Gill, P. M. W.; Johnson, B.; Chen, W.; Wong, M. W.; Gonzalez, C.; Pople, J. A. *Gaussian 03, Revision D.03*, 2004.
- (19) Reed, A. E.; Weinhold, F., *J. Chem. Phys.*, **1983**, *78*, 4066-4073.
- (20) Reed, A. E.; Weinstock, R. B.; Weinhold, F., *J. Chem. Phys.*, **1985**, *83*, 735-746.
- (21) Horsley, J. A., *J. Chem. Phys.*, **1982**, *76*, 1451-1458.
- (22) Westre, T. E.; Kennepohl, P.; DeWitt, J. G.; Hedman, B.; Hodgson, K. O.; Solomon, E. I., *J. Am. Chem. Soc.*, **1997**, *119*, 6297-6314.
- (23) Oikawa, T.; Ookoshi, T.; Tanaka, T.; Yamamoto, T.; Onaka, M., *Microporous Mesoporous Mater.*, **2004**, *74*, 93-103.
- (24) Kruger, G. J.; Reynhardt, E. C., *Acta Crystallogr. B*, **1978**, *34*, 259-261.
- (25) Jacob, B. De kristalstructuur der alkaliperrhenaten en -jodaten. University of Groningen, 1934.
- (26) Aritani, H.; Tanaka, T.; Funabiki, T.; Yoshida, S.; Kudo, M.; Hasegawa, S., *J. Phys. Chem.*, **1996**, *100*, 5440-5446.
- (27) George, S. D.; Brant, P.; Solomon, E. I., *J. Am. Chem. Soc.*, **2005**, *127*, 667-674.
- (28) Roe, A. L.; Schneider, D. J.; Mayer, R. J.; Pyrz, J. W.; Widom, J.; Que, L., *J. Am. Chem. Soc.*, **1984**, *106*, 1676-1681.
- (29) Krause, M. O.; Oliver, J. H., *J. Phys. Chem. Ref. Data*, **1979**, *8*, 329-338.
- (30) Clementi, E.; Raimondi, D. L., *J. Chem. Phys.*, **1963**, *38*, 2686-2689.
- (31) Clementi, E.; Raimondi, D. L.; Reinhard, W. P., *J. Chem. Phys.*, **1967**, *47*, 1300-1307.

Chapter 2

La L₁- and L₃-edge XANES spectra of Lanthanum Complex Oxides: Experimental and Theoretical Approach to Local Structure

Abstract

La L₁, and L₃-edge X-ray absorption near edge structure (XANES) of various La oxides were analyzed by both of experimental and theoretical approaches from the point of view of local configuration of La. The results demonstrate a correlation among both of the pre-edge peak areas of the La L₁-edge XANES spectra and the full width at half maximum (fwhm) of white line of La L₃-edge XANES spectra, and the local configuration of La. Theoretical calculation of the XANES spectra and local density of states reveals that the origin and the difference of La L₁ and L₃-edge XANES spectra of various La compounds is related to the p-d hybridization of the unoccupied states and broadening of the d band of La induced by the change of local configuration of adjacent atoms. In addition, a simple index for a local structure defined by the angles of a La atom and the two adjacent oxygen atoms, which could be an indicator of centrosymmetry or disorder of the local configuration at La site, is found to have a correlation with the pre-edge peak intensity of the La L₁-edge XANES spectra and the fwhm of white line of La L₃-edge XANES spectra. Medium scale systematic simulation of the La L₁-edge XANES spectra of thousands of virtual La aqueous complex models validated the indexing criterion of the local disorder is applicable to the local configuration analysis of La. These results indicate that quantitative analysis of La L₁ and L₃-edge XANES spectra could be a practical method for local structure analysis of La materials.

Introduction

In the previous chapter, the author reported a systematic change of the characteristic features of K, L₁ and L₃-edge XANES spectra of group V, VI, and VII elements (Nb, Mo, Ta, W, Re) among their complex oxides. It revealed quantitative analysis on the pre-edge peak area of the K or L₁-edge XANES spectra and the split width of white line of the L₃-edge XANES spectra can provide some information on the local structure of Nb, Mo, Ta, W, or Re compounds. This result encouraged the author to perform a basic research of the XANES spectra of lanthanide elements, which are not so much explored in the other elements such as 3d transition metal element or precious metal elements.

Lanthanide is used in various fields such as magnetic material, dielectric material¹, phosphor², or hydrogen storage³ because of its characteristic property derived from the unusual electronic configuration of 4f heavy electrons, and the large ionic radii. For example, doping of La into BaTiO₃ has strong influence on its dielectric property.⁴⁻⁷ Yb³⁺ and Nd³⁺-doped Bi₂O₃-B₂O₃ glass works as low coherent wideband light sources.^{8,9} In many cases, small amount of lanthanide elements is added or doped into materials to develop or improve their characteristic property. The effects of lanthanide additives must depend on their location or electronic state in the materials, but, in general, it is not easy to observe structural or chemical changes induced by trace amount of such additives or structural or chemical information of such dopants themselves.

One of widely used analytical techniques to clarify structural and chemical information of such trace element is X-ray absorption spectroscopy (XAS). In particular, extended X-ray absorption fine structure (EXAFS), one part of XAS, has been widely used in many fields including lanthanide materials. For example, Marcus *et al.* and Peters *et al.* studied local structure of Er cation incorporated into silica and sodium silicate glasses by means of Er L₃-edge EXAFS spectroscopy^{10,11} and they estimated the disorder of oxygen atoms around Er, which could be related to the photoluminescence property. Antonio *et al.* applied EXAFS spectroscopy to Er or Lu doped sodium silicate glasses to investigate local environments of Er and Lu atoms and also utilized the Er and Lu L₃-edge XANES spectra and their second derivatives to obtain geometric information around the X-ray absorbing elements. It is noteworthy that the curve fitting analysis which is the most common approach to EXAFS spectra based on the EXAFS equation proposed by Sayer, Stern and Lytle¹²

strongly depends on the initial structural model, which is usually difficult to construct on amorphous materials. Whereas EXAFS oscillation is a sum of discrete sine waves caused by the interference of photoelectron waves ejected from the X-ray absorbing atoms, XANES spectrum is a convolution of the XANES spectra of every X-ray absorbing atoms. Thus, we do not need a detail structural model before interpreting XANES spectrum even though characters of the local structure should be kept in mind such as electronic deficiency or local symmetry.

The relationship between XANES spectra and geometric and electronic structure of various elements has been already investigated in detail as discussed in the general introduction and the previous chapter. There are also several research papers on the XANES spectra of a series of lanthanide elements. For example, Mountjoy *et al.* reported L₁-edge XANES spectra of Ce, Nd and Eu phosphate glasses and crystals¹³ and ascribed the presence of the small pre-edge shoulder peaks into p-d hybridization which depends on the centrosymmetry in analogy with the La L₁-edge XANES of La species in K₂O-SiO₂-La₂O₃ glasses¹⁴. D'Angelo *et al.* have reported a series of K and L₃-edge XANES and/or EXAFS analysis of various lanthanide aqueous complexes.¹⁵⁻²³ In particular, they utilized molecular dynamics to interpret the Ln L₃-edge XANES spectra and obtained structural parameters such as atomic distance between the Ln and adjacent O or other (*e.g.* S of solvent molecule) atoms of plausible solvation model. However, to the best of the author's knowledge, fundamental and systematic study focused on one lanthanide element L-edge XANES spectra themselves are relatively scarce. It might be because the Ln L-edge XANES usually exhibit monotonous, featureless spectra.

In this chapter, the author studied La L₁ and L₃-edge XANES spectra of various La complex oxides and found a relationship among the pre-edge peak area of La L₁-edge XANES spectra and the full width at half maximum (fwhm) of white line of La L₃-edge XANES spectra, and the local configuration of La. The author also proposed a simple criterion to calculate an index defined by the angles of La atom and the two adjacent oxygen atoms, which could be an indicator of centrosymmetry or disorder of the local configuration at La site, bond angle analysis parameter (BAA). In addition, theoretical simulation of La L₁ and L₃-edge XANES spectra and local density of states (LDOS) were performed with the state-of-the-art theoretical simulation codes, ORCA²⁴ based on molecular orbital theory and FEFF²⁵⁻²⁷ based on multiple scattering theory to simulate the

pre-edge shoulder peak at the experimental La L₁-edge XANES of reference La compounds and explore the origin of the peaks. These theoretical simulation were also performed to validate the indexing criterion by medium scale simulation of the pre-edge peak at the La L₁-edge XANES spectra with ORCA and FEFF of thousands of virtual La aqueous complex models.

Experimental Section

Sample Preparation of Lanthanum Oxides

Lanthanum complex oxides, La₄PdO₇, La₂CuO₄, LaCuSrO₄, LaFeSrO₄, LaSrAlO₄, LaCoO₃, and LaAlO₃ were prepared by solid state reaction. La₄PdO₇: La₂O₃ (325 mg, 1.0 mmol) and Pd(OAc)₂ (124 mg, 0.5 mmol); La₂CuO₄: La₂O₃ (652 mg, 2.0 mmol) and Cu(OAc)₂ (363 mg, 2.0 mmol); LaCuSrO₄: La₂O₃ (322 mg, 1.0 mmol), Cu(OAc)₂ (362 mg, 2.0 mmol) and SrCO₃ (295 mg, 2.0 mmol); LaFeSrO₄: La₂O₃ (325 mg, 1.0 mmol), Fe(NO₃)₃·9H₂O (810 mg, 2.0 mmol), and SrCO₃ (300 mg, 2.0 mmol); LaSrAlO₄: La₂O₃ (328 mg, 1.0 mmol), SrCO₃ (310 mg, 2.0 mmol), Al(NO₃)₃·6H₂O (750 mg, 2.0 mmol); LaCoO₃: La₂O₃ (327 mg, 1.0 mmol), Co(NO₃)₂·6H₂O (614 mg, 2.0 mmol); LaAlO₃: La₂O₃ (325 mg, 1.0 mmol) and Al(NO₃)₃·6H₂O (764 mg, 2.0 mmol). These mixtures are put into alumina crucible and heated at 1423 K for 24 h. The identification was done by comparison of the XRD patterns of the prepared samples and the reported ones in literatures.

XAS Measurement and Data Reduction

La L₁ and L₃-edge XANES spectra of these materials were measured at the BL5S1, hard X-ray XAFS beamline, at Aichi Synchrotron Radiation Center²⁸ (AichiSR; Aichi Science and Technology Foundation, Aichi, Japan). The XANES spectra of their powder samples were recorded in transmission mode under ambient condition, using a Si(111) double crystal monochromator. The photon energy was calibrated with the pre-edge peak (4966.0 eV) observed in the Ti K-edge XANES spectrum of Ti foil. Powder samples were mixed with an appropriate amount of boron nitride and pressed into pellets. Incident and transmitted X-ray fluxes were measured with ion chambers filled with He(70%)/N₂(30%) and N₂(15%)/Ar(85%). Higher harmonic X-ray was cut off with proper glancing angle of Rh-coated collimating and focusing mirrors.

A typical data reduction procedure (*e.g.* background removal, or normalization) was carried out

with the Athena ver. 0.9.18 included in the Demeter package.²⁹ Curve fitting analyses on the La L₁, and L₃-edge XANES spectra were also done with the peak fitting function implemented into the Athena and the multiplex fitting procedure implemented in Igor Pro ver. 6.32 (Wavemetrics, Lake Oswego, OR, USA).

Theoretical Calculation

XANES and local density of states (LDOS) calculation of La complex oxides cluster models were performed with FEFF. The cluster models were constructed from the crystal structure with ATOMS package,³⁰ which contains all atoms within 10 Å around the target X-ray absorbing atom (*i.e.* La). If there were nonequivalent La sites, a structural model for each La site was constructed. Both of electric dipole transition and electric quadrupole transition were taken into account for the XANES simulation using the Hedin–Lundqvist function for the fine structure and the ground state function for the background function with self-consistent field (SCF) and full multiple scattering (FMS) calculations. For the LDOS calculation, the Lorentzian broadening parameter was 1.0 eV.

Theoretical simulation of the La L₁ and L₃-edge XANES spectra for various reference samples were performed with the open restricted configuration interaction single-excitation (ROCIS) method under the density functional theory (DFT) implemented into the ORCA package.²⁴ The geometry optimization and ROCIS calculations³¹⁻³⁴ under the DFT were conducted using the B3LYP functional with the Ahlrich's polarized def2-TZVP basis sets^{35, 36} of triple ζ quality for all the atoms in combination with the auxiliary basis set def2-TZVP/J for the resolution of identity. DFT/ROCIS calculation was performed with the converged restricted Kohn-Sham wavefunctions. Scalar relativistic effects were incorporated explicitly by the ZORA correction.³⁷

On the XANES simulation with ORCA, virtual La aqueous complex models, which are virtual minimal La aqueous complex with the exact relative positions of La and O atoms taken from the X-ray crystal structure, was used instead of a large cluster model of lanthanide complex oxides in a similar manner to the previous literature.³³ For example, an aqueous complex model for LaCoO₃ was constructed and examined in the following procedure (Figure 1). First, the positions of La and the adjacent 12 O atoms were extracted from the crystal structure reconstructed from the X-ray diffraction pattern of LaCoO₃, which matches that of the prepared LaCoO₃. Second, two H atoms

were put next to each O atom to terminate the O atoms and compensate the negative charges and their positions were optimized in the molecular dynamics framework with universal force field³⁸ keeping the positions of La and O atoms fixed using Avogadro³⁹, an advanced semantic chemical editor. Third, the positions of the H atoms were optimized in the same condition of DFT/ROCIS calculation described above.

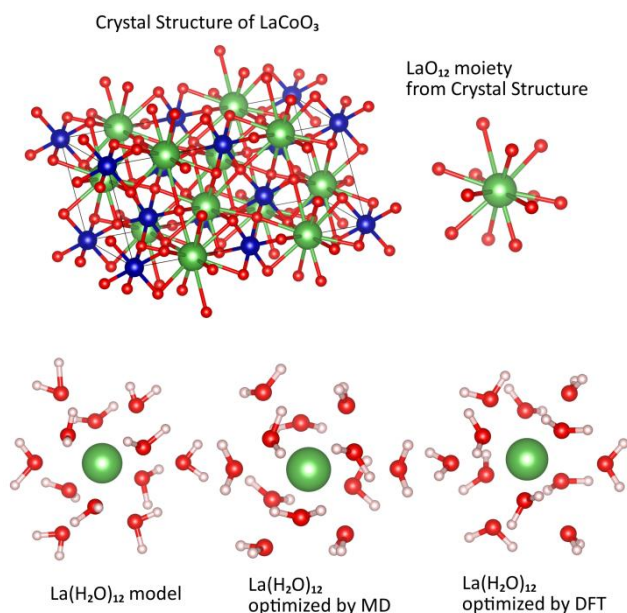


Figure 1. Example of an aqueous model complex of $\text{La}(\text{H}_2\text{O})_{12}$ from LaCoO_3 .

These calculations were performed on PC and the supercomputer located at Information Technology Center, Nagoya University.

Results and Discussion

La L₁-edge XANES Spectra of La Complex Oxides

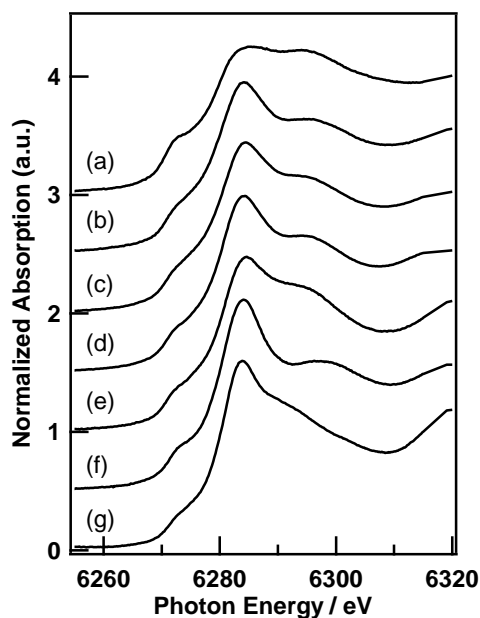


Figure 2. La L₁-edge XANES spectra of La complex oxides: (a) La₄PdO₇, (b) La₂CuO₄, (c) LaCuSrO₄, (d) LaFeSrO₄, (e) LaSrAlO₄, (f) LaCoO₃, and (g) LaAlO₃

Figure 2 shows the La L₁-edge XANES spectra of La₄PdO₇, La₂CuO₄, LaCuSrO₄, LaFeSrO₄, LaSrAlO₄, LaCoO₃, and LaAlO₃, which is the La is surrounded by several O atoms with various relative positions to La. The overall structure of the L₁-edge XANES spectrum of each compound is similar to each other, but the intensity of the characteristic pre-edge shoulder peaks at around 6275 eV varies among the samples. In the previous literature¹⁴, the pre-edge peaks are assigned to electronic transition from 2s to 5d unoccupied states. LaAlO₃ and LaCoO₃, which have 12 adjacent O atoms near the La, show the smallest shoulder peaks. LaSrAlO₄, LaFeSrO₄, and LaCuSrO₄ with 9 nearest O atoms exhibit a bit more evident pre-edge peaks. Furthermore, La₄PdO₇ with 7-coordinated O atoms and La₂CuO₄ bearing 8-coordinated O atoms have the largest and the second largest pre-edge peaks among the present La compounds. Thus, the pre-edge peak intensity roughly increases as the number of adjacent O atoms decreases.

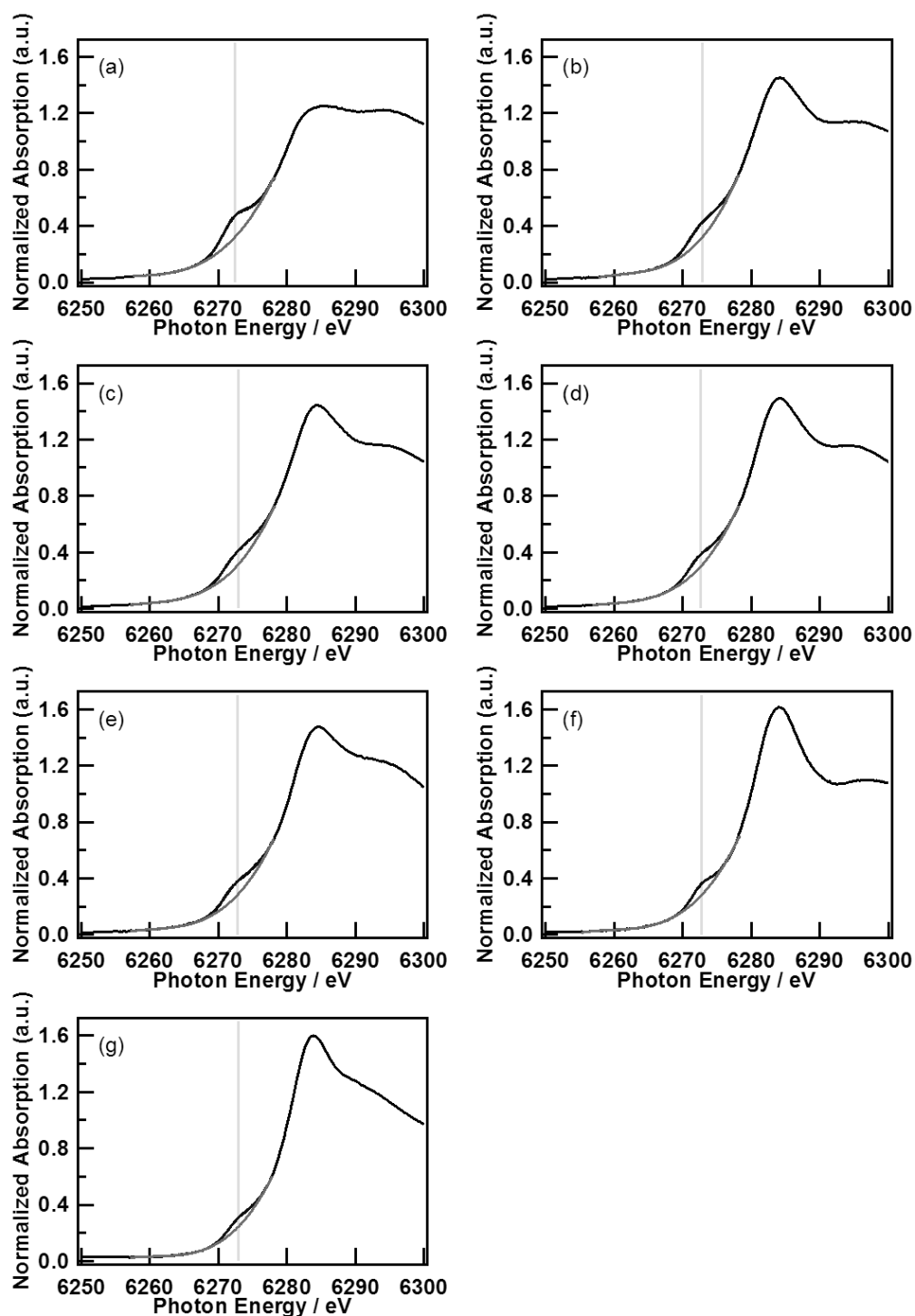


Figure 3. Curve fitting results of the pre-edge peak of La L_1 -edge XANES spectra of La complex oxides: (a) La_4PdO_7 , (b) La_2CuO_4 , (c) LaCuSrO_4 , (d) LaFeSrO_4 , (e) LaSrAlO_4 , (f) LaCoO_3 , and (g) LaAlO_3

Curve fitting analysis of the XANES spectrum with one Gaussian and one cubic function were performed to quantify the pre-edge peak area of each La L_1 -edge XANES spectrum as an indicator of

La local configuration. The results of La L_1 -edge XANES spectra are shown in Figure 3. As clearly seen, one Gaussian and one cubic function are enough to fit the experimental data. The peak area of LaCoO_3 and LaAlO_3 were the smallest values 0.290 and 0.263, respectively. La_4PdO_7 shows the largest pre-edge peak area, 0.721, and La_2CuO_4 , LaCuSrO_4 , LaSrAlO_4 and LaFeSrO_4 exhibit 0.555, 0.531, 0.495 and 0.388.

La L_3 -edge XANES Spectra of La Complex Oxides

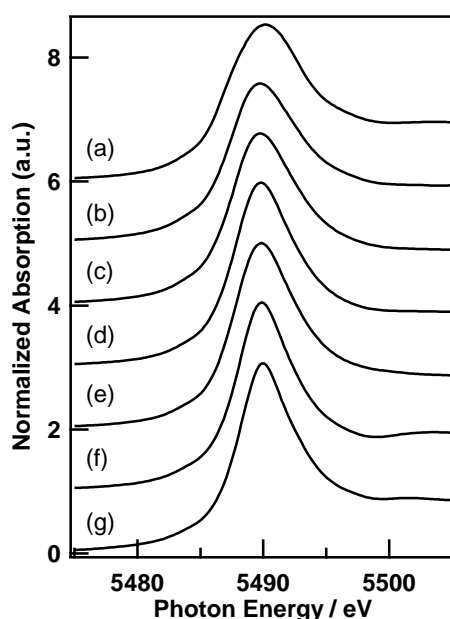


Figure 4. La L_3 -edge XANES spectra of La complex oxides: (a) La_4PdO_7 , (b) La_2CuO_4 , (c) LaCuSrO_4 , (d) LaFeSrO_4 , (e) LaSrAlO_4 , (f) LaCoO_3 , and (g) LaAlO_3

Figure 4 shows the La L_3 -edge XANES spectra of La_4PdO_7 , La_2CuO_4 , LaCuSrO_4 , LaFeSrO_4 , LaSrAlO_4 , LaCoO_3 , and LaAlO_3 . All spectra exhibit one slightly asymmetric and strong white line at around 5490 eV. These peaks are assignable to electric dipole transition from $2p_{3/2}$ to 5d state. LaAlO_3 and LaCoO_3 , which have 12 adjacent O atoms near the La^{3+} cation, show the narrowest white lines. LaSrAlO_4 , LaFeSrO_4 , and LaCuSrO_4 with 9 nearest O atoms exhibit slightly wider ones. Furthermore, La_4PdO_7 with 7-coordinated O atoms and La_2CuO_4 bearing 8-coordinated O atoms have the widest and the second widest white lines among the La samples. Aritani *et al.* reported the width of white line of La_2O_3 is significantly larger than that of $\text{La}(\text{OH})_3$ and pointed out that distortion of the local structure of LaO_6 unit of La_2O_3 and $\text{La}(\text{OH})_3$ could change the spectral shapes,

qualitatively⁴⁰. Similarly, the gradual change of the width of white line of La L₃-edge XANES spectra are assignable to the difference of the local configuration of LaO_x moiety.

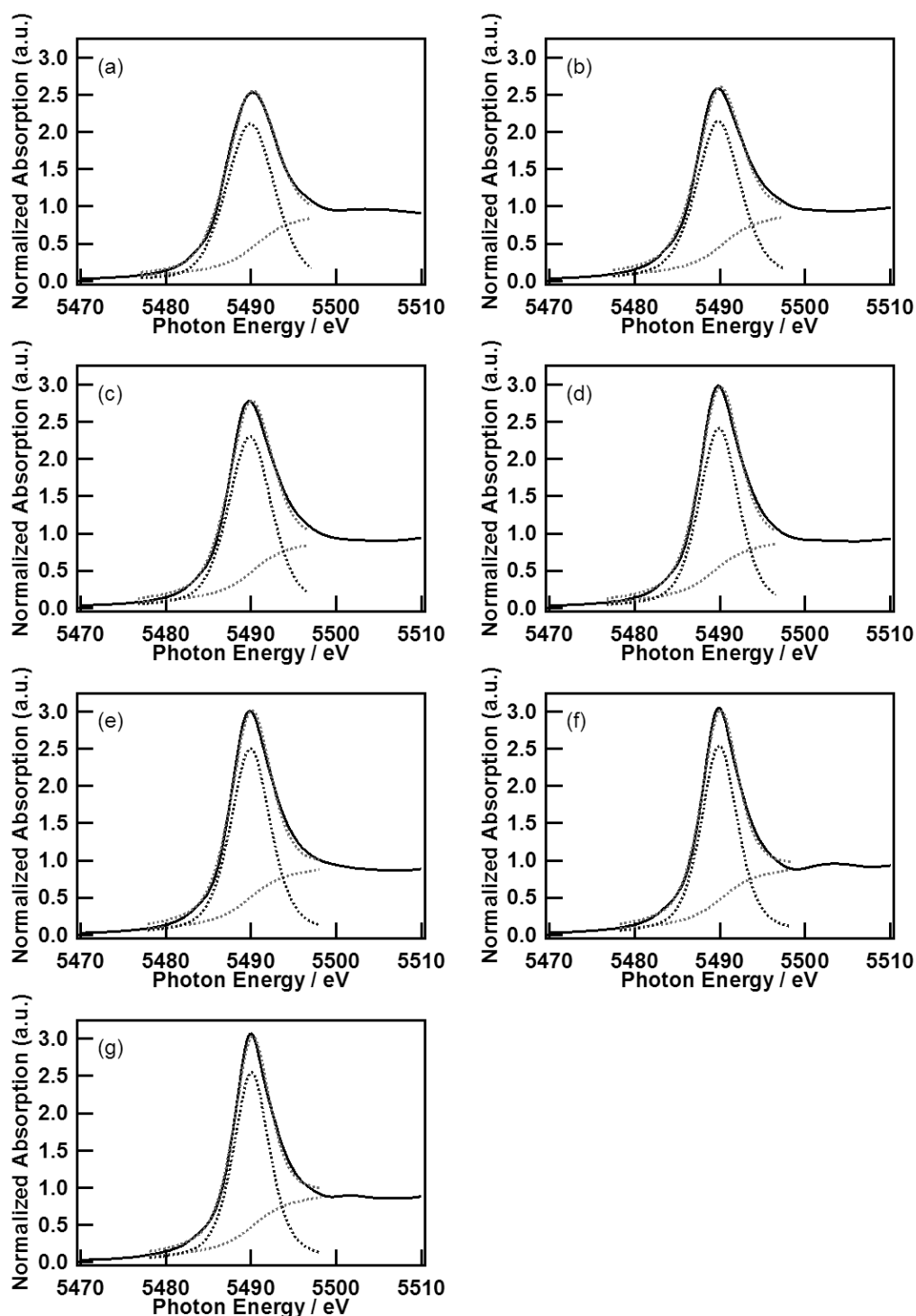


Figure 5. Peak fitting results of the white line of La L₃-edge XANES spectra of La complex oxides: (a) La₄PdO₇, (b) La₂CuO₄, (c) LaCuSrO₄, (d) LaFeSrO₄, (e) LaSrAlO₄, (f) LaCoO₃, and (g) LaAlO₃

We first calculated second derivatives of La L₃-edge XANES spectra to evaluate the d orbital

splitting depending on the local configuration of La in the same manner to the previous chapter. However, they were too noisy to evaluate the d orbital broadening quantitatively. Thus, the full width at half maximum (fwhm) of white line of each La L₃-edge XANES spectrum was estimated by curve analysis in a similar manner to the previous paper on Cs L₃-edge XANES spectra of Cs species in catalysts,⁴¹ for example. The La L₃-edge XANES spectrum was fitted with one arctangent function which means the electric transition from 2p_{3/2} to continuum states and one pseudo-Voigt function (Lorentzian:Gaussian=1:1) which represents the transition to the unoccupied states. Figure 5 shows the peak fitting results of La L₃-edge XANES spectra. As clearly seen, fitting procedure successfully reproduced the main shape of the white lines. The fwhm of white line of LaCoO₃ and LaAlO₃ display the smallest values, 5.09 and 5.05, respectively. La₄PdO₇ shows the largest fwhm of the white line, 6.70, and La₂CuO₄, LaCuSrO₄, LaSrAlO₄ and LaFeSrO₄ exhibit 6.19, 6.00, 5.57 and 5.51.

Relationship between the Pre-edge Peak Area of La L₁-edge and the fwhm of White Line of La L₃-edge XANES Spectra

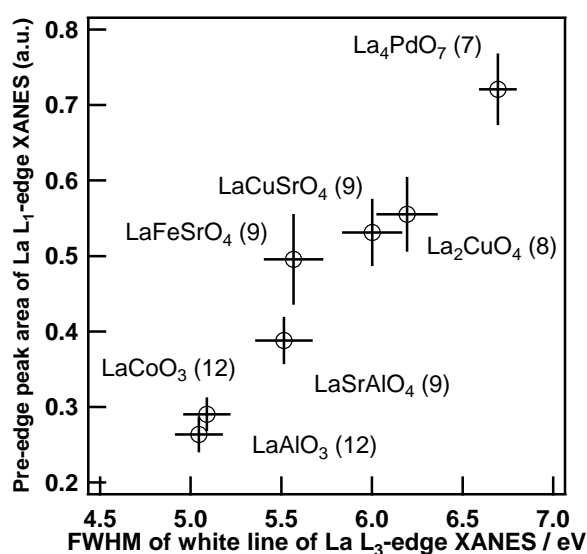


Figure 6. Dependence of pre-edge peak area of La L₁-edge XANES spectra on the FWHM of white line of La L₃-edge of La₄PdO₇, La₂CuO₄, LaCuSrO₄, LaFeSrO₄, LaSrAlO₄, LaCoO₃, and LaAlO₃ (The number in parentheses denotes the number of the coordinated oxygen atoms to La.)

Figure 6 shows a linear correlation ($R^2 = 0.95$) between the pre-edge peak areas of La L₁-edge XANES spectra and the fwhm of the white line of L₃-edge XANES of La compounds. This

phenomenon is not unexpected because the pre-edge peak which should be related to the mixing of p states into d states of La, and the d state broadening must be induced simultaneously by the change of the local configuration of La. Furthermore, there is an interesting relationship between the local structure and the electronic states observed by L_1 and L_3 -edge XANES spectra. That is La_4PdO_7 , which has the smallest number of coordinated atoms to La, shows the largest pre-edge peak area and the widest fwhm of the white line in its L_3 -edge XANES region and, as the number of the adjacent O atoms increases, the pre-edge peak intensity and the fwhm decreases, respectively.

Theoretical Calculation of L_1 and L_3 -edge La XANES Spectra and Local Density of States

The origin of the pre-edge peak of La L_1 -edge XANES spectra and the white line of La L_3 -edge XANES spectra are temporarily interpreted into electric dipole transition from 2s to p-d hybridized unoccupied states and from $2p_{3/2}$ to 5d states, respectively. Shoulder peaks at Ln L_1 -edge XANES spectra have been already discussed in several papers. Larson *et al.* reported that the shoulder peak at the La L_1 -edge XANES spectrum of $\text{K}_2\text{O-SiO}_2\text{-La}_2\text{O}_3$ glasses on their XAS study of La coordination environments is due to the 2s to nd transition, which maybe means the electric dipole transition to p-d hybridized states or electric quadrupole transition to d component.¹⁴ Materlik *et al.* discussed the Ce, Sm, Gd and Er L_1 -edge XANES spectra in the atomic and condensed (solid or metallic) states and concluded the shoulder peak can be associated to the p-projected density of conduction-band states.⁴² Chaboy *et al.* also explained the decrease of the shoulder peak intensity at the Ce and La L_1 -edge XANES spectra of CeFe_2 , CeRu_2 , LaRu_2 after hydrogenation by the change of the p-d hybridization of unoccupied states.⁴³ Ishimatsu *et al.* also explained the loss of the shoulder peak at the La L_1 -edge caused by hydrogenation of La metal in the same way.⁴⁴

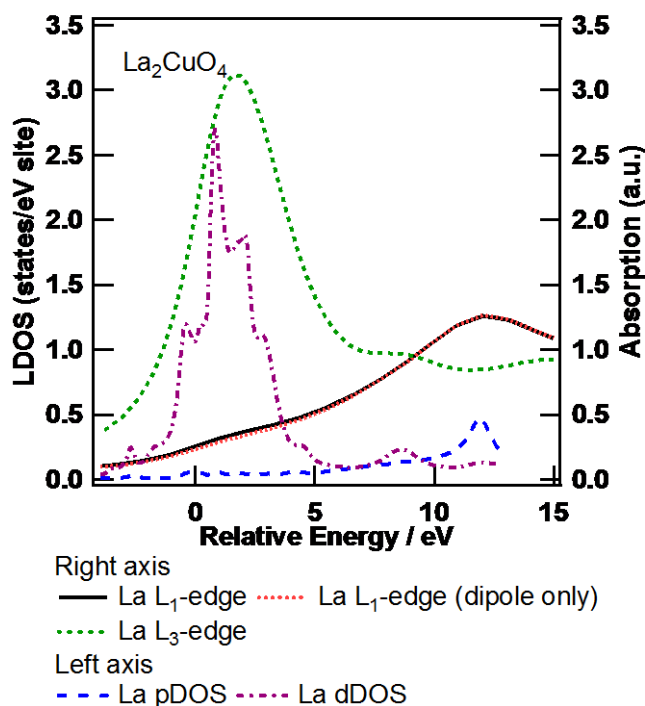


Figure 7. La L_1 and L_3 -edge XANES spectra and LDOS at La site of La_2CuO_4 calculated with FEFF 9.0. (The relative energy is originated by the estimated Fermi energy.)

To clarify the origin of each feature observed at La L_1 and L_3 -edge, theoretical calculation of L_1 , L_3 -edge XANES spectra and LDOS at La site were performed with FEFF 9.0 code. Figure 7 shows the La L_1 and L_3 -edge XANES spectra and LDOS at La site of La_2CuO_4 . The energy axis for both of the L_1 and L_3 -edge XANES spectra and LDOS is a relative value to the estimated Fermi level. The estimated Fermi level with FEFF code has an uncertainty by a few eV, and the absolute value may be a little different from the true value, but it does not matter to discuss the origin of the pre-edge peak of the L_1 -edge and white line of the L_3 -edge. As clearly seen, the strong white line of La L_3 -edge is ascribed to the unoccupied (mainly) d state. At the La L_1 -edge, a small but distinct shoulder peak is observed at around 1 eV. Both of them are consistent with the discussion above.

In the previous literature¹⁴, the pre-edge peak of the L_1 -edge pre-edge is assumed to be electric dipole and quadrupole electronic transitions. However, the quadrupole transition is two orders of magnitude weaker than dipole transition. As seen in Figure 7, both of electric dipole and quadrupole transition have distinct contribution, but the electric quadrupole transition is indeed significantly smaller than dipole transition. To evaluate the contribution of quadrupole transition of La materials quantitatively, we also calculated the La L_1 -edge XANES spectra of LaAlO_3 , and La_4PdO_7 .

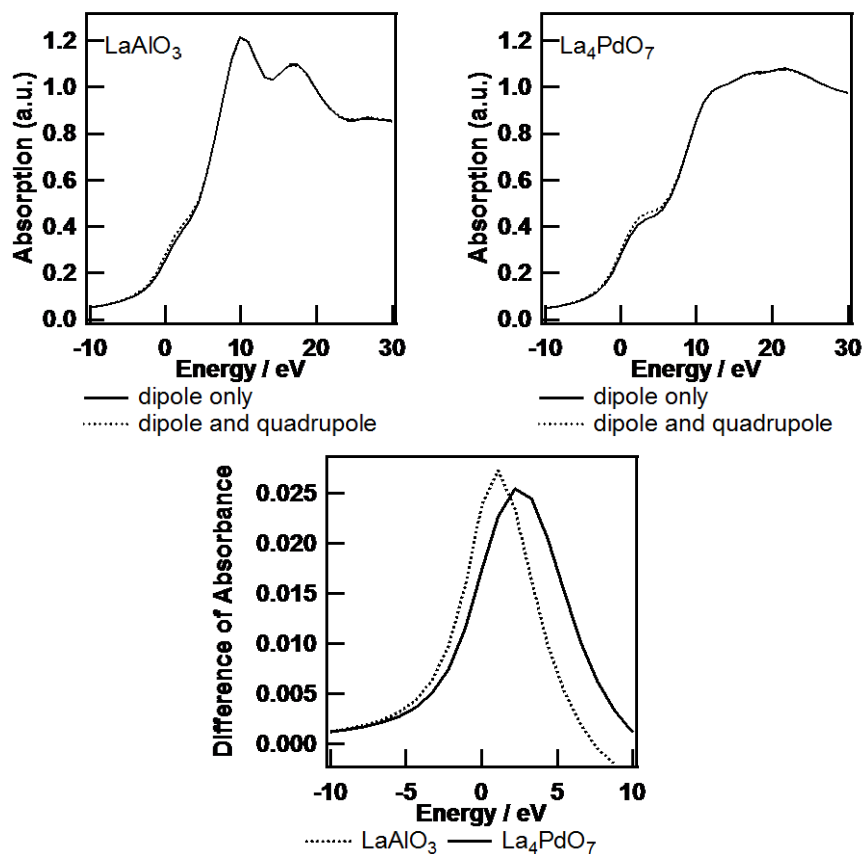


Figure 8. La L₁-edge XANES spectra of LaAlO₃ (left) and La₄PdO₇ (right) calculated with FEFF code with only electric dipole transition and with both of electric dipole and quadrupole transition and the differential spectra of electric quadrupole and dipole transitions in the pre-edge region (lower).

In Figure 8, La L₁-edge XANES spectra of LaAlO₃, which shows the smallest pre-edge peak, and La₄PdO₇, which shows the largest pre-edge peak, calculated with only electric dipole transition and with both of electric dipole and quadrupole transition are shown. The quadrupole transition has distinct, but weak contribution to the pre-edge peak in both of them. The differential spectrum was also calculated for each spectrum and the electric quadrupole contribution in these materials is almost same as also shown in Figure 8. This means the quadrupole transition does not depend on the local structure of La, but the dipole transition depends on it. It might be because the d character of the unoccupied state may be similar to each other among the La samples, but p character ratio of the unoccupied state is altered by the local configuration of La. In addition, this indicates the pre-edge peak area extracted by curve fitting of the L₁-edge XANES consists of an almost constant

contribution of quadrupole transition and varying contribution of dipole transition affected by La surroundings.

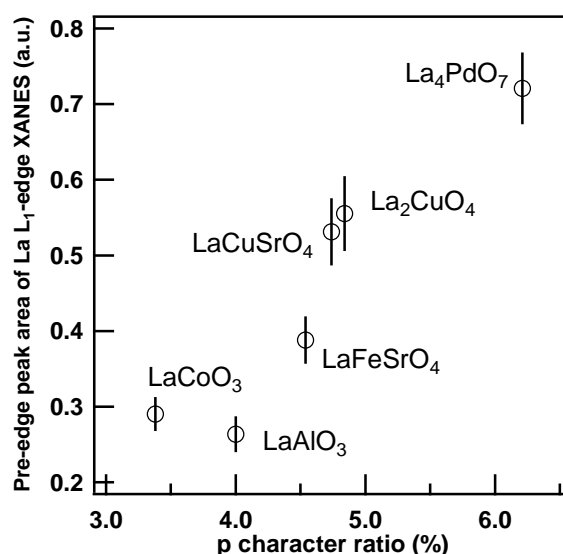


Figure 9. Dependence of pre-edge peak area of La L₁-edge XANES spectra on the p character ratio of LDOS around Fermi energy of La L₃-edge of La₄PdO₇, La₂CuO₄, LaCuSrO₄, LaFeSrO₄, LaCoO₃, and LaAlO₃

Figure 9 shows a relationship between the pre-edge peak area of La L₁-edge XANES and p component contribution to unoccupied states. This correlation ($R^2 = 0.87$) also quantitatively demonstrates the pre-edge peak of L₁-edge XANES spectra is a probe for the p character of the unoccupied states. For example, Roe *et al.* and Westre *et al.* have already reported similar analysis of the pre-edge peak of Fe K-edge XANES spectra of various Fe complexes, which are ascribed to the p-d hybridization of the unoccupied orbital in the final state. Roe *et al.* used extended-Hückel calculation to evaluate the Fe 4p character in the final state in order to understand the difference of the pre-edge peak area of Fe K-edge XANES spectra and found a clear correlation between the pre-edge peak area and the 4p contribution ratio.⁴⁵ Westre *et al.* performed theoretical calculation of various Fe model complexes based on density functional theory in a similar manner, evaluated the contribution of each orbitals by Mulliken population analysis, and clarified the relationship among the local symmetry, 4p character of the unoccupied orbitals, and the pre-edge peak structure of Fe K-edge XANES spectra.⁴⁶ Yamazoe *et al.* also reported a clear correlation among the energy gap of d orbital splitting,⁴⁷ the mixing ratio of 6p orbitals into 5d orbitals, and its local symmetry of various W

model molecules.

Attempt of Parameterization of La Local Configuration and its Relation to the XANES Spectra

As discussed in Chapter 1 on the XANES spectra and the local structure of some of group V, VI, VII metal (*i.e.* Nb, Mo, Ta, W, and Re) oxides, theoretical simulation of the electronic structure of minimal molecular models such as MH_4^{n+} , or MH_6^{m+} (M stands for Nb, Mo, Ta, W, or Re, and n or m stand for appropriate numbers for electrons) indicated that change of the atomic distance between the X-ray absorbing atom (M) and adjacent atoms had little influence on the pre-edge peak intensity, but angular change of ligand–M–ligand strongly affected the pre-edge peak intensity. The centrosymmetry of the M cation strongly affects their XANES spectra.

In group V, VI, VII elements, there are only 4, 5, and 6-coordinated unit such as lowly centrosymmetric tetrahedral WO_4 unit of highly centrosymmetric octahedral WO_6 unit, for example. On the other hand, in the case of elements with very large ionic radii such as La, its oxides could be accompanied with 7 to 12 coordinated O atoms. The centrosymmetry of La coordination sphere might be considered to be high with 12-coordinated atoms and low with 7-coordinated ones. In addition, atomic distance between La and coordinated atoms could also vary from about 2.0 Å to about 3.5 Å. Therefore, as discussed on lanthanide-doped glass in the introduction, it is not easy to determine the local configuration of lanthanide atoms in amorphous materials with EXAFS spectroscopy. Thus, a parameterization criterion is introduced for quantitative analysis on the local configuration of La.

In the field of metallurgy, the degree of distortion or defect of the microstructure of every metal atom in bulk metal could be evaluated on various criteria with the aid of molecular dynamics⁴⁸ (MD). For example, centrosymmetry parameter (CSP) is proposed by Kelchner *et al.* to evaluate the defect or dislocation of metal.⁴⁸ Ackland *et al.* used bond angle analysis (BAA) to identify the local coordination, distinguishing fcc, hcp, bcc, and other structures of each metal atom simulated by MD and so forth.⁴⁹ We applied the CSP and simplified BAA methods to parameterize the local configuration of the La center and found that a simplified BAA analysis could be used to produce well correlated parameters to the characteristic features of the XANES spectra in the following procedure. Simplified BAA parameter is defined in the following equation,

$$\text{BAA} = \frac{1}{n} \sum |\cos(\theta_{ijk})|$$

where n and θ_{ijk} denote the number of independent angles and the angle formed by the central atom j , and two of its adjacent atoms, i and k . If there are unidentical sites of La, the BAA parameter is calculated as an average value of the each BAA parameter on each site. First, the Cartesian coordinates of the nearest adjacent oxygen atoms with an assumption La is located at the origin (0, 0, 0) are extracted from the crystal structure within 3.3 Å from La center. Second, the absolute values of cosine of every angle formed by La and two adjacent oxygen atoms are summed up, and averaged by the number of independent angles. For example, the simplified BAA parameters of 6-coordinated regular octahedron, 8-coordinated cube, and 12-coordinated icosahedron are 0.2, 0.429, and 0.455, respectively. Thus, the simplified BAA parameter increases as the coordination number increases at least in the range from 6 to 12.

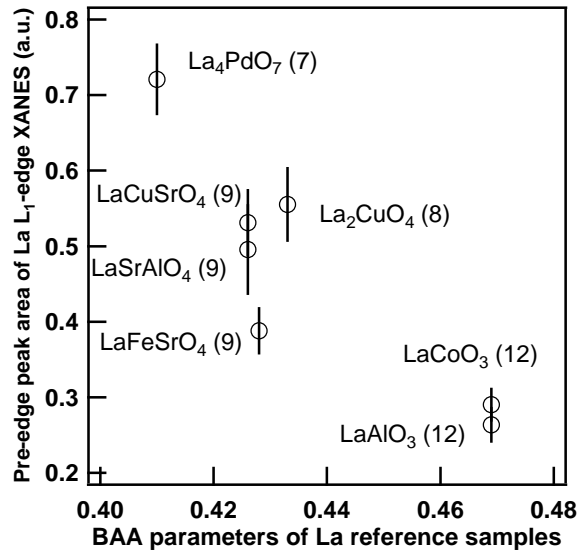


Figure 10 Dependence of pre-edge peak area of La L₁-edge XANES spectra on the BAA parameters of La₄PdO₇, La₂CuO₄, LaCuSrO₄, LaFeSrO₄, LaSrAlO₄, LaCoO₃, and LaAlO₃ (The number in parentheses denotes the number of the coordinated O atoms to La.)

The dependence of pre-edge peak area of La L₁-edge XANES spectra on the BAA parameters of the La oxides is summarized in Figure 10. The pre-edge peak areas of L₁-edge XANES spectra have a significant correlation ($R^2 = 0.79$) to the BAA parameters. This indicates the BAA parameter, which could be calculated from an arbitrary model, even an amorphous one, could be an indicator of the

coordination number, or at least the local configuration of La in the range from 7 to 12 of its coordination number. As mentioned above, the BAA parameter of the regular octahedron is 0.2 and it seems to be difficult to extend this criterion into 6 or less coordinated La moiety.

This result encouraged us to extend the well-known analysis strategy of the pre-edge peak of the K-edge XANES spectra of 3d early transition metals to that of the La L₁-edge XANES spectra. The BAA parameter was inspired by a discussion in metallurgy to interpret the local structure of a metal atom in ill-defined model generated by molecular dynamics and might have a relationship with the pre-edge peak intensity induced by the p-d hybridization. However, the definition of the BAA parameter may look too primitive to associate with some physical meaning straightforwardly.

Then, La L₁-edge XANES simulation of thousands of virtual La(H₂O)_n complex models was employed to validate the BAA parameter as an indicator of the local symmetry. Before the medium scale simulation, we first tried to reproduce the pre-edge peak feature at the La L₁-edge of the reference samples with the ORCA package based on time dependent density functional theory (TDDFT) or open restricted configuration interaction singles (ROCIS) and FEFF package based on multiple scattering theory.

ROCIS, TD-DFT, and FMS Calculation of La L₁-edge XANES of La Complex Oxides

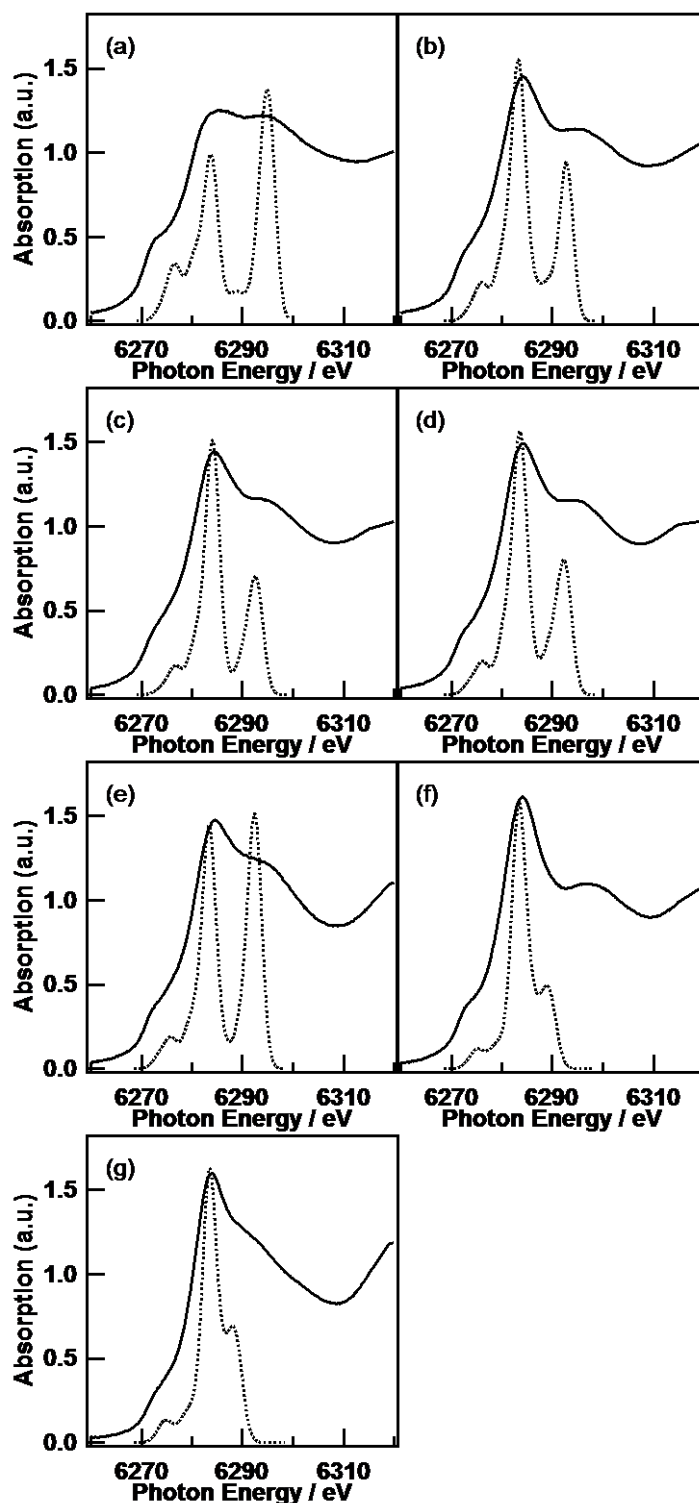


Figure 11. Experimental and DFT/ROCIS simulated La L₁-edge XANES spectrum of various La compounds and La(H₂O)_n model complexes: (a) La₄PdO₇, (b) La₂CuO₄, (c) LaCuSrO₄, (d) LaFeSrO₄, (e) LaSrAlO₄, (f) LaCoO₃, and (g) LaAlO₃ (Experimental: solid; simulated: dotted)

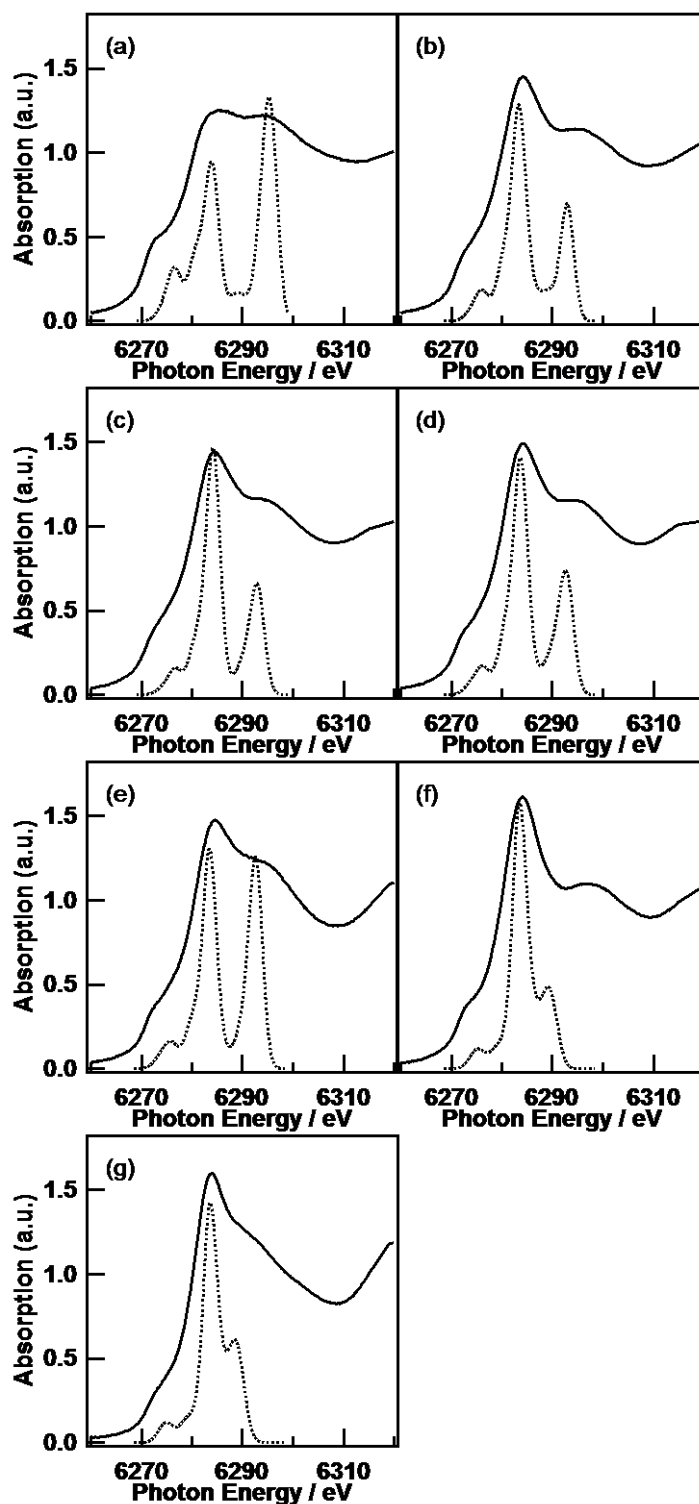


Figure 12. Experimental and TD-DFT simulated La L_1 -edge XANES spectrum of various La compounds and $\text{La}(\text{H}_2\text{O})_n$ model complexes: (a) La_4PdO_7 , (b) La_2CuO_4 , (c) LaCuSrO_4 , (d) LaFeSrO_4 , (e) LaSrAlO_4 , (f) LaCoO_3 , and (g) LaAlO_3 (Experimental: solid; simulated: dotted)

Figure 11 (a) shows the experimental La L_1 -edge XANES spectrum of La_4PdO_7 and the

corresponding simulated spectrum of $\text{La}(\text{H}_2\text{O})_7$ complex model by ROCIS calculation. The simulated spectrum was broadened by Gaussian function by 4 eV (fwhm), and shifted toward the higher energy by 19 eV to fit the peaks of the experimental spectrum. The peak positions of the simulated spectrum at around 6275, 6284, and 6288 eV reasonably match the three peak positions of the experimental one at around 6273, 6284, and 6292 eV. The reason of apparent slight difference of the peak positions of the simulated spectra and the experimental ones is maybe because the transition to the continuum state is not included in the present simulation, the line width broadening applied to each transition might be not appropriate to reproduce the experimental spectrum, and no multiple scattering effect, which can change the fine structure potentially, is not considered. The simulated La L_1 -edge XANES spectra of other virtual La aqueous model complexes also reproduce the corresponding La complex oxides (Figure 11), and the shoulder peaks of the experimental spectra were reproduced as the lowest peaks of the simulated spectra at least qualitatively. In addition, TD-DFT calculation on the same models was also performed in similar parameters, and found to also reproduce the dominant three peaks observed from 6270 eV to 6300 eV as shown in Figure 12.

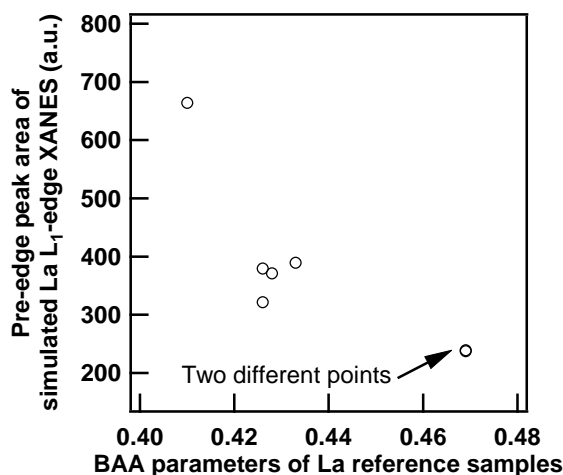


Figure 13. Dependence of the peak area at the lowest energy of simulated La L_1 -edge XANES spectra on the BAA parameters of La aqueous complex models of La_4PdO_7 , La_2CuO_4 , LaCuSrO_4 , LaFeSrO_4 , LaSrAlO_4 , LaCoO_3 , and LaAlO_3

For quantitative analysis of the shoulder peak simulated with ORCA, we compare the first prominent peak area integrated from 6270 eV to 6278 eV to the BAA parameters, which have been already proved to correlate to the experimental shoulder peak at the La L_1 -edge XANES extracted by

curve fitting analysis with a cubic function as a background and a Gaussian function (Figure 10). Figure 13 exhibits a monotonous dependence of the lowest energy peak area on the BAA parameters. Thus, these results demonstrate both of the DFT/ROCIS and TD-DFT calculation with ORCA are capable to simulate the La L_1 -edge XANES spectra at least in the lower unoccupied states region of various real compounds even though the structural model for the calculation is very simple aqueous La complex. However, one might be suspicious of the number of the reference samples. Thus, XANES simulation of the thousands of virtual La complex models is discussed to support the monotonous correlation in the following section.

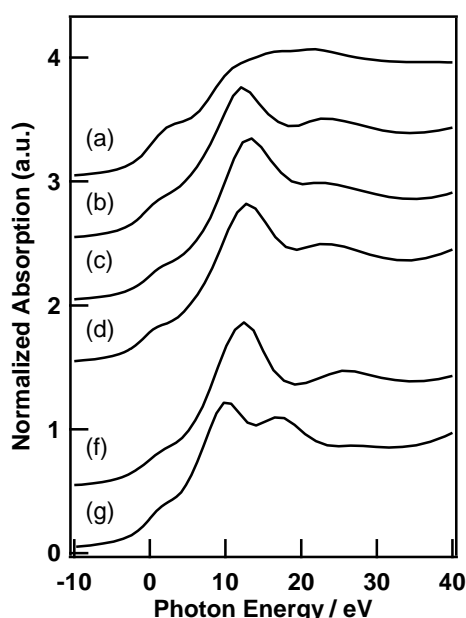


Figure 14. Simulated La L_1 -edge XANES spectra of various La complex oxides cluster models with FEFF: (a) La_4PdO_7 , (b) La_2CuO_4 , (c) LaCuSrO_4 , (d) LaFeSrO_4 , (f) LaCoO_3 , and (g) LaAlO_3

Figure 14 shows the simulated La L_1 -edge XANES spectra of the reference compounds with FEFF code under full multiple scattering (FMS) framework including electric dipole and quadrupole transition. The energy axis was shown as a relative energy to the predicted Fermi energy. FEFF calculation of the La complex oxide cluster models reproduced the La L_1 -edge XANES spectra comparable to the experimental ones except for LaSrAlO_4 including the pre-edge shoulder peaks observed right above the Fermi level. The order of the spectra is same as Figure 2, but the spectrum (e) LaSrAlO_4 is omitted because a plausible spectrum on the material cannot be achieved. The

pre-edge peak area were also evaluated quantitatively in the same manner to the experimental ones, that is curve fitting analyses by one background cubic function and one Gaussian function for the pre-edge peak. As a result, the peak area has a clear correlation with the BAA parameters again as shown in Figure 15.

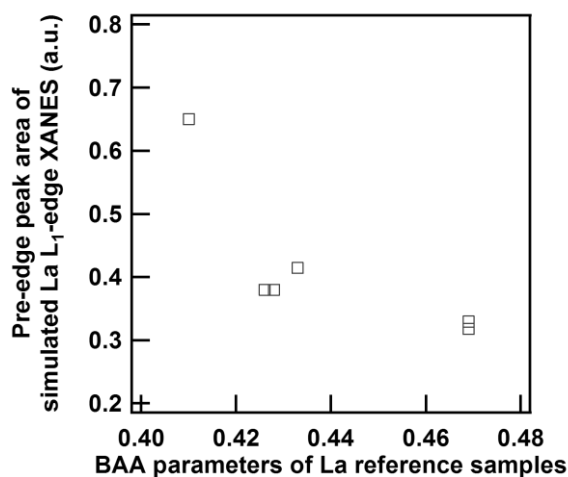


Figure 15. Dependence of the peak area at the pre-edge peak of FEFF simulated La L₁-edge XANES spectra on the BAA parameters of La aqueous complex models of La₄PdO₇, La₂CuO₄, LaCuSrO₄, LaFeSrO₄, LaCoO₃, and LaAlO₃

Thus, FEFF code is also capable to simulate the La L₁-edge XANES spectra quantitatively as same as ORCA. The contribution of electric quadrupole transition to the pre-edge peak is almost constant among the reference compounds. As discussed above, the pre-edge peak has been already discussed on Ln compounds having well-defined structure from the point of view of p component of the unoccupied states. However, to the best of the author's knowledge, it has not been discussed systematically on the shoulder peak and the p orbital hybridization of La, which has various irregular coordination environment of La.

A possible approach to evaluate the p component contribution to the unoccupied state is population analysis of virtual orbitals of the ground state model. For example, George *et al.* discussed the pre-edge peak observed at the Ti K-edge XANES spectra of TiCl₄, TiCpCl₃, and TiCp₂Cl₂ (Cp = cyclopentadienyl) by the ground state DFT calculation with ADF package on the point of the 3d-4p mixing and metal-ligand covalency.⁵⁰ They found the pre-edge peak area can be clearly explained by the amount of Ti 4p component of the unoccupied orbitals. Single point

calculation of the Ti complexes with ORCA package was also performed and confirmed the result of Löwdin population analysis agrees with the George's result. However, it was not the case of our virtual La aqueous complex models because of the complexity of the local environment of La. Even though the single point calculation of the tetrahedral TiCl_4 complex exhibits a clear picture of the ligand field splitting to e and t_2 states, the ground state calculation of the La aqueous model complexes, $\text{La}(\text{H}_2\text{O})_n$ ($n = 7 - 12$), exhibits very complicated virtual orbitals, which are not easy to find a relationship to the experimental results. The results indicate the virtual complex models and ground state calculation are not adequate for the pre-edge peak interpretation.

ROCIS simulation of La L_1 -edge XANES of a number of La aqueous complex models and the relationship between the pre-edge peak at the La L_1 -edge and local structure of La

As discussed above, both of the ROCIS and FMS calculation with ORCA or FEFF semi-quantitatively reproduced the characteristic features of the experimental data of the real La complex oxides and supported the BAA parameters can be an indicator of the local configuration of the La atoms. Unfortunately, there are two weak points, the validity of the BAA parameter definition and relatively small number of the reference samples. The former problem is not so easy. For example, perfect pentagonal bipyramid geometry for a 7-coordinated moiety belongs to the point group, D_{5h} and its electronic states could be explained in a similar manner to a 4-coordinated tetrahedral group or a 6-coordinated octahedral group based on the crystal field theory. However, the main objectives of the present analysis method such as an atom in amorphous material do have irregular configuration beyond the scope of the point group theory. Then, the author takes again a theoretical approach into the problems, that is a number of virtual $\text{La}(\text{H}_2\text{O})_n$ complex models whose the La atom is geometrically shifted from the original position. Suppose the La atom of virtual La aqueous complex model is located at the origin (0,0,0) in the Cartesian axis, we virtually construct a 0.40 \AA cubic grid meshed by 0.05 \AA , which has $729 = 9 \times 9 \times 9$ intersection points including the origin. Then, the La atom was moved to each intersection points without moving the other atoms to construct a new complex model. The calculation and evaluation of the pre-edge peak at the La L_1 -edge XANES spectrum was done in the same manner to the previous models.

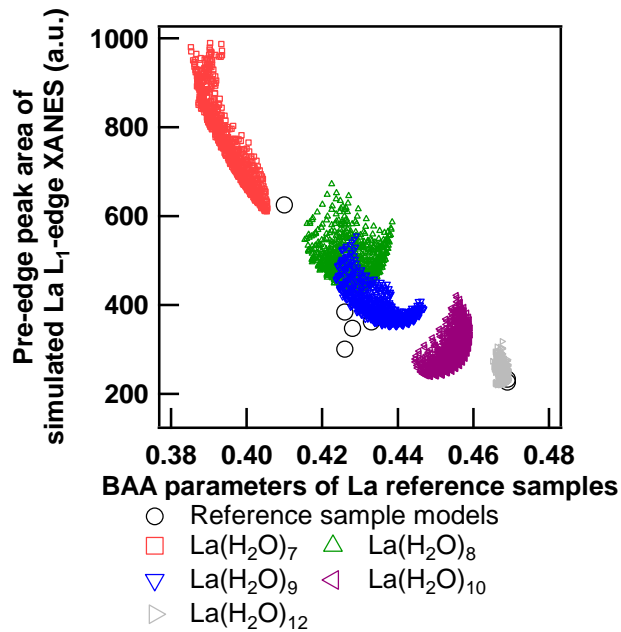


Figure 16. Dependence of the peak area at the lowest energy of simulated La L₁-edge XANES spectra on the BAA parameters of La aqueous complex models of La₄PdO₇, La₂CuO₄, LaCuSrO₄, LaFeSrO₄, LaSrAlO₄, LaCoO₃, and LaAlO₃ and virtual complex models of La(H₂O)_n (n = 7, 8, 9, 10, 12).

Figure 16 shows the simulated results of a number of virtual La(H₂O)_{7n} (n = 7, 8, 9, 10, 12) complex models and the reference models as already shown in Figure 13. Even though the parameterization criterion of BAA parameter is still unclear from the point of physical description, the result demonstrated a correlation between the pre-edge peak areas and the BAA parameters of each La complex model. It is noteworthy that the La(H₂O)₇ models exhibit the widest distribution in Figure 16. This may reflect the p contribution of La to the excited states can be easily changed by the perturbation of the adjacent atoms in the case of La(H₂O)₇. It is also good news because the lanthanide trace elements in glasses are usually coordinated to 6 to 8 adjacent atoms and Figure 16 indicates a possibility to distinguish the small structural change of lanthanide dopants based on the pre-edge peak analysis at the La L₁-edge.

This relationship also indicates a combination of XANES measurement and MD simulation or other analysis technique such as high energy X-ray diffraction could open a way for structural analysis of amorphous materials. For example, one can simulate the distribution of trace amount lanthanide atoms in a glass system with some MD code, but simulation of the XANES spectra of

lanthanide atoms in such system is generally very time-consuming because there are enormous numbers of lanthanide atoms in different local environments. The BAA parameters could be calculated easily from the simulated atomic positions with MD simulation. If the calculated BAA parameters of possible structures are significantly different from each other, it would be worth measuring their XANES spectra for semi-quantitative analysis of lanthanide local configuration.

Conclusion

La L_1 -edge and L_3 -edge XANES spectra of various La compounds are summarized and found to have a good correlation with the La local structure. These results indicate that quantitative analysis on the L_1 and L_3 -edge XANES spectra might give a piece of information of the local configuration of trace lanthanide elements in optical glasses, catalysts, magnetic materials, and so on. This methodology might also give some insight into thermal vibration of lanthanides element in lanthanide complex materials such as skutterudites, for example. Theoretical simulation of La L_1 - and L_3 -edge XANES spectra and LDOS at La site of various La compounds supported the relationship between the local structure of La and its XANES spectrum. The author proposed a new criterion to give an index of the distortion of local structure of La. It is a primitive and empirical method, and also difficult to directly linked to physical meanings at present, but practical as suggested by the theoretical calculation based on ROCIS, TD-DFT or FMS calculation. The present result also brought the following two insights. One is DFT/ROCIS, TD-DFT or FMS calculation can reproduce the dominant peaks of the La L_1 -edge XANES of various La complex oxides using simple La aqueous complex models or La oxide cluster models. It means the simulation procedures are potent to simulate the La L_1 -edge XANES spectra of La compounds with any structure at least in the XANES region. Second is the origin of the characteristic shoulder peak is found to be electric dipole transition from 2s to hybridized states with p component. It has been already discussed in previous literatures, but an interesting point is that the shoulder peak caused by the p component mixing can be an indicator of the geometric structure of La. Thus, the well-known pre-edge peak analysis of the K-edge XANES of 3d early transition metals, which is explained by the difference of the local structure of 3d metals, can be also applied to the shoulder peak at the L_1 -edge XANES spectra of La. The present results also indicate the possibility of local structure analysis on other lanthanide

elements by L-edge X-ray absorption spectroscopy. In addition, the XANES analysis might give a complementary insight into the geometrical approach to explore amorphous structure by molecular dynamics or Monte Carlo simulation in combination with experimental data such as pair distribution function based on hard X-ray or neutron diffraction.

References

- (1) Park, H.-B.; Park, C. Y.; Hong, Y.-S.; Kim, K.; Kim, S.-J., *J. Am. Ceram. Soc.*, **1999**, *82*, 94-102.
- (2) Wakefield, G.; Holland, E.; Dobson, P. J.; Hutchison, J. L., *Adv. Mater.*, **2001**, *13*, 1557-1560.
- (3) Sakai, T.; Hazama, T.; Miyamura, H.; Kuriyama, N.; Kato, A.; Ishikawa, H., *J. Less Common Metals*, **1991**, *172–174, Part 3*, 1175-1184.
- (4) Morrison, F. D.; Sinclair, D. C.; West, A. R., *J. Appl. Phys.*, **1999**, *86*, 6355-6366.
- (5) West, A. R.; Adams, T. B.; Morrison, F. D.; Sinclair, D. C., *J. Eur. Ceram Soc.*, **2004**, *24*, 1439-1448.
- (6) Morrison, F. D.; Sinclair, D. C.; West, A. R., *J. Am. Ceram. Soc.*, **2001**, *84*, 474-476.
- (7) Morrison, F.; Coats, A.; Sinclair, D.; West, A., *J. Electroceram.*, **2001**, *6*, 219-232.
- (8) Fuchi, S.; Sakano, A.; Mizutani, R.; Takeda, Y., *Glass Technology - Eur. J. Glass Sci. Technol. Part A*, **2009**, *50*, 319-322.
- (9) Fuchi, S.; Sakano, A.; Takeda, Y., *Jpn. J. Appl. Phys.*, **2008**, *47*, 7932.
- (10) Marcus, M. A.; Polman, A., *J. Non-Cryst. Solids*, **1991**, *136*, 260-265.
- (11) Peters, P. M.; Houde-Walter, S. N., *J. Non-Cryst. Solids*, **1998**, *239*, 162-169.
- (12) Sayers, D. E.; Stern, E. A.; Lytle, F. W., *Phys. Rev. Lett.*, **1971**, *27*, 1204-1207.
- (13) Mountjoy, G.; Cole, J. M.; Brennan, T.; Newport, R. J.; Saunders, G. A.; Wallidge, G. W., *J. Non-Cryst. Solids*, **2001**, *279*, 20-27.
- (14) Larson, E. M.; Ellison, A. J. G.; Lytle, F. W.; Navrotsky, A.; Gregor, R. B.; Wong, J., *J. Non-Cryst. Solids*, **1991**, *130*, 260-272.
- (15) Persson, I.; Damian Risberg, E.; D'Angelo, P.; De Panfilis, S.; Sandström, M.; Abbasi, A., *Inorg. Chem.*, **2007**, *46*, 7742-7748.
- (16) D'Angelo, P.; De Panfilis, S.; Filipponi, A.; Persson, I., *Chem. Eur. J.*, **2008**, *14*, 3045-3055.
- (17) Persson, I.; D'Angelo, P.; De Panfilis, S.; Sandström, M.; Eriksson, L., *Chem. Eur. J.*, **2008**, *14*, 3056-3066.
- (18) D'Angelo, P.; Zitolo, A.; Migliorati, V.; Mancini, G.; Persson, I.; Chillemi, G., *Inorg. Chem.*, **2009**, *48*, 10239-10248.
- (19) D'Angelo, P.; Zitolo, A.; Migliorati, V.; Persson, I., *Chem. Eur. J.*, **2010**, *16*, 684-692.
- (20) Lundberg, D.; Persson, I.; Eriksson, L.; D'Angelo, P.; De Panfilis, S., *Inorg. Chem.*, **2010**,

49, 4420-4432.

- (21) D'Angelo, P.; Zitolo, A.; Migliorati, V.; Chillemi, G.; Duvail, M.; Vitorge, P.; Abadie, S.; Spezia, R., *Inorg. Chem.*, **2011**, *50*, 4572-4579.
- (22) D'Angelo, P.; Migliorati, V.; Spezia, R.; De Panfilis, S.; Persson, I.; Zitolo, A., *Phys. Chem. Chem. Phys.*, **2013**, *15*, 8684-8691.
- (23) D'Angelo, P.; Spezia, R., *Chem. Eur. J.*, **2012**, *18*, 11162-11178.
- (24) Neese, F., *Wiley Interdiscip. Rev. Comput. Mol. Sci.*, **2012**, *2*, 73-78.
- (25) Rehr, J. J.; Kas, J. J.; Prange, M. P.; Sorini, A. P.; Takimoto, Y.; Vila, F., *C. R. Phys.*, **2009**, *10*, 548-559.
- (26) Rehr, J. J.; Kas, J. J.; Vila, F. D.; Prange, M. P.; Jorissen, K., *Physical Chemistry Chemical Physics*, **2010**, *12*, 5503-5513.
- (27) Ankudinov, A. L.; Bouldin, C. E.; Rehr, J. J.; Sims, J.; Hung, H., *Phys. Rev. B*, **2002**, *65*, 104107.
- (28) Tabuchi, M.; Asakura, H.; Takao, N.; Morimoto, H.; Watanabe, N.; Baba, Y.; Takeda, Y., *in preparation*.
- (29) Ravel, B.; Newville, M., *J. Synchrotron Rad.*, **2005**, *12*, 537-541.
- (30) Ravel, B., *J. Synchrotron Rad.*, **2001**, *8*, 314-316.
- (31) Maganas, D.; Roemelt, M.; Havecker, M.; Trunschke, A.; Knop-Gericke, A.; Schlogl, R.; Neese, F., *Phys. Chem. Chem. Phys.*, **2013**, *15*, 7260-7276.
- (32) Roemelt, M.; Maganas, D.; DeBeer, S.; Neese, F., *J. Chem. Phys.*, **2013**, *138*, -.
- (33) Maganas, D.; DeBeer, S.; Neese, F., *Inorg. Chem.*, **2014**, *53*, 6374-6385.
- (34) Maganas, D.; Roemelt, M.; Weyhermuller, T.; Blume, R.; Havecker, M.; Knop-Gericke, A.; DeBeer, S.; Schlogl, R.; Neese, F., *Phys. Chem. Chem. Phys.*, **2014**, *16*, 264-276.
- (35) Weigend, F.; Ahlrichs, R., *Phys. Chem. Chem. Phys.*, **2005**, *7*, 3297-3305.
- (36) Pantazis, D. A.; Neese, F., *J. Chem. Theory Comput.*, **2009**, *5*, 2229-2238.
- (37) van Wüllen, C., *J. Chem. Phys.*, **1998**, *109*, 392-399.
- (38) Rappe, A. K.; Casewit, C. J.; Colwell, K. S.; Goddard, W. A.; Skiff, W. M., *J. Am. Chem. Soc.*, **1992**, *114*, 10024-10035.
- (39) Hanwell, M.; Curtis, D.; Lonie, D.; Vandermeersch, T.; Zurek, E.; Hutchison, G., *J. Cheminformatics*, **2012**, *4*, 17.
- (40) Aritani, H.; Yamada, H.; Yamamoto, T.; Tanaka, T.; Imamura, S., *J. Synchrotron Rad.*, **2001**, *8*, 593-595.
- (41) Rossetti, I.; Sordelli, L.; Ghigna, P.; Pin, S.; Scavini, M.; Forni, L., *Inorg. Chem.*, **2011**, *50*, 3757-3765.
- (42) Materlik, G.; Sonntag, B.; Tausch, M., *Phys. Rev. Lett.*, **1983**, *51*, 1300-1303.
- (43) Chaboy, J.; García, J.; Marcelli, A., *J Magn. Magn. Mater.*, **1997**, *166*, 149-164.
- (44) Ishimatsu, N.; Sasada, R.; Maruyama, H.; Ichikawa, T.; Miyaoka, H.; Kimura, T.; Tsubota, M.; Kojima, Y.; Tsumuraya, T.; Oguchi, T.; Kawamura, N.; Machida, A., *J. Phys: Conf. Ser.*, **2009**,

190, 012070.

- (45) Roe, A. L.; Schneider, D. J.; Mayer, R. J.; Pyrz, J. W.; Widom, J.; Que, L., *J. Am. Chem. Soc.*, **1984**, *106*, 1676-1681.
- (46) Westre, T. E.; Kennepohl, P.; DeWitt, J. G.; Hedman, B.; Hodgson, K. O.; Solomon, E. I., *J. Am. Chem. Soc.*, **1997**, *119*, 6297-6314.
- (47) Yamazoe, S.; Hitomi, Y.; Shishido, T.; Tanaka, T., *J. Phys. Chem. C*, **2008**, *112*, 6869-6879.
- (48) Kelchner, C. L.; Plimpton, S. J.; Hamilton, J. C., *Phys. Rev. B*, **1998**, *58*, 11085-11088.
- (49) Ackland, G. J.; Jones, A. P., *Phys. Rev. B*, **2006**, *73*, 054104.
- (50) DeBeer George, S.; Brant, P.; Solomon, E. I., *J. Am. Chem. Soc.*, **2004**, *127*, 667-674.

Chapter 3

Local Structure and L_1 and L_3 -edge XANES spectra of Early Lanthanide Elements in Their Complex Oxides

Abstract

Pr, Nd, Sm, Eu, and Gd L_1 -edge and L_3 -edge X-ray absorption near edge structure (XANES) spectra of their complex oxides were measured to investigate the relationship between the characteristic feature of the spectra and the local structure around the Pr, Nd, Sm, Eu, and Gd atoms. The pre-edge peak area of the L_1 -edge and the full width at half-maximum (fwhm) of the white line of the L_3 -edge XANES spectra are extracted by curve fitting analyses with one Gaussian and one cubic function as a background or with one pseudo-Voigt and one arctangent function, respectively. The author found a significant correlation among the pre-edge peak area of the L_1 -edge or the full width at half maximum of white line of the L_3 -edge XANES spectra and abstract physical indexes, bond angle analysis (BAA) parameter, defined by the positions of the adjacent atoms around the lanthanide elements, which act as an indicator of disorder of local configuration of the lanthanide element. This finding will open a way to estimate the local structure of early lanthanide elements by means of L-edge XANES spectroscopy.

Introduction

In the previous chapter, the author demonstrated the La L₁ and L₃-edge XANES spectra can be used as an indicator of the local configuration of La from both of experimental and theoretical approaches. From the experimental data, the pre-edge peak area of La L₁-edge XANES spectra and the fwhm of white line of La L₃-edge XANES spectra are proved to have a clear correlation with the local environment of La. The author also proposed a primitive but practical structural indexing criterion to represent the complexity or disorder of the local environment of the La site and validate the indexing criterion by means of theoretical simulation of the La L₁-edge XANES spectra on thousands of virtual La aqueous complex models. These findings led the author to explore the L₁ and L₃-edge XANES spectra of early lanthanide elements to extend the simple and practical method to the other lanthanide elements for a quantitative analysis of the local structure.

XANES spectroscopy enables us to estimate not only the oxidation state but also centrosymmetry of the target atom; however, the fundamental XANES study on lanthanide elements from the point of view of geometry is relatively scarce. On the other hand, there are many examples of the lanthanide XANES analysis to estimate the valence states of lanthanide elements.¹ For example, a large energy shift of the absorption edge of the Eu L₃-edge is utilized to elucidate the chemical state of Eu in phosphor material² or to follow the change of the oxidation state of Eu in EuO under high pressure.³ Saines *et al.* used Pr L₃-edge XANES spectra to determine the oxidation state of the Pr atom in Ba₂PrSn_xSb_{1-x}O_{6-δ}.⁴ Yoshida *et al.* measured the valence state of Ce supported on silica by means of Ce L₃-edge XANES spectra.⁵ Hu *et al.* found peculiar and interesting absorption edge shifts of Pr, Nd, Sm, and Dy L-edge spectra of their halides compounds and mixed-valent compounds.⁶

Even though the studies of the local structure and XANES spectra of lanthanide compounds are not abundant, there are several papers on the local configuration of lanthanide complexes. Ellis *et al.* investigated lanthanide (Ln^{III}) coordination environments using Ln L₃-edge XANES and EXAFS spectra of the Ln^{III} complex and found that the fwhm's of the Ln L₃-edge XANES spectra are sensitive to the XANES spectra to elucidate the hydration environment of lanthanide triflates⁷ through a XANES fitting procedure with MXAN,⁸⁻¹⁰ not an EXAFS. D'Angelo *et al.* have reported a

series of K and L₃-edge XANES and/or EXAFS analysis of various lanthanide aqueous complexes.¹¹⁻¹⁹ In particular, they also incorporated molecular dynamics and XANES fitting procedure to interpret the Ln L₃-edge XANES spectra and proposed plausible solvation model. However, these papers mainly focused on the difference of a series of lanthanide elements and there are few papers focused on the XANES spectra of a specific lanthanide element.

In the meanwhile, extended X-ray absorption fine structure (EXAFS) spectroscopy, the other part of X-ray absorption spectroscopy (XAS), is more widely used technique to analyze the local structure around an X-ray absorbing atom based on the quantitative analysis procedure of EXAFS oscillation proposed by Sayers, Stern and Lytle.²⁰ EXAFS spectroscopy has been applied not only to 3d, 4d, 5d transition metal elements, but also to lanthanide elements in various materials such as semiconductors,^{21, 22} optical devices,^{23, 24} and so forth. On the EXAFS study of the lanthanide elements, the Ln L₃-edge is usually employed because even La K-edge, which is the lowest absorption edge among Ln K-edges, needs sufficient X-ray flux above 38 keV, only available at the world largest synchrotron radiation facilities such as SPring-8, Advanced Photon Source (APS) or European Synchrotron Radiation Facility (ESRF). And also, the L₁ or L₂-edge EXAFS can suffer from the interference of the EXAFS oscillation generated at the L₃-edge. Despite the Ln L₃-edge XANES spectra are frequently measured simultaneously for the EXAFS experiments, the detailed interpretation of the Ln L₃-edge XANES are sometimes ignored or limited because of its non-descript structure. However, one of the difficulties of the application of EXAFS spectra occurs during analysis step by curve fitting procedure based on the EXAFS equation requiring the initial structural model, which is not easy to construct on amorphous materials.

As discussed in the previous chapter, quantitative analysis on the La L₁ and L₃-edge XANES spectra could provide some information on the local structure of La in La complex oxides. Thus, the analytical technique could be also applied into early lanthanide elements. In this study, the author prepared various lanthanide complex oxides containing Pr, Nd, Sm, Eu, or Gd, measured their L-edge XANES spectra, and summarized a relationship between the feature quantities of the spectra and the local environment of lanthanide species in a similar manner to the previous chapter. In addition, the local structure of Sm of Sm-doped glasses is discussed based on the proposing structural–spectral relationship.

Experimental Section

Preparation of Lanthanide Complex Oxides

Samarium complex oxides, AlSrSmO_4 , NiSrSmO_4 , Sm_2CuO_4 , Sm_3GaO_6 , CoSmO_3 , SrCoSmO_4 , $\text{SrAl}_2\text{Sm}_2\text{O}_7$, and Sm_4CuO_7 , were prepared by solid state reaction. AlSrSmO_4 : Sm_2O_3 (174.7 mg, 0.5 mmol), $\text{Al}(\text{NO}_3)_3 \cdot 9\text{H}_2\text{O}$ (378.1 mg, 1.0 mmol), and SrCO_3 (148.4 mg, 1.0 mmol); NiSrSmO_4 : Sm_2O_3 (176.1 mg, 1.0 mmol), $\text{Ni}(\text{NO}_3)_2 \cdot 6\text{H}_2\text{O}$ (292.3 mg, 1.0 mmol), and SrCO_3 (148.4 mg, 1.0 mmol); Sm_2CuO_4 : Sm_2O_3 (87.3 mg, 0.25 mmol), and $\text{Cu}(\text{OAc})_2$ (45.0 mg, 0.25 mmol); Sm_3GaO_6 : Sm_2O_3 (87.5 mg, 0.25 mmol), and Ga_2O_3 (15.6 mg, 0.083 mmol); CoSmO_3 : Sm_2O_3 (148.2 mg, 0.25 mmol) and $\text{Co}(\text{NO}_3)_3 \cdot 6\text{H}_2\text{O}$ (148.2 mg, 0.51 mmol); SrCoSmO_4 : Sm_2O_3 (174.5 mg, 0.5 mmol), $\text{Co}(\text{NO}_3)_3 \cdot 6\text{H}_2\text{O}$ (290.5 mg, 1.0 mmol), and SrCO_3 (147.1 mg, 1.0 mmol); $\text{SrAl}_2\text{Sm}_2\text{O}_7$: Sm_2O_3 (349.8 mg, 1.0 mmol), $\text{Al}(\text{NO}_3)_3 \cdot 9\text{H}_2\text{O}$ (753.3 mg, 2.0 mmol), and SrCO_3 (148.3 mg, 1.0 mmol); Sm_4CuO_7 : Sm_2O_3 (695.0 mg, 2.0 mmol) and $\text{Cu}(\text{OAc})_2$ (183.4 mg, 1.0 mmol). These mixtures are put into alumina crucibles and heated at 1423 K for 24 h.

Neodymium complex oxides, Nd_4PdO_7 , Nd_2CuO_4 , SrAlNdO_4 , SrCoNdO_4 , CoNdO_3 , and MnNdO_3 , were prepared by solid state reaction. Nd_4PdO_7 : Nd_2O_3 (331.8 mg, 1.0 mmol) and $\text{Pd}(\text{OAc})_2$ (111.8 mg, 0.5 mmol); Nd_2CuO_4 : Nd_2O_3 (336.2 mg, 1.0 mmol) and $\text{Cu}(\text{OAc})_2$ (184.2 mg, 1.0 mmol); SrAlNdO_4 : Nd_2O_3 (168.2 mg, 0.5 mmol), $\text{Al}(\text{NO}_3)_3 \cdot 9\text{H}_2\text{O}$ (381.4 mg, 1.0 mmol), and SrCO_3 (149.8 mg, 1.0 mmol); SrCoNdO_4 : Sm_2O_3 (165.4 mg, 0.5 mmol), $\text{Co}(\text{NO}_3)_3 \cdot 6\text{H}_2\text{O}$ (298.9 mg, 1.0 mmol), and SrCO_3 (153.2 mg, 1.0 mmol); CoNdO_3 : Nd_2O_3 (338.5 mg, 1.0 mmol) and $\text{Co}(\text{NO}_3)_3 \cdot 6\text{H}_2\text{O}$ (501.1 mg, 2.0 mmol); MnNdO_3 : Nd_2O_3 (168.8 mg, 0.5 mmol) and MnO (71.8 mg, 1.0 mmol). These mixtures are put into alumina crucibles and heated at 1423 K for 24 h.

Praseodymium complex oxides, NbPrO_4 , VPrO_4 , AlSrPrO_4 , NiSrPrO_4 , CoPrO_3 , CuPr_2O_4 , and SrPrCoO_4 were prepared in a solid state reaction of vigorous grinding of precursors followed by high-temperature calcination. NbPrO_4 : Pr_6O_{11} (345.0 mg, 0.338 mmol) and Nb_2O_5 (265.1 mg, 1.0 mmol); VPrO_4 : Pr_6O_{11} (255.3 mg, 0.250 mmol) and V_2O_3 (114.9 mg, 0.77 mmol); AlSrPrO_4 : Pr_6O_{11} (172.7 mg, 0.169 mmol), $\text{Al}(\text{NO}_3)_3 \cdot 9\text{H}_2\text{O}$ (382.0 mg, 1.0 mmol), and SrCO_3 (150.2 mg, 1.0 mmol); NiSrPrO_4 : Pr_6O_{11} (170.5 mg, 0.166 mmol), $\text{Ni}(\text{NO}_3)_2 \cdot 6\text{H}_2\text{O}$ (293.8 mg, 1.0 mmol), and SrCO_3 (150.0 mg, 1.0 mmol); CoPrO_3 : Pr_6O_{11} (255.2 mg, 0.250 mmol) and $\text{Co}(\text{NO}_3)_3 \cdot 6\text{H}_2\text{O}$ (454.0 mg, 1.56

mmol); CuPr_2O_4 : Pr_6O_{11} (341.4 mg, 0.334 mmol) and $\text{Cu}(\text{OAc})_2$ (181.5 mg, 1.0 mmol); SrPrCoO_4 : Pr_6O_{11} (169.5 mg, 0.166 mmol), $\text{Co}(\text{NO}_3)_3 \cdot 6\text{H}_2\text{O}$ (292.0 mg, 1.0 mmol), and SrCO_3 (150.2 mg, 1.0 mmol). These mixtures were put into alumina crucibles and heated at 1273 K for 24 h (VPrO_4 , CoPrO_3 , and CuPr_2O_4) or at 1373 K for 24 h (NbPrO_4 , AlSrPrO_4 , NiSrPrO_4 , and SrPrCoO_4).

Europium complex oxides: Eu_3GaO_6 , Eu_2CuO_4 , EuNbO_4 , $\text{SrAl}_2\text{Eu}_2\text{O}_7$, SrNiEuO_4 , SrCoEuO_4 , and CoEuO_3 were prepared by solid state reaction. Eu_3GaO_6 : Eu_2O_3 (520.2 mg, 1.5 mmol), and Ga_2O_3 (92.8 mg, 0.50 mmol); Eu_2CuO_4 : Eu_2O_3 (351.2 mg, 1.0 mmol), and $\text{Cu}(\text{OAc})_2$ (182.0 mg, 1.0 mmol); EuNbO_4 : Eu_2O_3 (352.2 mg, 1.0 mmol), and Nb_2O_5 (265.9 mg, 1.0 mmol); $\text{SrAl}_2\text{Eu}_2\text{O}_7$: Eu_2O_3 (350.3 mg, 1.0 mmol), $\text{Al}(\text{NO}_3)_3 \cdot 9\text{H}_2\text{O}$ (759.1 mg, 2.0 mmol), and SrCO_3 (147.4 mg, 1.0 mmol); SrNiEuO_4 : Eu_2O_3 (350.3 mg, 1.0 mmol), $\text{Ni}(\text{NO}_3)_2 \cdot 6\text{H}_2\text{O}$ (290.3 mg, 1.0 mmol), and SrCO_3 (147.0 mg, 1.0 mmol); SrCoEuO_4 : Eu_2O_3 (176.5 mg, 0.5 mmol), SrCO_3 (147.8 mg, 1.0 mmol), and $\text{Co}(\text{NO}_3)_3 \cdot 6\text{H}_2\text{O}$ (293.2 mg, 1.0 mmol); CoEuO_3 : Eu_2O_3 (352.0 mg, 1.0 mmol), and $\text{Co}(\text{NO}_3)_3 \cdot 6\text{H}_2\text{O}$ (581.2 mg, 2.0 mmol); These mixtures were pelletized and put into alumina crucible and heated at 1373 K for 24h.

Gadolinium complex oxides: Gd_4CuO_7 , Gd_2CuO_4 , GdNbO_4 , $\text{SrAl}_2\text{Gd}_2\text{O}_7$, SrCoGdO_4 , and CoGdO_3 were also prepared by solid state reaction. Gd_4CuO_7 : Gd_2O_3 (538.5 mg, 1.5 mmol), and $\text{Cu}(\text{OAc})_2$ (134.9 mg, 0.75 mmol); Gd_2CuO_4 : Gd_2O_3 (362.9 mg, 1.0 mmol), and $\text{Cu}(\text{OAc})_2$ (180.7 mg, 1.0 mmol); GdNbO_4 : Gd_2O_3 (362.2 mg, 1.0 mmol), and Nb_2O_5 (265.5 mg, 1.0 mmol); $\text{SrAl}_2\text{Gd}_2\text{O}_7$: Gd_2O_3 (362.5 mg, 1.0 mmol), $\text{Al}(\text{NO}_3)_3 \cdot 9\text{H}_2\text{O}$ (757.0 mg, 2.0 mmol), and SrCO_3 (147.7 mg, 1.0 mmol); SrCoGdO_4 : Gd_2O_3 (363.1 mg, 1.0 mmol), SrCO_3 (296.4 mg, 2.0 mmol), and $\text{Co}(\text{NO}_3)_3 \cdot 6\text{H}_2\text{O}$ (590.6 mg, 2.0 mmol); CoGdO_3 : Gd_2O_3 (363.2 mg, 1.0 mmol), and $\text{Co}(\text{NO}_3)_3 \cdot 6\text{H}_2\text{O}$ (582.3 mg, 2.0 mmol); These mixtures were pelletized and put into alumina crucibles and heated at 1373 K for 12 h. The XRD patterns of the calcined samples were compared to that reported in previous literature.

X-ray Absorption Spectroscopy

Pr, Nd, Sm, Eu and Gd L_1 - and L_3 -edge XANES spectra of reference samples and Sm-doped Bi_2O_3 - B_2O_3 glass samples were measured at the BL5S1, hard X-ray XAFS beamline, and at Aichi Synchrotron Center (Aichi Science and Technology Foundation (AichiSR), Aichi, Japan). The

XANES spectra of their powder samples were recorded in transmission mode at ambient condition, using a Si(111) double-crystal monochromator. The photon energy was calibrated with the pre-edge peak of the Ti K-edge XANES spectrum of Ti foil as 4660 eV. Powder samples were mixed with an appropriate amount of boron nitride and pressed into pellets. Incident and transmitted X-ray fluxes were measured with ion chambers filled with He(70%)/N₂(30%) and N₂(15%)/Ar(85%), respectively. A higher harmonic X-ray was cut off with proper glancing angle of Rh-coated collimating and focusing mirrors. Data reduction was carried out with the Athena²⁵ ver. 0.9.18 included in the Demeter package and Igor Pro ver. 6.34 (WaveMetrics, Lake Oswego, OR, USA).

Results and Discussion

Sm L₁ and L₃-edge XANES Spectra of Sm Complex Oxides

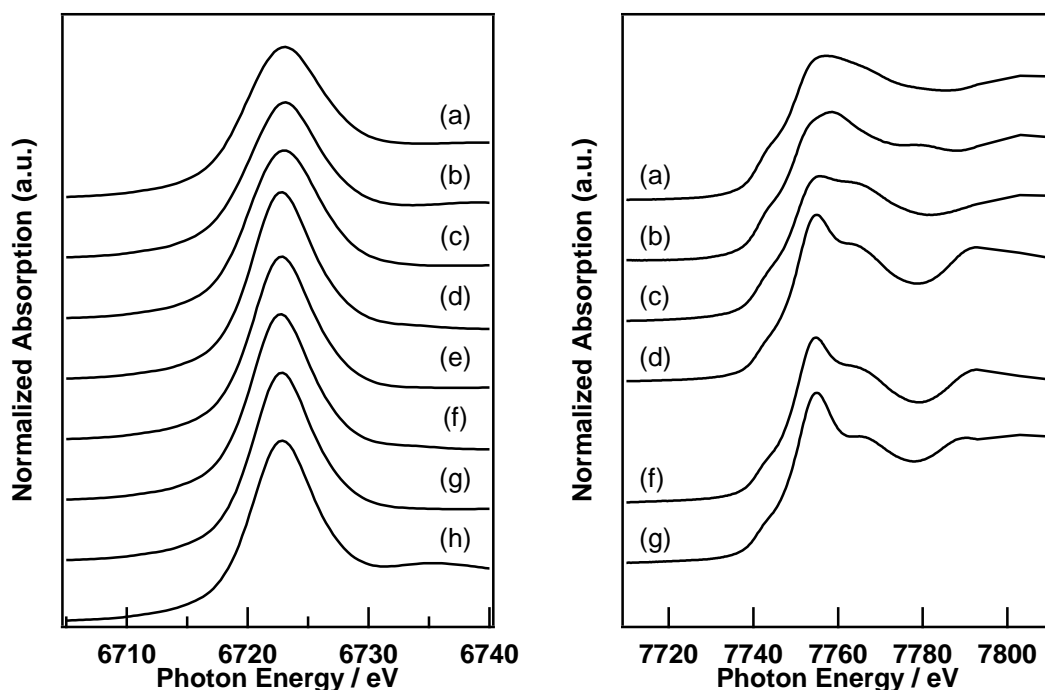


Figure 1. Sm L₃-edge (left) and L₁-edge (right) XANES spectra of Sm complex oxides: (a) Sm₄CuO₇, (b) Sm₂CuO₄, (c) Sm₃GaO₆, (d) AlSrSmO₄, (e) SrCoSmO₄, (f) SrAl₂Sm₂O₇, (g) NiSrSmO₄, and (h) CoSmO₃.

Figure 1 exhibits Sm L₃ and L₁-edge XANES spectra of Sm complex oxides, Sm₄CuO₇, Sm₂CuO₄, Sm₃GaO₆, AlSrSmO₄, SrCoSmO₄, SrAl₂Sm₂O₇, NiSrSmO₄, and CoSmO₃. All of the Sm

L_3 -edge XANES spectra have one almost symmetric peak called white line at around 6723 eV assigned to an electronic dipole transition from $2p_{3/2}$ states to 5d states. The white line of each spectrum looks almost the same; however, that of Sm_4CuO_7 is slightly wider than others, and CoSmO_3 looks to have a bit narrower white line. These featureless shape of the L_3 -edge XANES spectra is far from the L_3 -edge XANES spectra of complex metal oxides of 4d and 5d metals such as Nb, Mo, Ta, W, and Re with regular octahedral moiety (*e.g.* MO_6) exhibit two well-resolved peaks at the white line and with tetrahedral moiety (*e.g.*, MO_4) show ill-resolved peaks with apparent shoulder peaks at the white line. Thus, second derivatives of the L_3 -edge XANES spectra of Nb, Mo, Ta, W, Re clearly show separate electric dipole transition to d states split by crystal field effects as shown in Chapter 1, but the Sm L_3 -edge white lines of Sm atoms coordinated to 7 to 12 adjacent oxygen atoms exhibit only one ill-resolved asymmetric peaks, even though the lifetime broadening of the Sm L_3 -edge, 3.86 eV, is a bit smaller than that of Ta (4.88 eV), W (4.98 eV), or Re (5.04 eV). The reason why the spectral resolution of the Sm L_3 -edge XANES spectra is not better than that of Ta, W, or Re is their L_3 -edge XANES spectra were measured using the Si(111) double-crystal monochromator which is five or ten times worse energy resolution than Si(311). A conventional beamline capable of measuring extremely energy-resolved XANES spectra in the relatively low energy X-ray region (*e.g.* Sm L_3 -edge, 6.7 keV) is not available (*e.g.*, > 8.6 keV with Si(311) at BL01B1, SPring-8, Japan; > 8 keV with Si(311) at NW10A, PF-AR, KEK, Japan). A highly elaborate XAFS technique such as high-energy resolution fluorescence detection X-ray absorption spectroscopy²⁶ might give a better insight discussed below. In analogy with the previous study, the width of the white line of the Sm L_3 -edge XANES spectra should also reflect the d band broadening, which is subject to the local structure of lanthanide elements. Thus, in this study, the fwhm of the white line was estimated by curve fitting analysis on each spectrum with one arctangent function and one pseudo-Voigt function in order to evaluate the d band broadening.

Figure 1 also shows Sm L_1 -edge XANES spectra of the same Sm complex oxides, Sm_4CuO_7 , Sm_2CuO_4 , Sm_3GaO_6 , AlSrSmO_4 , $\text{SrAl}_2\text{Sm}_2\text{O}_7$, and NiSrSmO_4 . The Sm L_1 -edge XANES spectra of SrCoSmO_4 and CoSmO_3 (which are tagged as (e) and (h) in Figure 1) are omitted from the right graph of Figure 1 because of the presence of the Co K-edge. In each spectrum, there is a weak, but distinct pre-edge structure at around 7745 eV, which could be assigned to the dipole electric

transition from 2s to a new electronic state generated by hybridization of the p-d states. The degree of hybridization should also reflect the local disorder of the first coordination sphere of Sm.

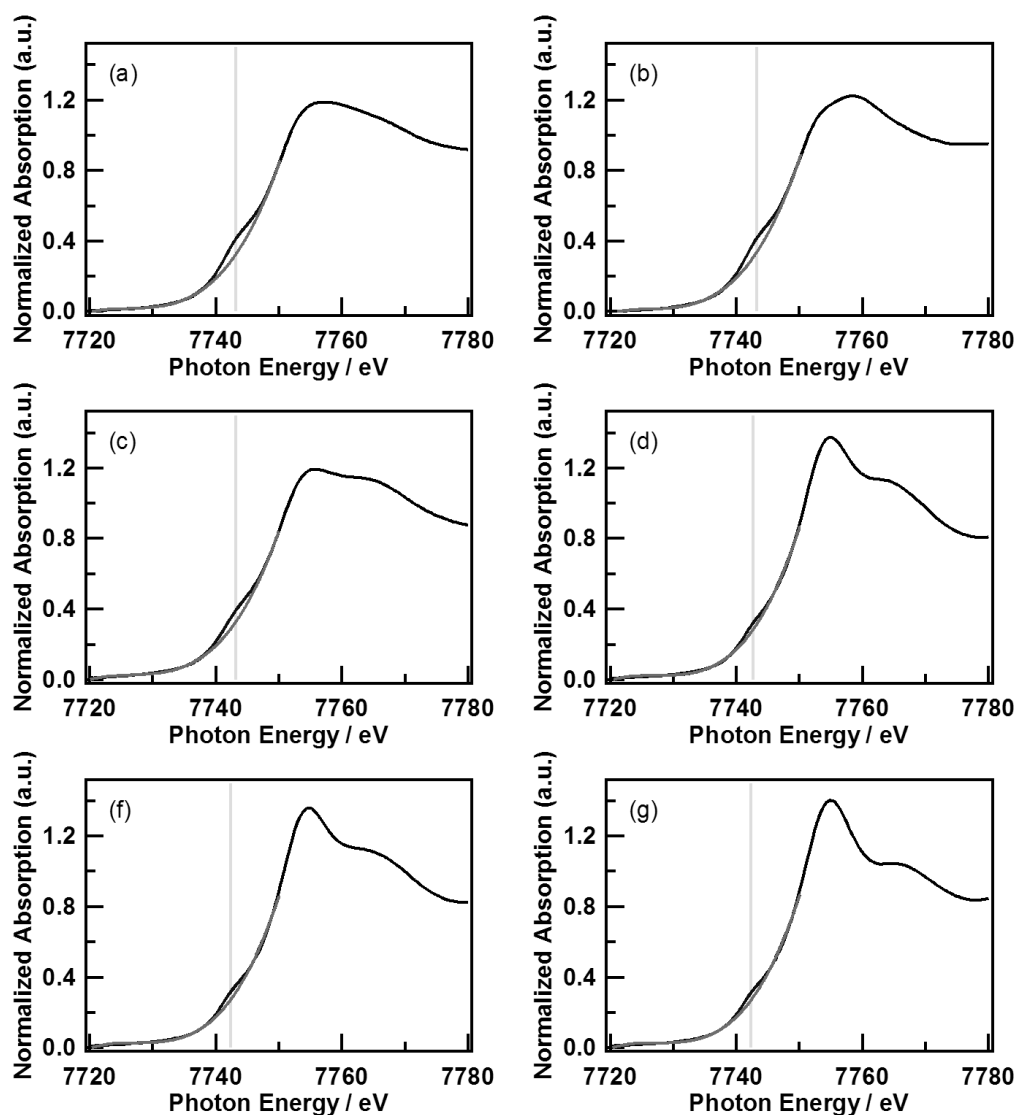


Figure 2. Curve fitting result of the Sm L_1 -edge XANES spectrum of Sm complex oxides: (a) Sm_4CuO_7 , (b) Sm_2CuO_4 , (c) Sm_3GaO_6 , (d) AlSrSmO_4 , (f) $\text{SrAl}_2\text{Sm}_2\text{O}_7$, and (g) NiSrSmO_4 with one Gaussian and one cubic spline function as a background.

Figure 2 shows curve fitting results of the pre-edge region of Sm L_1 -edge XANES spectrum of Sm complex oxides, Sm_4CuO_7 , Sm_2CuO_4 , Sm_3GaO_6 , AlSrSmO_4 , $\text{SrAl}_2\text{Sm}_2\text{O}_7$, and NiSrSmO_4 with one Gaussian and one cubic spline function as a background to extract the pre-edge peak area as an indicator of the local structure of the Sm. All of the Sm L_1 -edge XANES spectra are fitted well with these two functions. To link the estimated pre-edge peak area to a specific local environment of Sm,

the criterion for an index of the local environment, bond angle analysis (BAA) parameter, is employed to the Sm complex oxides. The simple BAA parameter is defined in the following equation,

$$\text{BAA} = \frac{1}{n} \sum |\cos(\theta_{ijk})|$$

where n and θ_{ijk} denote the number of independent angles and the angle formed by the central atom, j , and two of its neighbors, i and k . If there are unidentical sites for Sm, the BAA parameter is calculated as an average value of each BAA parameter on each site.

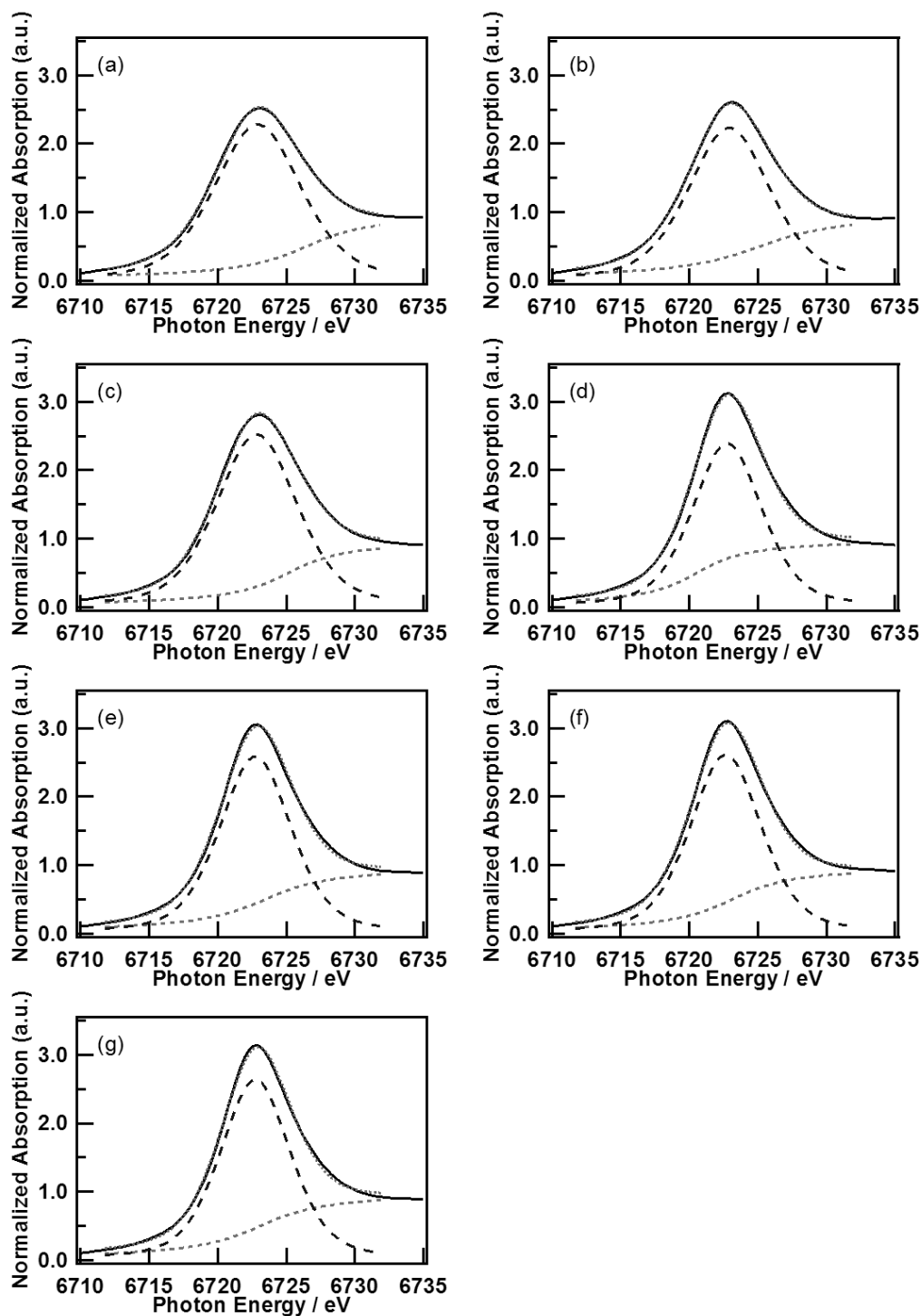


Figure 3. Peak fitting results of the white line of Sm L_3 -edge XANES spectra of Sm complex oxides: (a) Sm_4CuO_7 , (b) Sm_2CuO_4 , (c) Sm_3GaO_6 , (d) AlSrSmO_4 , (e) SrCoSmO_4 , (f) $\text{SrAl}_2\text{Sm}_2\text{O}_7$, and (g) NiSrSmO_4 .

Figure 3 shows the peak fitting results of La L_3 -edge XANES spectra. As clearly seen, fitting procedure successfully reproduced the main shape of the white lines. Sm_4CuO_7 shows the largest

fwhm of the white line, 7.29, and Sm_2CuO_4 , Sm_3GaO_6 , AlSrSmO_4 , SrCoSmO_4 , $\text{SrAl}_2\text{Sm}_2\text{O}_7$, and NiSrSmO_4 exhibit 6.86, 6.95, 6.06, 6.02, 5.97, and 5.93, respectively.

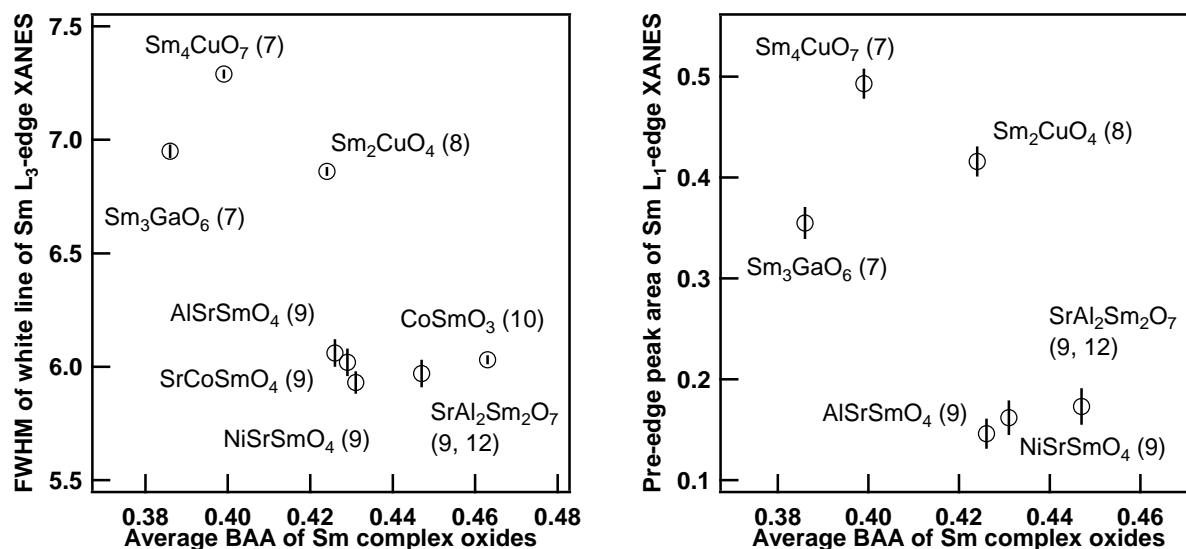


Figure 4. Correlation between averaged bond angle analysis (BAA) parameters and the fwhm of the white line of Sm L_3 -edge XANES spectra (left, $R^2 = 0.62$) or the pre-edge peak area of Sm L_1 -edge XANES spectra (right, $R^2 = 0.47$) of Sm complex oxides (the number in parentheses denotes the number of the coordinated oxygen atoms to Sm)

The fwhm of the white line of the Sm L_3 -edge XANES spectra and the pre-edge peak area of Sm L_1 -edge XANES spectra are plotted against simplified BAA parameters as shown in Figure 4. One can find a significant correlation with the average BAA parameters and also with the coordination number. This suggests two things. One is, if it was possible to obtain the Sm L_1 - or L_3 -edge XANES spectrum of a material containing Sm atoms with structurally unidentified Sm species, it might be possible to discuss the local structure of Sm in that material. The other is, if one has some idea on the structure of the material or can simulate structure with molecular dynamics or Monte Carlo simulation, for example, one might be able to judge the feasibility of distinguishing the local structure of Sm by Sm L_1 - and/or L_3 -edge XANES spectra or not, from the BAA parameters which could be calculated much easier than the XANES spectrum on each site.

The fwhm of white line of Sm L_3 -edge or the pre-edge peak of Sm L_1 -edge XANES spectra of the Sm complexes with smaller coordination numbers such as Sm_2CuO_4 , and Sm_4CuO_7 look a bit larger than the expected values from other samples. It must be because the characteristic features of

XANES spectra are subject not only to the coordination number but also to the subtle geometric or electronic structure difference of the Sm. In addition, even though the curve fitting analysis on the L₁-edge XANES spectra is basically done well as shown in Figure 2, it also suffers from the EXAFS oscillation at the L₂-edge. For example, the difference of the absorbance of the pre-edge region of Sm L₁-edge XANES spectra is larger than 0.1, and the EXAFS oscillation mainly at the L₂-edge in the pre-edge region at the L₁-edge is smaller than 0.01. This means there is some inevitable uncertainty of the pre-edge peak area maybe by ca. 10%. In addition, the standard materials prepared to discuss the local structure of lanthanides have their own crystal structure, which can have an influence on their L-edge spectra. But, in general, it is impossible to prepare structurally defined uniform amorphous reference samples with an exact number of coordinated atoms. It might be also possible to make some correction on the influence of the EXAFS oscillation at the L₂-edge, but it is difficult to perform reliable correction from the practical point of view. On the other hand, as discussed below, one can observe a clear systematic difference of the Sm L₃-edge XANES spectra of Sm-doped glasses, which does not suffer from EXAFS oscillation because of their amorphous nature. Therefore, the correlation observed in Figure 4 is plausible despite the uncertainty of the estimation of the pre-edge peak area of L₁-edge XANES. It should be also pointed out that the correlation cannot be extrapolated to six or less coordinated Sm species, which is not discussed in the present study.

In addition, the relationship between the pre-edge peak areas of Sm L₁-edge XANES spectra and the fwhm's of the white line of Sm L₃-edge XANES spectra is presented in Figure 5. As clearly seen, the two groups of parameters are linearly correlated. This correlation indicates an additional two points. One is that both the pre-edge structure of Sm L₁-edge XANES and the broadening of the main peak of Sm L₃-edge XANES spectra are mainly determined by the same parameters, which could be hybridization of the p orbital and d orbital induced by the p orbital of the adjacent atoms. The other is that, even if it was difficult to obtain both of the L₁- and L₃-edge XANES spectra because of the presence of the absorption edge of other elements, it is possible to estimate the local structure of the target atom only by the L₁-edge or L₃-edge XANES spectra.

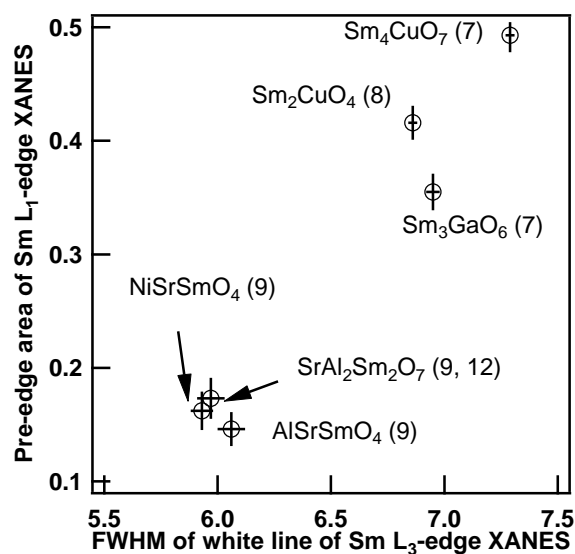


Figure 5. Correlation between the pre-edge peak area of Sm L₁-edge XANES spectra and the fwhm of the white line of Sm L₁-edge XANES spectra of Sm complex oxides (the number in parentheses denotes the number of the coordinated oxygen atoms to Sm) ($R^2 = 0.93$).

Nd L₃ and L₁-edge XANES Spectra of Nd Complex Oxides

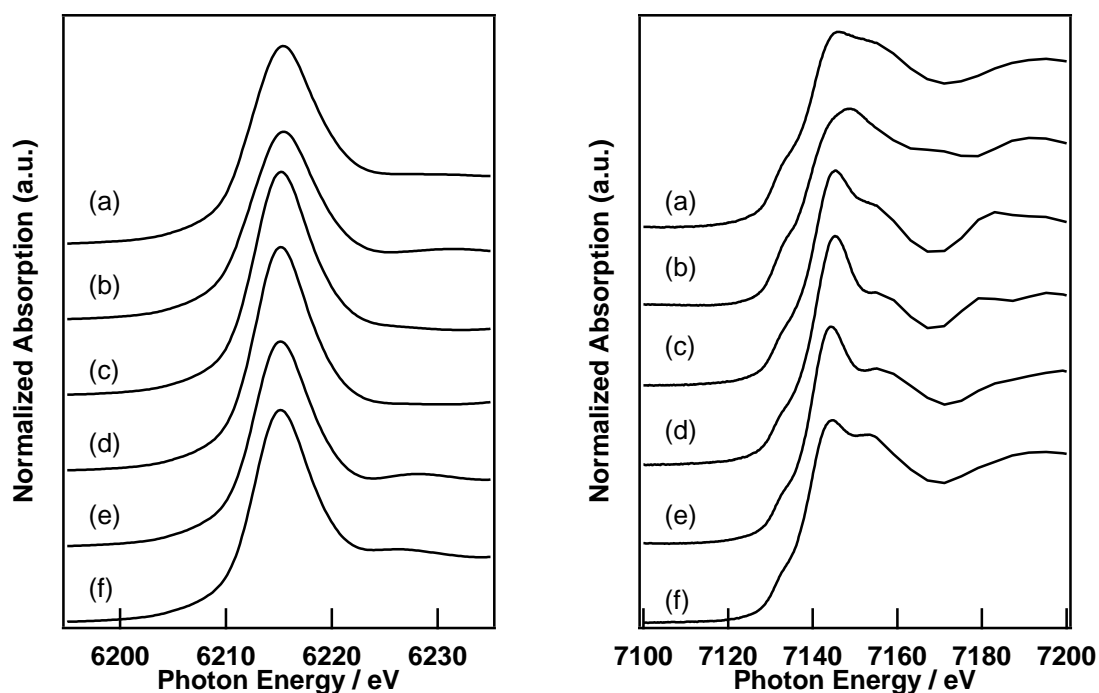


Figure 6. Nd L₃-edge (left) and L₁-edge (right) XANES spectra of Nd complex oxides: (a) Nd₄PdO₇, (b) Nd₂CuO₄, (c) SrAlNdO₄, (d) SrCoNdO₄, (e) CoNdO₃, and (f) MnNdO₃.

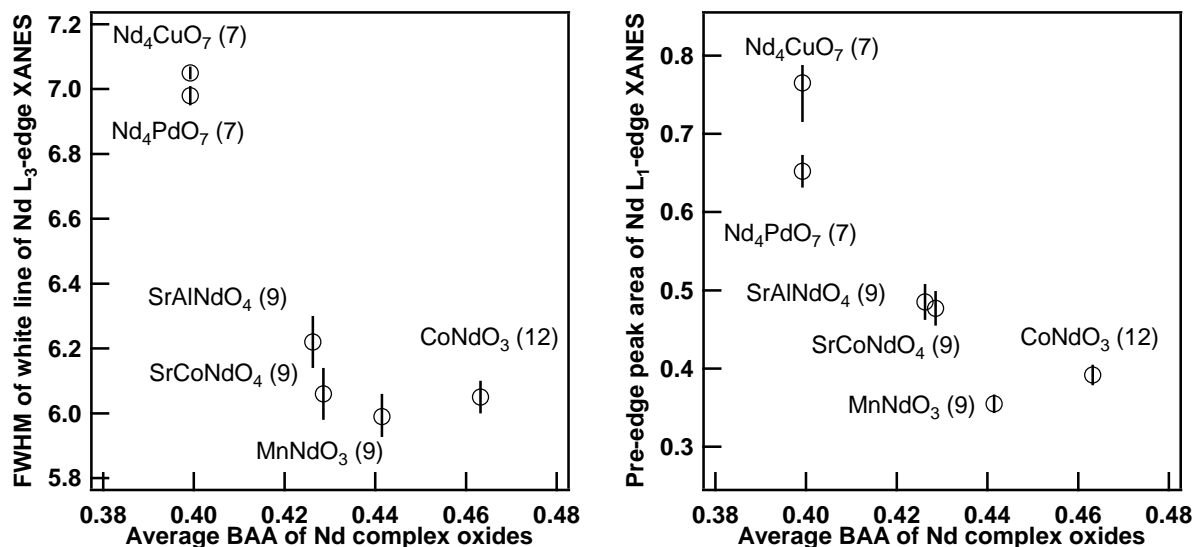


Figure 7. Correlation between averaged bond angle analysis (BAA) parameters and the fwhm of the white line of the Nd L₃-edge XANES spectra (left, $R^2 = 0.79$) and the pre-edge peak area of Nd L₁-edge XANES spectra (right, $R^2 = 0.78$) of Nd complex oxides (the number in parentheses denotes the number of the coordinated oxygen atoms to Nd)

Figure 6 shows the Nd L₃- and L₁-edge XANES spectra of Nd complex oxides, Nd₄PdO₇, Nd₂CuO₄, SrAlNdO₄, SrCoNdO₄, CoNdO₃, and MnNdO₃. The Nd L₃-edge XANES spectra exhibit one slightly asymmetric and strong white lines at around 6215 eV. The white lines of the Nd L₃-edge XANES spectrum of Nd₄PdO₇ and Nd₂CuO₄ are a bit wider than others, and CoNdO₃ having 12-coordinated Nd species exhibits a narrower white line. The Nd L₁-edge XANES spectra also exhibit a similar spectrum to each other and have small but distinct pre-edge peaks at around 7135 eV. This feature could be interpreted into an indicator of the local configuration of Nd as same way as Sm. For every Nd complex oxide, we also applied quantitative analysis on both of the L₁- and L₃-edge XANES spectra with averaged BAA parameters summarized in the same manner to Sm as shown in Figure 7. A series of Nd complex oxides have a similar correlation with the local structure and the XANES spectra to Sm complex oxides as shown in Figure 4. As expected from the results above, the pre-edge peak areas of Nd L₁-edge XANES spectra and the fwhm's of the white line of Nd L₃-edge XANES spectra are also correlated with each other as shown in Figure 8.

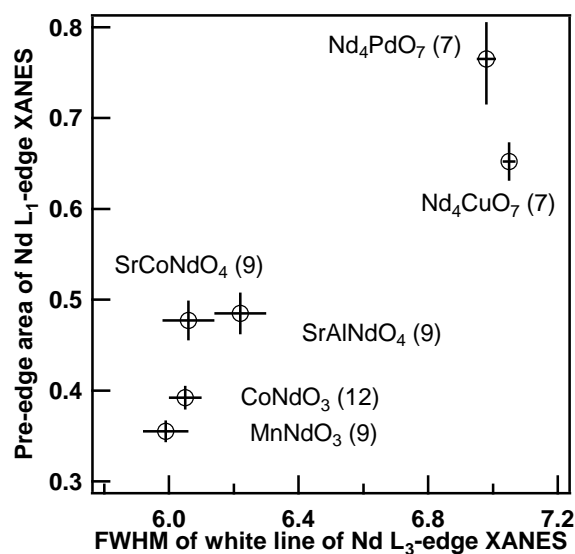


Figure 8. Correlation between the pre-edge peak area of Nd L₁-edge XANES spectra and the fwhm of the white line of Nd L₃-edge XANES spectra of Nd complex oxides. (The number in parentheses denotes the number of the coordinated oxygen atoms to Nd) ($R^2 = 0.89$)

Pr L₃ and L₁-edge XANES Spectra of Pr Complex Oxides.

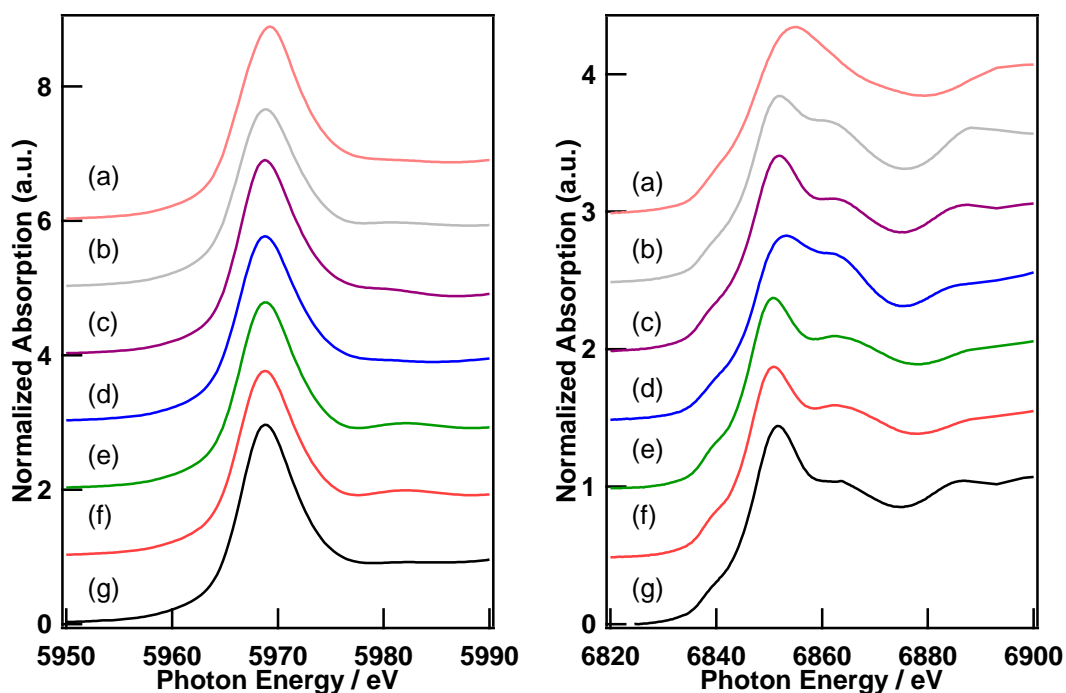


Figure 9. Pr L₃-edge (left) and L₁-edge (right) XANES spectra of Pr complex oxides: (a) NbPrO₄, (b) AlSrPrO₄, (c) NiSrPrO₄, (d) VPrO₄, (e) CoPrO₃, (f) CuPr₂O₄, and (g) SrPrCoO₄

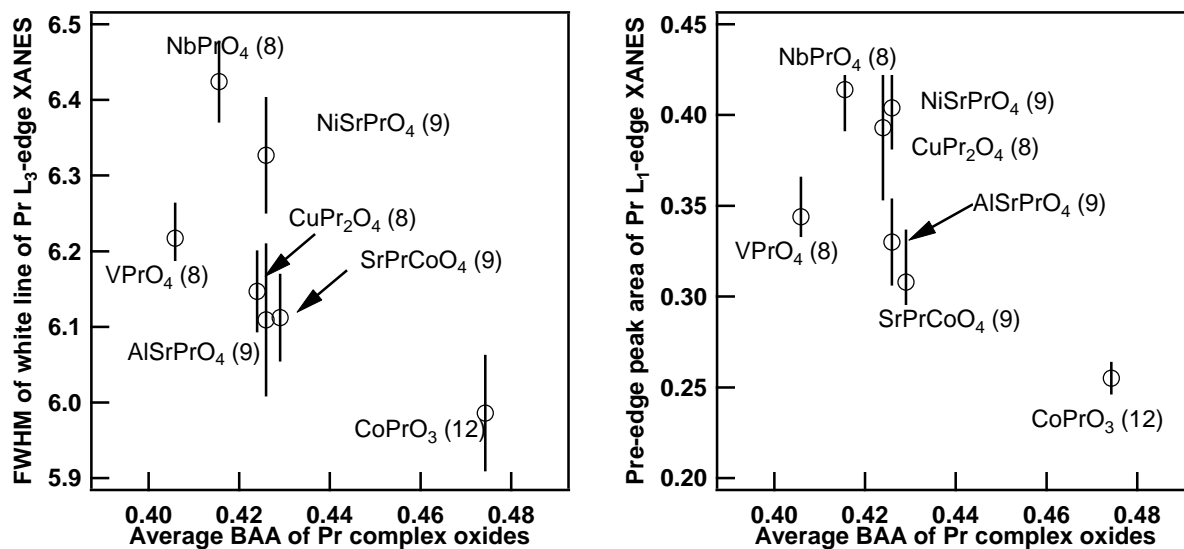


Figure 10. Relationship between averaged bond angle analysis (BAA) parameters and the fwhm of the white line of Pr L₃-edge XANES spectra (left, $R^2 = 0.46$) or the pre-edge peak area of Pr L₁-edge XANES spectra (right, $R^2 = 0.51$) of Pr complex oxides. (The number in parentheses denotes the number of the coordinated oxygen atoms to Pr)

Figure 9 shows Pr L₃-edge and L₁-edge XANES spectra of Pr complex oxides, NbPrO₄, AlSrPrO₄, NiSrPrO₄, VPrO₄, CoPrO₃, CuPr₂O₄, and SrPrCoO₄. Each Pr L₃-edge XANES spectra shows an almost symmetric and featureless white line at around 5970 eV. There is no apparent difference among them. The Pr L₁-edge XANES spectra show again small but evident pre-edge peaks at around 6840 eV. These spectra were analyzed in the same manner to Sm and Nd oxides. The Pr complex oxides also exhibit a linear relationship between the fwhm of the white line of Pr L₃-edge XANES spectra or the pre-edge peak area of Pr L₃-edge XANES spectra and the averaged BAA parameters (Figure 10). In a similar manner to Sm and Nd complex oxides, the pre-edge peak areas of Pr L₁-edge XANES spectra and the fwhm's of the white line of Pr L₃-edge XANES spectra are also correlated as shown in Figure 11.

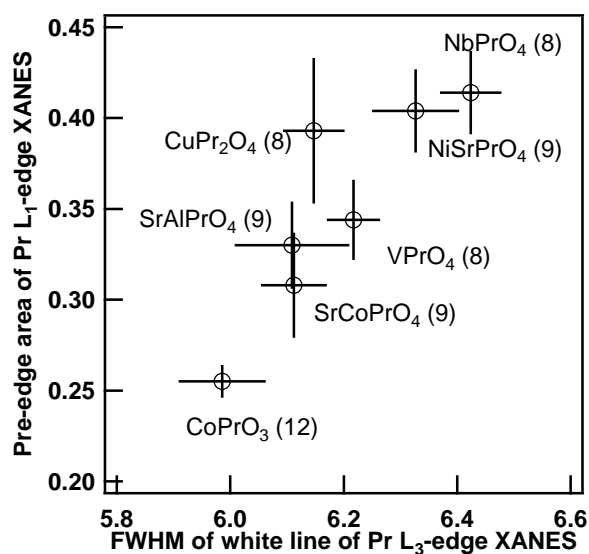


Figure 11. Correlation between the pre-edge peak area of Pr L₁-edge XANES spectra and the fwhm of the white line of Pr L₃-edge XANES spectra of Pr complex oxides. (The number in parentheses denotes the number of the coordinated oxygen atoms to Pr) ($R^2 = 0.76$).

Eu L₃ and L₁-edge XANES Spectra of Eu Complex Oxides

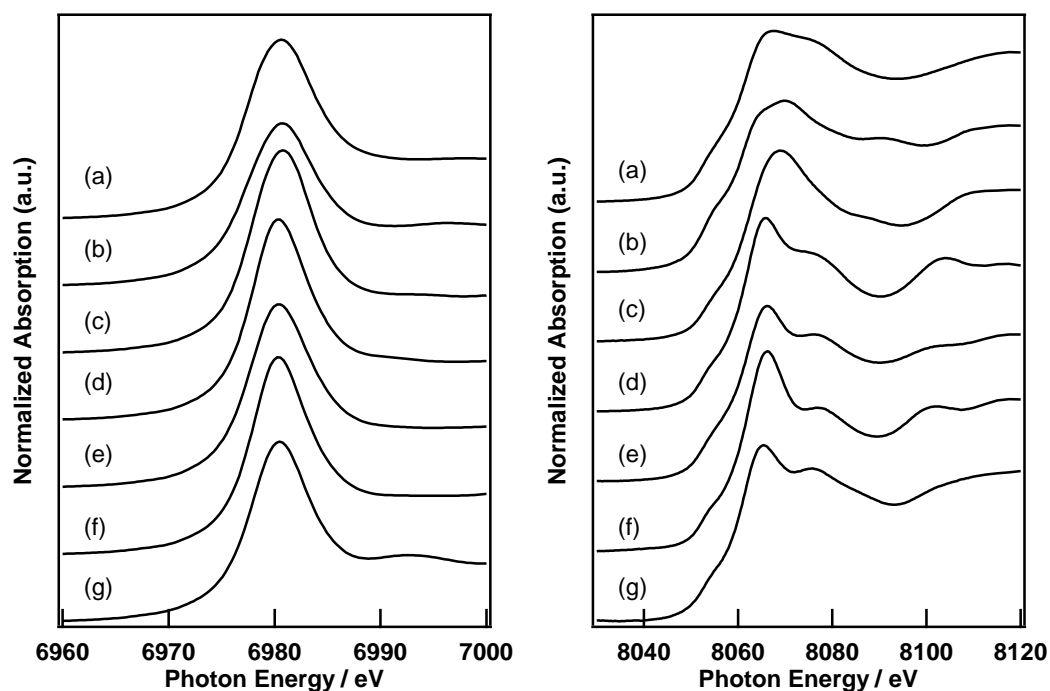


Figure 12. Eu L₃-edge (left) and L₁-edge (right) XANES spectra of Eu complex oxides: (a) Eu₃GaO₆, (b) Eu₂CuO₄, (c) EuNbO₄, (d) SrAl₂Eu₂O₇, (e) SrNiEuO₄, (f) SrCoEuO₄, and (g) CoEuO₃.

Figure 12 shows the Eu L₃ and L₁-edge XANES spectra of Eu₃GaO₆, Eu₂CuO₄, EuNbO₄,

SrAl₂Eu₂O₇, SrNiEuO₄, SrCoEuO₄, and CoEuO₃ with various local configuration of Eu cation. The absorption edge energy of each compound is similar to each other and this fact indicated all the Eu atoms in these compounds are trivalent. Each spectrum illustrates one almost symmetric white line at around 6980 eV. However, when one look into the spectra closely, Eu₃GaO₆ exhibits a bit wider white line than the others, and in contrast, SrAl₂Eu₂O₇, SrNiEuO₄, SrCoEuO₄, or CoEuO₃ show a little narrower one. The corresponding Eu L₁-edge XANES spectra also exhibit a similar spectral shape, but the intensity of the pre-edge shoulder peaks at around 8055 eV varies among the samples. Eu₃GaO₆, which has 7 adjacent oxygen atoms, show slightly larger pre-edge peaks than the others, and Eu₂CuO₄, or EuNbO₄ bearing 8 coordinated oxygen atoms look to exhibit a little smaller peaks. SrAl₂Eu₂O₇, SrNiEuO₄, or SrCoEuO₄ with 9 or 12 adjacent oxygen atoms also exhibit the small but still distinct pre-edge peaks. LaCoO₃ has 12 adjacent oxygen atoms around La and shows a very small pre-edge peak area as discussed in Chapter 2. CoEuO₃ also show the smallest pre-edge peak area of the Eu L₁-edge XANES spectrum, but has only 8 nearest oxygen atoms within 3 Å with highly distorted configuration around Eu, however, it has 12 nearest O atoms within 3.5 Å, which means the apparent coordination number is just a guide for the distortion of local configuration.

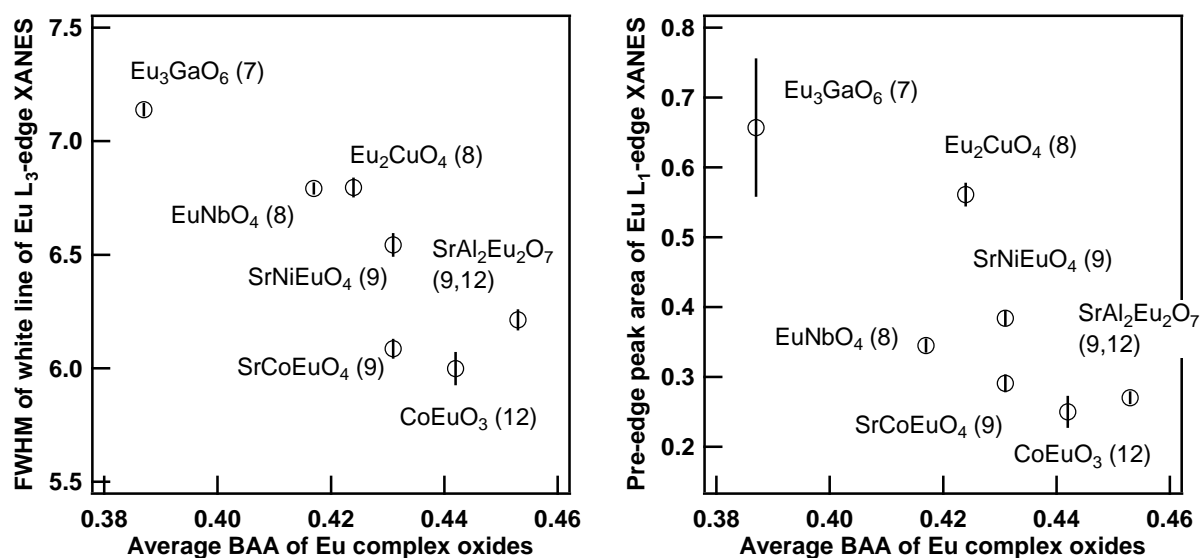


Figure 13. Relationship between averaged Bond Angle Analysis (BAA) parameters and the fwhm of the white line of Eu L₃-edge XANES spectra (left, $R^2 = 0.73$) and the pre-edge peak area of Eu L₁-edge XANES spectra (right, $R^2 = 0.69$) of Eu complex oxides. (The number in parentheses denotes the number of the coordinated oxygen atoms to Eu)

The relationship between the pre-edge peak area of Eu L₁-edge XANES spectra or the fwhm of white line of Eu L₃-edge XANES spectra of Eu complex oxides and their averaged BAA parameters is summarized in Figure 13. The pre-edge peak area of Eu L₁-edge XANES spectra is significantly correlated to their average BAA parameters. The author believes that this correlation suggests the pre-edge peak area could be an indicator of local configuration of lanthanide. However, the pre-edge peak area plots looks a bit more scattered from a possible linear regression. It must be because the EXAFS oscillation at the Eu L₂-edge inevitably affect the L₁-edge XANES spectrum. In general, it is quite difficult to quantitatively estimate the influence, but in our case, the amplitude of the EXAFS oscillation at the L₂-edge in the pre-edge region at the L₁-edge is about 0.01 and the pre-edge peak intensity is no less than about 0.06. Thus, the uncertainty of the pre-edge peak estimation could be no more than about 15%. It is also noteworthy that one of possible samples of the present analysis method on local configuration is an amorphous material lightly-doped with lanthanide atoms, which will not cause strong EXAFS oscillation at the L₂-edge at least in principle.

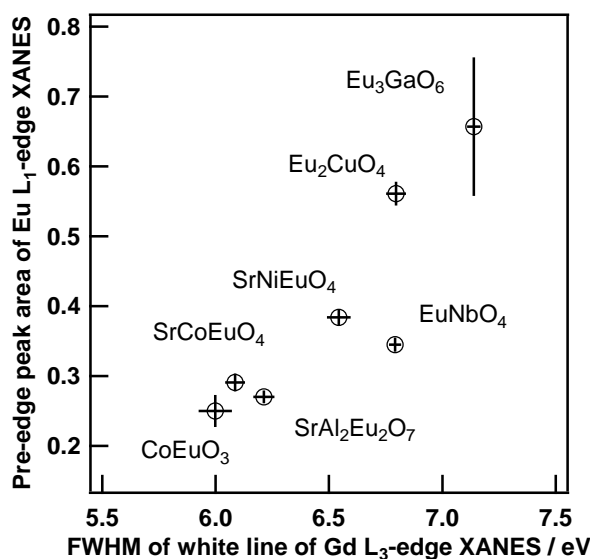


Figure 14. Correlation between the pre-edge peak area of Pr L₁-edge XANES spectra and the fwhm of the white line of Pr L₃-edge XANES spectra of Pr complex oxides. (The number in parentheses denotes the number of the coordinated oxygen atoms to Pr) ($R^2 = 0.78$).

Figure 13 also shows a relationship between the fwhm of white line at the Eu L₃-edge XANES spectra and their averaged BAA parameters. As expected from the absence of the interference from another absorption edge and the high intensity of the white line, the correlation between the two

parameters is clearer than that observed in Figure 3. In a similar manner to Sm, Nd, and Pr complex oxides, the pre-edge peak areas of Eu L₁-edge XANES spectra and the fwhm's of the white line of Eu L₃-edge XANES spectra are also correlated with each other as shown in Figure 14.

Gd L₃ and L₁-edge XANES Spectra of Gd Complex Oxides

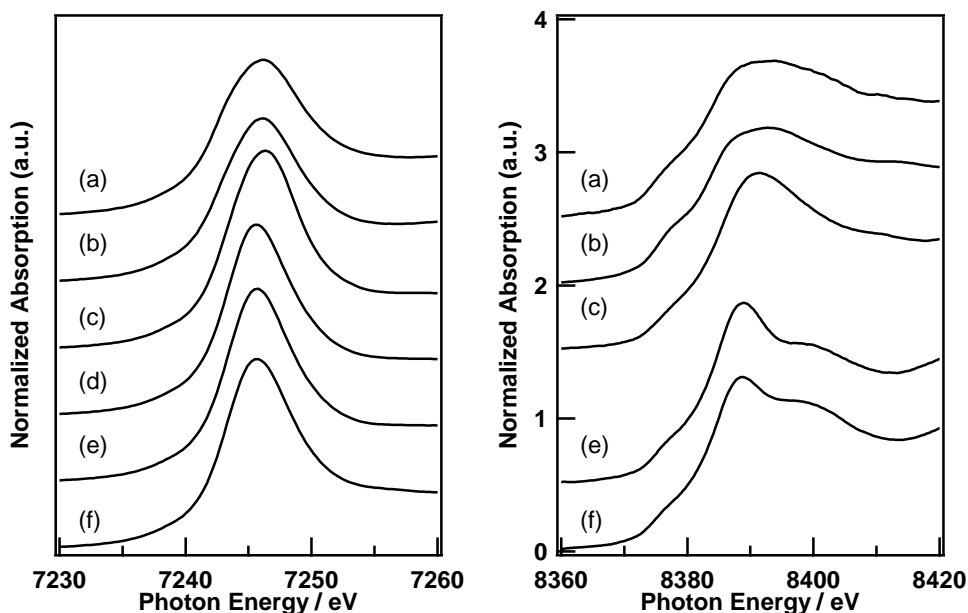


Figure 15. Gd L₃-edge (left) and L₁-edge (right) XANES spectra of Gd complex oxides: (a) Gd₄CuO₇, (b) Gd₂CuO₄, (c) GdNbO₄, (d) SrNiGdO₄, (e) SrCoGdO₄, and (f) SrAl₂Gd₂O₇.

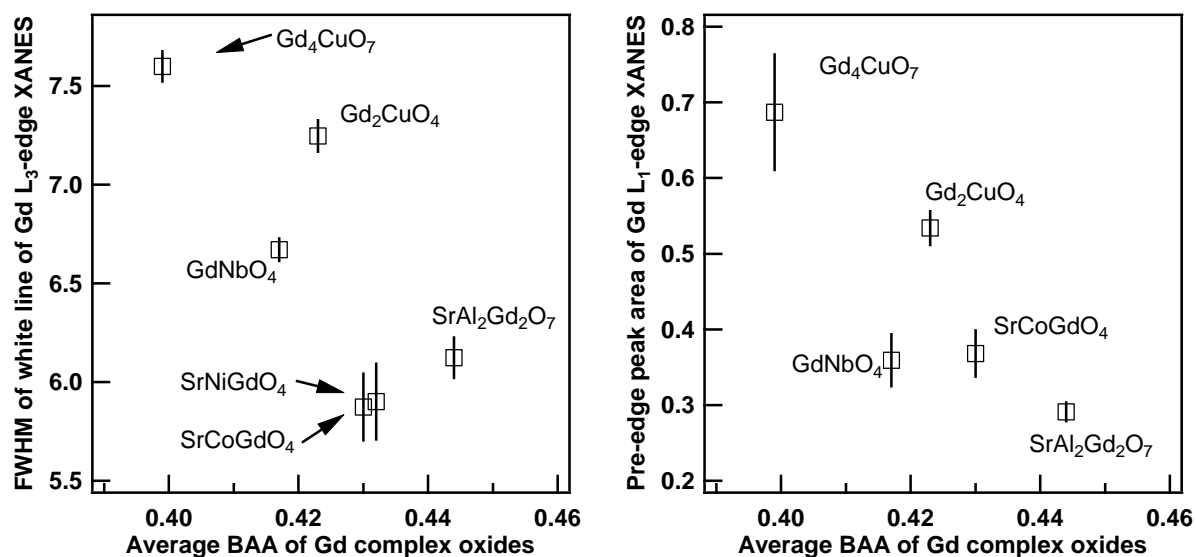


Figure 16. Relationship between averaged Bond Angle Analysis (BAA) parameters and the fwhm of the white line of Gd L₃-edge XANES spectra (left, $R^2 = 0.68$) and the pre-edge peak area of Gd L₁-edge XANES spectra (right, $R^2 = 0.65$) of Gd complex oxides.

Figure 15 shows Gd L₃ and L₁-edge XANES spectra of Gd complex oxides: Gd₄CuO₇, Gd₂CuO₄, GdNbO₄, SrAl₂Gd₂O₇, SrNiGdO₄, and SrCoGdO₄. All of the Gd L₃-edge XANES spectra shows one asymmetric peak at around 7250 eV. Gd₄CuO₇, which has 7-coordinated oxygen atoms around the Gd atom, exhibits the widest white line among the samples. In contrast, 9-coordinated Gd complex oxides such as SrAl₂Gd₂O₇, SrNiGdO₄, or SrCoGdO₄ express the narrower white lines. The other Gd samples, Gd₂CuO₄, and GdNbO₄ show medium width of the white line. The corresponding Gd L₁-edge XANES spectra are also summarized in Figure 15. Gd L₁-edge XANES spectrum of SrNiGdO₄ is not shown because of the presence of the Ni K-edge at around 8330 eV. The absorption edge energy of each spectrum is similar to each other and exhibits a small but distinct shoulder peak at around 8375 eV. Gd₄CuO₇ exhibits the largest and the second largest shoulder peak and Gd₂CuO₄ also show relatively large shoulder peaks. In contrast, the shoulder peaks of SrAl₂Gd₂O₇ and SrCoGdO₄ are small among the samples. To quantitatively evaluate the shoulder peak areas, curve fitting analyses on them were performed in the same manner as performed on the other lanthanide complex oxides. Figure 16 shows the dependence of the pre-edge peak area at the Gd L₁-edge or the fwhm of white line at the Gd L₃-edge on the averaged BAA parameters of Gd complex oxides. Similarly to the case of Eu oxides, there are significant correlations between the spectral feature quantity and the local structure of Gd. Also, the apparent correlation between the fwhm of white line at the L₃-edge and the BAA parameters is a bit stronger against the pre-edge peak area at the L₁-edge.

Local Structure of Sm in Sm-Doped Bi₂O₃–B₂O₃ Glass.

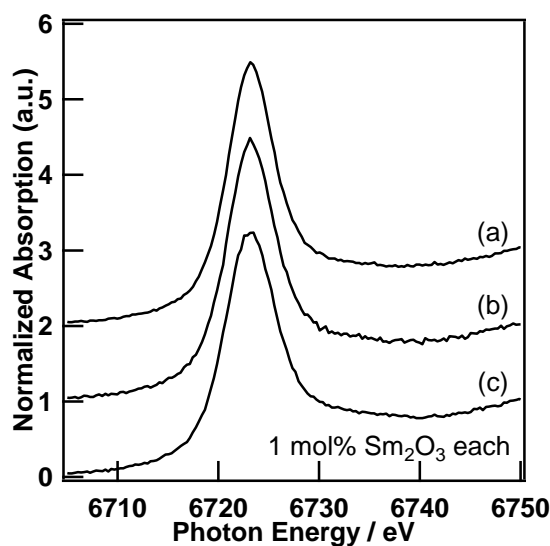


Figure 17 Sm L₃-edge XANES spectra of Sm-doped Bi₂O₃–B₂O₃ glass: (a) Bi₂O₃:B₂O₃ = 25:75, (b) Bi₂O₃:B₂O₃ = 50:50, and (c) Bi₂O₃:B₂O₃ = 75:25, 1 mol % Sm₂O₃ each.

One of the most important applications of lanthanide elements are dopants for various optical glass. For example, Er-doped silica fiber is an important optical amplifier widely used for optical communication. A combination of Sm- or Pr-doped glass phosphor realizes a wide-band near-infrared light source which could be used for a medical or agricultural apparatus. The local structure of the dopant has an influence on the optical property of these materials because of the strong relationship between the electronic the local structures. One of the potent analytical tools of the local structure of dopants is EXAFS spectroscopy. However, in general, it is not easy to estimate structural parameters by curve fitting analysis because of the amorphous nature. The atomic distance of the X-ray absorbing atom and scattering atom has a strong correlation with its displacement or disorder, which leads to the uncertainty of these parameters during the curve fitting procedure. XANES spectra may have less information than EXAFS, but quantitative analysis is also possible. Therefore, we tried to apply the relationship discussed above to Sm-doped Bi₂O₃–B₂O₃ glass as an example of the local structure estimation by means of XANES spectroscopy.

Figure 17 shows Sm L₃-edge XANES spectra of 1 mol % Sm-doped Bi₂O₃–B₂O₃ glass. Fuchi *et al.* reported the optical property of these materials in their previous literature.^{27, 28} The shapes of the white lines are similar to each other and have almost no characteristic feature the same as that of

other Sm reference compounds. However, there are some differences among the width of their white lines. Thus, we performed curve fitting analyses with one arctangent function and one pseudo-Voigt function in the range from 6715 to 6730 eV. The curve fitting analysis was done well with one arctangent function and a pseudo-Voigt function (Lorentzian:Gaussian = 1:1).

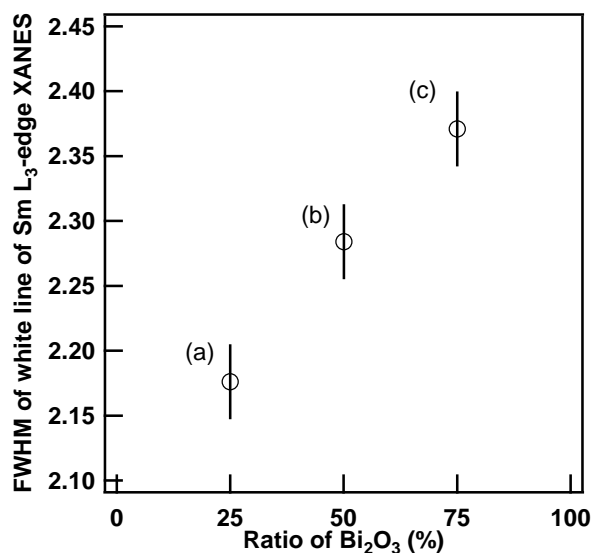


Figure 18 Dependence of the fwhm of the white line of Sm L₃-edge XANES spectrum of Sm-doped Bi₂O₃-B₂O₃ glass on the ratio of Bi₂O₃ and B₂O₃: (a) Bi₂O₃:B₂O₃ = 25:75, (b) Bi₂O₃:B₂O₃ = 50:50, and (c) Bi₂O₃:B₂O₃ = 75:25, 1 mol % Sm₂O₃ each.

Figure 18 shows the dependence of the fwhm of the white line of the Sm L₃-edge XANES spectrum of Sm-doped Bi₂O₃-B₂O₃ glass on the ratio of Bi₂O₃ and B₂O₃. The fwhm, which is an indicator of the d band broadening, increases from 5.2 to 5.7 as the ratio of the amount of Bi₂O₃ of the matrix increases from 25% to 75%. The dependency is clear, but the physical meaning is unclear. The fwhm's of the Sm-doped glasses are smaller than that of the present Sm reference samples. Thus, it must be inappropriate to simply extend the discussion above to the Sm-doped glass samples, unfortunately. The author believes this observation indicates that the coordination number of Sm-O of Sm species in the Bi₂O₃-B₂O₃ decreases, and/or the disorder degree of the first coordination sphere of Sm increases as the ratio of amount of Bi₂O₃ in the matrix increases. Further discussion should be followed by experiments such as high-energy X-ray diffraction and theoretical simulation of L₃-edge XANES spectra.

Conclusion

L-edge XANES spectra of Pr, Nd, Sm, Eu, and Gd complex oxides were classified on the basis of coordination number and complexity of the first coordination sphere of lanthanide elements. As a result, the study found an interesting relationship between their characteristic features of XANES spectra and local structure, which could be used to estimate the local structure of structurally unknown materials. This simple XANES analysis strategy was applied to Sm-doped $\text{Bi}_2\text{O}_3\text{-B}_2\text{O}_3$ glasses to obtain some knowledge on the local structure of Sm. It was suggested that the first coordination sphere of Sm of Sm-doped $\text{Bi}_2\text{O}_3\text{-B}_2\text{O}_3$ glass changed systematically depending on the matrix composition, which must have a strong influence on the photoluminescence property as a phosphor. The structural analysis of Sm must be discussed with more pieces of evidence based on other analytical tools such as high-energy X-ray diffraction patterns with reverse Monte Carlo simulation, but we believe the present method could be a complementary technique for the analysis of local structure of lanthanide elements. In addition, it is important that it is easy to calculate the BAA parameters on any structural model, which could be a model with thousands of atoms generated by molecular dynamics or Monte Carlo simulation. On the basis of the BAA parameters, one might be able to judge whether it is worth measuring the L-edge XANES spectra in order to distinguish the local structure of the target materials.

References

- (1) Yamamoto, T.; Yukumoto, A., *Bunseki Kagaku*, **2013**, *62*, 555-563.
- (2) Shioi, K.; Hirosaki, N.; Xie, R.-J.; Takeda, T.; Li, Y. Q., *J. Alloy. Compd.*, **2010**, *504*, 579-584.
- (3) Souza-Neto, N. M.; Zhao, J.; Alp, E. E.; Shen, G.; Sinogeikin, S. V.; Lapertot, G.; Haskel, D., *Phys. Rev. Lett.*, **2012**, *109*, 026403.
- (4) Saines, P. J.; Kennedy, B. J.; Elcombe, M. M.; Harris, H. H.; Jang, L.-Y.; Zhang, Z., *J. Solid State Chem.*, **2008**, *181*, 2941-2952.
- (5) Yoshida, H.; Yuliati, L.; Hamajima, T.; Hattori, T., *Mater. Trans.*, **2004**, *45*, 2062-2067.
- (6) Hu, Z.; Kaindl, G.; Meyer, G., *J. Alloy. Compd.*, **1997**, *246*, 186-192.
- (7) Ellis, R. J.; Meridiano, Y.; Chiarizia, R.; Berthon, L.; Muller, J.; Couston, L.; Antonio, M. R., *Chem. Eur. J.*, **2013**, *19*, 2663-2675.
- (8) Benfatto, M.; Della Longa, S., *J. Synchrotron Rad.*, **2001**, *8*, 1087-1094.
- (9) Benfatto, M.; Congiu-Castellano, A.; Daniele, A.; Della Longa, S., *J. Synchrotron Rad.*,

2001, 8, 267-269.

- (10) Benfatto, M.; Della Longa, S.; Natoli, C. R., *J. Synchrotron Rad.*, **2003**, 10, 51-57.
- (11) Persson, I.; Damian Risberg, E.; D'Angelo, P.; De Panfilis, S.; Sandström, M.; Abbasi, A., *Inorg. Chem.*, **2007**, 46, 7742-7748.
- (12) D'Angelo, P.; De Panfilis, S.; Filipponi, A.; Persson, I., *Chem. Eur. J.*, **2008**, 14, 3045-3055.
- (13) Persson, I.; D'Angelo, P.; De Panfilis, S.; Sandström, M.; Eriksson, L., *Chem. Eur. J.*, **2008**, 14, 3056-3066.
- (14) D'Angelo, P.; Zitolo, A.; Migliorati, V.; Mancini, G.; Persson, I.; Chillemi, G., *Inorg. Chem.*, **2009**, 48, 10239-10248.
- (15) D'Angelo, P.; Zitolo, A.; Migliorati, V.; Persson, I., *Chem. Eur. J.*, **2010**, 16, 684-692.
- (16) Lundberg, D.; Persson, I.; Eriksson, L.; D'Angelo, P.; De Panfilis, S., *Inorg. Chem.*, **2010**, 49, 4420-4432.
- (17) D'Angelo, P.; Zitolo, A.; Migliorati, V.; Chillemi, G.; Duvail, M.; Vitorge, P.; Abadie, S.; Spezia, R., *Inorg. Chem.*, **2011**, 50, 4572-4579.
- (18) D'Angelo, P.; Migliorati, V.; Spezia, R.; De Panfilis, S.; Persson, I.; Zitolo, A., *Phys. Chem. Chem. Phys.*, **2013**, 15, 8684-8691.
- (19) D'Angelo, P.; Spezia, R., *Chem. Eur. J.*, **2012**, 18, 11162-11178.
- (20) Sayers, D. E.; Stern, E. A.; Lytle, F. W., *Phys. Rev. Lett.*, **1971**, 27, 1204-1207.
- (21) Ofuchi, H.; Kawamura, D.; Tsuchiya, J.; Matsubara, N.; Tabuchi, M.; Fujiwara, Y.; Takeda, Y., *J. Synchrotron Rad.*, **1998**, 5, 1061-1063.
- (22) Ofuchi, H.; Tsuchiya, J.; Matsubara, N.; Tabuchi, M.; Fujiwara, Y.; Takeda, Y., *Appl. Surf. Sci.*, **1997**, 117-118, 781-784.
- (23) Marcus, M. A.; Polman, A., *J. Non-Cryst. Solids*, **1991**, 136, 260-265.
- (24) Peters, P. M.; Houde-Walter, S. N., *J. Non-Cryst. Solids*, **1998**, 239, 162-169.
- (25) Ravel, B.; Newville, M., *J. Synchrotron Rad.*, **2005**, 12, 537-541.
- (26) Glatzel, P.; Sikora, M.; Smolentsev, G.; Fernández-García, M., *Catal. Today*, **2009**, 145, 294-299.
- (27) Fuchi, S.; Sakano, A.; Mizutani, R.; Takeda, Y., *Glass Technology - Eur. J. Glass Sci. Technol. Part A*, **2009**, 50, 319-322.
- (28) Fuchi, S.; Sakano, A.; Takeda, Y., *Jpn. J. Appl. Phys.*, **2008**, 47, 7932.

Chapter 4

Local Structure and L₁ and L₃-edge XANES spectra of Late Lanthanide Elements in Their Complex Oxides

Abstract

Characteristic features of Ho, Er and Yb L₁-edge and L₃-edge X-ray absorption near edge structure (XANES) spectra of their various complex oxides were investigated to find a relationship to the local configuration around these late lanthanide atoms. A pre-edge peak area of the L₁-edge XANES or a full width at half maximum of white line of the L₃-edge XANES spectra have a significant correlation with an abstract geometrical index defined by bond angles formed by a center atom, Ho, Er, or Yb, and two adjacent oxygen atoms, which acts as an indicator of disorder of local configuration. Theoretical calculation based on multiple scattering theory revealed a general trend of dependence of the pre-edge peak at the Ln L₁-edge XANES spectra and the broadening of the white line of the Ln L₃-edge XANES spectra on the local environment of the Ln atoms. This finding will open a way to analyze the local structure of late lanthanide elements by means of the Ln L-edge XANES spectroscopy.

Introduction

In the previous chapter 2 and 3, the author discussed on the characteristic structures of Ln L₁ and L₃-edge XANES spectra of early lanthanide elements and the local configuration around the Ln atom from both of experimental and theoretical viewpoints. These results suggest the feature quantities of the XANES spectra provide semi-quantitative information on the local structure of the early lanthanide atoms in their complex oxides such as the number of adjacent atoms or the degree of disorder. The characteristic features at the L₁ and L₃-edge XANES spectra can be also classified on an abstract physical index defined by the geometry of the nearest atoms.

XANES study on late lanthanide elements is also relatively rare to the 3d, 4d, or 5d metal elements used in various materials. For example, Ho L₃-edge XANES spectra were reported in several papers¹⁻⁵ according to the high resolution XANES measurement beyond the limitation of lifetime broadening, or electronic structure study of superconductors using lanthanide elements. In particular, Lytle *et al.* reported an early example of the Ho L₃-edge XANES spectra of Ho₂O₃ and found its second derivative shows two minimum, but did not give a clear explanation at that time. However, to the best of the author's knowledge, a detail discussion on Ho L₁-edge XANES spectra is not known. Erbium has much wider application than holmium as a dopant for laser devices and its L₃-edge XANES studies have been reported elsewhere.⁶⁻¹⁴ For example, Ishii *et al.* measured the Er L₃-edge XANES spectra of Er₂O₃ and Si:Er₂O₃ thin film prepared by laser ablation method to investigate the optical activation process of Er and found the second derivatives of the Er L₃-edge XANES spectra exhibit two minima related to the split 5d orbitals induced by the local configuration of Er.¹⁴ Yb L-edge XANES spectra were also used to investigate the local structure of Yb in various materials.¹⁵⁻¹⁸ Lanthanide L₁-edge XANES spectra have been rarely reported, but Quartieri *et al.* used Yb L₁ and L₃-edge XANES spectra of Yb in synthetic pyrope and grossularite garnets for structural analysis in combination with full multiple scattering calculations.¹⁵ It is also noteworthy that Yamamoto *et al.* utilized Yb L₃-edge XANES spectra and their second derivatives to clarify the local structure of Yb species supported on silica.¹⁶

However, these studies usually present only a few reference XANES spectra for comparison to that of the target materials and have not clarified a general trend of the characteristic features of late

lanthanide L-edge XANES spectra. In this work, the author investigated a relationship between characteristic features of Ho, Er and Yb L₁-edge and L₃-edge XANES spectra of their various complex oxides and the local configuration around these late lanthanide atoms.

Experimental Section

Sample Preparation of Holmium Complex Oxides

Holmium complex oxides, SrHo₂O₄, Ho₃Al₅O₁₂, HoNbO₄, HoVO₄, Ho₂Cu₂O₅, and HoMn₂O₅ were prepared in solid-state reaction. SrHo₂O₄: Ho₂O₃ (188.0 mg, 0.5 mmol), and SrCO₃ (74.5 mg, 0.5 mmol); Ho₃Al₅O₁₂: Ho₂O₃ (188.4 mg, 0.5 mmol) and Al(NO₃)₃·9H₂O (628.1 mg, 0.833 mmol); HoNbO₄: Ho₂O₃ (187.4 mg, 0.5 mmol) and Nb₂O₅ (133.2 mg, 0.5 mmol); HoVO₄: Ho₂O₃ (186.9 mg, 0.5 mmol), and V₂O₃ (75.0 mg, 0.5 mmol); Ho₂Cu₂O₅: Ho₂O₃ (188.7 mg, 0.5 mmol), and Cu(OAc)₂ (182.0 mg, 1.0 mmol); HoMn₂O₅: Ho₂O₃ (188.3 mg, 0.5 mmol), and MnO (143.4 mg, 2.0 mmol). These mixtures were put into alumina crucible and heated at 1423 K for 24 h. The identification was done by comparison of the XRD patterns of the prepared samples and those of the ones reported in literatures.

Sample Preparation of Erbium Complex Oxides

Erbium complex oxides, BaCuEr₂O₅, BaNiEr₂O₅, ErVO₄, ErNbO₄, Er₃Al₅O₁₂, and Er₂Cu₂O₅ were prepared in solid-state reaction. BaCuEr₂O₅: Er₂O₃ (191.3 mg, 0.5 mmol), Cu(OAc)₂ (91.0 mg, 0.5 mmol), and BaCO₃ (98.4 mg, 0.5 mmol); BaNiEr₂O₅: Er₂O₃ (191.7 mg, 0.5 mmol), Ni(NO₃)₂·6H₂O (148.5 mg, 0.5 mmol) and BaCO₃ (98.9 mg, 0.5 mmol); ErVO₄: Er₂O₃ (383.1 mg, 1.0 mmol), and V₂O₃ (153.3 mg, 1.0 mmol); ErNbO₄: Er₂O₃ (381.9 mg, 1.0 mmol), and Nb₂O₅ (265.0 mg, 1.0 mmol); Er₃Al₅O₁₂: Er₂O₃ (191.5 mg, 0.5 mmol) and Al(NO₃)₃·9H₂O (632.8 mg, 0.833 mmol); Er₂Cu₂O₅: Er₂O₃ (191.7 mg, 0.5 mmol) and Cu(OAc)₂ (181.2 mg, 1.0 mmol). These mixtures were put into alumina crucible and heated at 1423 K for 24 h. The identification was done by comparison of the XRD patterns of the prepared samples and those of the ones reported in literatures.

Sample Preparation of Ytterbium Complex Oxides

Ytterbium complex oxides, YbFeO₃, Yb₃Fe₅O₁₂, Yb₂Cu₂O₅, Yb₃Al₅O₁₂, YbVO₄, and YbNbO₄

were prepared in solid-state reaction. YbFeO₃: Yb₂O₃ (196.1 mg, 0.5 mmol) and Fe(NO₃)₃·9H₂O (404.8 mg, 1.0 mmol); Yb₃Fe₅O₁₂: Yb₂O₃ (196.7 mg, 0.5 mmol) and Fe(NO₃)₃·9H₂O (672.8 mg, 1.67 mmol); Yb₂Cu₂O₅: Yb₂O₃ (198.0 mg, 0.5 mmol), and Cu(OAc)₂ (183.1 mg, 1.0 mmol); Yb₃Al₅O₁₂: Yb₂O₃ (197.6 mg, 0.5 mmol), and Al(NO₃)₃·9H₂O (631.6 mg, 0.833 mmol); YbVO₄: Yb₂O₃ (592.0 mg, 1.5 mmol), and V₂O₃ (226.1 mg, 1.5 mmol); YbNbO₄: Yb₂O₃ (393.5 mg, 1.0 mmol) and Nb₂O₅ (268.0 mg, 1.0 mmol). These mixtures were put into alumina crucible and heated at 1423 K for 24 h. The identification was done by comparison of the XRD patterns of the prepared samples and those of the ones reported in literatures.

XAS Measurement and Data Reduction

Ln (Ln = Ho, Er, Yb) L₁ and L₃-edge XANES spectra of these materials were measured at the BL5S1, a hard X-ray XAFS beamline, at Aichi Synchrotron Radiation Center¹⁹ (AichiSR; Aichi Science and Technology Foundation, Aichi, Japan). The XANES spectra of their powder samples were recorded in transmission mode under ambient condition, using a Si(111) double crystal monochromator. The photon energy was calibrated at the pre-edge peak (8980.3 eV) observed in the Cu K-edge XANES spectrum of Cu foil. Powder samples were mixed with an appropriate amount of boron nitride and pressed into pellets. Incident and transmitted X-ray fluxes were measured with ion chambers filled with He(70%)/N₂(30%) and N₂(75%)/Ar(25%). Higher harmonic X-ray was cut off with proper glancing angle of Rh-coated collimating and focusing mirrors. A typical data reduction procedure (*e.g.* background removal, or normalization) was carried out with the Athena ver. 0.9.20 included in the Demeter package²⁰. Curve fitting analyses on the Ln L₁ and L₃-edge and XANES spectra were also done with the peak fitting function implemented into the Athena and the multipeak fitting procedure implemented into Igor Pro ver. 6.35 (Wavemetrics, Lake Oswego, OR, USA).

Results and Discussion

Ho L₁ and L₃-edge XANES spectra of Ho complex oxides

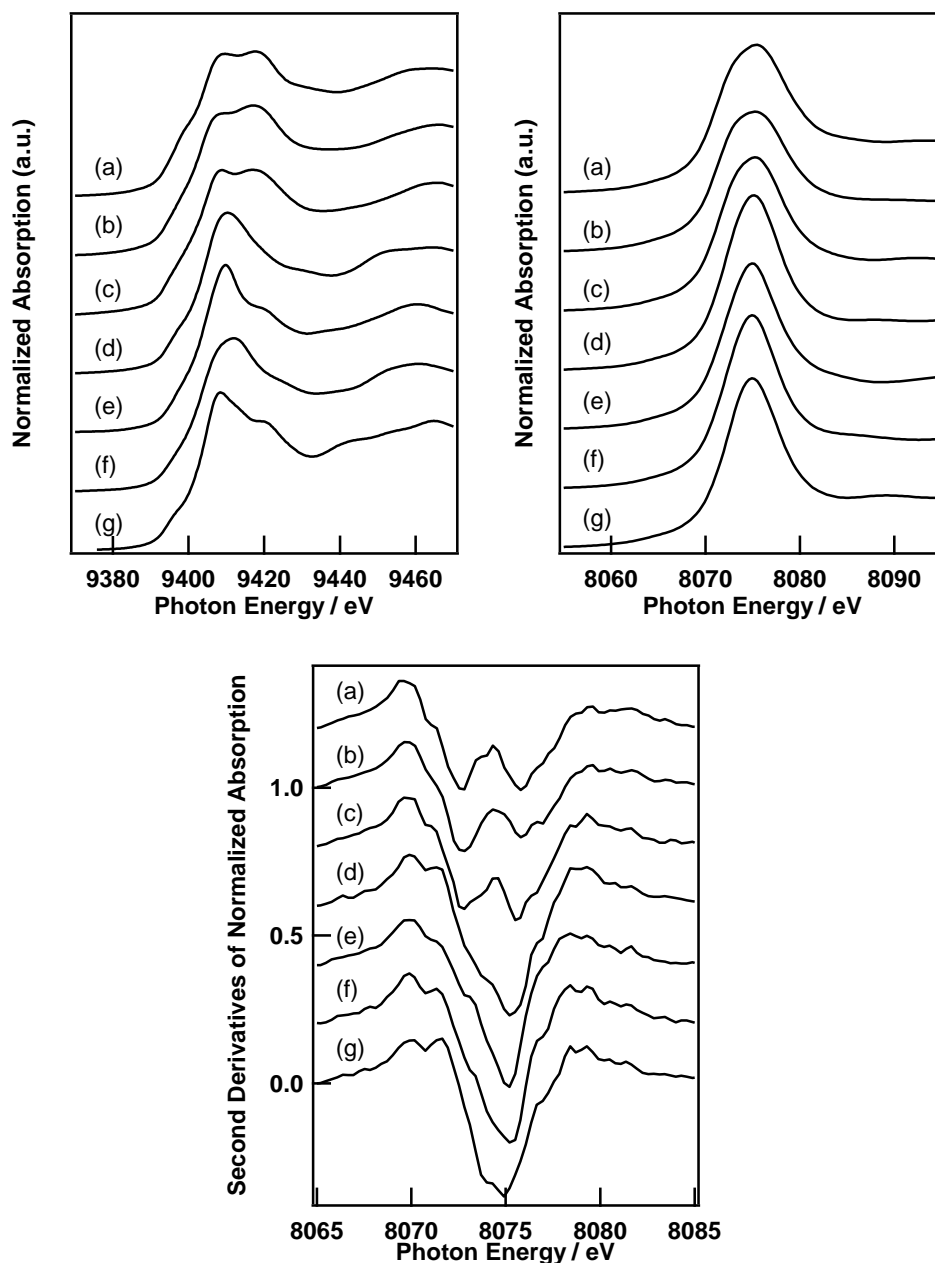


Figure 1. Ho L₁ (upper left), L₃-edge (upper right) XANES spectra and the second derivatives of Ho L₃-edge XANES (lower) spectra of Ho complex oxides: (a) SrHo₂O₄, (b) Ho₂Cu₂O₅, (c) Ho₂O₃, (d) HoNbO₄, (e) Ho₃Al₅O₁₂, (f) HoMn₂O₅, and (g) HoVO₄.

Figure 1 shows the Ho L₁ and L₃-edge XANES spectra of SrHo₂O₄, Ho₂Cu₂O₅, Ho₂O₃, HoNbO₄, Ho₃Al₅O₁₂, HoMn₂O₅, and HoVO₄, of which Ho atoms are surrounded by several O atoms in their

crystal lattice. The Ho L₁-edge XANES spectrum of each Ho compound is those of the other Ho compounds in whole, but exhibits characteristic peaks at around 9395, 9408, and 9420 eV. The XANES spectrum of SrHo₂O₄, which has an almost regular octahedral HoO₆ unit and a highly distorted octahedral HoO₆ unit, shows a distinct and the largest pre-edge peak intensity among the present Ho samples. Ho₂Cu₂O₅ and Ho₂O₃ bearing significantly distorted HoO₆ units or HoVO₄ with distorted HoO₈ units also exhibit noticeable pre-edge peaks. The pre-edge region of the other Ho compounds, HoNbO₄, Ho₃Al₅O₁₂, and HoMn₂O₅ looks featureless at a glance, but the second derivatives of the Ho L₁-edge XANES spectra clearly indicate the presence of small pre-edge peaks. The Ho L₃-edge XANES spectra of the corresponding Ho compounds with no characteristic feature are shown in Figure 1 (right). However, there are slight differences in the width of the white line at around 8075 eV. The width of white line of SrHo₂O₄ looks significantly larger than that of the other Ho compounds.

Discussion or even the measurement of Ho L₁ and L₃-edge XANES spectra have been very rare because trace element structural analysis of Ho in its compounds is unimportant due to the high cost and limited application of Ho element to practical materials or devices. However, recently, Ho element has been used as a dopant for YAG laser to generate a laser emission wavelength in 2 μm²¹, which have been already applied into medicinal surgery. Then, even though Ho element is not abundant, further applications of Ho element are expected and element specific analytical technique for the element should be also important.

In analogy with the previous analysis strategy on the L₁ and L₃-edge XANES spectra of early lanthanide elements such as La, Pr, Nd, Sm, Eu, and Gd, the author tried to perform curve fitting analysis on both of the pre-edge peak intensity of the Ho L₁-edge and the full width at half maximum of the white line of the Ho L₃-edge XANES spectra quantitatively to evaluate the p states mixing into unoccupied d states and the broadening of unoccupied d states. The pre-edge region of Ho L₁-edge XANES spectra were fitted with a cubic function as a background and one Gaussian function for the peak and the white line region of Ho L₃-edge XANES spectra were fitted with an arctangent function as a background and one pseudo-Voigt function (Lorentzian:Gaussian = 1:1). Figure 2 shows all the curve fitting analysis on the Ho L₁-edge XANES spectra were performed well with only the two functions. The pre-edge peak area of Ho compounds are about 0.959 (SrHo₂O₄), 0.667 (Ho₂Cu₂O₅),

0.547 (Ho_2O_3), 0.348 (HoNbO_4), 0.277 ($\text{Ho}_3\text{Al}_5\text{O}_{12}$), 0.212 (HoMn_2O_5), and 0.289 (HoVO_4). The relationship between the pre-edge peak area and the local structure of each Ho site is discussed below.

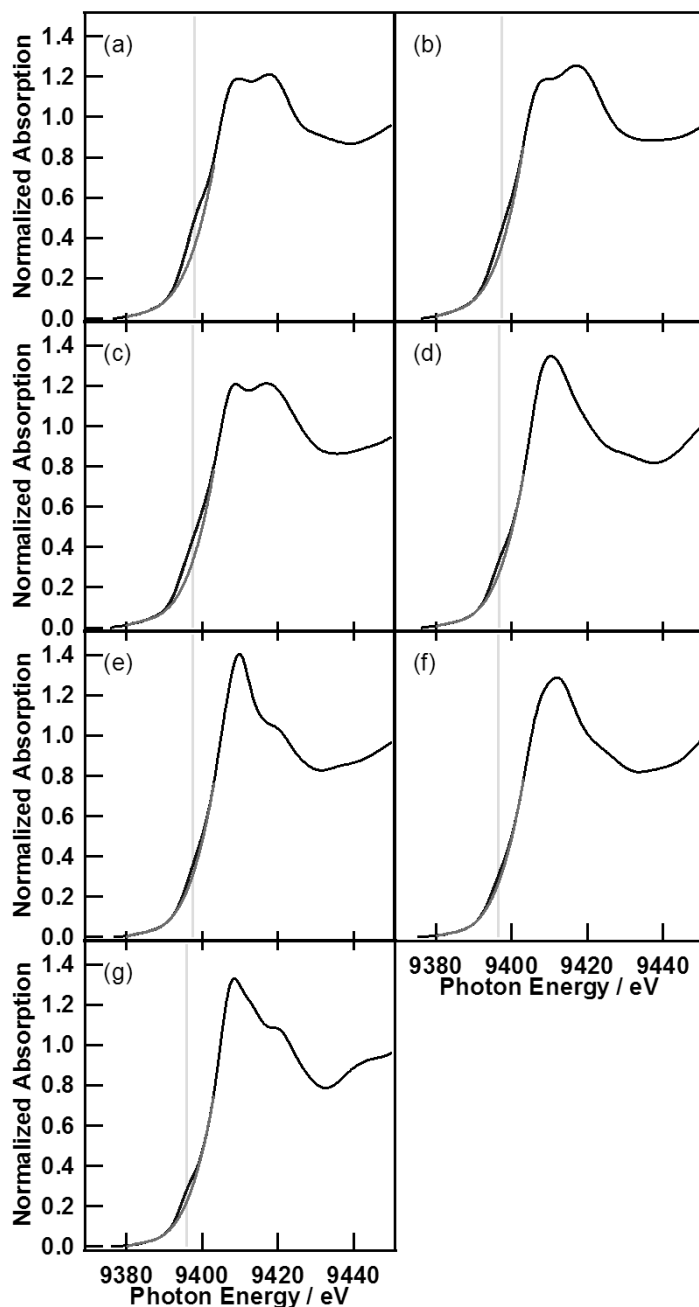


Figure 2. Curve fitting results of the pre-edge region of Ho L_1 -edge XANES spectra of Ho complex oxides: (a) SrHo_2O_4 , (b) $\text{Ho}_2\text{Cu}_2\text{O}_5$, (c) Ho_2O_3 , (d) HoNbO_4 , (e) $\text{Ho}_3\text{Al}_5\text{O}_{12}$, (f) HoMn_2O_5 , and (g) HoVO_4 .

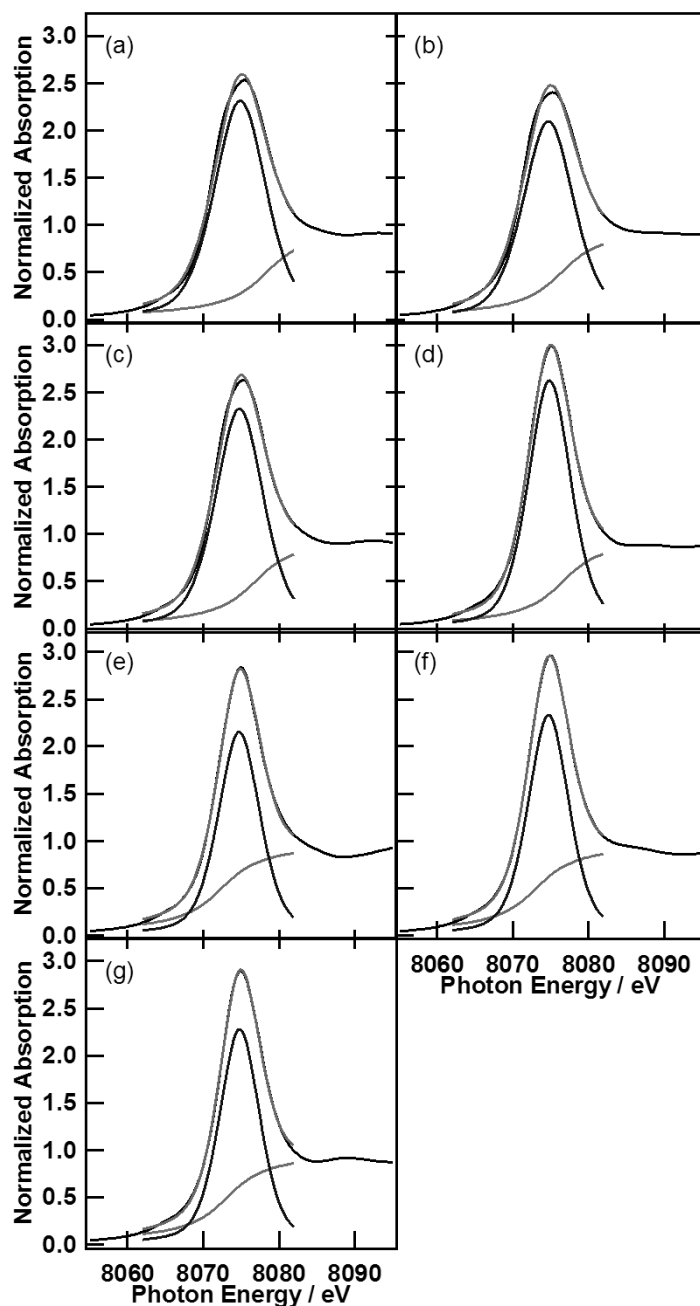


Figure 3. Curve fitting results of the white line of Ho L_3 -edge XANES spectra of Ho complex oxides: (a) SrHo_2O_4 , (b) $\text{Ho}_2\text{Cu}_2\text{O}_5$, (c) Ho_2O_3 , (d) HoNbO_4 , (e) $\text{Ho}_3\text{Al}_5\text{O}_{12}$, (f) HoMn_2O_5 , and (g) HoVO_4 .

To investigate the broadening of unoccupied d states from the shape of white line structure of L_3 -edge XANES spectra, one of the most common techniques is calculating secondary derivatives of them as reported in the previous literature (Figure 1, lower). The second derivatives of Ho L_3 -edge XANES spectra of SrHo_2O_4 , $\text{Ho}_2\text{Cu}_2\text{O}_5$, and Ho_2O_3 with 6-coordinated Ho atoms (two slightly

different sites in each unit cell) exhibit clear two minima, which indicate degenerate d states split into two main e_g and t_{2g} like states, but those of the other Ho compounds, HoNbO_4 , $\text{Ho}_3\text{Al}_5\text{O}_{12}$, HoMn_2O_5 , and HoVO_4 , do not show distinct minima assignable to split d states. From the fundamental crystal field theory, the split d orbitals of 4, 5, or 6-coordinated atoms such as tetrahedral, pentagonal bipyramidal, or octahedral geometries are well known as e and t_2 states or e_g and t_{2g} states and so forth. However, d orbital splitting states of an atom coordinated by no less than 7 atoms cannot be easily deduced from the crystal field theory. Then, we took a bit more primitive approach to estimate the d states broadening from the L_3 -edge XANES spectra by curve fitting analysis described above as shown in Figure 3. The curve fitting results of Ho L_3 -edge XANES spectra of HoNbO_4 , $\text{Ho}_3\text{Al}_5\text{O}_{12}$, HoMn_2O_5 , and HoVO_4 looks satisfactory. Those of the other Ho compounds, SrHo_2O_4 , $\text{Ho}_2\text{Cu}_2\text{O}_5$, and Ho_2O_3 , show small differences between the experimental data and fitting lines, but also look enough to estimate the fwhm of white line of each spectrum. The fwhm of white line of Ho L_3 -edge XANES spectra are found to be 8.14 (SrHo_2O_4), 7.96 ($\text{Ho}_2\text{Cu}_2\text{O}_5$), 7.53 (Ho_2O_3), 6.59 (HoNbO_4), 6.48 ($\text{Ho}_3\text{Al}_5\text{O}_{12}$), 6.39 (HoMn_2O_5), and 6.25 (HoVO_4).

Relationship between the pre-edge peak area of Ho L_1 -edge XANES or fwhm of white line of Ho L_3 -edge XANES and the local structure of Ho in their complex oxides

Common coordination number of lanthanide elements ranges from 6 or 7 to 12 due to their large ionic radii. Information on the local geometry of the nearest neighbor atoms to lanthanide atoms must be important to understand the electronic state, which should be strongly related to the desirable properties such as fluorescence or phosphorescence, for example. EXAFS has been applied to this issue as one of the widely accepted analytical techniques to estimate the local structure of X-ray absorbing atoms. Even though combinations of EXAFS spectroscopy with Monte Carlo simulation, molecular dynamics, and/or hard X-ray diffraction are promising tools for the elucidation of short range or even middle range order of amorphous materials having lanthanide atoms, the main drawback of EXAFS spectroscopy is the fact that it heavily depends on an initial model of the target structure. Curve fitting procedure on EXAFS spectra based on the EXAFS equation and Fourier transform of EXAFS oscillation has been winning great success of application of X-ray absorption spectroscopy to various materials. However, in some cases, it is quite difficult to construct a

plausible initial structure around the X-ray absorbing atom. If a target material was amorphous and it was apparent that the X-ray absorbing atoms could be located in enormous different sites, or structurally unknown in any sense, it would be impossible to prepare a valid model. In contrast, XANES region including pre-edge peaks, white lines and some characteristic structures above the absorption edge, can be interpreted into a simple linear superposition of XANES spectra of every X-ray absorbing atom. It means that XANES spectra can provide average or statistical information of the electronic and geometrical structure.

$$BAA = \frac{1}{n} \sum |\cos(\theta_{ijk})|$$

In the previous chapters of study on the XANES spectra of early lanthanide elements, the author proposed an abstract physical index, “bond angle analysis parameter” (BAA), which is defined in the following simple equation, where n and θ_{ijk} denote the number of independent angles and the angle formed by the central atom j and two of its adjacent atoms i and k , respectively. Then, the author calculated and the BAA indexes of the Ho compounds and tried to find a relationship to the experimental feature quantities. If there are unidentical sites of Ln, the BAA parameter is calculated as an average value of each BAA parameter on each site.

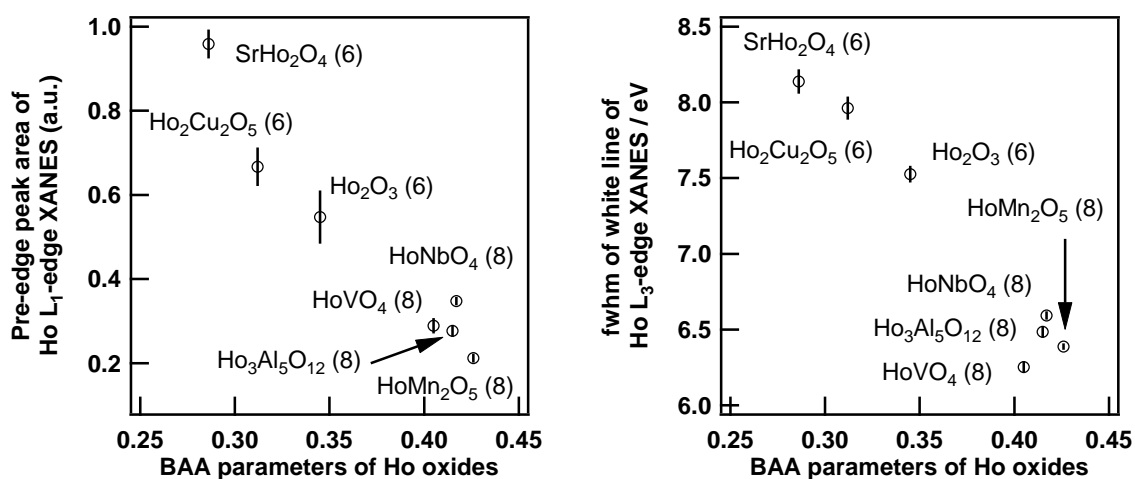


Figure 4. Dependence of pre-edge peak area of Ho L₁-edge or the fwhm of Ho L₃-edge XANES spectra on the BAA parameters of SrHo₂O₄, Ho₂Cu₂O₅, Ho₂O₃, HoNbO₄, Ho₃Al₅O₁₂, HoMn₂O₅, and HoVO₄. (The number in parentheses denotes the number of the coordinated oxygen atoms to Ho)

Figure 4 shows dependence of the pre-edge peak area of Ho L₁-edge or the fwhm of Ho L₃-edge

XANES spectra of Ho complex oxides on the BAA parameters. Surprisingly, both of them indicate the presence of significant correlation between these indexes. If one postulates presence of a linear correlation, the correlation coefficients can be 0.94 for the pre-edge peak area of Ho L₁-edge XANES spectra and 0.95 for the fwhm of white line of Ho L₃-edge XANES spectra. At present, the physical meaning on the linear correlation hypothesis is vague, but it might be related to the degree of hybridization of orthogonal p orbitals into d orbitals, which can increase the pre-edge peak intensity and broaden the unoccupied d states. This fact implies both of the pre-edge peak area at Ho L₁-edge and the fwhm of white line at Ho L₃-edge XANES spectra can be an indicator of the local structure of Ho atoms. In addition, it is easy to infer a presence of a linear correlation between the pre-edge peak at the Ho L₁-edge and the fwhm of white line at the Ho L₃-edge XANES spectra. For example, Ho:YAG lasers utilize not only Ho, but also Tm or other lanthanide elements. On the local structure analysis of Ho of a Ho:YAG laser with EXAFS spectroscopy, the presence of Tm could be an obstacle because of the absorption edge of Tm at the L₃-edge located at 8.6 keV near to that of Ho L₃-edge at 8.1 keV. Then, the Ho L₁ and L₃-edge XANES spectroscopy, not EXAFS, can be an option.

Er and Yb L_1 and L_3 -edge XANES spectra of Er or Yb complex oxides

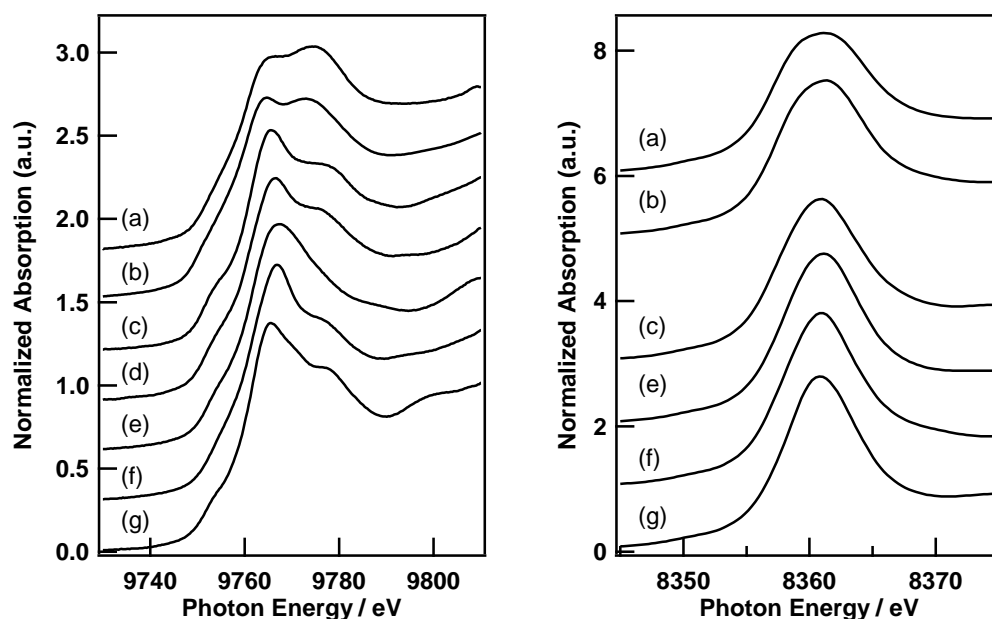


Figure 5. Er L_1 and L_3 -edge (right) XANES spectra of Er oxides: (a) $\text{Er}_2\text{Cu}_2\text{O}_5$, (b) Er_2O_3 , (c) $\text{BaNiEr}_2\text{O}_5$, (d) $\text{BaCuEr}_2\text{O}_5$, (e) ErNbO_4 , (f) $\text{Er}_3\text{Al}_5\text{O}_{12}$, and (g) ErVO_4 .

Figure 5 (left) shows the Er L_1 and L_3 -edge XANES spectra of $\text{Er}_2\text{Cu}_2\text{O}_5$, Er_2O_3 , $\text{BaNiEr}_2\text{O}_5$, $\text{BaCuEr}_2\text{O}_5$, ErNbO_4 , $\text{Er}_3\text{Al}_5\text{O}_{12}$, and ErVO_4 of which Er atoms are surrounded by several O atoms (Er L_3 -edge XANES spectrum of $\text{BaNiEr}_2\text{O}_5$ is not shown in Figure 5 (right) because of the presence of Ni K-edge (8.33 keV)). The Er L_1 -edge XANES spectrum of each Er compound is similar to those of the other Er compounds, and exhibits characteristic peaks at around 9753, 9765, and 9778 eV. The Er L_1 -edge XANES spectra of $\text{Er}_2\text{Cu}_2\text{O}_5$ and Er_2O_3 , which have distorted octahedral ErO_6 unit, show the largest and the second largest pre-edge peak intensities among the present Er samples. $\text{BaCuEr}_2\text{O}_5$ and $\text{BaNiEr}_2\text{O}_5$ bearing ErO_7 units also exhibit distinct pre-edge peaks. The pre-edge region of the other Er compounds, ErNbO_4 , $\text{Er}_3\text{Al}_5\text{O}_{12}$, and ErVO_4 are still noticeable. The Er L_3 -edge XANES spectra of the Er compounds are shown in Figure 5 (right) just with one asymmetric large white line. There are small differences in the width of the white line at around 8360 eV and the width of white line of $\text{Er}_2\text{Cu}_2\text{O}_5$, and Er_2O_3 look significantly larger than that of the other Er oxides. Quantitative analysis of the pre-edge peak area at the L_1 -edge and the fwhm of white line at the L_3 -edge XANES spectra was performed in the same way of the Ho case to extract feature quantities

from the XANES spectra.

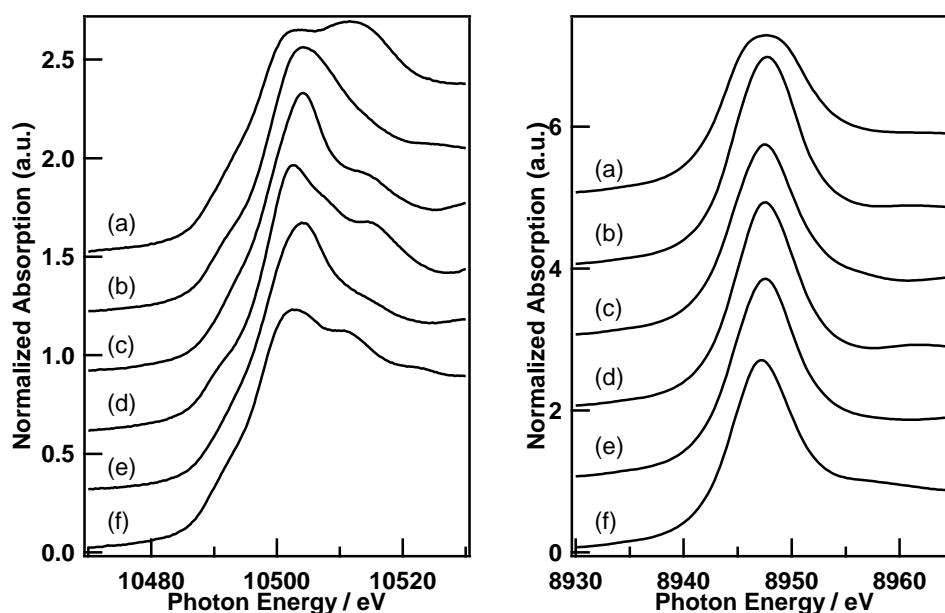


Figure 6. Yb L_1 (left) and L_3 -edge (right) XANES spectra of Er oxides: (a) $\text{Yb}_2\text{Cu}_2\text{O}_5$, (b) YbNbO_4 , (c) $\text{Yb}_3\text{Al}_5\text{O}_{12}$, (d) YbVO_4 , (e) $\text{Yb}_3\text{Fe}_5\text{O}_{12}$, and (f) YbFeO_3 .

Figure 6 shows the Yb L_1 and L_3 -edge XANES spectra of $\text{Yb}_2\text{Cu}_2\text{O}_5$, YbNbO_4 , $\text{Yb}_3\text{Al}_5\text{O}_{12}$, YbVO_4 , $\text{Yb}_3\text{Fe}_5\text{O}_{12}$, and YbFeO_3 . The Yb L_1 -edge XANES spectrum of each Yb compound exhibits characteristic peaks at around 10490, 10503, and 10512 eV. The Yb L_1 -edge XANES spectrum of $\text{Yb}_2\text{Cu}_2\text{O}_5$, which have distorted octahedral YbO_6 unit, shows the largest broad shoulder peak intensities among the present Yb samples. The pre-edge peaks at the Yb L_1 -edge of the other Yb compounds, YbNbO_4 , $\text{Yb}_3\text{Al}_5\text{O}_{12}$, YbVO_4 , $\text{Yb}_3\text{Fe}_5\text{O}_{12}$, and YbFeO_3 are also noticeable. The Yb L_3 -edge XANES spectra of the Yb compounds are shown in Figure 6 (right). Only the Yb L_3 -edge XANES spectrum of $\text{Yb}_2\text{Cu}_2\text{O}_5$ shows a broad white line, but the others are narrow and similar to each other. Quantitative analysis of these spectra was also performed in the same procedure above and discussed later.

Relationship between the pre-edge peak area of L₁-edge XANES or fwhm of white line of L₃-edge XANES and the local structure of Er or Yb atoms in their complex oxides

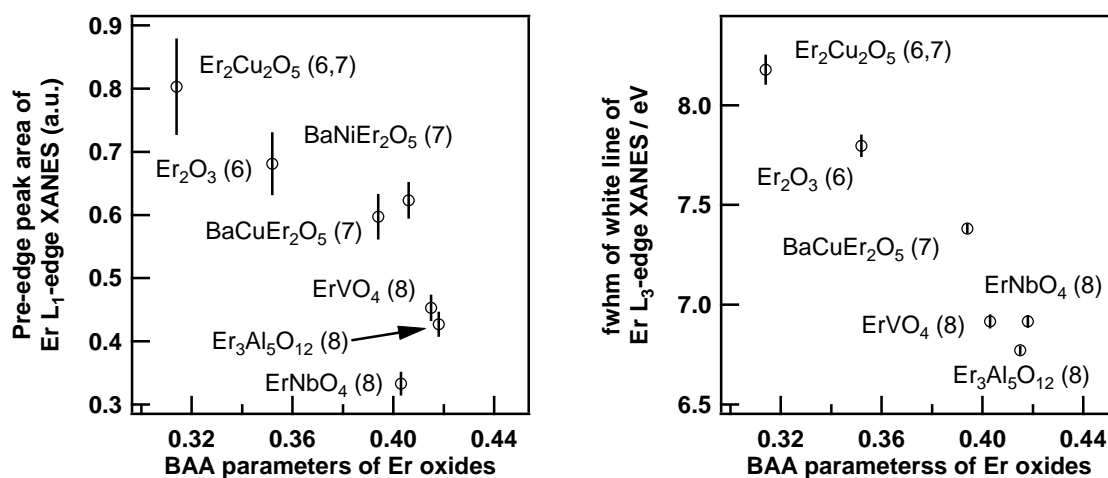


Figure 7. Dependence of pre-edge peak area of Er L₁-edge or the fwhm of Er L₃-edge XANES spectra on the BAA parameters of Er₂Cu₂O₅, Er₂O₃, BaNiEr₂O₅, BaCuEr₂O₅, ErNbO₄, Er₃Al₅O₁₂, and ErVO₄. (The number in parentheses denotes the number of the coordinated oxygen atoms to Er)

Figure 7 shows dependence of the pre-edge peak area of the Er L₁-edge or the fwhm of white line of the Er L₃-edge XANES spectra of Er complex oxides on the BAA parameters. The relationships between these indexes are not so clear like the Ho case, but the correlation looks significant, again. The correlation coefficients can be 0.81 for the pre-edge peak area of the Er L₁-edge XANES spectra and 0.94 for the fwhm of white line of the Er L₁-edge XANES spectra under a linear correlation assumption. This means both of the pre-edge peak area at the Er L₁-edge and the fwhm of white line at the Er L₃-edge XANES spectra can be an indicator of the local structure of Er atoms, again. In addition, a linear correlation between the pre-edge peak at the L₁-edge and the fwhm of white line at the Er L₃-edge XANES spectra was also found ($R^2 = 0.98$).

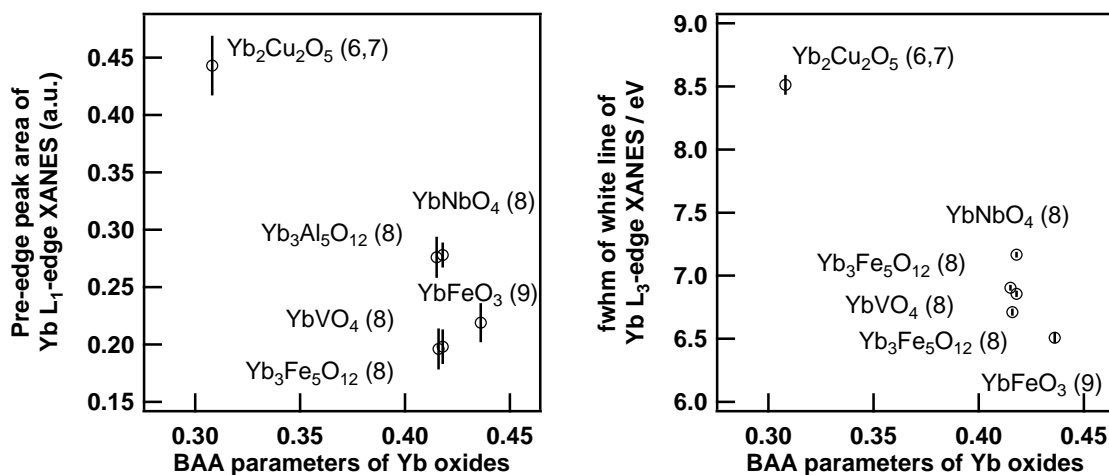


Figure 8. Dependence of pre-edge peak area of Yb L₁-edge or the fwhm of Yb L₃-edge XANES spectra on the BAA parameters of Yb₂Cu₂O₅, YbNbO₄, Yb₃Al₅O₁₂, YbVO₄, Yb₃Fe₅O₁₂, and YbFeO₃. (The number in parentheses denotes the number of the coordinated oxygen atoms to Yb)

Dependence of the pre-edge peak area of the Yb L₁-edge or the fwhm of the Yb L₃-edge XANES spectra of the Yb complex oxides on the BAA parameters are shown in Figure 8. Unfortunately, characteristics of the Yb L-edge XANES of the present Yb complex oxides were classified into two main groups and did not show a gradual change, but a correlation between the feature quantities of L-edge XANES spectra and the local structure is plausible in analogy with the previous two element cases. Furthermore, a linear correlation between the pre-edge peak at the L₁-edge and the fwhm of white line at L₃-edge XANES spectra exists again ($R^2 = 0.95$ for the pre-edge peak area (Figure 8, left); $R^2 = 0.85$ for the fwhm of white line (Figure 8, right)).

Theoretical calculation of Ho L₁ and L₃-edge XANES spectra of virtual Ho aqueous complexes

As mentioned above, one of the characteristic properties of lanthanide elements is its large coordination number. Yamazoe *et al.* discussed the relationship between the shape of the W L₁ and L₃-edge XANES spectra and their local structures of various W reference compounds, which have 4 or 6 coordinated O atoms around the W atom²². They classified the local symmetries of W species into three groups, tetrahedral (*i.e.* 4-coordinated WO₄ unit), “distorted” octahedral, and octahedral (*i.e.* 6-coordinated WO₆ unit) ones and found that the pre-edge peak area at the W L₁-edge XANES spectrum decreases and the width of white line at the W L₃-edge XANES spectrum related to d orbital splitting increases as the coordination number of W increases from 4 to 6. In the present cases of Ho,

Er, and Yb, the pre-edge peak area of Ln L₁-edge XANES spectrum also decreases as the coordination number of Ln atoms increases, but, in contrast, the fwhm of white line at the Ln L₃-edge XANES spectrum decreases as the coordination number of Ln atoms increases from 6 to 8. To review the experimental results by means of theoretical simulation, the author calculated Ho L₁ and L₃-edge XANES spectra of virtual Ho aqueous complexes, Ho(H₂O)_n (n = 4 – 9) of which geometry were optimized by molecular dynamics and quantum mechanics in the same procedure of the previous chapter.

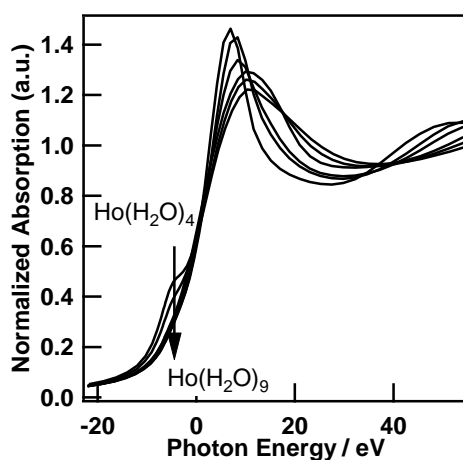


Figure 9. Simulated Ho L₁-edge XANES spectra of virtual Ho aqueous complexes, Ho(H₂O)_n (n = 4 – 9).

Figure 9 shows the simulated Ho L₁-edge XANES spectra of virtual Ho aqueous complexes with FEFF²³, including electric dipole and quadrupole transitions. Four or five-coordinated Ho species, Ho(H₂O)₄ or Ho(H₂O)₅ must be unreal because there is still large vacancy around Ho with only 4 or 5 O atoms, but it is enough to investigate the effect of the geometrical environment of Ho on the Ho L-edge XANES spectrum. As expected from the W case²² or many other 3d, 4d, 5d metal elements, the pre-edge peak gradually decreases as the number of adjacent O atom increases, which can be explained by the contribution of p component to the unoccupied states related to the pre-edge peak decreases as the intersection of d and p orbitals decreases. Furthermore, the pre-edge peak intensity continues to decrease monotonously as the number of coordinated water molecule increases from 6 to 9. This trend is consistent with the experimentally observed phenomena. In addition, the contribution of the electric quadrupole transition is also evaluated in the same manner to the La case.

As a result, the quadrupole contribution is found to be significantly larger than the electric dipole transition, but is constant among the Ho aqueous complex models. This means the pre-edge peak area can be still an indicator of the local environment of Ho atom.

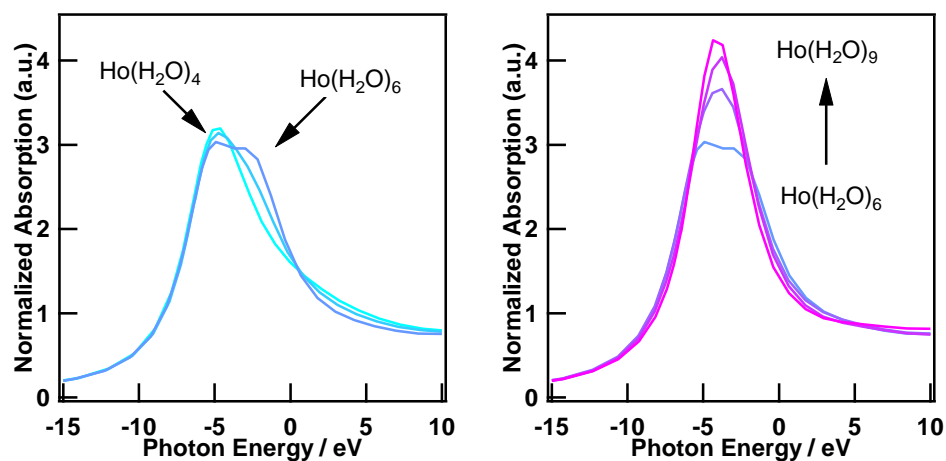
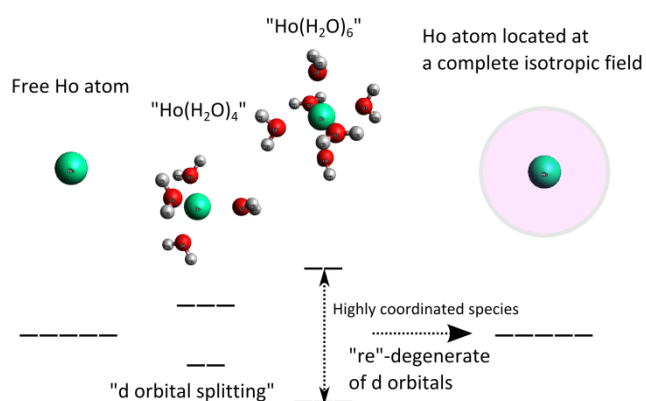


Figure 11. Simulated Ho L_3 -edge XANES spectra of virtual Ho aqueous complexes, $\text{Ho}(\text{H}_2\text{O})_n$ (left: $n = 4 - 6$; right: $n = 6 - 9$).

Figure 11 shows simulated Ho L_3 -edge XANES spectra of the virtual Ho aqueous complexes, $\text{Ho}(\text{H}_2\text{O})_n$ (left: $n = 4 - 6$; right: $n = 6 - 9$). As expected, $\text{Ho}(\text{H}_2\text{O})_4$ exhibits one asymmetric white line at the Ho L_3 -edge XANES spectrum and the width of white line increases as the number of coordinated O atoms increases to 6. In contrast, as the hydration water increases from 6 to 9, the fwhm of white line at the Ho L_3 -edge XANES gets narrower (Figure 11, right). This is also consistent with the experimental results.

Scheme 1. Schematic view of d orbital splitting dependency on the number of coordinated atoms to Ho.



This phenomenon can be simply interpreted into “re”-degeneracy of d orbital of Ho caused by averaging the potential field Ho feels by a number of adjacent ligand atoms because the Ho L₃-edge absorption derives from 2p_{3/2} to 5d electric dipole transition. All the five 5d orbitals of an atomic Ho atom (*i.e.* Ho gas) are degenerate in principle. If the Ho atom was located at a potential field generated by four atoms tetrahedrally coordinated to the Ho atom, the d orbitals are split into two degenerate e state and three degenerate t₂ state. When another 2 other ligands are coordinated to the Ho atom and forms regular octahedral environment, the d orbitals are a bit widely split into three degenerate t_{2g} state and two degenerate e_g state. However, if the coordinated atoms were more than 6, the d orbital splitting should be very complicated. One simple model can be the Ho atom located at the center of a complete sphere of enormous number of atoms or electrons (Scheme 1). Then, the potential field the Ho atom feels should be a similar one in the gas phase, and all five d orbitals are degenerate because all the potential fields of the surrounding atoms annihilate the others’ and the Ho atom feels a completely isotropic potential field.

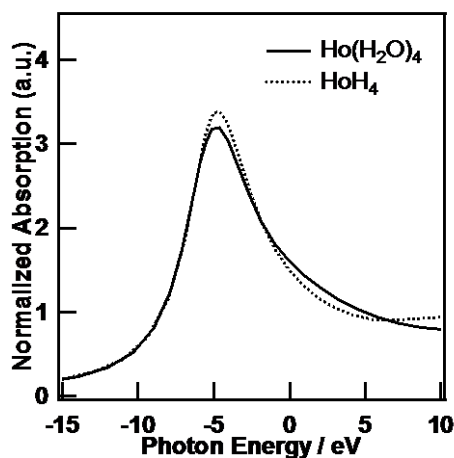


Figure 12. Simulated Ho L₃-edge XANES spectra of virtual Ho complexes, HoH₄ as a free Ho atom analog and Ho(H₂O)₄.

The Ho L₃-edge XANES spectrum of an atomic Ho was also calculated with a HoH₄ model (Figure 12). Because the XANES simulation of FEFF code is based on multiple scattering theory, a Ho atom only model cannot be processed. In addition, the contribution of H atoms to the XANES spectrum is negligible. Indeed, the Ho L₃-edge XANES spectrum of a HoH₄ model exhibits a narrower white line than that of the Ho(H₂O)₄ model, which proved the hypothesis illustrated in

Scheme 1.

Conclusion

A systematic survey of Ho, Er, or Yb L₁ and L₃-edge XANES spectra of their complex oxides and theoretical calculation of the L₁ and L₃-edge XANES spectra of virtual Ho aqueous complexes gave the following two insights. One is that the intensity of the pre-edge peak at the Ho, Er, or Yb L₁-edge XANES spectra and the width of white line at the L₃-edge XANES spectra can be an indicator of the local configuration of the target atom such as distortion or coordination number of the local environment. The other is the decrease of the fwhm of white line at the L₃-edge caused by the increase of the coordination number of lanthanide from 6 to more can be explained by the re-degeneracy of d orbitals by averaging of a potential field a lanthanide atom feels. Application of the lanthanide XANES spectroscopy to practical material may be not easy because the change of the Ln L-edge XANES spectra depending on the small difference of local environment is quite subtle. However, the present result indicates a new approach to structural study of local configuration of the lanthanide compounds.

References

- (1) Hayashi, H.; Kawata, M.; Sato, A.; Udagawa, Y.; Inami, T.; Ishii, K.; Ogasawara, H.; Nanao, S., *Phys. Rev. B*, **2005**, 72, 045114.
- (2) Wang, Y. K.; Hsu, L. S.; Lan, M. D., *J. Alloy. Compd.*, **2005**, 389, 1-4.
- (3) Loeffen, P. W.; Pettifer, R. F.; Müllender, S.; van Veenendaal, M. A.; Röhlér, J.; Sivia, D. S., *Phys. Rev. B*, **1996**, 54, 14877-14880.
- (4) Etalaniemi, V.; Hamalainen, K.; Manninen, S.; Suortti, P., *J. Phys: Cond. Matter*, **1992**, 4, 879.
- (5) Lytle, F. W.; van der Laan, G.; Greegor, R. B.; Larson, E. M.; Violet, C. E.; Wong, J., *Phys. Rev. B*, **1990**, 41, 8955-8963.
- (6) Mao, Y.; Bargar, J.; Toney, M.; Chang, J. P., *J. Appl. Phys.*, **2008**, 103, 094316.
- (7) Yamamoto, K.; Kojima, K.; Handa, K.; Wada, N.; Ozutsumi, K., *Nippon Seramikkusu Kyokai gakujutsu ronbunshi*, **2004**, 112, 245-251.
- (8) Mignotte, C., *Appl. Surf. Sci.*, **2004**, 226, 355-370.
- (9) Mignotte, C., *Nucl. Instrum. Methods Phys. Res., Sect. B*, **2002**, 187, 95-110.
- (10) Ishii, M.; Tanaka, Y.; Komuro, S.; Morikawa, T.; Aoyagi, Y.; Ishikawa, T., *J. Electron. Spectrosc. Relat. Phenom.*, **2001**, 114-116, 521-525.

- (11) Ishii, M.; Tanaka, Y.; Komuro, S.; Morikawa, T.; Aoyagi, Y.; Ishikawa, T., *J. Synchrotron Rad.*, **2001**, *8*, 372-374.
- (12) Ishii, M.; Tanaka, Y.; Ishikawa, T.; Komuro, S.; Morikawa, T.; Aoyagi, Y., *Appl. Phys. Lett.*, **2001**, *78*, 183-185.
- (13) Ishii, M.; Komuro, S.; Morikawa, T.; Aoyagi, Y.; Oyanagi, H.; Ishikawa, T.; Ueki, T., *J. Synchrotron Rad.*, **1999**, *6*, 477-479.
- (14) Ishii, M.; Komuro, S.; Morikawa, T.; Aoyagi, Y.; Ishikawa, T.; Ueki, T., *Jpn. J. Appl. Phys.*, **1999**, *38*, 191.
- (15) Quartieri, S.; Chaboy, J.; Antonioli, G.; Geiger, C. A., *Phys Chem Min*, **1999**, *27*, 88-94.
- (16) Yamamoto, T.; Tanaka, T.; Matsuyama, T.; Funabiki, T.; Yoshida, S., *Solid State Commun.*, **1999**, *111*, 137-142.
- (17) Baba, T.; Hikita, S.; Koide, R.; Ono, Y.; Hanada, T.; Tanaka, T.; Yoshida, S., *J. Chem. Soc. Faraday Trans.*, **1993**, *89*, 3177-3180.
- (18) Tanaka, T.; Hanada, T.; Yoshida, S.; Baba, T.; Ono, Y., *Jpn. J. Appl. Phys.*, **1993**, *32*, 481.
- (19) Tabuchi, M.; Asakura, H.; Takao, N.; Morimoto, H.; Watanabe, N.; Baba, Y.; Takeda, Y., *in preparation*.
- (20) Ravel, B.; Newville, M., *J. Synchrotron Rad.*, **2005**, *12*, 537-541.
- (21) Tso Yee, F.; Huber, G.; Byer, R. L.; Mitzscherlich, P., *IEEE J. Quant. Electron.*, **1988**, *24*, 924-933.
- (22) Yamazoe, S.; Hitomi, Y.; Shishido, T.; Tanaka, T., *J. Phys. Chem. C*, **2008**, *112*, 6869-6879.
- (23) Rehr, J. J.; Kas, J. J.; Vila, F. D.; Prange, M. P.; Jorissen, K., *Physical Chemistry Chemical Physics*, **2010**, *12*, 5503-5513.

Chapter 5

In Situ Time-Resolved DXAFS Study of Rh Nanoparticle Formation Mechanism in Ethylene Glycol at Elevated Temperature

Abstract

A combination of *in situ* time-resolved dispersive XAFS and ICP-MS techniques reveals that the formation process of Rh nanoparticles (NPs) from rhodium trichloride trihydrate ($\text{RhCl}_3 \cdot 3\text{H}_2\text{O}$) in ethylene glycol with polyvinylpyrrolidone (PVP) at elevated temperature is a first-order reaction, which indicates that uniform size Rh NPs appear consecutively and these Rh NPs do not aggregate with each other.

Introduction

Metal nanoparticles (NPs) are getting much more attention than ever in both fields of fundamental science and engineering. Metal NPs have several unique properties or applications, such as surface plasmon resonance,¹ magnetism,^{2,3} imaging,⁴ or catalysis.⁵ For example, metal NPs have several catalytic activities, such as hydrogenation by Rh NPs,⁶⁻⁸ and C–C coupling reaction by Pd NPs.^{9,10} These days, various scientists' efforts have enabled us to control NP size and/or shape. Their formation mechanisms are also vigorously investigated, but still under discussion. To the best of the author's knowledge, there are two common formation mechanisms of NPs proposed by LaMer¹¹ and Finke.^{12,13} LaMer *et al.* studied the formation mechanism of sulphur sol and proposed that the sol is formed by simultaneous nucleation from a supersaturated solution of monomer and its growth is by attachment of monomers to the resulting nuclei. On the other hand, Finke *et al.* have studied the formation kinetics and mechanism of iridium NPs from iridium precursors by H₂ reduction. They proposed a different mechanism from LaMer's in that the nuclei are formed slowly but constantly and the NPs grow mainly by autocatalytic reduction of metal precursors on the particle surface, which can be called a two-step mechanism¹² or a four step mechanism for transition metal NP formation and agglomeration.¹³ The Finke–Watzky two-step mechanism of Ir nanoparticle preparation with hydrogen can be summarized with the equation below.

$$[A]_t = \left(\frac{k_a}{k_b} + [A]_0 \right) / \left(1 + \left(\frac{k_a}{k_b} [A]_0 \right) \exp(k_a + k_b [A]_0 t) \right)$$

where k_a and k_b are the average rate constants for nucleation and autocatalytic growth, respectively. $[A]_t$ and $[A]_0$ are the concentrations of nanocluster precursor A at reaction time of t and 0, respectively.¹²

X-ray absorption near-edge structure (XANES) and extended X-ray absorption fine structure (EXAFS) spectroscopy was regarded as a potentially powerful method for directly observing the nucleation process of nanoparticles.¹⁴ Indeed, several research groups have recently applied X-ray absorption fine structure (XAFS) measurements to investigate the formation mechanism of NPs. For example, Harada *et al.* has investigated Pt,¹⁵ Rh,^{16,17} Pd,¹⁷ Ag,¹⁸ and Au¹⁹ metal NP formation by photoreduction in polymer solutions and confirmed the two step mechanism proposed by Finke *et al.*

Nishimura *et al.* studied the formation mechanism of Cu NPs in aqueous PVP solution with NaBH₄ reduction at ambient conditions by means of *in situ* quick XAFS technique (QXAFS) in fluorescence mode and found that stable intermediates such as Cu(OH)₂ and Cu⁺-PVP were formed during an induction period of nucleation of Cu NPs.²⁰ Teramura and Ohyama *et al.* have investigated the photodeposition process of Rh cations on a TiO₂ photocatalyst by means of *in situ* dispersive XAFS (DXAFS) technique and proposed consecutive deposition of Rh NPs,^{21, 22} and the nucleation and growth process of Au nanoparticles by means of the newly developed *in situ* fast QXAFS technique and found a four atom Au cluster during the induction period.^{23, 24}

In this study, *in situ* time-resolved XAFS technique was employed in order to understand the formation mechanism of Rh NPs in ethylene glycol (EG) at elevated temperature.²⁵⁻²⁸ Interestingly, the Rh NP growth does not seem to occur during NP formation and Finke's two-step mechanism in the case of photoreduction condition could satisfactorily address all the experimental observations and a distinct scenario could be envisaged for Rh NP formation in EG at elevated temperatures.

Experimental Section

Materials and General Procedures of Rh NP Preparation

RhCl₃·3H₂O (Wako, Japan), polyvinylpyrrolidone (PVP) (Mw = 40000, Yili Chemical, China), and ethylene glycol (EG) (Wako, Japan) were purchased and used without further purification. Rh NPs were prepared as follows. RhCl₃·3H₂O and PVP are dissolved into appropriate amount of EG with sonication and are poured into a tube reactor equipped with Dimroth condenser. The concentration of Rh is 0.02 mol/L and the Rh/PVP ratios are 1/15, 1/30 or 2/15 (Rh: 0.04 mol/L). Reaction conditions are summarized in Table 1.

Table 1. Summary of experimental conditions

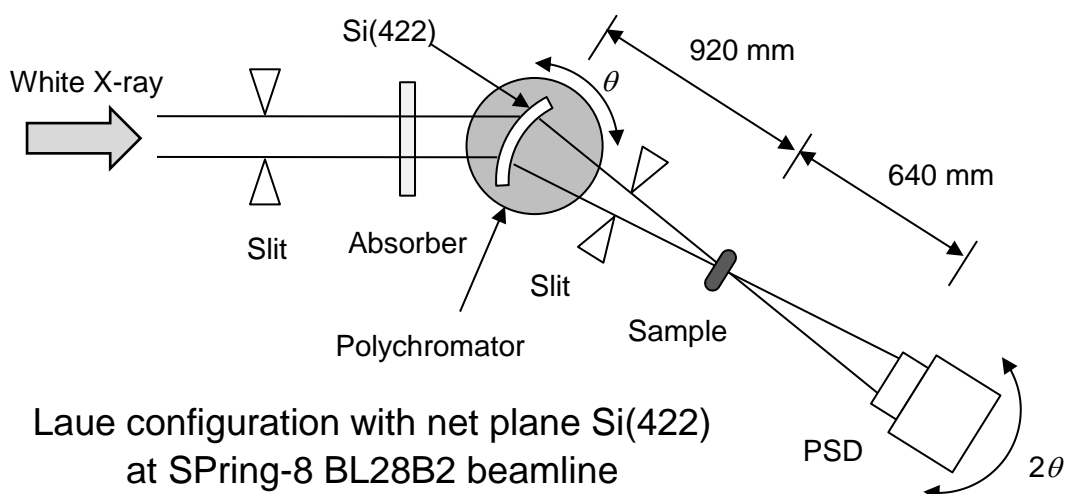
Run	[Rh] mol/L	[PVP] mol/L	Temperature ^a /°C
A	0.02	0.30	135
B	0.02	0.30	100
C	0.02	0.60	125
D	0.04	0.30	125

^a Temperature was measured by thermocouple immersed into the reaction mixture.

In situ Rh K-edge Dispersive XAFS Measurement and Data Reduction

In situ time-resolved Rh K-edge XAFS spectra were recorded at the BL28B2 beamline of the SPring-8 (Ako, Japan). The DXAFS measurement system consists of a polychromator set to a Laue configuration with a Si(422) net plane and a position sensitive detector (PSD) mounted on a θ - 2θ diffractometer (Scheme 1).

Scheme 1. Main equipment of the DXAFS spectroscopy system at the BL28B2 beamline, SPring-8



The size of an X-ray focal spot on the sample is 0.16 mm in width and 2.4 mm in height and the distance between the polychromator and the sample, and the sample and PSD are 920 mm and 640 mm, respectively. The total energy bandwidth is 22950–24010 eV. The X-ray energy was calibrated by the spectrum of a Rh foil. The oil bath filled with silicon oil was placed on a movable stage. A side-arm Pyrex reactor equipped with Dimroth condenser and thermocouple was fixed with a clamp and immersed into the reaction solution at around the X-ray focal spot. In the beginning of the DXAFS measurement, the oil bath was automatically moved up to heat the tube reactor, thus there are some delays between the starting time of DXAFS measurements and that of solution heating. The exposure time of the PSD depends on the contents of the reaction mixture because the X-ray transparency of each reaction mixture is different. Usually, one hundred shots were accumulated for

spectral quality. Data reduction of the XAFS spectra was performed through a previously described²¹ procedure by REX2000²⁹ (Rigaku, Japan). The k^3 -weighted EXAFS oscillation in the range of 2.8–11 Å⁻¹ was Fourier transformed. Linear combination fitting (LCF) of a series of XANES spectra was performed with Athena included in IFEFFIT package.³⁰ In the LCF procedure, the absorption edges (E_0) of the reference spectra were fixed and the sum of the weights of the reference spectra was also fixed to 1 and each weight was between 0 and 1. Fitting was performed in a range of photon energies between –30 eV to 50 eV from E_0 as a base position in all cases.

ICP-MS

The EG solution containing both Rh NPs and Rh³⁺ were first treated with ultrafiltration in special tubes (Amicon Ultra 0.5 ml Ultracel 3 k) over a centrifuge operating at 12000 rpm for 0.5 h. The filtrate was diluted, digested by 10% HNO₃ and finally was diluted again to match an acid concentration of about 1%. An Agilent 7500ce ICP-MS, interfaced to a CETAC CEI-100 microconcentric nebulizer, was used to determine the Rh content in the aqueous phase. Instrument control as well as data analysis was carried out using ChemStation B.03.03 software. The nebulizer was operated in self-aspiration mode with the sheath liquid (50 mM formic acid, 20 ppb Ge) closing the electrical circuit. Analyses were only started when a sufficiently stable signal (RSD 72Ge < 5%) was obtained. An ICP-MS tuning solution containing lithium, yttrium, cerium, thallium, and cobalt in 2% HNO₃ (each 10 mg/L, Agilent Technologies) was used for calibration.

TEM observation

The high resolution transmission electronic microscope (HR-TEM) images were taken with a Tecnai F20 microscopy operating under 200 kV accelerating voltage and JEOL JEM-2100F operating at an accelerating voltage of 200 kV. The samples were prepared as follows. Rh nanoparticles were precipitated from the EG solution after addition of 4 quantities of acetone (v/v), then separated by centrifugation (10 000 rpm for 5 min). Finally, the precipitate was re-dispersed in an appropriate amount of methanol (0.08 mol/L) under ultrasonication. One drop of the above solution containing Rh nanoparticles was deposited on carbon-coated copper grids and dried at room temperature *in vacuo*.

Results and discussion

TEM observation

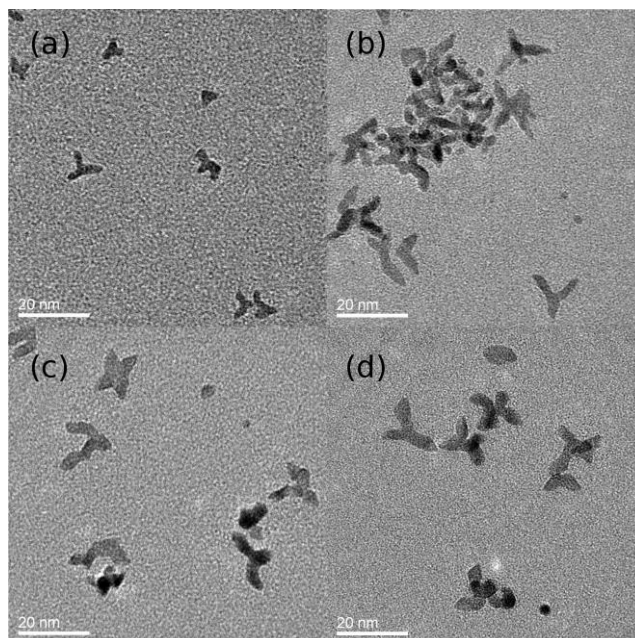


Figure 1. TEM images of Rh NPs in the condition of $\text{RhCl}_3 \cdot 3\text{H}_2\text{O} = 0.02 \text{ mol/L}$, $\text{Rh/PVP} = 1/15$, 403 K after the reaction for (a) 5 min, (b) 10 min, (c) 30 min, (d) 120 min

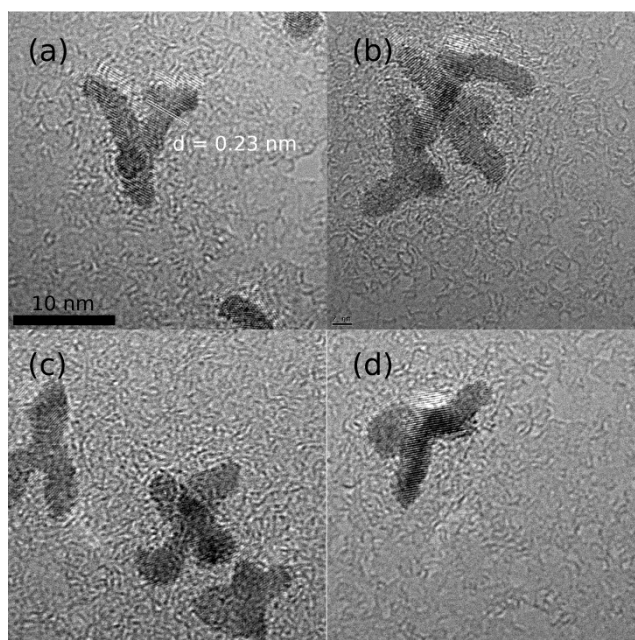


Figure 2. TEM images of Rh NPs in the condition of $\text{RhCl}_3 \cdot 3\text{H}_2\text{O} = 0.02 \text{ mol/L}$, $\text{Rh/PVP} = 1/15$, 373 K after the reaction for (a) 25 min, (b) 35 min, (c) 65 min, (d) 85 min

Figure 1 shows TEM images of Rh NP samples obtained during the Rh NP formation reaction of 0.02 mol/L $\text{RhCl}_3 \cdot 3\text{H}_2\text{O}$ and PVP/EG solution ($\text{Rh/PVP} = 1/15$) at 403 K after reaction for 5, 10, 30, and 120 min. All Rh NPs were observed as multipod-type NPs and their average width of branch is ca. 3 nm and the average length of the particles is ca. 12 nm. However, at the very beginning, the elongation of the branch is observed in Figure 1(a) and (b). It may be because of the aggregation of the small Rh units to the multipod NPs, but there is no evidence in the present study.

Figure 2 shows TEM images of Rh NP samples obtained during the Rh NP formation reaction of a 0.02 mol/L $\text{RhCl}_3 \cdot 3\text{H}_2\text{O}$ and PVP/EG solution ($\text{Rh/PVP} = 1/15$) at 373 K (*e.g.* run B) after the reaction for 25, 35, 65, and 85 min. All Rh NPs were observed as multipod-type NPs and their average particle size is as same as run A. These results indicate that the Rh NP size did not grow under these reaction conditions once formed.

Rh K-edge in situ dispersive XAFS measurement

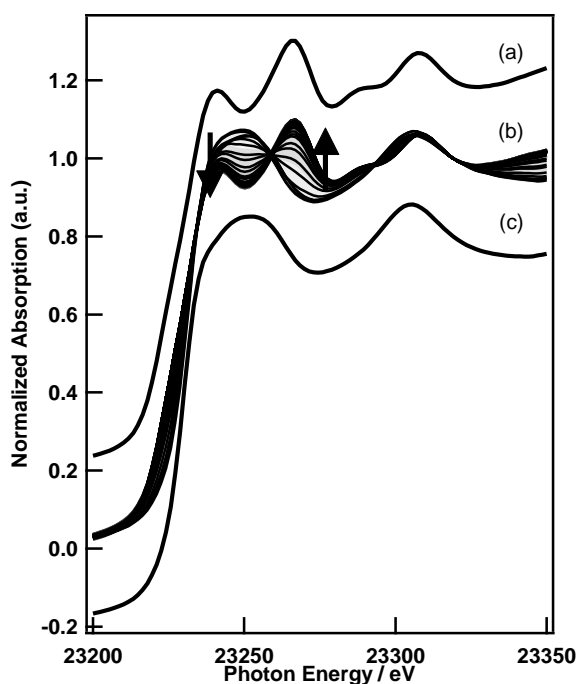


Figure 3. Rh K-edge XANES spectra (a) Rh foil, (b) a series of Rh K-edge XANES spectra of reaction solution containing $\text{RhCl}_3 \cdot 3\text{H}_2\text{O}$ at 408 K for 1 h, and PVP in EG (Run A), (c) $\text{RhCl}_3 \cdot 3\text{H}_2\text{O}$. (Arrows indicate spectral change for 1 hour)

Figure 3 shows a series of Rh K-edge XANES spectra of the reaction mixture of $\text{RhCl}_3 \cdot 3\text{H}_2\text{O}$

and PVP EG solution (Rh/PVP = 1/15) (run A) and the reference spectra of $\text{RhCl}_3 \cdot 3\text{H}_2\text{O}$ (solid) and Rh foil. The exposure time of the X-ray on the reaction mixture is 66 msec and good quality XAFS spectra were obtained by accumulating the spectra in every 6.6 sec to form a series of spectra. The XANES spectrum of the initial state is similar to that of the $\text{RhCl}_3 \cdot 3\text{H}_2\text{O}$. The shift of X-ray absorption edge energy (E_0) from 23229 eV to 23224 eV indicates a reduction of Rh^{3+} cation to Rh^0 species during the polyol process. The XANES spectra after 15 min thermal reduction were similar to that of the Rh foil as presented in Figure 3(a). The XANES spectra gradually changed from that of the Rh^{3+} cation to that of the Rh^0 metal with an isosbestic point at around 23259 eV. Thus, the Rh^{3+} ions are reduced to Rh^0 during the polyol process without any intermediates on this timescale.

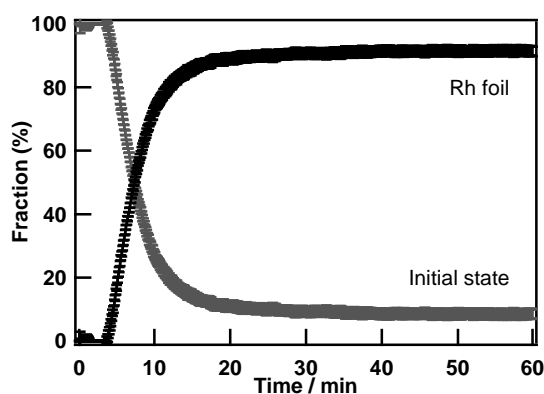


Figure 4. Time course of two fractions of a series of XANES spectra during polyol process at 408 K for 1 h (Run A). XANES spectra of initial state (gray cross) and Rh foil (black circle) were used for standard spectra of linear combination fitting.

All Rh K-edge XANES spectra were reproduced with the linear combination fitting of XANES spectra of the initial state (Rh^{3+} ; before heating) and Rh foil. Figure 4 shows the time course of the fractions of initial state of Rh^{3+} precursor and Rh foil, respectively. The exponential decay of the fraction of Rh^{3+} indicated that the Rh NP formation process depends with pseudo-first order kinetics on Rh^{3+} concentration. It is noteworthy that the final XANES spectrum is seen to consist of ca. 90% of Rh foil and ca. 10% Rh^{3+} because the XANES spectrum of NPs is usually different from that of bulk state.²⁴

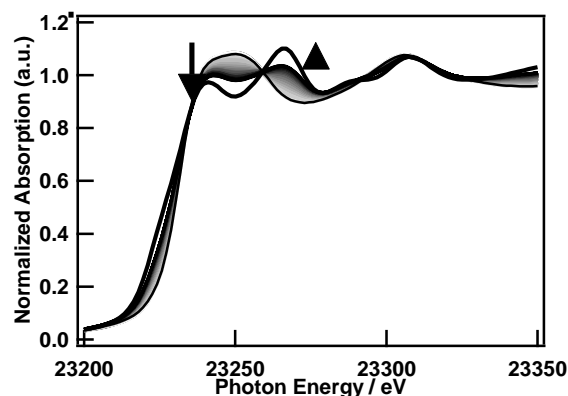


Figure 5. A series of Rh K-edge XANES spectra of reaction solution containing $\text{RhCl}_3 \cdot 3\text{H}_2\text{O}$, and PVP in EG at 373 K for 1 h. (Run B; Arrows indicates spectral change for 1 hour) (Thick black line: Rh foil)

Figure 5 shows a series of Rh K-edge XANES spectra of the reaction mixture during the Rh NPs preparation from $\text{RhCl}_3 \cdot 3\text{H}_2\text{O}$ with PVP in EG ($\text{Rh}/\text{PVP} = 1/15$) at 373 K for 1 h (run B). In this case, the XANES spectra also gradually changed from that of the Rh^{3+} cation to that of the Rh^0 metal with the isosbestic point at around 23259 eV, but the final XANES spectrum is not identical to that of Rh foil because the reduction of Rh^{3+} did not complete.

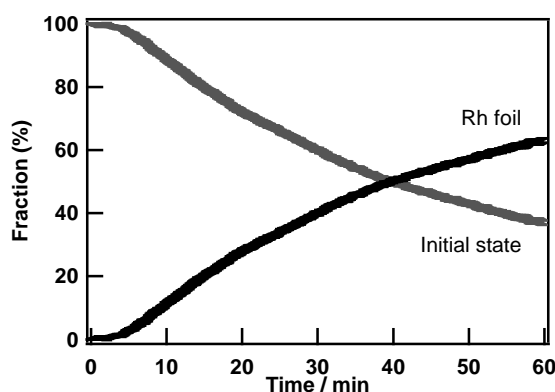


Figure 6. Time course of two fractions of a series of XANES spectra during polyol process at 373 K for 1 h (Run B). XANES spectra of initial state (gray cross) and Rh metal (black circle) were used for standard spectra of linear combination fitting.

To determine the progress rate of Rh NP formation, these spectra were analyzed by linear combination fitting of initial state and Rh metal again (Figure 6). The Rh^{3+} consumption rate looks like pseudo-first order kinetics just as at 408 K, but the Finke–Watzky mechanism is also possible.

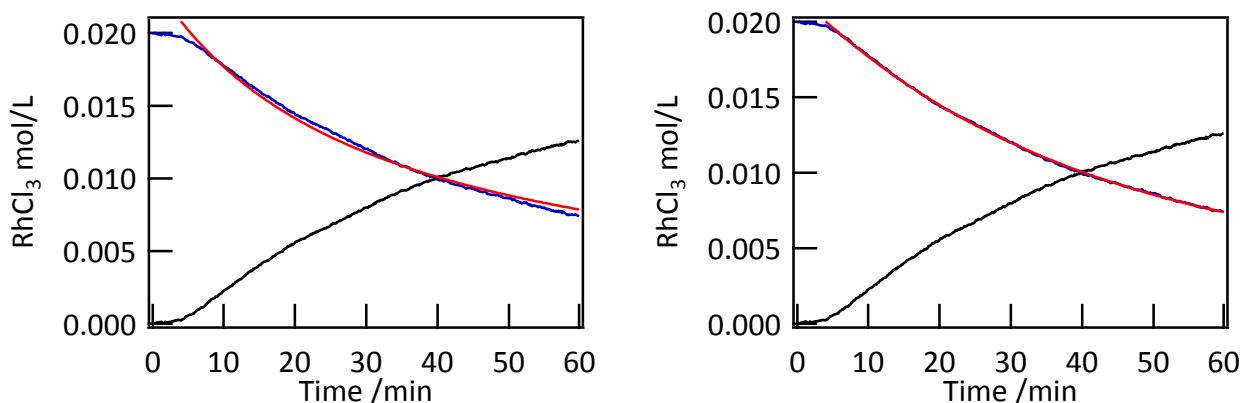


Figure 7. Fitting result of the consumption curve of Rh^{3+} with Finke's two step mechanism (left) and simple exponential curve (right).

Thus, we attempted to fit the decay of the initial state fraction with eq. (1) and simple exponential curve based on the pseudo-first order kinetics. The fitting precision with exponential curve is higher (Figure 7) than that with eq. (1) since eq. (1) is based on the assumption that the rate of the nucleation and the autocatalytic growth is similar to each other. The stable trend of the first few minutes is not well matched with the model of eq. (1) because the temperature rapidly increased in this term. In the present system, the autocatalytic step is much faster than the nucleation step. Thus, the pseudo-first order kinetics is a much better hypothesis for the present reaction.

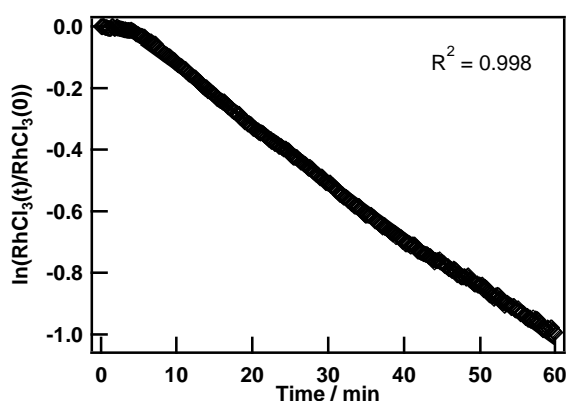


Figure 8. Time course of $\ln([\text{Rh}^{3+}(t)]/[\text{Rh}^{3+}(0)])$ derived from linear combination fitting of XANES (Run B)

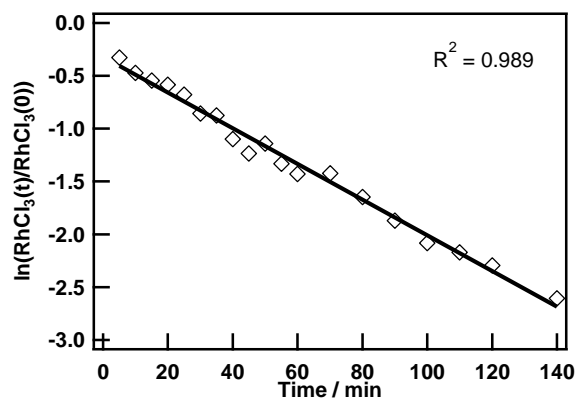


Figure 9. Time course of $\ln([\text{Rh}^{3+}(t)]/[\text{Rh}^{3+}(0)])$ derived from $[\text{Rh}^{3+}(t)]$ evaluated by ultrafiltration and ICP-MS

Figure 8 shows the time course of the value of $\ln([\text{Rh}^{3+}(t)]/[\text{Rh}^{3+}(0)])$ against reaction time, which exhibits a clear linear relationship and the slope is 0.0179 min^{-1} . The Rh^{3+} consumption rate was also evaluated by means of ultrafiltration and ICP-MS technique under the same condition. Figure 8 shows the time course of the value of $\ln([\text{Rh}^{3+}(t)]/[\text{Rh}^{3+}(0)])$ evaluated by ICP-MS. The value of $\ln([\text{Rh}^{3+}(t)]/[\text{Rh}^{3+}(0)])$ clearly depends on reaction time in a linear manner and the slope is 0.0169 min^{-1} . Thus, the Rh^{3+} consumption rate is consistent with the *in situ* DXAFS results and obeys (pseudo) first order kinetics. As mentioned above, the essence of the Finke–Watzky mechanism¹² is that the precursor is consumed by two elementary steps, which are the direct reduction of precursor over reductant and catalytic reduction of precursor over the surface atoms on NPs, and in the same process, new metal–metal bond forms.

Under these scenarios, the rate law of Rh^{3+} is expressed as

$$r = k_{\text{obs}}[\text{Rh}^{3+}]^x = k_1[\text{Rh}^{3+}] + k_2[\text{Rh}^{3+}][\text{Rh}^0]$$

After derivation, it can be found that the apparent reaction order “x” could not be 1 (which is the fitting results of the DXAFS and ICP-MS data) unless $[\text{Rh}^0]=\text{constant}$ (which is clearly against reality) or $k_1 \gg k_2[\text{Rh}^0]$ (which means the second step is negligible). Therefore, the dominant pathway of Rh^{3+} reduction in our system appears to be the direct reaction between Rh^{3+} and ethylene glycol. Next, we carried out *in situ* DXAFS experiments in the condition of $\text{Rh}/\text{PVP} = 1/30$ (run C), $2/15$ (run D) at 398 K to investigate the effect of the Rh^{3+} or PVP concentration. In run C or D, the overall change of XAFS spectra during Rh NP formation is similar to that of run A.

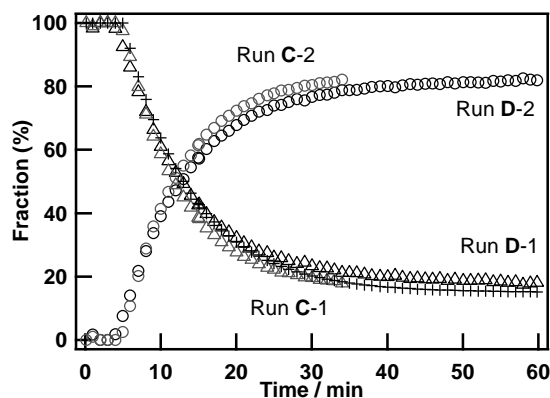


Figure 10. Change of two fractions of a series of XANES spectra during polyol process at 393 K for 1 h. (Rh/PVP = 1/30 (Run C), Rh/PVP = 2/15 (Run D)) XANES spectra of initial state (“1”, triangle) and Rh foil (“2”, circle) were used for standard spectra of linear combination fitting. Cross plots are calculated Rh^{3+} consumption at 398 K.

First, we calculate the apparent kinetic constant k_{obs} of run A in the same manner as Figure 7 and it was found to be 0.0219 min^{-1} . From the Arrhenius plot of the kinetic constants of run A and run B, the kinetic constant at 398 K was estimated to be 0.0112 min^{-1} and the activation energy of the reduction step of Rh^{3+} is estimated to be 90.6 kJ/mol. The results of linear combination analysis of the XANES spectra of run C and D are shown in Figure 10. In Run C, the concentration of PVP is fourfold denser than that in run D. However, the fraction changes are almost identical to each other. This indicates PVP concentration has no effect on the Rh NP formation process and may only affect the final size of Rh NPs. Cross plots are used to calculate Rh^{3+} consumption at 398 K (“run E”) using the kinetic constant above and on the assumption that the final XANES spectrum is similar to those in run C and D. The Rh^{3+} consumption rates in run C, D and the calculated “run E” are also identical to each other. This result is consistent with the fact that the Rh NPs formation rate depends on the concentration of Rh^{3+} in first order kinetics as discussed above.

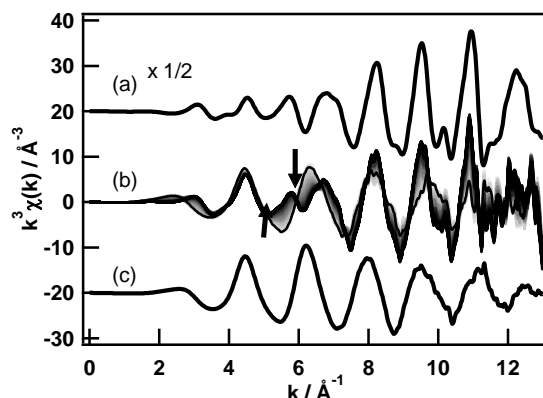


Figure 11. Rh K-edge EXAFS spectra (a) Rh foil ($\times 1/2$), (b) a series of Rh K-edge EXAFS spectra of reaction solution containing $\text{RhCl}_3 \cdot 3\text{H}_2\text{O}$ at 373 K for 1 h, and PVP in EG (run B), (c) $\text{RhCl}_3 \cdot 3\text{H}_2\text{O}$. (Arrows indicate spectral change for 1 h).

Figure 11 shows a series of Rh K-edge EXAFS oscillations (run B) and reference spectra of $\text{RhCl}_3 \cdot 3\text{H}_2\text{O}$ and Rh foil. The EXAFS oscillation of Rh foil is divided in half for clarity. It is clearly observed that the $\text{RhCl}_3 \cdot 3\text{H}_2\text{O}$ contribution to the obtained EXAFS oscillation gradually decreased and the Rh metal contribution increased through a single isosbestic point, just as in their XANES spectra.

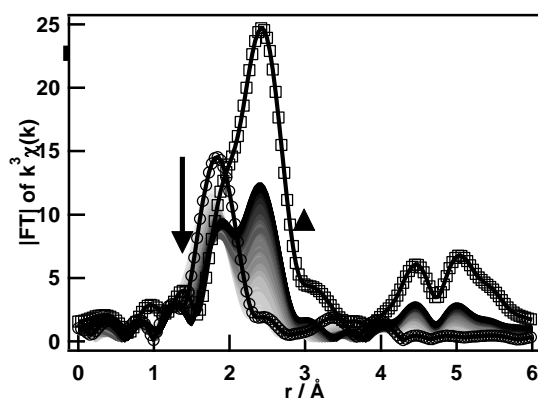


Figure 12. A series of Fourier transformed spectra of k^3 -weighted Rh K-edge EXAFS of reaction solution containing $\text{RhCl}_3 \cdot 3\text{H}_2\text{O}$ at 373 K for 1 h, and PVP in EG (run B; circle: $\text{RhCl}_3 \cdot 3\text{H}_2\text{O}$; square: Rh foil) (phase correction has not been performed).

Figure 12 shows a series of Fourier transformed Rh K-edge EXAFS spectra (run B), which are not phase corrected and hence the atomic distance (x axis) does not indicate the actual bond length. The peak located at 1.80 Å is assignable to the convolution of Rh–Cl scattering of RhCl_3 and Rh–O

scattering of Rh ions coordinated to the oxygen of EG. The height of the peak at 1.80 Å decreased as reaction time advances, and an alternative peak appeared at 2.42 Å, which is assigned to the Rh–Rh scattering of Rh NPs generated during the polyol process, in comparison to the Fourier transformed EXAFS spectrum of the Rh foil as a reference. The peak height at 2.42 Å rose during the reaction, but the growth of the peak is not saturated because the reduction of Rh precursor was not completed, as shown in Figure 5 and 6.

Table 2. Structural parameters obtained from the curve fitting analysis of the initial and final EXAFS spectra (Rh/PVP = 1/15, 408 K, 1 h, run A)^a

Ab–Sc ^b	CN ^c	r ^d /Å	DW ^e /Å ⁻²	R ^f
Initial				
Rh–Cl	3.4	2.31	0.0031	0.00221
Rh–O	1.9	2.06	0.0028	
Final				
Rh–Rh	10.2	2.68	0.0047	0.00126

^a For the initial spectrum: $\Delta k = 2.8\text{--}11 \text{ \AA}^{-1}$, $\Delta R = 0.9\text{--}2.3 \text{ \AA}$; the curve fitting procedure is performed by REX2000 with backscattering factor and phase shift parameters obtained from $\text{RhCl}_3 \cdot 3\text{H}_2\text{O}$ and Rh_2O_3 standard samples. Other conditions are the same as the final spectrum described below. For final spectrum: $\Delta k = 2.8\text{--}11 \text{ \AA}^{-1}$, $\Delta R = 1.7\text{--}2.9 \text{ \AA}$; the curve fitting procedure is performed by Artemis with back scattering and phase shift parameters calculated by FEFF ver. 8.40, and fell within the Nyquist criteria. Curve fitting was done in R space. R factor is defined as

$$R = \sum_i^{N_{\text{pts}}} \frac{[\text{Im}((\chi_{\text{dat}}(R_i) - \chi_{\text{th}}(R_i)))]^2 + [\text{Re}((\chi_{\text{dat}}(R_i) - \chi_{\text{th}}(R_i)))]^2}{[\text{Im}(\chi_{\text{dat}}(R_i))]^2 + [\text{Re}(\chi_{\text{dat}}(R_i))]^2}$$

where $i = 1, 2, \dots, N_{\text{pts}}$, N_{pts} : number of data points, χ_{dat} : EXAFS oscillation of experimental data, χ_{th} : EXAFS oscillation of theoretical data. ^b X-ray absorbing and scattering atoms. ^c Coordination number. ^d Atomic distance. ^e XAFS Debye–Waller factor. ^f R factor.

To evaluate the structural parameters of the Rh precursor at the initial state and the Rh NPs at the saturated final state, curve fitting analyses on the initial and final EXAFS spectra of run A and

their results are summarized in Table 2. For the initial spectrum, the coordination numbers of the Rh–Cl and Rh–O shells are estimated to be 3.4 and 1.9, respectively. These parameters indicate that the structure of the initial Rh precursor can be expressed as $\text{RhCl}_3(\text{EG}^2)$ or $\text{RhCl}_3(\text{PVP})(\text{EG}^1)$ where, EG^1 means the coordination of one oxygen of two hydroxyl groups of ethylene glycol, EG^2 means the coordination of two O atoms of two hydroxyl groups of ethylene glycol and PVP means the coordination of one O atom of pyrrolidone moiety. However, in general, an EXAFS spectrum reflects an averaged coordination environment of Rh species. Moreover, it is known that an aqueous solution of rhodium chloride consists of several Rh species which can be expressed as $\text{Rh}(\text{H}_2\text{O})_n\text{Cl}_{(6-n)}$ ($n = 1, 2, \dots, 6$) by means of a ^{103}Rh NMR study.³¹ Thus, the structure of the initial Rh species is still unclear. However, for the final spectrum, the Rh–Rh atomic distance of the Rh NPs is 2.68 Å, which is slightly shorter than 2.70 Å of the Rh foil model structure input into the FEFF program for parameter calculation, indicating the smallness of the obtained Rh NPs. The coordination number, 10.2, also indicates small Rh NPs. If the shape of the Rh NPs is spherical, CN 10.2 is assignable to a particle size of ca. 3.0 nm.

It is difficult to associate the obtained EXAFS spectra directly with the obtained Rh NPs because the shape of the Rh NPs is of a multipod-type. From the HRTEM image of typical Rh NPs (Figure 13), the multipod-type NPs can be imagined to be aggregated material of spherical NPs (average particle size: ca. 3 nm). It may indicate that curve fitting results of the EXAFS spectra are consistent with the obtained Rh NP shape.

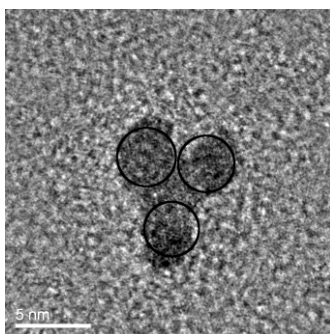


Figure 13. HRTEM image of Rh NPs in the condition of $\text{RhCl}_3 \cdot 3\text{H}_2\text{O} = 0.02$ mol/L, $\text{Rh}/\text{PVP} = 1/15$, 403 K after the reaction for 120 min

In order to verify the hypothesis that uniform size Rh NPs are generated consecutively, we utilized the EXAFS spectra. EXAFS spectra obtained in transmission mode reflects the averaged

state of the target element. In this case, each EXAFS spectrum is a combination of Rh^{3+} and Rh metallic species. The aforementioned ICP-MS study revealed the time course of the concentration of Rh^{3+} species. Thus, the EXAFS spectrum originated from Rh NPs can be calculated by subtracting the Rh^{3+} contribution from each EXAFS spectrum. As shown in Figure 8, the reduction of Rh^{3+} started at 2 min ($= t_0$) and its reaction constant k_{obs} was obtained as 0.0169 min^{-1} . Thus, the Rh^{3+} ratio of the reaction mixture is expressed as

$$(\text{Rh}^{3+} \text{ ratio}) = \exp(-k_{\text{obs}}(t - t_0)) \quad (t \geq t_0)$$

where t is reaction time, and the absorption of XAFS spectrum at time t was calculated by subtracting the Rh^{3+} contribution from each original EXAFS spectrum and normalized by the Rh^0 species concentration, which is expressed as

$$\mu(t; \text{Rh}^0) = \frac{\mu(t)(\text{Rh}^{3+} \text{ ratio}) \times \mu(t = t_0)}{1 - (\text{Rh}^{3+} \text{ ratio})}$$

where $\mu(t)$ is the absorption of XAFS spectrum at time t , $\mu(t; \text{Rh}^0)$ is the calculated absorption of XAFS spectrum of Rh^0 species at time t .

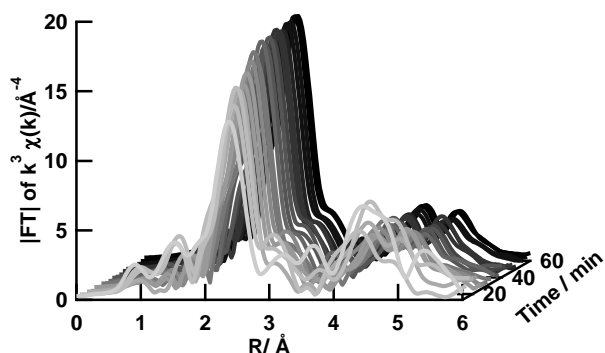


Figure 14. A series of calculated and Fourier transformed spectra of k^3 -weighted Rh K-edge EXAFS from Run B

Figure 14 shows a series of Fourier transformed calculated Rh K-edge EXAFS spectra $\mu(t; \text{Rh}^0)$. The first several spectra are not shown because almost all of them are derived from the Rh^{3+} species and have a lot of noise. The peak height at 2.42 \AA is almost constant during the reaction, which indicates that the shape and size of the Rh^0 species in the reaction mixture do not change during reaction, at least from 12 min to 60 min.^{32, 33} The XANES region of the calculated XAFS spectrum shows an identical spectrum to each other from 12 min onwards. This result also indicates

that the once formed Rh NPs did not grow anymore. Finally, to have some insight of the nucleation step, we focused attention on the intensity change of the Fourier transformed EXAFS spectra at 2.42 Å.

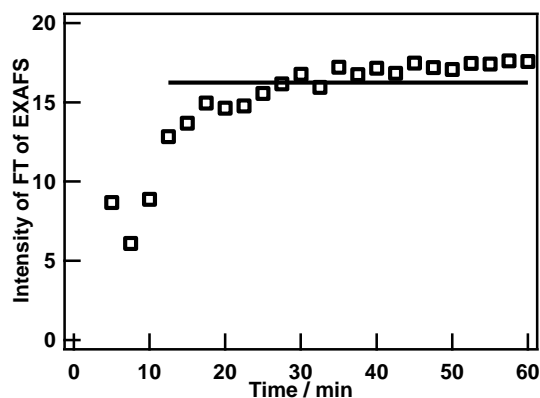


Figure 15. Intensity of Fourier transformed EXAFS spectra at 2.42 Å (Rh-Rh) as a function of time (plotted the values from the peak intensity at 2.42 Å of Fig. 13)

Figure 15 shows some plots of the intensity of Fourier transformed EXAFS spectra. The first several plots are not shown because of the same reason above. These FT of EXAFS spectra are almost identical to each other, and it indicates again the continuous generation of uniform Rh NPs. Moreover, when we performed curve fitting analyses on the series of Rh K-edge EXAFS spectra (Figure 12), the coordination number change of the Rh–Rh shell resulted in a constant value (ca. 9.7), which is comparable to the curve fitting analysis of the final EXAFS spectrum of run A. To shed light on the nucleation step in this condition, the initial change of FT of EXAFS was also analyzed as below.

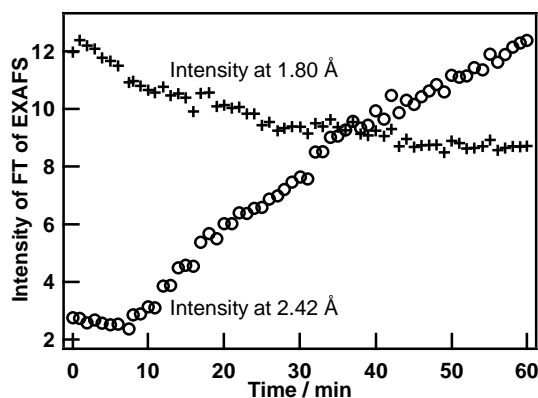
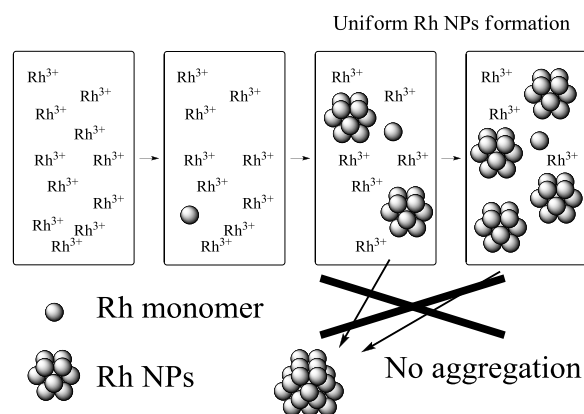


Figure 16. The temporal change of intensity of Fourier transformed EXAFS spectra (Run B)

Figure 16 shows the temporal change of intensities of Fourier transformed EXAFS spectra at 1.80 Å and 2.42 Å (run B). Over the first 5 min of the NP formation, the peak intensity at 1.80 Å gradually decreased (dissociation of the ligand), but that at 2.42 Å did not change at all. This phenomenon might be interpreted to be an observation of a small amount of $(\text{Rh}^0)_n$ ($n = 1, 2, 3, \dots$) nuclei formation. Namely, at this first step, a portion of Rh^{3+} precursor was reduced by EG to form the $(\text{Rh}^0)_n$ nuclei and the chloride anion or oxygen of EG dissociated from $(\text{Rh}^0)_n$ because of a lowering ionic bond strength. However, the concentration of $(\text{Rh}^0)_n$ species is very dilute, so the explicit Rh–Rh bond is not observed in the FT of EXAFS at this step. This study is summarized as follows. Using a combination of *in situ* time-resolved DXAFS, ICP-MS, and TEM observation, the following scheme for the Rh NPs formation mechanism is suggested (Scheme 2). In the first step of Rh NPs formation, Rh^{3+} precursor might be thermally reduced by EG to nucleate to be Rh^0 monomer. In the second step, the Rh NPs formed very rapidly to be uniform size NPs, which are stable under the reaction conditions. The last step is a repeat of the second step, which is the repeat of uniform Rh NP formation.

Scheme 2. Schematic view of Rh NPs formation mechanism in the present condition



Conclusions

The polyol process of Rh NP formation, which was performed in the presence of RhCl_3 as a precursor, PVP as a capping reagent and ethylene glycol as medium and reductant, was observed by *in situ* time-resolved DXAFS measurement, TEM and ICP-MS analysis. These analyses revealed that the polyol process of Rh species proceeds with pseudo-first order kinetics of Rh precursor

concentration, and produces Rh NPs of a uniform size. PVP concentration does not affect the Rh NP formation, at least under the present conditions.

References

- (1) Kelly, K. L.; Coronado, E.; Zhao, L. L.; Schatz, G. C., *J. Phys. Chem. B*, **2003**, *107*, 668-677.
- (2) Hyeon, T., *Chem. Commun.*, **2003**, 927-934.
- (3) Lu, A. H.; Salabas, E. L.; Schuth, F., *Angew. Chem. Int. Ed.*, **2007**, *46*, 1222-1244.
- (4) Medintz, I. L.; Uyeda, H. T.; Goldman, E. R.; Mattoussi, H., *Nat. Mater.*, **2005**, *4*, 435-446.
- (5) Yan, N.; Xiao, C.; Kou, Y., *Coord. Chem. Rev.*, **2010**, *254*, 1179-1218.
- (6) Yan, N.; Yuan, Y. A.; Dyson, P. J., *Chem. Commun.*, **2011**, *47*, 2529-2531.
- (7) Dykeman, R. R.; Yan, N.; Scopelliti, R.; Dyson, P. J., *Inorg. Chem.*, **2011**, *50*, 717-719.
- (8) Yang, X.; Yan, N.; Fei, Z. F.; Crespo-Quesada, R. M.; Laurency, G.; Kiwi-Minsker, L.; Kou, Y.; Li, Y. D.; Dyson, P. J., *Inorg. Chem.*, **2008**, *47*, 7444-7446.
- (9) Li, Y.; Hong, X. M.; Collard, D. M.; El-Sayed, M. A., *Org. Lett.*, **2000**, *2*, 2385-2388.
- (10) Li, Y.; El-Sayed, M. A., *J. Phys. Chem. B*, **2001**, *105*, 8938-8943.
- (11) Lamer, V. K.; Dinegar, R. H., *J. Am. Chem. Soc.*, **1950**, *72*, 4847-4854.
- (12) Watzky, M. A.; Finke, R. G., *J. Am. Chem. Soc.*, **1997**, *119*, 10382-10400.
- (13) Besson, C.; Finney, E. E.; Finke, R. G., *J. Am. Chem. Soc.*, **2005**, *127*, 8179-8184.
- (14) Finney, E. E.; Finke, R. G., *J. Colloid. Interf. Sci.*, **2008**, *317*, 351-374.
- (15) Harada, M.; Einaga, H., *Langmuir*, **2006**, *22*, 2371-2377.
- (16) Harada, M.; Abe, D.; Kimura, Y., *J. Colloid. Interf. Sci.*, **2005**, *292*, 113-121.
- (17) Harada, M.; Inada, Y., *Langmuir*, **2009**, *25*, 6049-6061.
- (18) Harada, M.; Inada, Y.; Nomura, M., *J. Colloid. Interf. Sci.*, **2009**, *337*, 427-438.
- (19) Harada, M.; Einaga, H., *Langmuir*, **2007**, *23*, 6536-6543.
- (20) Nishimura, S.; Takagaki, A.; Maenosono, S.; Ebitani, K., *Langmuir*, **2010**, *26*, 4473-4479.
- (21) Teramura, K.; Okuoka, S.; Yamazoe, S.; Kato, K.; Shishido, T.; Tanaka, T., *J. Phys. Chem. C*, **2008**, *112*, 8495-8498.
- (22) Ohyama, J.; Teramura, K.; Okuoka, S.; Yamazoe, S.; Kato, K.; Shishido, T.; Tanaka, T., *Langmuir*, **2010**, *26*, 13907-13912.
- (23) Ohyama, J.; Teramura, K.; Higuchi, Y.; Shishido, T.; Hitomi, Y.; Aoki, K.; Funabiki, T.; Kodera, M.; Kato, K.; Tanida, H.; Uruga, T.; Tanaka, T., *Phys. Chem. Chem. Phys.*, **2011**, *13*, 11128-11135.
- (24) Ohyama, J.; Teramura, K.; Higuchi, Y.; Shishido, T.; Hitomi, Y.; Kato, K.; Tanida, H.; Uruga, T.; Tanaka, T., *ChemPhysChem*, **2011**, *12*, 127-131.
- (25) Hoefelmeyer, J. D.; Niesz, K.; Somorjai, G. A.; Tilley, T. D., *Nano Lett*, **2005**, *5*, 435-438.
- (26) Borodko, Y.; Humphrey, S. M.; Tilley, T. D.; Frei, H.; Somorjai, G. A., *J. Phys. Chem. C*,

2007, *111*, 6288-6295.

(27) Humphrey, S. M.; Grass, M. E.; Habas, S. E.; Niesz, K.; Somorjai, G. A.; Tilley, T. D., *Nano Lett*, **2007**, *7*, 785-790.

(28) Zhang, Y. W.; Grass, M. E.; Kuhn, J. N.; Tao, F.; Habas, S. E.; Huang, W. Y.; Yang, P. D.; Somorjai, G. A., *J. Am. Chem. Soc.*, **2008**, *130*, 5868-5869.

(29) Taguchi, T.; Ozawa, T.; Yashiro, H., *Physica Scripta*, **2005**, *T115*, 205-206.

(30) Ravel, B.; Newville, M., *J. Synchrotron. Rad.*, **2005**, *12*, 537-541.

(31) Carr, C.; Glaser, J.; Sandström, M., *Inorg. Chim. Acta*, **1987**, *131*, 153-156.

(32) Benfield, R. E., *J. Chem. Soc., Faraday Trans.*, **1992**, *88*, 1107-1110.

(33) Jentys, A., *Phys. Chem. Chem. Phys.*, **1999**, *1*, 4059-4063.

Chapter 6

Insights into the Formation Mechanism of Rhodium Nanocubes

Abstract

The mechanism of formation of rhodium nanocubes in the presence of tetradecyltrimethylammonium bromide and polyvinylpyrrolidone in ethylene glycol was studied *in situ* by XAFS, in conjunction with other *ex situ* techniques including MALDI-TOF MS, XRD, TEM, and UV–vis spectroscopy. Detailed analysis of the XAFS data reveals that Rh nanocubes are formed in four distinct stages comprising ligand substitution, slow nucleation, continued nucleation/fast growth of nuclei, and shape reconstruction, which were corroborated by the other techniques. All the main types of Rh species and the chemical transformations taking place at each stage were clearly identified. In particular, combined XAFS and MAILD-TOF MS techniques provide compelling evidence that Rh₄ cluster act as the critical nuclei species for the formation of the nanocubes. Other key findings include (1) RhBr₃ is the true precursor of the Rh nanocubes, (2) the consumption rate of the precursor appears to follow Finke–Watzky type kinetics, and (3) non-cubic-shaped nanoparticles can be transformed into nanocubes, even if all the precursor has been exhaust. These results provide a clear understanding of the formation mechanism of the rhodium nanocubes, which is essential for rational design of nanoparticles.

Introduction

The shape of transition metal nanoparticles (NPs), defined by the crystallographic orientation of the surface facets, is widely regarded to be imperative in controlling their optical, magnetic, electronic, and catalytic properties.¹⁻³ Numerous studies have been devoted to the development of shape-controlled NP synthesis.^{4,5} Nanocubes (NCs), with (100) facet as the only exposed facet, have been successfully synthesized in a variety of noble metals, including Ag,⁶⁻¹⁰ Au,¹¹⁻¹³ Pt,^{14, 15} Rh,¹⁶⁻²¹ and Pd.²²⁻²⁴ Capping reagents are generally believed to be crucial in controlling the shape of metallic NCs, by preferential adsorption on (111) facet to (100) facet.² Br⁻ is one of the most commonly used capping reagents, and others like sulfur²⁵ and carbonyl^{26, 27} have similar effects. Although it is generally accepted that a thorough understanding on the mechanism, especially the original nucleation of metallic atoms and further growth to nanoscale particle with well-defined shape, is important for developing rational shape-controlled methods, knowledge on the formation mechanism of metallic NCs such as the structure of the nuclei, the kinetic profile of the reduction, and the function of the additives in the entire process sometimes remains experimentally elusive due to the limitation of the conventional characterization methods.²⁸

A number of theoretical and experimental approaches have been carried out to study the formation mechanism of nanostructures and colloids. Frenkel *et al.*,^{29, 30} Finke *et al.*,³¹⁻³³ and Bawendi *et al.*³⁴ have developed several general kinetic models to simulate the rate of nucleation and growth as well as the size evolution during the formation process of nanoparticles. These methods are unable to provide detailed structural information on intermediate species. Therefore, *in situ* experimental characterizations with relative fast time resolution are highly desirable. Several *in situ* techniques like UV-vis, SAXS/WAXS, TEM, and XAFS have been used in the study of NP formation mechanisms. For example, *in situ* UV-vis spectrometry has been widely used in studying Au, Ag, and Cu colloids systems.³⁵⁻³⁷ Kraehnert *et al.* applied millisecond resolution SAXS study on a series of Au NPs.³⁸⁻⁴⁰ Recently, Alivisatos *et al.* successfully observed the growth of Pt NPs with *in situ* TEM in the solution.⁴¹ Among these, *in situ* XAFS is regarded as a “potentially powerful method for directly observing the nucleation process” since “they give information about the identity of atoms in the nanoclusters, as well as information about the nearest neighbors of the atoms, allowing

atomic-level characterization.”²⁸ In fact, a number of *in situ* XAFS investigations into the synthesis of metal nanoparticles have been reported recently.⁴²⁻⁵⁶ Several of them have gained valuable structural information on early stage subnano nuclei, by analyzing the XANES spectra with *ab initio* multiple scattering FEFF calculation.^{50, 54-56} Despite these efforts, no such investigations following the formation of cubic NPs have been undertaken.

In this study, the author applied *in situ* DXAFS measurements, together with a few *ex situ* techniques, to reveal the formation mechanism of Rh NCs. Detailed analysis of the DXAFS data, and in particular the Fourier transformed EXAFS spectra, strongly suggests a four stage scenario for the formation of Rh NCs, including (1) exchange of Rh³⁺ ligand sphere, (2) formation of Rh NC nuclei, in which the major species are identified as well as their composition, (3) evolution of nuclei into Rh NCs, and (4) shape reconstructions, in which the intermediates of shape reconstruction are confirmed. In all of these stages, the participation of Br⁻ was found to be crucial. Further confirmation by MALDI-TOF, TEM, and XRD analyses has enabled a novel understanding and a detailed experimental approach to the sequence of events during Rh NC formation in the presence of TTAB and PVP in ethylene glycol.

Experimental Section

Materials

RhCl₃·3H₂O and ethylene glycol were obtained from Wako, Japan. Polyvinylpyrrolidone (PVP, K30) was purchased from Yili Chemical, China. Tetradecyltrimethylammonium bromide (TTAB) and RhBr₃ were obtained from Aldrich. All chemicals and solvents were used as received without any purification.

Synthesis of Rh NCs

The synthetic procedure of cubic Rh NPs was adapted from a literature method.¹⁶ For the DXAFS measurement a special apparatus was designed and used (see DXAFS measurements below). In a typical experiment, RhCl₃·3H₂O (53 mg, 0.2 mmol), TTAB (1.009 g, 3 mmol), and PVP (0.333 g, 3 mmol, in terms of the repeating unit) were added to ethylene glycol (10 mL) in a 25 mL side-arm Pyrex reactor. The mixture was stirred at room temperature until all solids were fully

dissolved, typically 20–30 min. The solution was heated to 130 °C with vigorous stirring in a preheated oil bath, and the reaction temperature was monitored with a thermocouple immersed into the solution. In general, the mixture reached the desired temperature within 3 min, and this temperature was maintained for 1 h under N₂, resulting in a dark brown solution.

Dispersive XAFS measurements

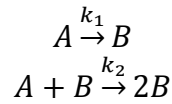
The procedure for the DXAFS measurements was similar to that established previously.⁴⁵ Briefly, the *in situ* DXAFS spectra of Rh K-edge were recorded on a system consisting of a polychromator set to a Laue configuration with a Si (422) net plane and a position-sensitive detector (PSD) mounted on a θ – 2θ diffractometer at the BL28B2 beamline of the SPring-8 (Ako, Japan), and the X-ray energy was calibrated from an inflection point of Rh foil in the XANES spectrum. The size of an X-ray focal spot on the sample is 0.16 mm in width and 2.4 mm in length, and the distance between the polychromator and the sample and the sample and PSD are 920 mm and 640 mm, respectively. The total energy bandwidth is 23000–24000 eV. A side-arm Pyrex reactor equipped with a Dimroth condenser was placed at the X-ray focal spot and used as the *in situ* cell. Signals are recorded as the X-ray passes through the tube. Temperature variations are recorded automatically via the thermocouple which is immersed into the reaction mixture. The exposure time of the PSD depends on the contents of the reaction mixture because the X-ray transparency of the samples differs, ranging from 66 to 198 msec. One hundred shots were accumulated to obtain suitable spectral quality. Data reduction of the XAFS spectra was performed procedure with Athena and Artemis included in Ifeffit package. Linear combination fitting of a series of XANES spectra was performed with Athena. The k^3 -weighted EXAFS oscillation in the range of 2–13 Å⁻¹ was Fourier transformed, and curve fitting analyses were performed in the range 1.6–2.8 Å in R space. For curve fitting analyses, the backscattering factor and the phase shift of each scattering paths were calculated with FEFF 8.4^{57, 58} using the crystal structures of Rh metal, RhCl₃, RhBr₃, and Rh₂O₃. The amplitude reduction factor was also estimated by fitting the reference spectra with the parameters calculated with FEFF. For the simultaneous fitting of the Rh–Br and the Rh–Rh first shell, the value of σ^2 was fixed to be 0.006.

Microscopy and Other Spectroscopic Techniques

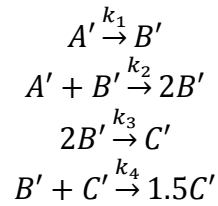
An excess of acetone was added at room temperature to the Rh NC ethylene glycol solution, resulting in a cloudy dark suspension, which was centrifuged at 6000 rpm for 6 min. The Rh NCs (black solid) was collected by decanting the supernatant. The Rh NCs were stored at room temperature under N₂. TEM was performed on a JEOL JEM-2010 microscope operating at 300 keV. One drop of the Rh NP solution in ethanol was placed on a copper grid coated with a carbon film. The grids were dried under N₂ for 24 h at room temperature. The size distributions of Rh NCs were determined from at least 150 particles. MALDI-TOF spectra were recorded on a Kratos Axima-CFR MALDI-TOF MS (Shimadzu Biotech, Kyoto Japan), using Kompact Software v.2.4.1. The mass spectrometer was set in linear mode for both positive and negative ion analysis. The dried droplet method was applied for all sample preparations. Briefly, a saturated matrix solution of 2,5-dihydroxybenzoic acid (DHB) or α -cyano-4-hydroxycinnamic acid (CHCA) in methanol and the sample suspended in methanol were mixed, deposited (0.5 μ L) onto the MALDI plate, and dried at ambient temperature of 15 min before analysis. The UV/vis absorption spectra were recorded on a Lambda 850 UV/vis spectrometer (Perkin-Elmer) at 25 °C. The ethylene glycol solution was diluted 100 times by ethylene glycol before measurements. XRD data were measured in transmission mode (between two acetate films) on a STOE transmission X-ray powder diffraction system (STADIP) using Cu K $_{\alpha 1}$ radiation (Ge(111) monochromator) and a linear position sensitive detector (PSD). The data were collected for all samples in the 2θ range of 2°–90° (step size 0.1, 30 s per step). Using the full widths at half-maximum (fwhm) of the Rh reflections of the diffraction patterns, the average crystallite size was estimated by applying the Scherrer equation. For the calculation of the crystallite size the contribution of peak width from the instrument was taken into account (Si powder was used).

Kinetic analysis

The kinetic fitting of Rh³⁺ consumption curve using both of Finke-Watzky two-step or four-step mechanism is carried out according to the previous paper⁵⁹. The pseudo-elementary step (A as the Rh³⁺ precursor, B as the Rh NC, or A' as the Rh³⁺ precursor, B' as the Rh NC and C' as the agglomerated Rh NCs)



or



equivalent to the differential equations system:

$$\frac{d[A]}{dt} = -k_1[A] - k_2[A][B]$$

or

$$\frac{d[A']}{dt} = -k_1[A'] - k_2[A'][B']$$

$$\frac{d[B']}{dt} = k_1[A'] + k_2[A'][B'] - 2k_3[B']^2 - k_4[B'][C']$$

$$\frac{d[C']}{dt} = k_3[B']^2 + 0.5k_4[B'][C']$$

$$[A'] + [B'] + 2[C'] = [A'_0]$$

This four-parameter differential equations system can only be solved with numerical solution. MatLab 7.12.0.635 was employed to gain the global best fit for Rh^{3+} consumption curve, using a Runge-Kutta method. All four parameters were searched in a range of assumed possible value, specifically k_1 and k_2 from 10^{-6} to 10^4 , k_3 and k_4 from 10^{-6} to 10^2 .

Results and discussion

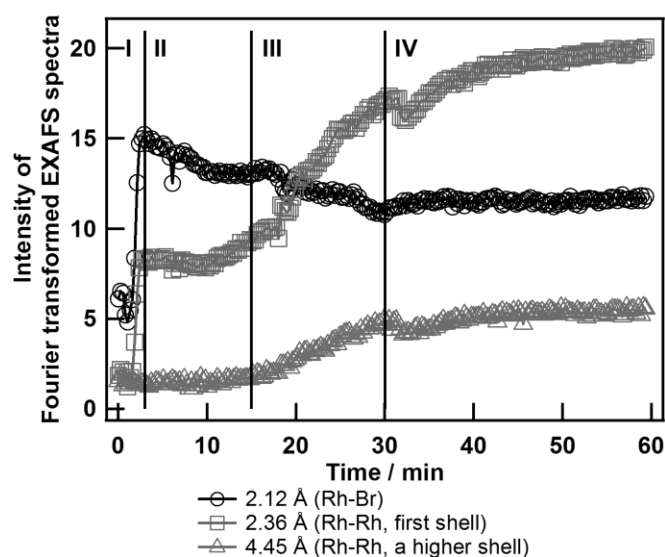


Figure 1. Four distinct stages for the formation of Rh NCs in EG, defined by the peak intensity variations in the Fourier transformed EXAFS spectra.

Rh NCs were prepared according to a well-documented method developed by Somorjai *et al.*,¹⁶ in which RhCl_3 was reduced in the presence of TTAB and PVP in ethylene glycol (denoted as the RhCl_3 -TTAB-PVP-EG system). The concentration of the $\text{RhCl}_3 \cdot 3\text{H}_2\text{O}$ precursor and the $\text{Rh}:\text{Br}^-:\text{PVP}$ ratio used were slightly modified in order to obtain high quality *in situ* EXAFS spectra. The reaction temperature was set at 130 °C, as control experiments indicated that the formation of Rh NCs at this temperature is complete in about 1 h. A typical temperature profile recorded by the thermocouple indicates that the temperature of the system rises from below 40 to 120 °C in 3 min and further increases to the set temperature (130 °C) over another 7 min. Thereafter, the temperature stabilizes at 130 °C with fluctuations of ± 3 °C. The time course of the intensities of Fourier transformed EXAFS spectra at characteristic peaks (Figure 1) indicates that the RhCl_3 is converted into Rh NCs via a four stage process — the key chemical transformations of each of the stages are discussed below.

Modification of the Rh^{3+} Ligand Sphere (*ca.* 0–3 min)

Previously, it has been proposed that RhCl_3 and TTAB in ethylene glycol react to form the species $[(n\text{-C}_{14}\text{H}_{29})\text{-(CH}_3)_3\text{N}]^+[\text{RhCl}_{4-x}\text{Br}_x]^-$ under similar conditions to those used herein,¹⁸ with the

assignment of the species based on the appearance of a new absorption band in the UV–vis spectrum at 275 nm. Indeed, we observed a change in the UV–vis spectrum 3 min after the start of the reduction process, with the formation of a new peak at 330 nm. It would appear that this band belongs to an intermediate species since its intensity continuously decreases after reaching a maximum and eventually disappears after about 30 min (Figure 2).

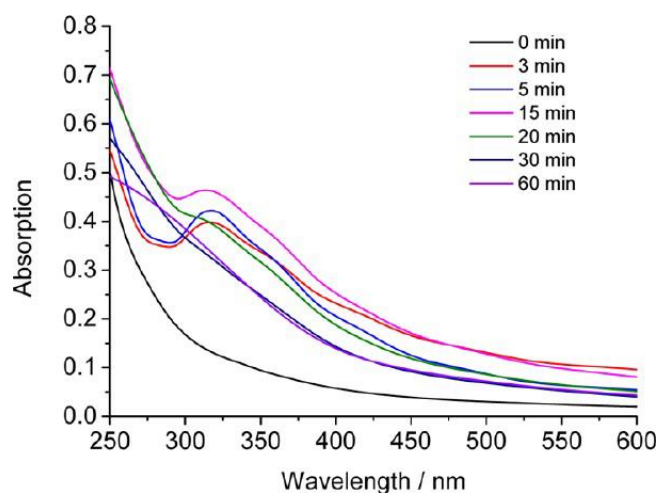


Figure 2. UV–vis spectra of the Rh samples taken at different stages of the reduction.

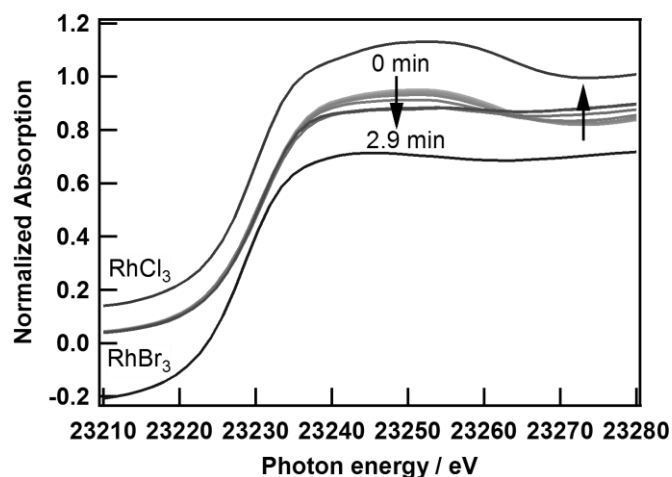


Figure 3. Rh K-edge XANES spectra evolution of the reaction solution of RhCl₃–TTAB–PVP–EG system in Stage I (Arrows indicate spectral change direction) and reference spectra of RhCl₃ and RhBr₃.

The DXAFS measurements provide further details concerning this initial transformation, indicative of substitution of the ligands around the Rh³⁺ ion in the first 3 min, which, coincidentally, corresponds to the period of rapid temperature increase from 40 to 120 °C. Figure 3 shows the Rh

K-edge XANES spectral variations during stage I (0–2.9 min), and the reference spectra of RhCl_3 and RhBr_3 . At first, the XANES spectrum is similar to that of RhCl_3 . Over the range of 23235–23280 eV, the spectrum gradually becomes “smoother” and its shape becomes more similar to the spectrum of RhBr_3 (see the arrows in Figure 3). A linear combination fit performed on the spectrum at 2.9 min, using RhBr_3 and RhCl_3 as references, indicates RhBr_3 and RhCl_3 composition of 100 and 0%, respectively. Although one should always be cautious with linear combination fitting, because the reference samples do not necessarily represent the real species in the sample, the close similarity in XANES spectrum between RhBr_3 and the Rh species in the reaction solution at the end of stage I suggests the quantitative substitution of Cl^- by Br^- around the Rh^{3+} ion. Another useful piece of information provided by XANES spectra is that no appreciable amount of Rh^{3+} ions were reduced at this stage, since the X-ray absorption edge energy (E_0) did not change.

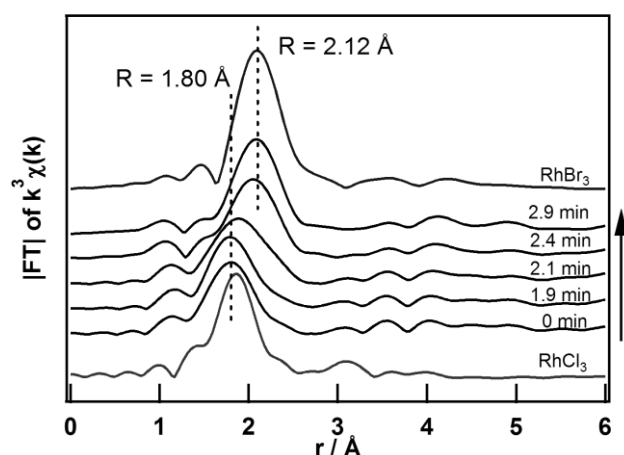


Figure 4. Fourier transformed spectra evolution of k^3 -weighted Rh K-edge EXAFS of reaction solution of RhCl_3 –TTAB–PVP–EG system in stage I and reference spectra of RhCl_3 and RhBr_3 .

Substitution of the ligands is also apparent from the Fourier transformed EXAFS spectra shown in Figure 4. The two reference samples, RhCl_3 and RhBr_3 , exhibit a broad band centered at 1.85 and 2.12 Å, respectively, which may be assigned to Rh–Cl and Rh–Br scatterings of Rh^{3+} ions, respectively. At the start of the reduction process (0 min), the peak located at 1.80 Å is mainly due to Rh–Cl scattering. Rh–O scattering, originating from the interactions between Rh^{3+} and carbonyl group in PVP or hydroxyl group in ethylene glycol, may contribute to this peak as well, but to a relatively smaller extent. The intensity and position of this peak did not change until the temperature

increased above 100 °C (1.9 min), after which the peak maxima quickly shifted to 2.12 Å (1.9–2.9 min), indicating that Cl⁻ ligands have been substituted by Br⁻ ligands around the Rh³⁺ ions. The coordination number (CN) of Rh–Br at 2.9 min is estimated to be 3.1 ± 0.4, based on the curve-fitting for the Fourier transformed EXAFS data presented in Figure 4, which highlights that the major Rh species at the end of the stage I has an average, empirical formula of RhBr₃.

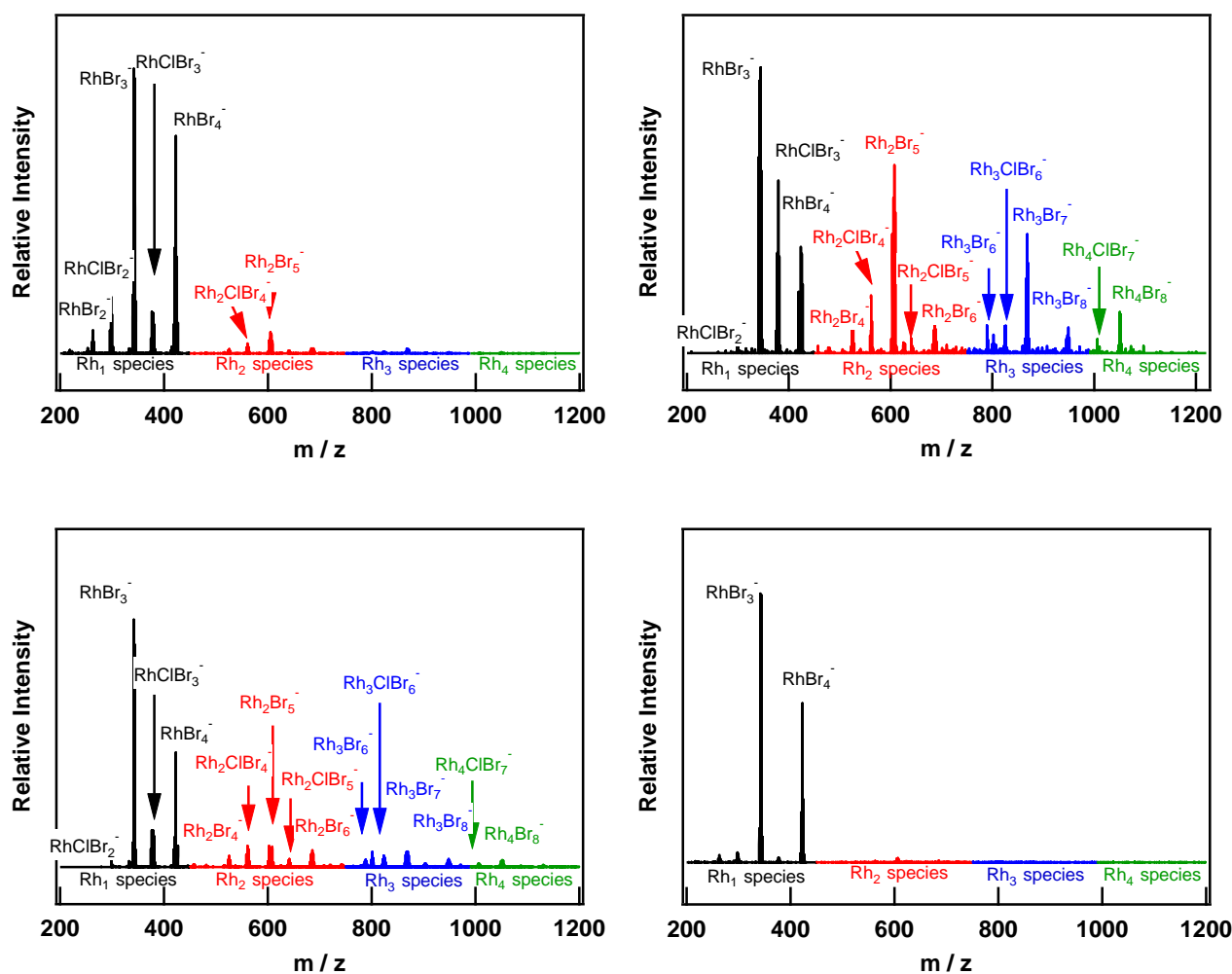


Figure 5. Negative ion MALDI-TOF mass spectra of the RhCl₃-TTAB-PVP-EG sample: (a) 3 min after reduction; (b) 15 min after reduction; (c) 20 min after reduction; (d) 60 min after reduction.

The XANES and Fourier transformed EXAFS studies prompted us to carry out a MALDI-TOF analysis to confirm the identity of the new Rh species generated during stage I. MALDI-TOF has emerged as a powerful technique for NP analysis recently;⁶⁰⁻⁶⁵ however, careful selection of the MALDI matrix is critical. The sample at the end of stage I (3 min after reduction) was examined in

the presence of different matrices including 2,5-dihydroxybenzoic acid (DHB) and α -cyano-4-hydroxycinnamic acid (CHCA) and also in the absence of a matrix, using positive and negative ion modes. In positive ion mode, only one group of peaks centered at 256.3 (m/z) was observed, corresponding to the TTAB cation, irrespective of the matrix applied.

In negative ion mode, the best signals were obtained in the absence of a matrix, giving rise to a series of peaks, enabling unambiguous identification of various Rh species (see Figure 5a). The spectrum was dominated by two sets of peaks at $m/z \approx 342$ and ≈ 422 . Their m/z ratios and isotopic distributions may be assigned to RhBr_3^- (the dominant species) and RhBr_4^- , respectively, corroborating the XAFS analysis that Rh is coordinated to Br^- ions with an average coordination number of 3. RhBr_3 is likely to be ionized by accepting an electron to form RhBr_3^- anions. The RhBr_4^- ion, on the other hand, is probably an artifact of the experiment, generated from the reaction of RhBr_3 with Br^- , which is present in excess. Moreover, if RhBr_4^- was actually present in solution, then it should be possible to detect it using ESI-MS; however, this technique failed to identify any Rh species, which was not entirely unexpected if the actual species in solution are uncharged. Several other Rh monomers, including RhBr_2^- , RhClBr_2^- , and RhClBr_3^- , were also observed in low abundance. Peaks are also observed at higher masses, indicating that during stage I some degree of clustering takes place — signals may be assigned to Rh_2 and Rh_3 clusters, albeit with much lower intensities compared to those of Rh_1 species.

RhBr_3 appears to be the actual (main) precursor for the formation of Rh NCs. Indeed, Rh NCs with similar size and morphology could be obtained when RhCl_3 was replaced by RhBr_3 as the precursor (in the presence of TTAB), suggesting Cl^- is not playing an essential role in Rh NC formation. Király *et al.* reported that PdCl_4^{2-} transforms to PdBr_4^{2-} prior to Pd NP formation in the presence of TTAB in water, confirmed by UV-vis, IR, and Raman spectroscopy.⁶⁶ Commencing with PtCl_4^{2-} , Yang *et al.* proposed that PtBr_4^{2-} is the NP precursor in the preparation of Pt NPs with various shapes in an aqueous solution containing TTAB.⁶⁷ Consequently, it appears to be a common phenomenon that metal chlorides transform, at least partially, to the corresponding bromides when Br^- ions are present in excess.

While bromide is essential to modify the ligand exchange kinetics and the reduction potential of the central metal ion, it has also been shown that an excess of bromide ions is required to give high

quality Rh NCs. Excess Br^- ions appear to prevent exchange for other donor groups present in the reaction mixture such as the O atoms in PVP and ethylene glycol. This feature has been verified from DXAFS experiments performed in the absence of TTAB which implies that the Rh–Br CN decreases.

Nuclei Formation (ca. 3–15 min)

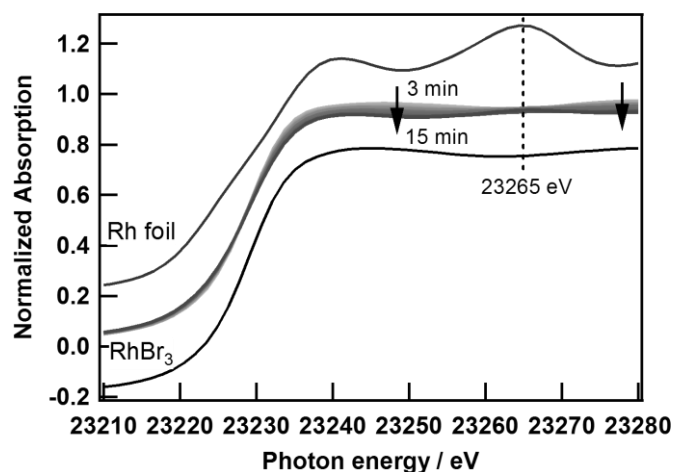


Figure 6. Rh K-edge XANES spectra evolution of the reaction solution of the RhCl_3 –TTAB–PVP–EG system in stage II and reference spectra of Rh foil and RhBr_3 (arrows indicate the direction of spectral change)

After reaching its maxima at about 3 min, the Rh–Br peak at 2.12 \AA in the Fourier transformed EXAFS spectra decreases in intensity (Figure 7, left), signaling the start of stage II, which lasts for about 12 min (3–15 min). During this period, a gradual decrease in E_0 in the XANES spectra (Figure 6) provides evidence that the reduction of Rh ions has begun. However, since the E_0 remains much higher than that of Rh foil, the reduction was deemed to be incomplete. Other changes in the XANES spectra (two perpendicular arrows in Figure 6) suggest the formation of new Rh species. However, Rh NCs are unlikely to exist at this stage since the absorption peak at around 23265 eV, which is characteristic of Rh foil (dashed line in Figure 6) and hence Rh NPs, has not yet appeared. It is therefore not unreasonable to speculate that some intermediate Rh species, possibly small (sub-nanometer) Rh NC nuclei, start to accumulate during stage II. Indeed, analysis of the Fourier transformed EXAFS spectra over 3–15 min strongly supports this assumption.

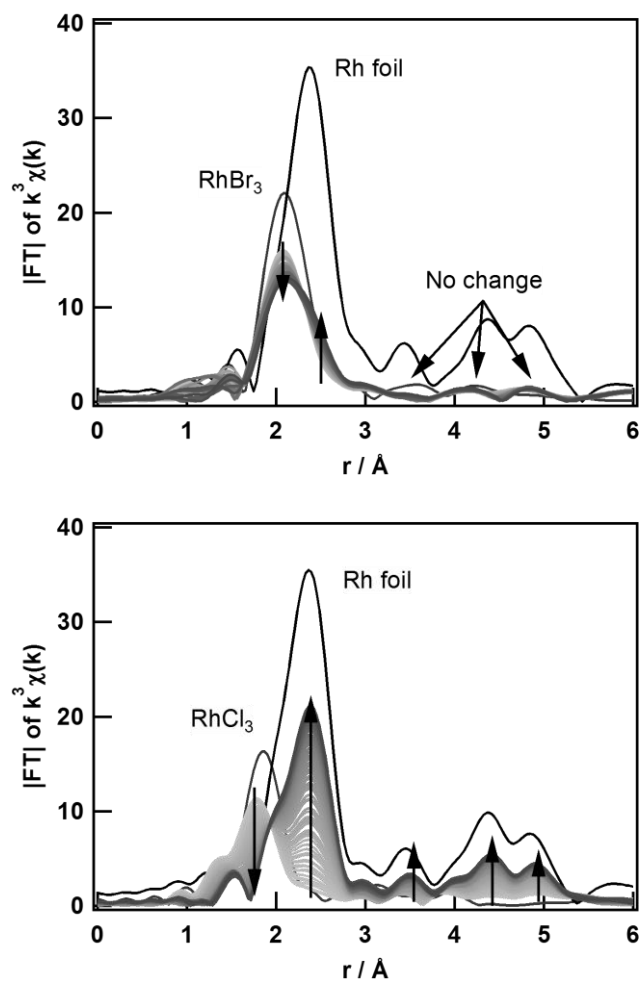
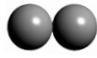

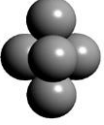
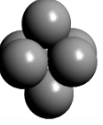



Figure 7. Fourier transformed spectra of k^3 -weighted Rh K-edge EXAFS of the reaction solution in stage II (3–15 min) and reference spectra of Rh foil and RhBr_3 . (Upper: the RhCl_3 –TTAB–PVP–EG system; Lower: without TTAB)

During stage II, the intensity of the Rh–Br scattering peak centered at 2.12 Å decreases. Simultaneously, a shoulder peak at higher R, most likely from first shell Rh–Rh scattering, appears and grows in intensity (Figure 7, upper; the two arrows indicate the variation of the spectra). Taken together, it can be concluded that some of the Rh^{3+} ions are reduced at this stage, possibly resulting in the formation of some partially reduced, coordinately unsaturated Rh monomers which subsequently react to form Rh_x species. It is particularly interesting that the spectra in the range 3–6 Å remain essentially unchanged during this period; *i.e.*, no significant scattering arising from higher shells of surrounding Rh atoms was detected (cf. the Fourier transformed EXAFS spectrum of Rh foil between 3 and 6 Å shows three distinct peaks resulting from higher shell Rh–Rh scattering); in

other words, the major Rh_x species at stage II are very small and comprise sub-nanometer scale clusters.

Table 1. The structure and first shell Rh-Rh CN of selected, close packed Rh clusters.

Hypothetical Rh clusters					
	Rh ₂	Rh ₄	Rh ₅	Rh ₆	Rh ₁₃
First shell Rh-Rh CN	1.0	3.0	3.6	4.0	5.5
Second shell Rh-Rh CN	None	None	0.4	1.0	1.8

Any close packed clusters with more than 4 atoms will have a second and even higher shell of Rh–Rh scattering (see Table 1), and therefore, the major Rh clusters formed at stage II are presumably no larger than Rh₄. XAFS is a powerful technique capable of revealing structural information on sub-nanometer species and can be used to determine the identity of the elements coordinated to the metal center as well as their coordination numbers (CNs), albeit with limited accuracy. At the sub-nanometer scale, the CN is very sensitive to the size of the cluster, as shown in Table 1. For example, a Rh dimer, a tetrahedral Rh₄ cluster, and a cuboctahedral structured Rh₁₃ cluster have Rh–Rh CNs of 1, 3, and 5.5, respectively.

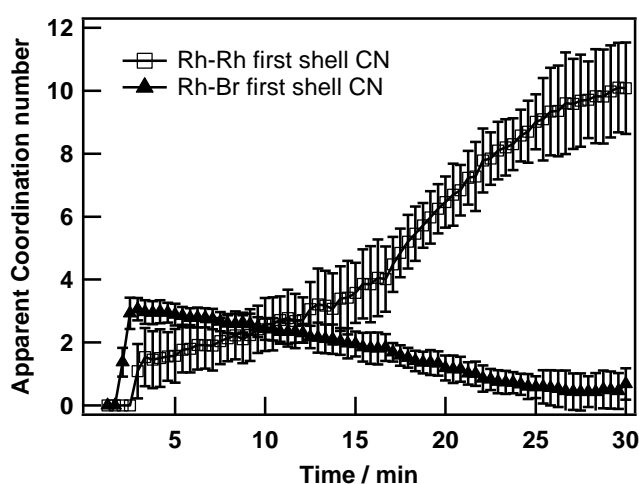


Figure 8. CNs as a function of the reaction time, obtained by fitting of the curves shown in Figures 6 and 9, for the Rh–Rh and Rh–Br bonds in the RhCl₃–TTAB–PVP–EG system (3–30 min).

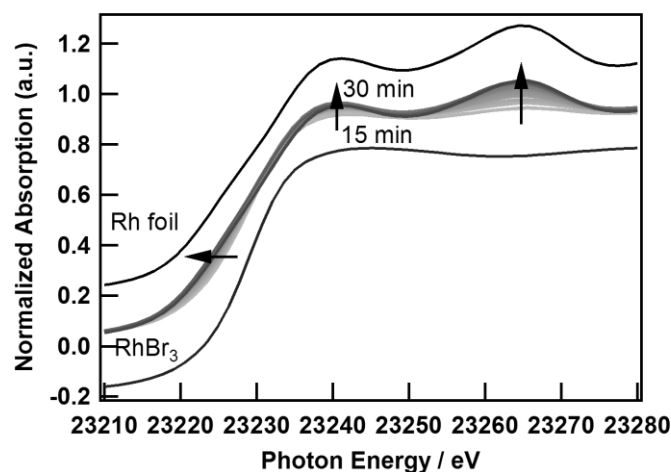


Figure 9. Rh K-edge XANES spectra evolution of the reaction solution of the RhCl_3 -TTAB-PVP-EG system in stage III and reference spectra of Rh foil and RhBr_3 (arrows indicate the direction of spectral change).

Figure 8 shows the plot of the CNs for the Rh-Rh and Rh-Br bonds as a function of the time. The CNs were calculated on the basis of the curve-fitting for the data presented in Figures 6 and 9. It is known that the degree of the disorder of coordination (DW factor) influences the EXAFS intensities, which makes the curve fitting challenging as multiple Rh species; coexist in the system, whose DW factors could not be determined accurately. To address the problem, fixed DW factors were applied for both the Rh-Br scattering peak and the first shell Rh-Rh scattering peak. For example, the σ^2 (the fitting parameter related to the DW factor) for Rh-Rh scattering was fixed to be 0.006, as this value is close to that of both Rh_{4-6} clusters^{54, 56} and small Rh NPs^{42, 68} reported in recent literature. As mentioned before, the CN of the Rh-Br bond at the start of stage II is 3.1 ± 0.4 , and this number decreases to 2.0 ± 0.4 over the following 12 min. At the same time, the CN of the Rh-Rh bond gradually increases to 3.6 ± 0.9 at 15 min. The average Rh-Rh bond length may be estimated as $2.71 \pm 0.01 \text{ \AA}$. For Rh_4 clusters (whose abundant existence was evidenced by MALDI-TOF analysis, vide infra), this bond length is indicative of Rh-Rh single bonds in a tetrahedral cluster^{54, 69} (planar Rh_4 clusters generally exhibit shorter Rh-Rh bond lengths, 2.58–2.63 \AA).⁷⁰ Taking into account the errors of the XAFS curve fitting, at the end of stage II the Rh species have an average formula of Rh_xBr_y ($x = 3-6$, $y = 6-12$; note that the EXAFS curve fitting is not able to identify the actual Rh species since several are likely to coexist at this stage and EXAFS provides

averaged information on all Rh species present). It is noteworthy that XRD analysis further supports the XAFS study (the predominant Rh species are very small), as characteristic peaks for Rh NPs in the XRD pattern are not observed (Figure 13). MALDI-TOF MS analysis was applied to identify the possible composition of the Rh clusters present at the end of stage II, and consequently a sample taken at 15 min was analyzed (Figure 5b). Relative to the mononuclear Rh species that dominates the spectrum of the sample taken at 3 min, appreciable amounts of di-, tri-, and tetra-Rh clusters are observed. As expected, as the nuclearity of the clusters grows the Br:Rh ratio decreases due to the increasing number of Rh–Rh contacts. The average valence of the Rh species decreases as the clusters grow, indicating that cluster formation is accompanied by (partial) reduction of the Rh^{3+} ions, which is expected for the formation of Rh–Rh bonds. Samples taken after different reaction times during stage II were also analyzed by MALDI-TOF MS, and it is found that the relative intensity of the peaks corresponding to the Rh_2 – Rh_4 clusters increases with time, indicating that cluster formation takes place during this stage and accumulate in the reaction medium. Clusters with nuclearities > 4 were not observed, in agreement with several recent papers. For example, studies on the catalytic dehydrocoupling of amine borane suggested a subnanometer nuclei Rh_{4-6} cluster as true active species in the reaction using $[\text{Rh}(1,5\text{-COD})\text{Cl}]_2$ as the precursor.^{54, 55} Another study employing $[\text{RhCp}^*\text{Cl}_2]_2$ as precursor led to a conclusion that Rh_4 -based subnanometer cluster is active for benzene hydrogenation.⁵⁶ Interestingly, in a previous work, a Au_4 cluster acting as the nuclei species for the Au NP formation was supported by analyzing the XANES spectra with ab initio multiple-scattering FEFF calculation.⁵² In this current study, the existence of Rh_4 clusters was unambiguously supported by MALDI-TOF MS analysis.

TTAB appears to be critical for the stabilization of these clusters as shown from a comparison with *in situ* XAFS data on a sample prepared in the absence of TTAB (denoted as the RhCl_3 –PVP–EG system, Chapter 5). As shown in Figure 7 (lower), striking differences between the two systems were observed. First, the reduction was considerably faster for the RhCl_3 –PVP–EG system — the peak for Rh–Cl scattering is very weak at 15 min, and the peak for first shell Rh–Rh scattering significantly increases. In contrast, the peaks for Rh–Br and the first shell Rh–Rh scattering only change moderately when TTAB is present, due to the ligand exchange processes that occur during stage I discussed in the previous section. Another significant difference is that for the

RhCl₃-PVP-EG system the peaks for higher shells of Rh-Rh scattering (R from 3 to 6 Å, see the arrows) grow simultaneously with the evolution of the first shell Rh-Rh scattering peak, indicative of the formation of much larger Rh species compared to those in the RhCl₃-TTAB-PVP-EG system. These comparisons imply that in the RhCl₃-PVP-EG system the nuclei are unstable and increase in size once formed, leading to the rapid formation of NPs. The subnanometer nuclei do not appear to be the dominant species in the reaction mixture; instead, the system mainly consists of the precursor (RhCl₃) and the resulting Rh NPs, with the nuclei present in low abundance, being short-lived, transient species. In contrast, during stage II the RhCl₃-TTAB-PVP-EG system appears to be dominated by “RhBr₃” and, relatively stable, intermediate Rh₂₋₄ clusters.

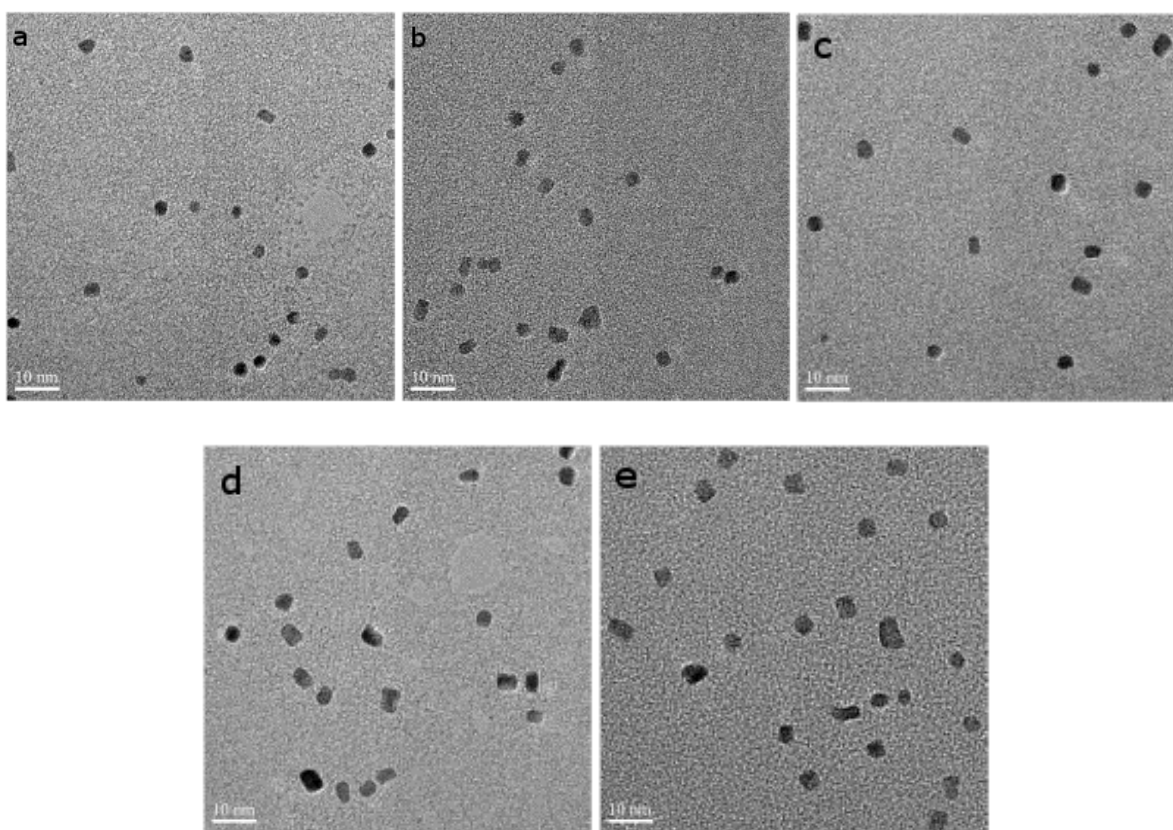


Figure 10. TEM images of Rh NP samples taken at a) 7 min, b) 9 min, c) 11 min, d) 13 min, e) 15 min after reduction.

Although XAFS and XRD measurements provide unambiguous information that the vast majority of the Rh species in stage II are very small clusters, samples taken at 3, 5, 7, 9, 11, 13, and 15 min were also analyzed by TEM in order to “see” if any Rh NPs are present. Interestingly, both

irregular-shaped and truncated cubic-shaped Rh NPs were observed in all the samples taken between 7 and 15 min (Figure 10), indicating there is no absolute boundary between stage II and stage III (the main stage of NP formation, see below). On the other hand, it is a reminder that what are focused under TEM might be in fact unrepresentative species in the system, highlighting the importance of combining different techniques before reaching a valid conclusion in the study of NP formation.

Evolution of the Nuclei into Rh NCs (ca. 15–30 min)

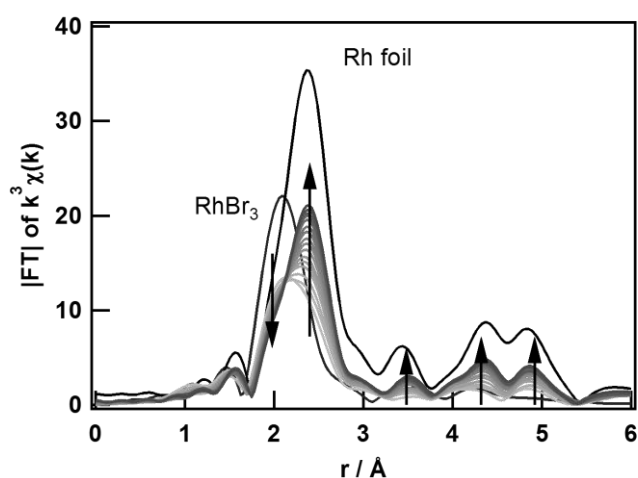


Figure 11. Fourier transformed spectral evolution of k^3 -weighted Rh K-edge EXAFS of the RhCl_3 -TTAB-PVP-EG system in stage III and reference spectra of Rh foil and RhBr_3 .

Stage III appears to be the main stage during which the Rh NCs form with both XANES and Fourier transformed EXAFS spectra exhibiting dramatic changes. The shape of the XANES spectra clearly evolve toward that of Rh foil, and the absorption edge moves to significantly lower values (Figure 9), both of which are indicative of a fast reduction process and the formation of Rh(0) particles. In contrast to the Fourier transformed EXAFS spectra recorded in stage II, where only the first shell Rh–Rh scattering peak increased, during stage III all Rh–Rh scattering peaks grow (Figure 11), demonstrating unequivocally the formation of Rh NPs. Over the 15–20 min period, the Rh–Rh CN increases from 3.6 ± 0.9 to 6.5 ± 0.8 , whereas the Rh–Br CN decreases from 2.0 ± 0.4 to 1.2 ± 0.4 . From the densest sphere packing model, in which a one shell Rh_{13} cluster has a Rh–Rh CN of 5.5 and a two shell Rh_{55} cluster has a Rh–Rh CN of 7.8, clusters with between 13 and 55 Rh atoms containing 15–66 Br^- ligands appear to be present in solution. It should be noted that XAFS gives an

averaged composition of the Rh species in the solution rather than the exact species present, and combined with TEM, XRD, and MALDI-TOF MS data, it becomes apparent that the system is composed of a mixture of Rh NCs (which are much bigger than $\text{Rh}_{13-55}\text{Br}_{15-66}$) and Rh_{1-4} species (which are much smaller than $\text{Rh}_{13-55}\text{Br}_{15-66}$). TEM shows Rh NCs with an average size of 4.7 nm with the majority of the particles being cubic, and the others (*ca.* 20%) having either elliptical or irregular shapes. From HRTEM images (Figure 15) most of the Rh NCs are not perfect cubes but are truncated. XRD analysis confirms the TEM data with the average size of the NCs estimated as 4.8 nm (Figures 13 and 14 and Table 2). The MALDI-TOF spectrum shows the presence of Rh_{2-4} clusters, but with lower relative intensities compared to the samples at the end of stage II (Figure 5c). Rh_{4+} clusters were not observed. Together, it is proposed that Rh_4 nuclei transformed into Rh NC one after another, instead of the slow, diffusion-controlled growth of all Rh_4 nuclei (otherwise Rh_{4+} clusters should be detectable). Our assumption is that the formation of a ≈ 5 nm Rh NC starts from the transformation of a Rh_4 nuclei into a larger cluster (rate determining step), after which it becomes a surface catalytic, autoaccelerated process that is completed in a very short time (less than 5 min). Although current XAFS and MALDI-TOF data support this hypothesis, a thorough understanding of this process requires theoretical approaches in the future.

Based on EXAFS curve fittings, from 20 to 30 min, the Rh–Rh CN increases further to 10.1 ± 1.4 . TEM indicates that the size of Rh NCs does not change substantially, and hence, the increase in the Rh–Rh CN may be attributed to the increased concentration of Rh NCs derived from the Rh_4 nuclei. In addition, the XRD pattern of the Rh peaks sharpen during this time interval compared to that observed at 20 min, indicating that crystalline Rh NPs are accumulating relative to the amorphous Rh NPs.

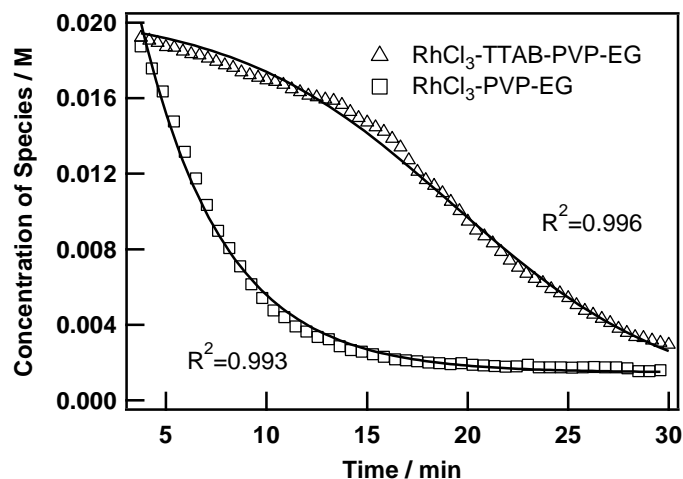


Figure 12. Kinetic fit of Rh^{3+} consumption curve of $\text{RhCl}_3\text{-PVP-EG}$ and $\text{RhCl}_3\text{-TTAB-PVP-EG}$ systems. Rh^{3+} consumption in the $\text{RhCl}_3\text{-PVP-EG}$ system (triangle) is fitted using pseudo-first-order law (square) and the $\text{RhCl}_3\text{-TTAB-PVP-EG}$ system is fitted using the Finke–Watzky two-step mechanism ($A \rightarrow B$, nucleation step rate constant k_1 , $A + B \rightarrow 2B$, growth step rate constant k_2).

A striking difference is observed in the DXAFS spectra of stages II and III; it takes 12 min for the Rh monomers to undergo an incomplete transformation into Rh_{2-4} clusters, whereas it takes only another 15 min for these clusters to grow into 5.2 nm Rh NCs ($\approx \text{Rh}_{7000}$ “clusters”). Based on the interpretation of the data obtained from stages II and III, a Finke–Watzky two-step mechanism³¹⁻³³ is strongly supported for the formation of Rh NCs. In the first step RhBr_3 is transformed slowly and continuously into Rh_{2-4} clusters, with Rh_4 act as plausible critical nuclei for further growth, and this process continues throughout stages II and III. The second step involves the fast, autocatalytic surface growth of nuclei into Rh NCs. A kinetic simulation and comparison of the consumption rate of the Rh precursor between the $\text{RhCl}_3\text{-TTAB-PVP-EG}$ system and the $\text{RhCl}_3\text{-PVP-EG}$ system, based on a linear combination analysis of the XANES spectra using the starting solution (representing RhCl_3), RhBr_3 and Rh foil as standards, was undertaken (Figure 12).

$$[\text{Rh}_t^{3+}] = [\text{Rh}_0^{3+}] \exp(-k_1 t) \quad (\text{eq. 1})$$

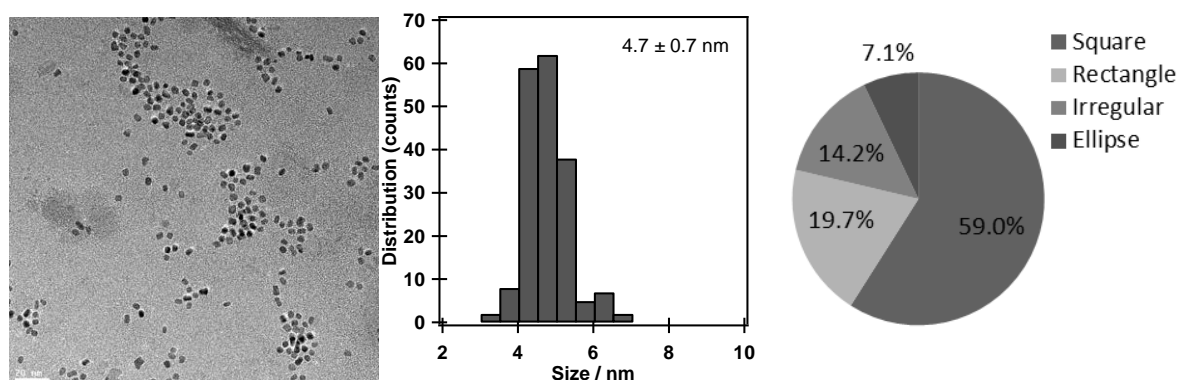
$$[\text{Rh}_t^{3+}] = [\text{Rh}_0^{3+}] \frac{k_1 + k_2 [\text{Rh}_0^{3+}]}{k_2 [\text{Rh}_0^{3+}] + k_1 \exp(k_1 + k_2 [\text{Rh}_0^{3+}]) t} \quad (\text{eq. 2})$$

It is clear that the Rh^{3+} consumption in the $\text{RhCl}_3\text{-PVP-EG}$ system follows the pseudo-first-order law (eq. 1) with the observed rate constant of 0.0179 min^{-1} as discussed in the

previous chapter. In contrast, the sigmoidal-character Rh^{3+} decay in the RhCl_3 -TTAB-PVP-EG system can be fitted with Finke-Watzky two-step mechanism (eq. 2) with relatively high accuracy. According to the fitting result, the rate constant k_1 of the nucleation step is 0.00533 min^{-1} and the rate constant k_2 of the autocatalytic surface growth step is $8.77 \text{ min}^{-1}\text{M}^{-1}$. The fitting result is consistent with the *in situ* DXAFS and MALDI-TOF observation of stages II and III. The significant difference between the rate of nucleation and growth enables the well separation of the two elementary steps and also explains the reason why Br^- addition ensures the final Rh NCs monodisperse. It is also noticed that the two-step fitting curve did not precisely follow the experimental curve in the range of 3–20 min. We attempted to improve the fitting result by applying the Finke-Watzky four-step mechanism which takes Rh NCs' agglomeration into consideration. However, the quality of fitting was not considerably improved ($R^2 = 0.998$), which implies that the agglomeration steps can be omitted in Rh NC synthesis. From the kinetic simulation, it appears that the RhCl_3 -TTAB-PVP-EG shows a typical feature of Finke-Watzky type kinetics. To the best of the author's knowledge, this is the first time that the kinetic profile of the formation of cubic metal NPs has been obtained based on firm experimental evidence.

It should be noticed that the Rh^{3+} consumption curve based on linear combination analysis is informative but not highly accurate. The XANES spectrum of Rh foil was used as the standard spectra of Rh NCs, which is not a perfectly representative for Rh NCs. Nevertheless, such analysis shed some lights into the kinetic profile of this process.

Shape Reconstruction (ca. 30–60 min).



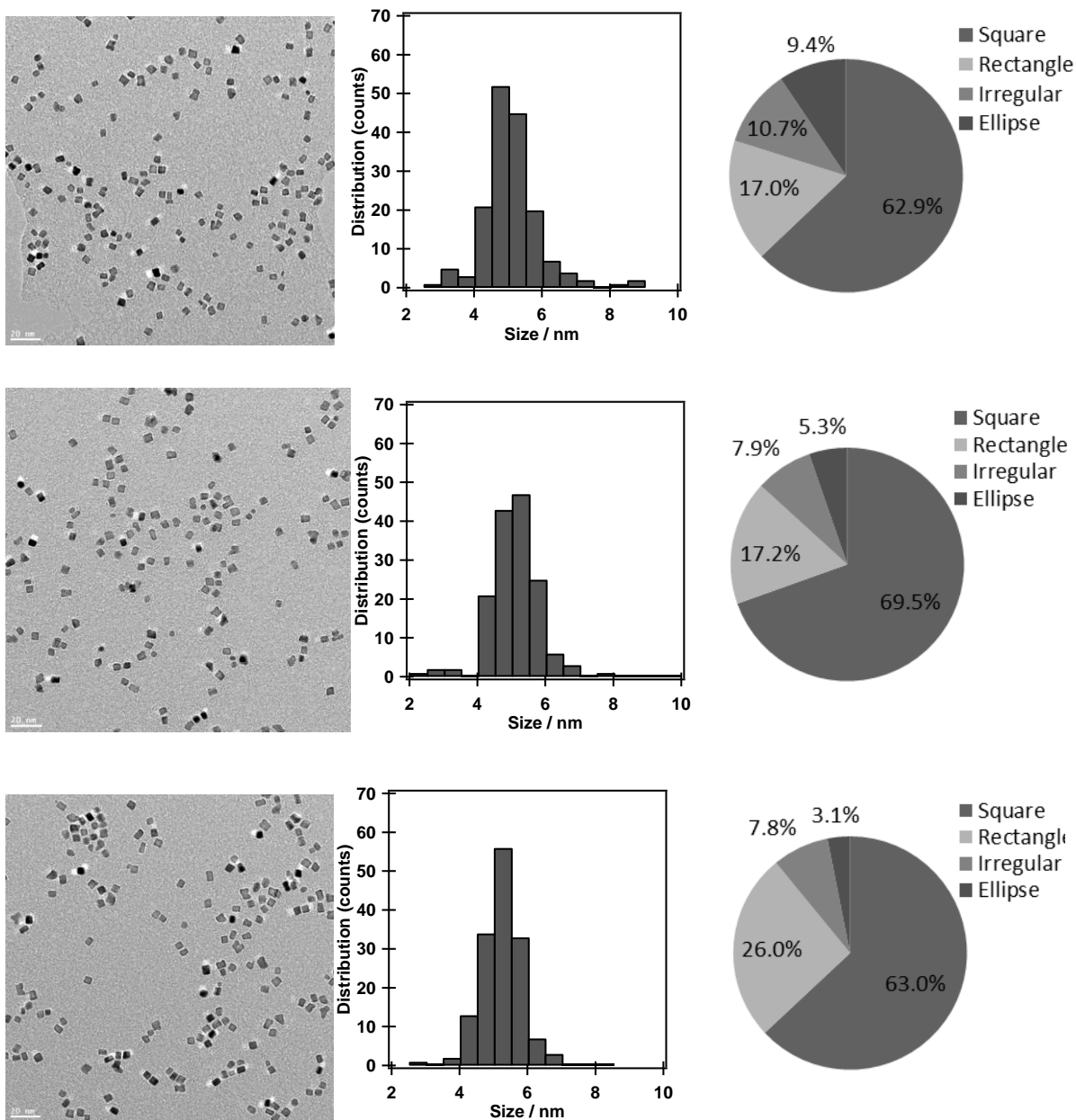


Figure 13. TEM images of Rh NCs in the RhCl_3 -TTAB-PVP-EG system after different reaction times (from top to bottom: 20, 25, 30, and 60 min).

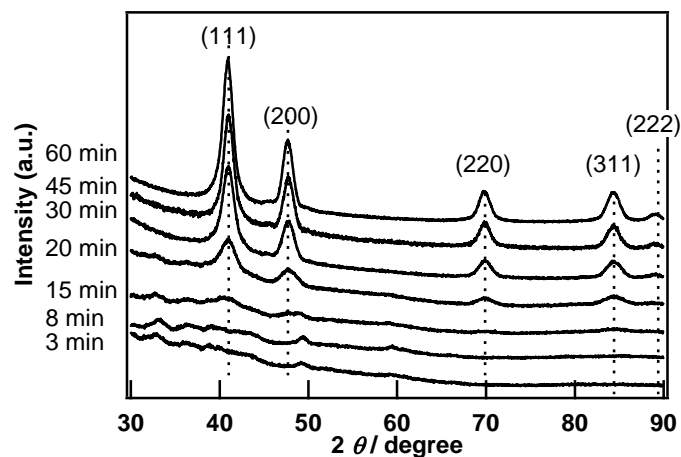


Figure 14. XRD patterns of Rh samples after different reaction times.

Table 2. Intensity ratios of different reflection planes and size of Rh NPs estimated by Scherrer equation

	Rh metal	Rh species (≤ 15 min)	Rh species (20 min)	Rh species (30 min)	Rh species (45 min)	Rh species (60 min)
Size / nm	-	-	4.8	7.0	8.9	8.3
$I_{(111)}/I_{(200)}$	2.13	-	2.03	2.15	2.00	2.09
$I_{(111)}/I_{(220)}$	3.58	-	4.64	5.02	4.41	4.85
$I_{(111)}/I_{(311)}$	3.23	-	4.19	4.90	4.60	4.86

After *ca.* 30 min the Rh–Br scattering intensity in the Fourier transformed EXAFS spectra remains constant (Figure 1), which suggests that the Rh–Br monomers and small cluster NC precursors have either been exhausted or remained in very low concentration, and consequently the RhCl₃–TTAB–PVP–EG system moves into a new phase (stage IV). During stage IV both of the XANES and the Fourier transformed EXAFS spectra show further variations toward the reference spectra of Rh foil; however, these changes are relatively minor. Similarly, changes in the Rh–Rh bond and Rh–Br CNs are essentially constant. Notably, the DXAFS analysis reveals that the surface of Rh NCs are coated by Br[−] ligands, as the Rh–Br CN remains at about 0.4 throughout stage IV. Despite the fact that the Rh NCs remain similar in size during stage IV, they do not remain unchanged. TEM shows that the percentage of cubic and rectangular bar-shaped Rh NPs slightly increases from 86% to 89% (Figure 13). At high magnifications (HRTEM), it is clearly seen that the sample taken at 30 min contains a mixture of well-defined Rh NCs, truncated NCs, and irregular,

amorphous NPs, whereas the sample taken at 60 min is mainly composed of cubic or rectangle Rh NCs (Figure 15). The Rh NC crystalline size calculated from XRD also increases from 7.0 to 8.3 nm. Combined, these results highlight that the main process that takes place during stage IV is the shape reconstruction of irregular, amorphous Rh NPs, generated together with the Rh NCs during stage III, to yield Rh NCs (since the cubic form is the thermodynamically favored form under the conditions).

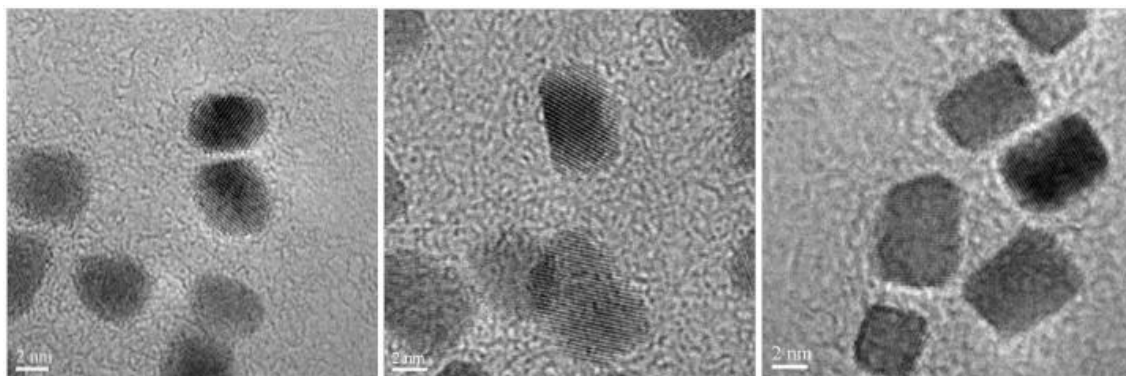


Figure 15. HRTEM images of the Rh NCs observed at different reaction times: left, 20 min; middle, 30 min; right, 60 min.

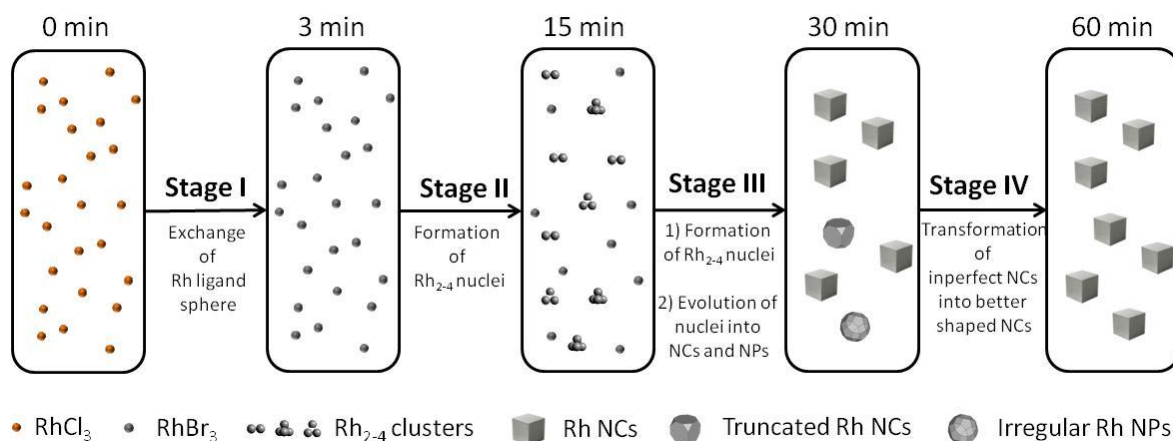
Such a shape reconstruction process could, in principle, be achieved in two ways, both of which represent thermodynamically driven, spontaneous processes. The first way is via surface atom diffusion — atoms migrate to cover the higher energy facet (the (111) facet in this case), resulting in the progressive development of (100) facets at the expense of (111) facets. The second way involves a “detachment–readhesion” mechanism. The surface Rh atoms with higher energies have a higher tendency to detach and diffuse into solution, and when they condense with the surface, they tend to favor attachment to more stable facets, during which the thermodynamically stable structures accumulate. The first mechanism, which involves surface atom diffusion, is unlikely to be the major pathway as it generally requires high temperatures — the Tammann temperature (the temperature at which bulk mobility of the metal particles becomes measurable in the solid state) of Rh is as high as 845 °C.⁷¹ There have been instances reported of atom diffusion occurring at temperatures lower than the Tammann temperature on the nanoscale. (For example, Pd has a Tammann temperature of 640 °C, but Pd NPs with sizes of 10 nm reconstruct their shapes at 550 °C with exposure to O₂.⁷² Likewise, Pt NPs undergo similar changes at 350 °C despite a Tammann temperature of 750 °C.⁷³) In these aforementioned examples the temperatures are considerably higher than those used in the Rh NC

synthesis, and therefore this process is unlikely to take place. On the other hand, leaching of metal ions from metal NPs into the solution is a well-known phenomenon in catalytic reactions.⁷⁴⁻⁷⁷ If the “detachment–readhesion” process dominates the reconstruction of the Rh NPs, it is not unreasonable to assume that during stage IV the system is in a dynamic state with both Rh NPs and leached Rh species present, and therefore it should be possible to detect the leached Rh species by MALDI-TOF MS, which is exactly the case (see Figure 4d, sample taken at 60 min). During this stage, the MALDI-TOF spectra only showed the presence of monomer species, and no clusters remain. This indicates that the nucleation is complete, which corroborates the XAFS findings, and that the “detachment–readhesion” process takes place, possibly facilitated by the presence of Br⁻ ions in the solution. Once again, the involvement of Br⁻ is critical for this shape reconstruction stage.

Conclusion

The formation of Rh NCs from RhCl₃ in the presence of PVP and TTAB in ethylene glycol involves four distinct stages (Scheme 1), comprising ligand substitution, slow nucleation, continued nucleation/fast growth of nuclei, and shape reconstruction. The salient mechanistic features of the Rh NC formation process include (1) RhBr₃ as the actual Rh NC precursor, (2) Rh₄ clusters act as the plausible NC nuclei, (3) the kinetics of the formation of Rh NCs can be quantitatively described by the Finke–Watzky mechanism, *i.e.*, the formation of nuclei is a slow and continuous process whereas the evolution of nuclei into NCs is a fast autoaccelerated process during which Rh NCs with similar sizes (≈ 5 nm) are constantly forming, and the significant difference between nucleation and growth rate ensures a narrow size distribution, and (4) the formation of the Rh NCs is a highly dynamic process, in which irregularly shaped Rh NPs are transformed into Rh NCs through a “detachment–readhesion” process, even after all the precursor molecules have been exhausted.

Scheme 1. Summary of the Four-Stage Formation Process of Rh NCs from RhCl₃^a



^aThe Rh species shown in the five boxes represent the predominant but not the exclusive Rh species present, and the chemical transformations illustrated under each arrow represent the major characteristic, but not necessarily the only process involved during each stage.

By combining different experimental techniques, it was shown conclusively that Br⁻ dominates the inner sphere of Rh from the end of stage I and furthermore plays an integral role in every single stage of the Rh NC formation. Although the system studied here concerns Rh NCs, the four-stage scenario described in this paper and other key findings are likely to be applicable to a wide range of NP systems providing general insights into the formation mechanism of metal NCs and NPs.

Reference

- (1) McClure, S. M.; Lundwall, M. J.; Goodman, D. W., *Proc. Natl. Acad. Sci.*, **2011**, *108*, 931-936.
- (2) Xiong, Y.; Wiley, B. J.; Xia, Y., *Angew. Chem. Int. Ed.*, **2007**, *46*, 7157-7159.
- (3) Zettsu, N.; McLellan, J. M.; Wiley, B.; Yin, Y.; Li, Z.-Y.; Xia, Y., *Angew. Chem. Int. Ed.*, **2006**, *45*, 1288-1292.
- (4) Xia, Y.; Xiong, Y.; Lim, B.; Skrabalak, S. E., *Angew. Chem. Int. Ed.*, **2009**, *48*, 60-103.
- (5) Yuan, Q.; Wang, X., *Nanoscale*, **2010**, *2*, 2328-2335.
- (6) Yu, D.; Yam, V. W., *J. Am. Chem. Soc.*, **2004**, *126*, 13200-13201.
- (7) Yu, D.; Yam, V. W., *J. Phys. Chem. B*, **2005**, *109*, 5497-5503.
- (8) Wiley, B. J.; Chen, Y.; McLellan, J. M.; Xiong, Y.; Li, Z.-Y.; Ginger, D.; Xia, Y., *Nano Lett.*, **2007**, *7*, 1032-1036.
- (9) Zhang, Q.; Li, W.; Moran, C.; Zeng, J.; Chen, J.; Wen, L.; Xia, Y., *J. Am. Chem. Soc.*, **2010**, *132*, 11372-11378.

- (10) Zhang, Q.; Li, W.; Wen, L.; Chen, J.; Xia, Y., *Chem. Eur. J.*, **2010**, *16*, 10234-10239.
- (11) Gou, L.; Murphy, C. J., *Chem. Mater.*, **2005**, *17*, 3668-3672.
- (12) Chen, H.; Kou, X.; Yang, Z.; Ni, W.; Wang, J., *Langmuir*, **2008**, *24*, 5233-5237.
- (13) Zhang, J.; Langille, M. R.; Personick, M. L.; Zhang, K.; Li, S.; Mirkin, C. A., *J. Am. Chem. Soc.*, **2010**, *132*, 14012-14014.
- (14) Bratlie, K. M.; Lee, H.; Komvopoulos, K.; Yang, P.; Somorjai, G. A., *Nano Lett.*, **2007**, *7*, 3097-3101.
- (15) Huang, X.; Zhang, H.; Guo, C.; Zhou, Z.; Zheng, N., *Angew. Chem. Int. Ed.*, **2009**, *48*, 4808-4812.
- (16) Zhang, Y.; Grass, M. E.; Kuhn, J. N.; Tao, F.; Habas, S. E.; Huang, W.; Yang, P.; Somorjai, G. A., *J. Am. Chem. Soc.*, **2008**, *130*, 5868-5869.
- (17) Long, N. V.; Chien, N. D.; Hirata, H.; Matsubara, T.; Ohtaki, M.; Nogami, M., *J. Cryst. Growth*, **2011**, *320*, 78-89.
- (18) Zhang, Y.; Grass, M. E.; Huang, W.; Somorjai, G. A., *Langmuir*, **2010**, *26*, 16463-16468.
- (19) Yuan, Q.; Zhou, Z.; Zhuang, J.; Wang, X., *Inorg. Chem.*, **2010**, *49*, 5515-5521.
- (20) Kundu, S.; Wang, K.; Liang, H., *J. Phys. Chem. C*, **2009**, *113*, 18570-18577.
- (21) Zhang, H.; Li, W.; Jin, M.; Zeng, J.; Yu, T.; Yang, D.; Xia, Y., *Nano Lett.*, **2010**, *11*, 898-903.
- (22) Fan, F.; Attia, A.; Sur, U. K.; Chen, J.; Xie, Z.-X.; Li, J.; Ren, B.; Tian, Z., *Cryst. Growth Des.*, **2009**, *9*, 2335-2340.
- (23) Sun, Y.; Zhang, L.; Zhou, H.; Zhu, Y.; Sutter, E.; Ji, Y.; Rafailovich, M. H.; Sokolov, J. C., *Chem. Mater.*, **2007**, *19*, 2065-2070.
- (24) Xiong, Y.; Cai, H.; Wiley, B. J.; Wang, J.; Kim, M. J.; Xia, Y., *J. Am. Chem. Soc.*, **2007**, *129*, 3665-3675.
- (25) Harris, P. J. F., *Nature*, **1986**, *323*, 792-794.
- (26) Seo, D.; Park, J. C.; Song, H., *J. Am. Chem. Soc.*, **2006**, *128*, 14863-14870.
- (27) Sun, Y.; Xia, Y., *Science*, **2002**, *298*, 2176-2179.
- (28) Finney, E. E.; Finke, R. G., *J. Colloid. Interf. Sci.*, **2008**, *317*, 351-374.
- (29) Auer, S.; Frenkel, D., *Nature*, **2001**, *409*, 1020-1023.
- (30) Auer, S.; Frenkel, D., *Nature*, **2001**, *413*, 711-713.
- (31) Watzky, M. A.; Finke, R. G., *J. Am. Chem. Soc.*, **1997**, *119*, 10382-10400.
- (32) Hornstein, B. J.; Finke, R. G., *Chem Mater*, **2003**, *16*, 139-150.
- (33) Besson, C.; Finney, E. E.; Finke, R. G., *J. Am. Chem. Soc.*, **2005**, *127*, 8179-8184.
- (34) Rempel, J. Y.; Bawendi, M. G.; Jensen, K. F., *J. Am. Chem. Soc.*, **2009**, *131*, 4479-4489.
- (35) Alsawafta, M.; Badilescu, S.; Packirisamy, M.; Truong, V., *Reac. Kinet. Mech. Cat.*, **2011**, *104*, 437-450.
- (36) Sardar, R.; Shumaker-Parry, J. S., *J. Am. Chem. Soc.*, **2011**, *133*, 8179-8190.
- (37) Stampelcoskie, K. G.; Scaiano, J. C., *J. Am. Chem. Soc.*, **2011**, *133*, 3913-3920.
- (38) Polte, J.; Herder, M.; Eler, R.; Rolf, S.; Fischer, A.; Wurth, C.; Thunemann, A. F.; Kraehnert,

- R.; Emmerling, F., *Nanoscale*, **2010**, *2*, 2463-2469.
- (39) Polte, J.; Ahner, T. T.; Delissen, F.; Sokolov, S.; Emmerling, F.; Thünemann, A. F.; Kraehnert, R., *J. Am. Chem. Soc.*, **2010**, *132*, 1296-1301.
- (40) Polte, J.; Erler, R.; Thünemann, A. F.; Sokolov, S.; Ahner, T. T.; Rademann, K.; Emmerling, F.; Kraehnert, R., *ACS Nano*, **2010**, *4*, 1076-1082.
- (41) Zheng, H.; Smith, R. K.; Jun, Y.; Kisielowski, C.; Dahmen, U.; Alivisatos, A. P., *Science*, **2009**, *324*, 1309-1312.
- (42) Harada, M.; Einaga, H., *Langmuir*, **2007**, *23*, 6536-6543.
- (43) Harada, M.; Inada, Y.; Nomura, M., *J. Colloid. Interf. Sci.*, **2009**, *337*, 427-438.
- (44) Shimizu, K.-i.; Sugino, K.; Kato, K.; Yokota, S.; Okumura, K.; Satsuma, A., *The Journal of Physical Chemistry C*, **2007**, *111*, 1683-1688.
- (45) Teramura, K.; Okuoka, S.; Yamazoe, S.; Kato, K.; Shishido, T.; Tanaka, T., *J. Phys. Chem. C*, **2008**, *112*, 8495-8498.
- (46) Harada, M.; Inada, Y., *Langmuir*, **2009**, *25*, 6049-6061.
- (47) Shishido, T.; Asakura, H.; Amano, F.; Sone, T.; Yamazoe, S.; Kato, K.; Teramura, K.; Tanaka, T., *Catal Lett*, **2009**, *131*, 413-418.
- (48) Nishimura, S.; Takagaki, A.; Maenosono, S.; Ebitani, K., *Langmuir*, **2009**, *26*, 4473-4479.
- (49) Weir, M. G.; Myers, V. S.; Frenkel, A. I.; Crooks, R. M., *ChemPhysChem*, **2010**, *11*, 2942-2950.
- (50) Yao, T.; Sun, Z.; Li, Y.; Pan, Z.; Wei, H.; Xie, Y.; Nomura, M.; Niwa, Y.; Yan, W.; Wu, Z.; Jiang, Y.; Liu, Q.; Wei, S., *J. Am. Chem. Soc.*, **2010**, *132*, 7696-7701.
- (51) Caetano, B. L.; Santilli, C. V.; Meneau, F.; Briois, V. r.; Pulcinelli, S. H., *J. Phys. Chem. C*, **2011**, *115*, 4404-4412.
- (52) Ohyama, J.; Teramura, K.; Higuchi, Y.; Shishido, T.; Hitomi, Y.; Kato, K.; Tanida, H.; Uruga, T.; Tanaka, T., *ChemPhysChem*, **2011**, *12*, 127-131.
- (53) Asakura, H.; Teramura, K.; Shishido, T.; Tanaka, T.; Yan, N.; Xiao, C.; Yao, S.; Kou, Y., *Phys. Chem. Chem. Phys.*, **2012**, *14*, 2983-2990.
- (54) Fulton, J. L.; Linehan, J. C.; Autrey, T.; Balasubramanian, M.; Chen, Y.; Szymczak, N. K., *J. Am. Chem. Soc.*, **2007**, *129*, 11936-11949.
- (55) Rousseau, R.; Schenter, G. K.; Fulton, J. L.; Linehan, J. C.; Engelhard, M. H.; Autrey, T., *J. Am. Chem. Soc.*, **2009**, *131*, 10516-10524.
- (56) Bayram, E.; Linehan, J. C.; Fulton, J. L.; Roberts, J. A. S.; Szymczak, N. K.; Smurthwaite, T. D.; Özkar, S.; Balasubramanian, M.; Finke, R. G., *J. Am. Chem. Soc.*, **2011**, *133*, 18889-18902.
- (57) Newville, M., *J. Synchrotron Rad.*, **2001**, *8*, 322-324.
- (58) Ankudinov, A. L.; Nesvizhskii, A. I.; Rehr, J. J., *Phys. Rev. B*, **2003**, *67*, 115120.
- (59) Besson, C.; Finney, E. E.; Finke, R. G., *Chem Mater*, **2005**, *17*, 4925-4938.
- (60) Dass, A.; Holt, K.; Parker, J. F.; Feldberg, S. W.; Murray, R. W., *J. Phys. Chem. C*, **2008**, *112*, 20276-20283.

- (61) Navin, J. K.; Grass, M. E.; Somorjai, G. A.; Marsh, A. L., *Anal. Chem.*, **2009**, *81*, 6295-6299.
- (62) Dass, A.; Stevenson, A.; Dubay, G. R.; Tracy, J. B.; Murray, R. W., *J. Am. Chem. Soc.*, **2008**, *130*, 5940-5946.
- (63) Boisselier, E.; Diallo, A. K.; Salmon, L.; Ornelas, C.; Ruiz, J.; Astruc, D., *J. Am. Chem. Soc.*, **2010**, *132*, 2729-2742.
- (64) Tsunoyama, H.; Tsukuda, T., *J. Am. Chem. Soc.*, **2009**, *131*, 18216-18217.
- (65) Tsunoyama, R.; Tsunoyama, H.; Pannopard, P.; Limtrakul, J.; Tsukuda, T., *J. Phys. Chem. C*, **2010**, *114*, 16004-16009.
- (66) Veisz, B.; Király, Z., *Langmuir*, **2003**, *19*, 4817-4824.
- (67) Lee, H.; Habas, S. E.; Kweskin, S.; Butcher, D.; Somorjai, G. A.; Yang, P., *Angew. Chem. Int. Ed.*, **2006**, *45*, 7824-7828.
- (68) Ferrandon, M.; Kropf, A. J.; Krause, T., *Appl. Catal. A: Gen.*, **2010**, *379*, 121-128.
- (69) Shido, T.; Okazaki, T.; Ichikawa, M., *J. Catal.*, **1995**, *157*, 436-449.
- (70) Lahoz, F. J.; Martin, A.; Esteruelas, M. A.; Sola, E.; Serrano, J. L.; Oro, L. A., *Organometallics*, **1991**, *10*, 1794-1799.
- (71) Golunski, S., *Platinum Met. Rev.*, **2007**, *51*, 162.
- (72) Graoui, H.; Giorgio, S.; Henry, C. R., *Surf. Sci.*, **1998**, *417*, 350-360.
- (73) Cabié, M.; Giorgio, S.; Henry, C. R.; Axet, M. R.; Philippot, K.; Chaudret, B., *J. Phys. Chem. C*, **2010**, *114*, 2160-2163.
- (74) Yan, N.; Yang, X.; Fei, Z.; Li, Y.; Kou, Y.; Dyson, P. J., *Organometallics*, **2009**, *28*, 937-939.
- (75) Kyriakou, G.; Beaumont, S. K.; Humphrey, S. M.; Antonetti, C.; Lambert, R. M., *ChemCatChem*, **2010**, *2*, 1444-1449.
- (76) Borodko, Y.; Lee, H. S.; Joo, S. H.; Zhang, Y. W.; Somorjai, G., *J. Phys. Chem. C*, **2010**, *114*, 1117-1126.
- (77) Yang, Y.; Unsworth, L. D.; Semagina, N., *J. Catal.*, **2011**, *281*, 137-146.

Chapter 7

***In situ* Time-Resolved XAFS Study of the Reaction Mechanism of Bromobenzene Homocoupling Mediated by [Ni(cod)(bpy)]**

Abstract

A homocoupling reaction mechanism of bromobenzene mediated by the [Ni(cod)(bpy)] (cod = 1,5-cyclooctadiene; bpy = 2,2'-bipyridine) complex was investigated by means of *in situ* time-resolved X-ray absorption fine structure (XAFS) with the aid of factor analysis and kinetic analysis. A dimer intermediate [Ni(bpy)(Ph)Br]₂ proposed in the previous studies by other groups is too dilute to observe with the XAFS technique; however, the structures and concentrations on the time course of a reactant [Ni(cod)(bpy)], an intermediate [Ni(bpy)(Ph)Br(dmf)₂], and a byproduct [Ni(bpy)Br₂(dmf)] during reaction are revealed.

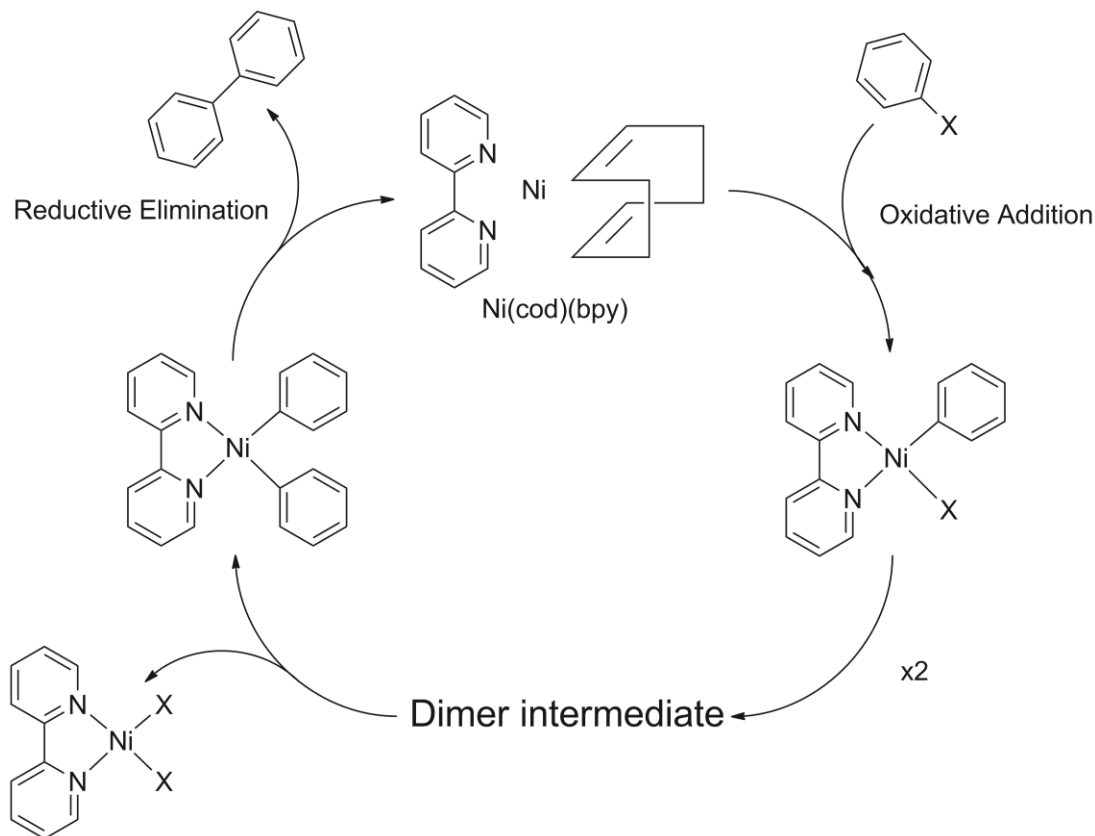
Introduction

It is significant to elucidate a detailed reaction mechanism in order to design an efficient complex catalyst. Up to now, isolation of intermediates, reaction results of various conditions, spectroscopy such as UV–vis, IR, and NMR, or computational chemistry has mainly contributed to reveal the reaction mechanism of a complex catalyst. However, it is difficult to determine the structure of reaction intermediates that are not isolable by these techniques. On one hand, X-ray absorption spectroscopy (XAS) has been applied to various heterogeneous catalysts such as supported metal oxides, nanoparticles, or fixed complex catalysts. The X-ray absorption fine structure (XAFS) technique can determine the oxidation number, local symmetry, and coordination environment of the target element based on the core electron transition spectra induced by high-energy X-ray. Thus, these features give significant insight into the focused element and could determine the molecular structure of the complex in some cases. In the heterogeneous catalyst field, for instance, Tromp *et al.* studied the activation of oxygen on Au/Al₂O₃ catalysts by *in situ* high-energy resolution fluorescence-detected (HERFD) X-ray spectroscopy and time-resolved XAFS and reported that the catalytic activity of small Au nanoparticles in the oxidation of CO arises from their ability to transfer charge to oxygen¹ and other CO adsorption on Pt or Rh particles.^{2,3} Newton *et al.* also studied CO or NO adsorption process on Pd⁴ or Rh⁵⁻⁷ nanoparticles by time-resolved XAFS. Grunwaldt and Topsoe *et al.* investigated the temperature-dependent reduction process of Cu of CuO/ZnO by *in situ* XAFS combined with XRD and TPR.⁸⁻¹⁰ For further examples, Nagai *et al.* reported redox and catalytic behavior of various Pt/support automotive catalysts,¹¹⁻¹⁴ and Yamamoto *et al.* observed the redox of Ce of an ordered CeO₂–ZrO₂ catalyst by time-resolved XAFS.¹⁵

Besides, XAFS applications to homogeneous catalysts have been getting more attention than ever. For example, Fiddy *et al.* applied the *in situ* XAFS technique to the Pd complex in the Mizorogi–Heck reaction¹⁶ to determine the real active species or the intermediate species and found that Pd clusters in the solution act as a reservoir of the active Pd monomer. Smolentsev *et al.* reported the intermediate structure of the polymerization step of methyltrioxorhenium by means of *in situ* Re L₃-edge XAFS and factor analysis,¹⁷ and Tromp *et al.* used energy dispersive XAFS and time-resolved UV–vis spectroscopy and revealed reaction intermediates of Cu(II)-catalyzed

N-arylation of imidazole.¹⁸

Scheme 1. Reaction Mechanism of the Aryl Halides Homocoupling Reaction Mediated by [Ni(cod)(bpy)] Proposed by Yamamoto *et al.*



In 1992, Yamamoto *et al.* proposed the reaction mechanism of the homocoupling reaction of bromobenzene promoted by [Ni(cod)₂] (cod = 1,5-cyclooctadiene) in the presence of 2,2'-bipyridine and/or triphenylphosphine to give biaryls¹⁹ (Scheme 1). Its mechanism is considered to consist of oxidative addition, transmetalation, and reductive elimination as elementary steps. The proposed mechanism is as follows. An aryl halide reacts with [Ni(cod)(bpy)] and forms [Ni(bpy)PhX] first, and a disproportionation process of two intermediate species occurs. After that, the [Ni(bpy)(Ph)₂] rapidly gives out a biaryl product. Many observations are reported about oxidative addition and reductive elimination, but a detailed transmetalation mechanism is still unclear. Therefore, in this study, the author applied the *in situ* time-resolved XAFS technique and factor analysis to a bromobenzene homocoupling reaction mediated by [Ni(cod)(bpy)] (bpy = 2,2'-bipyridine) to investigate the structure and the concentration of existing species including the intermediate because XAFS spectra can be used to determine the oxidation state and/or local structure of the target atom

and the number or atomic distance of coordination atoms. Unfortunately, we could not find the dimer intermediate during the reaction by means of XAFS, but instead, we found the direct observation of the coordination of the solvent molecule to some Ni complexes. There is a problem that XAFS spectra obtained during catalytic reaction consisted of several components of Ni species formed. Thus, factor analysis²⁰ was performed to try to extract the XAFS spectrum assignable to each species.

Experimental Section

Ni K-Edge X-ray Absorption Spectroscopy

Ni K-edge *in situ* time-resolved XAFS data were recorded in transmission and quick scan mode at SPring-8 BL01B1²¹ (8 GeV, 100 mA). A fixed exit Si(111) double-crystal monochromator with an energy resolution of ca. 1.3 eV was used. A Rh-coated mirror was used at a glancing angle of 3.5 mrad at around 9 keV to cut the high-energy X-ray harmonics off. For all spectra, a metallic Cu reference foil was used to provide an energy calibration for the monochromator. First, 100 mM bpy/DMF 0.7 mL was injected into a custom built XAFS cell containing [Ni(cod)₂] (20 mg, 0.073 mmol) located in the high-temperature controller equipped cryostat with a microsyringe through the rubber septum under N₂, and the solution was shaken immediately. The solution was heated to 323 K for 30 min to form the [Ni(cod)(bpy)]/DMF precatalyst solution. After the precatalyst formation, bromobenzene (2 equiv, 0.14 mmol) was injected into the solution. XAFS data were acquired for 30 scans per 1.5 h during the catalytic reaction (3 min/spectrum) at 323 K.

Data Reduction

XAFS data reduction was performed with REX2000 version 2.5.9 (Rigaku Co., Japan). Backscattering factor and phase shift parameters for a curve fitting analysis were calculated with the FEFF 8.4 code²² using the Hedin–Lundqvist exchange potential. EXAFS spectra were smoothed with the Savitzky–Golay algorithm. As Smolentsev *et al.* discussed in their previous paper,¹⁷ one can estimate the number of existing species in the reaction mixture with the combination of a series of XAFS spectra and factor analysis, especially by two empirical functions, the imbedded error (IE) and factor indicator (IND) functions, calculated by singular value decomposition (SVD). A matrix of

experimental XAFS spectra with elements is symbolized as m_{ij} , where subscript index i refers to a particular energy point of the spectrum while j refers to a particular time point. The SVD allows decomposition of this matrix as $m_{ij} = s_{ik}l_{km}v_{mj}$, where s_{ik} is an absorption coefficient for the component number k , l_{km} are the elements of the diagonal matrix with the diagonal elements sorted in decreased order, and $w_{kj} = l_{km}v_{mj}$ is the concentration dependence for the component k . IE function and IND function are expressed as

$$IE(n) = \sqrt{\frac{n \sum_{j=n+1}^c l_{jj}^2}{rc(c-n)}}$$

$$IND(n) = \sqrt{\frac{\sum_{j=n+1}^c l_{jj}^2}{r(c-n)^5}}$$

where r is the number of rows of the data matrix, c is the number of columns of the data matrix, and n is the number of components. The minimum of IE and IND as a function of n corresponds to the correct number of components present. Thus, these criteria allow determination of the number of observed intermediates. The minimum will not clearly be defined if the errors are not truly random, that is, the systematic error does not exist. Such contributions can lead to appearance of the nonchemical components. In this study, IE and IND functions are calculated with the PCA function implemented in a commercial software, Igor Pro version 6.22. On the basis of the number of the observed components in the reaction mixture, kinetic analysis (global fitting analysis) was performed on the series of spectra with Specfit version 2.12 for MS-DOS. The fitting scheme is described in the Results and Discussion section.

Results and Discussion

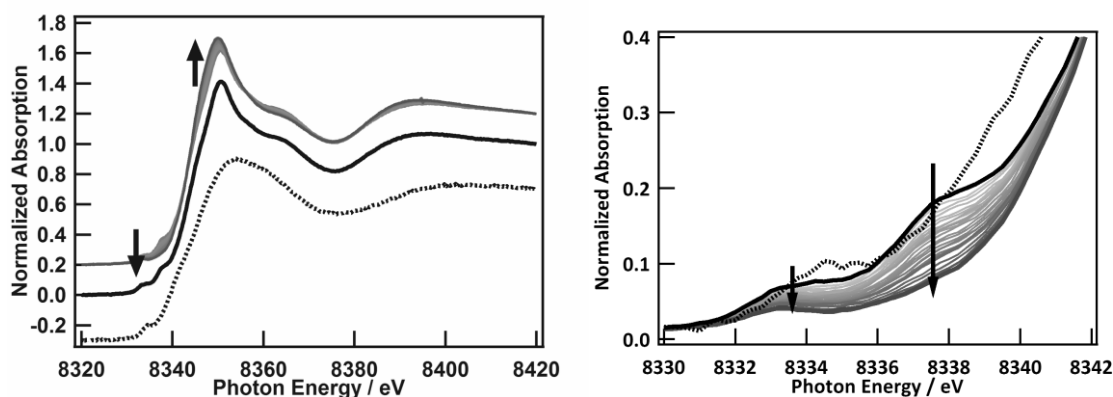


Figure 1. A series of Ni K-edge XANES spectra under the reaction of [Ni(cod)(bpy)] and PhBr (dotted: before addition of PhBr; black solid: just after the addition of PhBr (acquired for 0–3 min); Arrows indicate time course in 1.5 h (acquired for 3–90 min); right: magnified view).

Figure 1 shows a series of Ni K-edge XANES spectra under the reaction of [Ni(cod)(bpy)] and PhBr for 1.5 h. The drastic change of the XANES spectrum after the injection of PhBr within 3 min indicates rapid oxidative addition of PhBr to [Ni(cod)(bpy)]. Focusing on the pre-edge region, one pre-edge peak at around 8334.0 eV, which can be assigned to an electron transition from the Ni 1s orbital to the 3d orbital, was shifted to 8333.4 eV, and a new pre-edge peak at around 8337.5 eV, which can be assigned to an electron transition from the Ni 1s orbital to Ni 4p_z orbital,²³ emerged first.

In general, the 1s → 3d transitions of octahedral Ni complexes are forbidden; however, a small orbital mixing by lower local symmetry gives some probability for the 1s → 3d transition. Thus, in octahedral complexes, the 1s → 4p_z pre-edge peak at around 8337.5 eV is absent, and the 1s → 3d pre-edge peak shows a much smaller intensity than that in square-planar complexes. Therefore, octahedral and square-planar complexes can be distinguished by the presence or absence of the 1s → 4p_z transition. Then, the rise of the white line at around 8350.0 eV and the fall of the two pre-edge peaks implies an increase of the average oxidation number of the Ni species and the local environment of the center Ni atom, that is, an exchange of ligands, and the formation of a higher symmetric Ni complex from [Ni(bpy)PhBr].

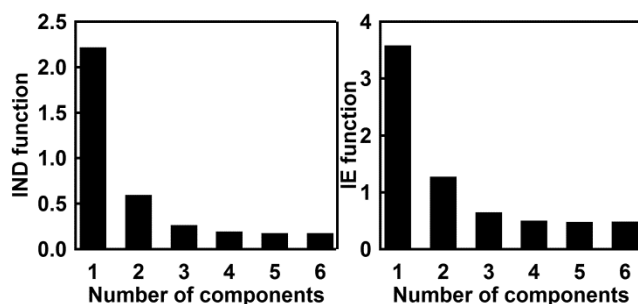
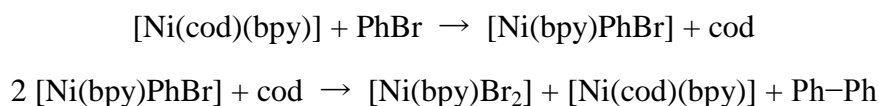


Figure 2. IE and IND functions calculated on the XANES spectra.

Factor analyses on the XANES spectra were performed to determine the number of Ni species in the reaction solution, and the results are shown in Figure 2. Usually, the minimum of IE and IND as a function of n is considered for the number of components present. In the present case, the decrement of the value of the IE and IND functions for more than three components is smaller than that of one or two components; thus, the number of components was estimated to be three; that is to say, there are three Ni species during the reaction.

Scheme 2. Two Reaction Steps of Oxidative Addition of PhBr to [Ni(cod)(bpy)] and Reductive Elimination of Ph–Ph from [Ni(cod)(Ph)Br]



Yamamoto *et al.* have already reported that the formation rate of biphenyl products is proportional to the square of [Ni(cod)(bpy)] concentration and that the reductive elimination of biphenyl products is generally rapid in their paper.¹⁹ A dimer intermediate or an intermediate complex of the transmetalation step must be a short-lived species, and the three intermediates are considered to be [Ni(cod)(bpy)], [Ni(bpy)PhBr], and [Ni(bpy)Br₂]. Unfortunately, at present study, we could not find any intermediate species in the transmetalation step. The reaction scheme including observed Ni species is summarized in Scheme 2. Then, kinetic analysis based on this reaction equation was performed. In the kinetic analysis, an individually recorded XANES spectrum of Ni(bpy)Br₂ was used as the final spectrum.

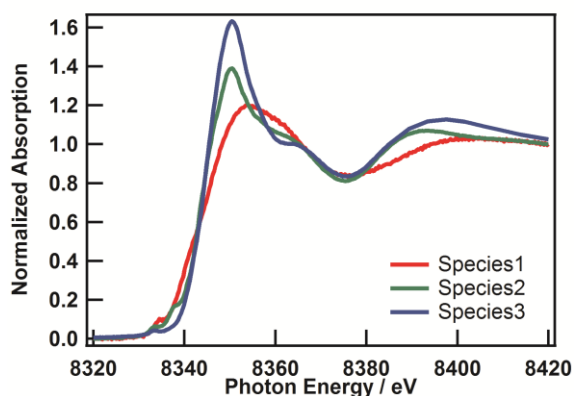


Figure 3. XANES spectra extracted by kinetic analysis

Figure 3 shows three individual spectra extracted by kinetic analysis. Spectrum 1 is identical to the XANES spectrum of $[\text{Ni}(\text{cod})(\text{bpy})]$, which was recorded individually, and the characteristic pre-edge peak at 8335 eV was reproduced. Thus, spectrum 1 was assigned to $[\text{Ni}(\text{cod})(\text{bpy})]$. Spectrum 2 has two pre-edge peaks at 8333 and 8337.5 eV, which were observed by square-planar coordinated Ni species, and has three characteristic peaks at 8350, 8365, and 8395 eV, which were also observed on the XANES spectrum of $\text{Ni}(\text{bpy})(\text{mesityl})\text{Br}$ measured by Feth *et al.*;²⁴ thus, spectrum 2 is assignable to $[\text{Ni}(\text{bpy})\text{PhBr}]$. However, the pre-edge peak of spectrum 2 is smaller than that of $\text{Ni}(\text{bpy})(\text{mesityl})\text{Br}$. Feth *et al.* also reported that the pre-edge peak of the Ni K-edge XANES spectrum of $\text{Ni}(\text{bpy})(\text{mesityl})\text{Br}$ decreases when it is treated with polar solvent. Thus, this result may indicate the solvation of DMF to $[\text{Ni}(\text{bpy})\text{PhBr}]$.

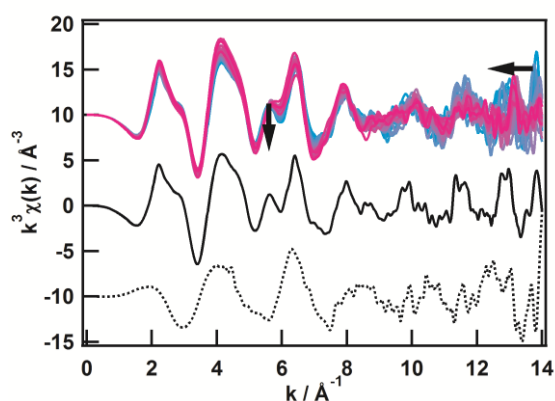


Figure 4. A series of Ni K-edge k^3 -weighted EXAFS oscillations under the reaction of $[\text{Ni}(\text{cod})(\text{bpy})]$ and PhBr smoothed by the Savitzky–Golay algorithm. (black dotted line: before addition of PhBr; black solid line: just after the addition of PhBr (acquired for 0–3 min); gradation

from blue to magenta: time course in 1.5 h (acquired for 3–90 min)).

Figure 4 shows a series of Ni K-edge EXAFS spectra under the reaction of [Ni(cod)(bpy)] and PhBr (smoothed by the Savitzky–Golay algorithm). PhBr addition caused a dramatic change of the EXAFS spectrum, and the gradual change of the EXAFS oscillation indicates fast oxidation addition of PhBr to [Ni(cod)(bpy)] and slow transformation of [Ni(bpy)PhBr] to another Ni species. In the same manner of XANES spectra analysis, factor analysis on the EXAFS oscillation was performed.

Unfortunately, the primitive component numbers could not be determined from the IE function, which is consistent with XANES analysis, but the IND function indicated three individual species, as same as XANES analysis. For example, Malinowski reported the application of IE and IND functions to the gas–liquid chromatographic retention indices of 22 ethers on 18 chromatographic columns. The IE function does not show minima; however, the IND function shows a clear minimum, which emphasizes the higher sensitivity of the IND function than the IE function.^{25, 26}

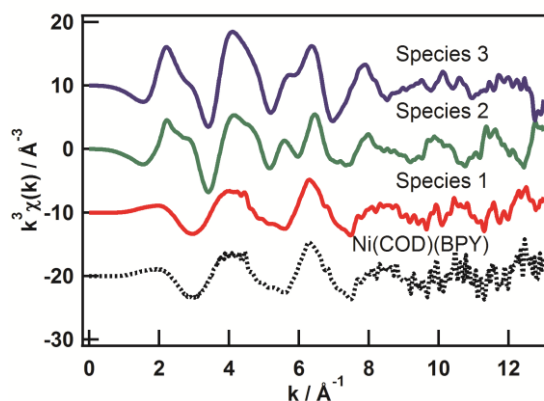


Figure 5. EXAFS spectra extracted by kinetic analysis and [Ni(cod)(bpy)] and [Ni(bpy)Br₂] for reference.

Kinetic analysis on the EXAFS spectra was also performed on the assumption of three Ni species and three EXAFS spectra were extracted as a consequence (Figure 5). Figure 5 also shows a comparison between the spectra of species 1 and [Ni(cod)(bpy)], and they are like one another. Thus, spectrum 1 is assigned to [Ni(cod)(bpy)] again.

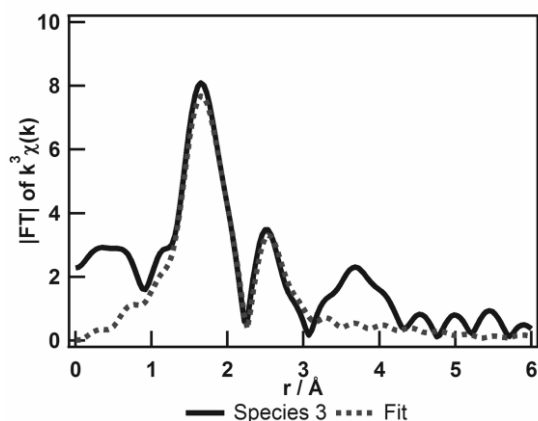


Figure 6. A curve fitting analysis of spectrum 3.

Next, to evaluate the molecular structures of each Ni species represented by the extracted EXAFS spectra, curve fitting analysis to each extracted spectrum was performed. A result of curve fitting analysis on spectrum 3 is shown in Figure 6, and their structural parameters are summarized in Table 1.

Table 1. Structural Parameters of Spectrum 3^a

Ab–Sc	CN	R/Å	dE/eV	DW/Å ⁻¹
Ni–N(O)	4.3	2.06	0.9	0.086
Ni–Br	2.0	2.47	–	0.115
Ni–C	6.7	2.94	–	0.127

^a $\Delta k = 2.9\text{--}12 \text{ \AA}^{-1}$; $\Delta R = 1.3\text{--}3.0 \text{ \AA}$; R factor = 30% (Ab–Sc: X-ray absorbing atom and scattering atom; CN: coordination number; R: atomic distance; dE: edge shift; DW: so-called XAFS Debye-Waller factor).

A curve fitting analysis confirms four N atoms coordinated to the Ni atom by 2.06 Å and two Br atoms coordinated by 2.47 Å. Two Br atoms coordinated to the Ni atom means that spectrum 3 is assignable to the Ni(bpy)Br₂ complex; however, the number of nearest N atoms is ca. 4, despite the fact that the Ni(bpy)Br₂ complex must have two N atoms. Taking into account that the back-scattering factor and phase shift of nitrogen and oxygen are essentially indistinguishable, this result indicates an association of two dimethylformamide (DMF) molecules (solvation) to the Ni atom. The XANES spectrum of Ni(bpy)Br₂ has a small pre-edge peak, which indicates that the local structure of the Ni species is a six-coordinated octahedral. Therefore, spectrum 3 stands for the

formation of $[\text{Ni}(\text{bpy})\text{Br}_2(\text{dmf})_2]$ in the reaction solution. The coordination number of the third shell of Ni–C, 6.7, which can be assigned to the carbons of 2,2'-bipyridine positioned at 1, 1', 3, and 3' and the carbons of the amide moiety of two dmf molecules, is consistent with the assumption of $[\text{Ni}(\text{bpy})\text{Br}_2(\text{dmf})_2]$.

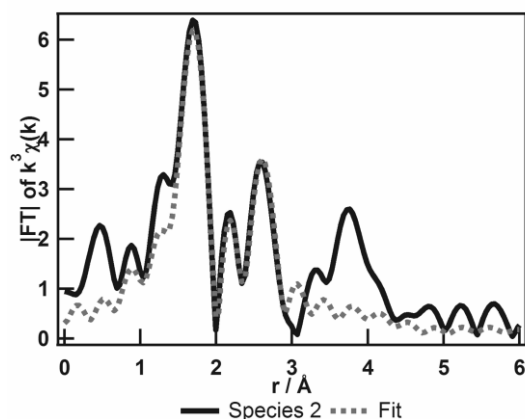


Figure 7. A curve fitting analysis of spectrum 2.

Table 2. Structural Parameters of Spectrum 2^a

Ab–Sc	CN	R/Å	dE/eV	DW/Å ⁻¹
Ni–C(N or O)	3.5	2.08	2.5	0.066
Ni–Br	0.7	2.61	–	0.106
Ni–C	5.9	2.98	–	0.084

^a $\Delta k = 2.9\text{--}12 \text{ \AA}^{-1}$; $\Delta R = 1.3\text{--}3.0 \text{ \AA}$; R factor = 22% (Ab–Sc: X-ray absorbing atom and scattering atom; CN: coordination number; R: atomic distance; dE: edge shift; DW: so-called XAFS Debye-Waller factor).

Finally, a result of curve fitting analysis on spectrum 2 that seems to be assigned to a reaction intermediate is shown in Figure 7, and the structural parameters are summarized in Table 2. A curve fitting analysis suggests three or four C (or N) atoms coordinated to the Ni atom by 2.08 Å and one Br atom coordinated by 2.61 Å. Three or four C (or N) atoms and a Br atom and six distant C atoms interacting with the Ni center means that spectrum 2 is assignable to the $[\text{Ni}(\text{bpy})\text{PhBr}]$ complex. However, taking into account that the back-scattering factors and phase shifts of carbon, nitrogen, and oxygen are essentially indistinguishable, the nearest four light atoms' coordination can be also

interpreted as an association of one DMF to the Ni atom. XANES spectrum 2 also has a small pre-edge peak, which indicates that the local structure of the Ni species is five- or six-coordinated.²³ Therefore, the curve fitting results suggests that spectrum 2 is assignable to [Ni(bpy)PhBr(dmf)] in the reaction solution.

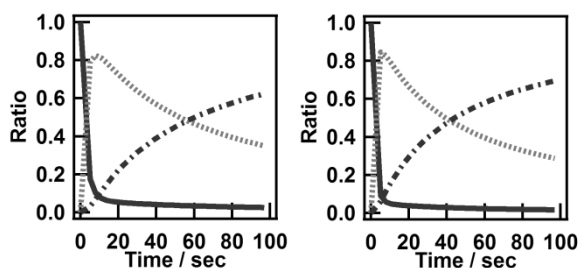


Figure 8. Time course of the concentration of each extracted species (left: XANES; right: EXAFS; solid line: species 1; dotted line: species 2; hashed line: species 3).

Figure 8 shows time course of the concentration of each Ni species. It is confirmed that the intermediates extracted from XANES and EXAFS spectra correspond to each other because these individually calculated time courses are similar to each other.

Conclusion

A combination of *in situ* time-resolved XAFS measurement and factor analysis clarified the structure and concentration on the time course of the reactant [Ni(cod)(bpy)], an intermediate [Ni(bpy)(Ph)Br(dmf)₂], and a subproduct [Ni(bpy)Br₂(dmf)] during reaction. The solvation of dmf to the intermediate and subproduct Ni species is found by the present *in situ* study. It is consistent with the previously reported fact that this homocoupling reaction proceeds in polar solvent faster than in nonpolar solvent. However, the transmetalation step of homocoupling PhBr mediated by [Ni(cod)(bpy)] could not be elucidated in this study. *In situ* XAFS technique can be applied to various homogeneous catalysts in order to shed light on the structures of intermediates and the detailed reaction mechanism in near future.

References

- (1) van Bokhoven, J. A.; Louis, C.; Miller, J. T.; Tromp, M.; Safonova, O. V.; Glatzel, P., *Angew. Chem. Int. Ed.*, **2006**, *45*, 4651-4654.

- (2) Safonova, O. V.; Tromp, M.; van Bokhoven, J. A.; de Groot, F. M. F.; Evans, J.; Glatzel, P., *J. Phys. Chem. B*, **2006**, *110*, 16162-16164.
- (3) Dent, A. J.; Evans, J.; Fiddy, S. G.; Jyoti, B.; Newton, M. A.; Tromp, M., *Angew. Chem. Int. Ed.*, **2007**, *46*, 5356-5358.
- (4) Newton, M. A.; Belver-Coldeira, C.; Martinez-Arias, A.; Fernandez-Garcia, M., *Nat. Mater.*, **2007**, *6*, 528-532.
- (5) Newton, M. A.; Burnaby, D. G.; Dent, A. J.; Diaz-Moreno, S.; Evans, J.; Fiddy, S. G.; Neisius, T.; Pascarelli, S.; Turin, S., *J. Phys. Chem. A*, **2001**, *105*, 5965-5970.
- (6) Newton, M. A.; Jyoti, B.; Dent, A. J.; Fiddy, S. G.; Evans, J., *Chem. Commun.*, **2004**, 2382-2383.
- (7) Newton, M. A.; Dent, A. J.; Diaz-Moreno, S.; Fiddy, S. G.; Jyoti, B.; Evans, J., *Chem. Eur. J.*, **2006**, *12*, 1975-1985.
- (8) Grunwaldt, J. D.; Molenbroek, A. M.; Topsøe, N. Y.; Topsøe, H.; Clausen, B. S., *J. Catal.*, **2000**, *194*, 452-460.
- (9) Grunwaldt, J. D.; Clausen, B. S., *Top. Catal.*, **2002**, *18*, 37-43.
- (10) Grunwaldt, J. D.; Caravati, M.; Hannemann, S.; Baiker, A., *Phys. Chem. Chem. Phys.*, **2004**, *6*, 3037-3047.
- (11) Nagai, Y.; Hirabayashi, T.; Dohmae, K.; Takagi, N.; Minami, T.; Shinjoh, H.; Matsumoto, S. i., *J. Catal.*, **2006**, *242*, 103-109.
- (12) Nagai, Y.; Dohmae, K.; Teramura, K.; Tanaka, T.; Guilera, G.; Kato, K.; Nomura, M.; Shinjoh, H.; Matsumoto, S., *Catal. Today*, **2009**, *145*, 279-287.
- (13) Shinjoh, H.; Hatanaka, M.; Nagai, Y.; Tanabe, T.; Takahashi, N.; Yoshida, T.; Miyake, Y., *Top. Catal.*, **2009**, *52*, 1967-1971.
- (14) Tanabe, T.; Nagai, Y.; Dohmae, K.; Takagi, N.; Takahashi, N.; Shinjoh, H., *Top. Catal.*, **2009**, *52*, 1433-1439.
- (15) Yamamoto, T.; Suzuki, A.; Nagai, Y.; Tanabe, T.; Dong, F.; Inada, Y.; Nomura, M.; Tada, M.; Iwasawa, Y., *Angew. Chem. Int. Ed.*, **2007**, *46*, 9253-9256.
- (16) Fiddy, S. G.; Evans, J.; Neisius, T.; Newton, M. A.; Tsoureas, N.; Tulloch, A. A. D.; Danopoulos, A. A., *Chem. Eur. J.*, **2007**, *13*, 3652-3659.
- (17) Smolentsev, G., *J. Chem. Phys.*, **2009**, *130*, 174508.
- (18) Tromp, M.; van Strijdonck, G. P. F.; van Berkel, S. S.; van den Hoogenband, A.; Feiters, M. C.; de Bruin, B.; Fiddy, S. G.; van der Eerden, A. M. J.; van Bokhoven, J. A.; van Leeuwen, P. W. N. M.; Koningsberger, D. C., *Organometallics*, **2010**, *29*, 3085-3097.
- (19) Yamamoto, T.; Wakabayashi, S.; Osakada, K., *J. Organomet. Chem.*, **1992**, *428*, 223-237.
- (20) Malinowski, E. R., *Factor Analysis in Chemistry, 3rd Edition*. Wiley-Interscience: 2002.
- (21) Uruga, T.; Tanida, H.; Kato, K.; Furukawa, Y.; Kudo, T.; Azumi, N., *J. Phys: Conf. Ser.*, **2009**, *190*, 012041.
- (22) Ankudinov, A. L.; Nesvizhskii, A. I.; Rehr, J. J., *Phys. Rev. B*, **2003**, *67*, 115120.

- (23) Colpas, G. J.; Maroney, M. J.; Bagyinka, C.; Kumar, M.; Willis, W. S.; Suib, S. L.; Mascharak, P. K.; Baidya, N., *Inorg. Chem.*, **1991**, *30*, 920-928.
- (24) Feth, M. P.; Klein, A.; Bertagnolli, H., *Eur. J. Inorg. Chem.*, **2003**, *2003*, 839-852.
- (25) Selzer, R. B.; Howery, D. G., *J. Chromatogr. A*, **1975**, *115*, 139-151.
- (26) Malinowski, E. R., *Anal. Chem.*, **1977**, *49*, 612-617.

Summary

In this thesis, the author summarized the results of the evaluation of group V, VI, VII or lanthanide K, L₁ and/or L₃-edge XANES spectra from both of experimental and theoretical viewpoints and applications of statistical and kinetic analysis to time-resolved XAFS spectra during chemical reaction. As a result, the author proposed a new analytical technique of local structure of lanthanide elements by the lanthanide L₁ and L₃-edge XANES spectra and possible application of statistics and kinetics to time-resolved XAFS spectra for the elucidation of the transient chemical species.

In Chapter 1, the author reported that the characteristic features at the K, L₁ and L₃-edge XANES spectra of Nb, Mo, Ta, W, and Re in their complex oxides can provide quantitative information on the local structure of each element. The area of the pre-edge peak of K or L₁-edge XANES spectrum, the split width of L₃-edge XANES spectrum and the local symmetry of each element are correlated with each other. Theoretical calculation based on density function theory of simple virtual model compounds clarified the origin of the peaks and the relationship between the electronic states and the XANES spectra. The author also proposed an indexing criterion on the local configuration based on the angles formed by the target atom and adjacent oxygen atoms.

In Chapter 2, the author extended the characterization methodology discussed in Chapter 1 to La complex oxides and found systematic change of the characteristic features at the La L₁ and L₃-edge XANES spectra, depending on the local structure of La. The pre-edge peaks of La L₁-edge XANES spectra show similar dependency on the local structure of La to the Nb, Mo K-edge and Ta, W, Re L₁-edge XANES spectra. In contrast, the La L₃-edge only shows less resolved XANES spectrum than those of group V, VI, and VII elements discussed in Chapter 1, and then another curve fitting procedure were employed to extract characteristic parameter of the local structure. The author also proposed a new primitive, but practical criterion to calculate a geometrical index related to the local structure, which is different from the criterion for group V, VI, and VII elements. Theoretical simulation of La L₁ and L₃-edge XANES spectra clarified the origin of the prominent peaks and demonstrated the validity of the new criterion for local structure parameterization.

In Chapter 3, a systematic survey on the L₁ and L₃-edge XANES spectra of five early lanthanide

elements, Pr, Nd, Sm, Eu and Gd, was performed in a similar manner to Chapter 2. As a result, the spectral-structural relationship between the XANES spectra and local structure was also validated in various complex oxides of these elements. The analysis approach was applied to Sm-doped $\text{Bi}_2\text{O}_3\text{-B}_2\text{O}_3$ glass materials to extract the information on the location of Sm species and found a significant difference among the samples, which have different photoluminescence property.

In Chapter 4, a systematic survey on the L_1 and L_3 -edge XANES spectra of three late lanthanide elements, Ho, Er and Yb, was performed in a similar manner to Chapter 3. As a result, the spectral-structural relationship between the XANES spectra and local structure was again validated in various complex oxides of these elements. Theoretical simulation of Ho L_1 - and L_3 -edge XANES spectra of virtual Ho aqueous complex models exhibits a consistent result with the experimental data and explained a general trend of the dependence of the spectral shape of the L_1 - and L_3 -edge XANES spectra on the local environment of the Ho atom.

In Chapter 5, the formation mechanism of Rh nanoparticles via a polyol process was investigated by *in situ* time-resolved XAFS. Kinetic analysis combined with ICP-MS and conventional TEM measurements revealed the continuous appearance of multipod type Rh nanoparticles in a uniform size without further aggregation.

In Chapter 6, the detailed formation mechanism of Rh nanocubes was investigated by *in situ* time-resolved XAFS in combination with MALDI-TOF MS, TEM, or XRD. Kinetic analysis combined with MALDI-TOF MS and conventional TEM measurements revealed the four stages of the Rh nanocube formation, ligand exchange of Rh cations, formation of transient Rh_{2-4} clusters, formation of Rh nanocubes or nanoparticles from Rh_{2-4} clusters, and shape reconstruction of Rh nanoparticles into well-defined Rh nanocubes.

In Chapter 7, the author applied *in situ* time-resolved XAFS technique to an organometallic catalytic cycle of a Ni complex to perform characterization of the intermediate complexes and analyzed the XAFS spectra in the aid of statistical and kinetic methods to extract hidden spectra of the intermediates. As a result, a transient Ni dimer predicted by other researchers could not be observed in the experimental condition, but structure and kinetic behavior of the other important intermediate complex generated by an oxidative addition were clarified.

In short, the author found a new analytical scheme for the estimation of the local configuration

of group V, VI, and VII elements, Nb, Mo, Ta, W, and Re and lanthanide elements, La, Pr, Nd, Sm, Eu, Gd, Ho, Er, and Yb by means of K, L₁, and L₃-edge XANES spectroscopy. This strategy gives a complementary method for the local structure analysis on them to EXAFS spectroscopy. The author also demonstrated the effectiveness of the combination of statistical and kinetic analysis with time-resolved XAFS measurement, which will shed light on the further application of XAFS technique to nanoscience and homogenous system.

List of Publications

Chapter 1

1. Structural Analysis of Group V, VI, VII Metal Compounds by XAFS and DFT Calculation
Tetsuya Shishido, Hiroyuki Asakura, Seiji Yamazoe, Kentaro Teramura, and Tsunehiro Tanaka
Journal of Physics: Conference Series, **2009**, 190, 012073.
2. Structural Analysis of Group V, VI, and VII Metal Compounds by XAFS
Hiroyuki Asakura, Tetsuya Shishido, Seiji Yamazoe, Kentaro Teramura, and Tsunehiro Tanaka
The Journal of Physical Chemistry C, **2011**, 115, 23653–23663.

Chapter 2

3. Local Structure and La L₁ and L₃-Edge XANES Spectra of Lanthanum Complex Oxides
Hiroyuki Asakura, Tetsuya Shishido, Kentaro Teramura, and Tsunehiro Tanaka
Inorganic Chemistry, **2014**, 53, 6048–6053.
4. A Theoretical Approach to La L₁-Edge XANES Spectra of La Complex Oxides and Their Local Configuration
Hiroyuki Asakura, Tetsuya Shishido, Kentaro Teramura, and Tsunehiro Tanaka
Submitted to The Journal of Chemical Physics.

Chapter 3

5. Local Structure of Pr, Nd, and Sm Complex Oxides and Their X-ray Absorption Near Edge Structure Spectra
Hiroyuki Asakura, Tetsuya Shishido, Shingo Fuchi, Kentaro Teramura, and Tsunehiro Tanaka
The Journal of Physical Chemistry C, **2014**, 118, 20881–20888.

6. Local Structure of Eu, and Gd Complex Oxides and Their XANES Spectra
Hiroyuki Asakura, Tetsuya Shishido, Kentaro Teramura, and Tsunehiro Tanaka
Submitted to Physical Chemistry Chemical Physics.

Chapter 4

7. Local Structure and L₁ and L₃-edge X-ray Absorption Near Edge Structure of Late Lanthanide Elements (Ho, Er, Yb) in Their Complex Oxides
Hiroyuki Asakura, Tetsuya Shishido, Kentaro Teramura, and Tsunehiro Tanaka
Submitted to The Journal of Physical Chemistry C.

Chapter 5

8. In Situ Time-Resolved DXAFS Study of Rh Nanoparticle Formation Mechanism in Ethylene Glycol at Elevated Temperature
Hiroyuki Asakura, Kentaro Teramura, Tetsuya Shishido, Tsunehiro Tanaka, Ning Yan, Chaoxian Xiao, Siyu Yao, and Yuan Kou
Physical Chemistry Chemical Physics, 2012, 14, 2983–2990.

Chapter 6

9. Insights into the Formation Mechanism of Rhodium Nanocubes
Siyu Yao, Yuan Yuan, Chaoxian Xiao, Weizhen Li, Yuan Kou, Paul J. Dyson, Ning Yan, Hiroyuki Asakura, Kentaro Teramura, and Tsunehiro Tanaka
The Journal of Physical Chemistry C, 2012, 116, 15076–15086.

Chapter 7

10. In Situ Time-Resolved XAFS Study of the Reaction Mechanism of Bromobenzene Homocoupling Mediated by [Ni(cod)(bpy)]
Hiroyuki Asakura, Tetsuya Shishido, and Tsunehiro Tanaka
The Journal of Physical Chemistry A, 2012, 116, 4029–4034.

Other Publications

1. In Situ Time-Resolved Energy-Dispersive XAFS Study on Reduction Behavior of Pt Supported on TiO₂ and Al₂O₃
Tetsuya Shishido, Hiroyuki Asakura, Fumiaki Amano, Takayoshi Sone, Seiji Yamazoe, Kazuo Kato, Kentaro Teramura, and Tsunehiro Tanaka
Catalysis Letters, **2009**, *131*, 413–418.
2. Incarceration of (PdO)_n and Pd_n Clusters by Cage-Templated Synthesis of Hollow Silica Nanoparticles
Kiyotaka Takao, Kosuke Suzuki, Tatsuya Ichijo, Sota Sato, Hiroyuki Asakura, Kentaro Teramura, Kazuo Kato, Tomonori Ohba, Takeshi Morita, Makoto Fujita
Angewandte Chemie International Edition, **2012**, *51*, 5893–5896.
3. Rational Design of a Molecular Nanocatalyst-Stabilizer that Enhances both Catalytic Activity and Nanoparticle Stability
Ryan R. Dykeman, Yuan Yuan, Ning Yan, Hiroyuki Asakura, Kentaro Teramura, Tsunehiro Tanaka, Paul J. Dyson,
ChemCatChem, **2012**, *4*, 1907–1910.
4. Development of Palladium Surface-Enriched Heteronuclear Au-Pd Nanoparticle Dehalogenation Catalysts in an Ionic Liquid
Xiao Yuan, Geng Sun, Hiroyuki Asakura, Tsunehiro Tanaka, Xi Chen, Yuan Yuan, Gabor Laurenczy, Yuan Kou, Paul J. Dyson, Ning Yan
Chemistry – A European Journal, **2013**, *19*, 1227–1234.
5. Bifunctionality of Rh³⁺ Modifier on TiO₂ and Working Mechanism of Rh³⁺/TiO₂ Photocatalyst under Irradiation of Visible Light
Sho Kitano, Naoya Murakami, Teruhisa Ohno, Yasufumi Mitani, Yoshio Nosaka, Hiroyuki

Asakura, Kentaro Teramura, Tsunehiro Tanaka, Hiroaki Tada, Keiji Hashimoto, and Hiroshi Kominami

The Journal of Physical Chemistry C, **2013**, *117*, 11008–11016.

6. Ultrathin rhodium nanosheets

Haohong Duan, Ning Yan, Rong Yu, Chun-Ran Chang, Gang Zhou, Han-Shi Hu, Hongpan Rong, Zhiqiang Niu, Junjie Mao, Hiroyuki Asakura, Tsunehiro Tanaka, Paul J. Dyson, Jun Li, and Yadong Li

Nature Communications, **2014**, *5*, 3093.

7. Highly efficient, NiAu-catalyzed hydrogenolysis of lignin into phenolic chemicals

Jianguang Zhang, Hiroyuki Asakura, Jeaphianne van Rijn, Jun Yang, Paul Duchesne, Bin Zhang, Xi Chen, Peng Zhang, Mark Saeys and Ning Yan

Green Chemistry, **2014**, *16*, 2432–2437.

8. A Series of NiM (M = Ru, Rh, and Pd) Bimetallic Catalysts for Effective Lignin Hydrogenolysis in Water

Jianguang Zhang, Jason Teo, Xi Chen, Hiroyuki Asakura, Tsunehiro Tanaka, Kentaro Teramura, and Ning Yan

ACS Catalysis, **2014**, *4*, 1574–1583.

9. Order-to-disorder structural transformation of a coordination polymer and its influence on proton conduction

Satoshi Horike, Wenqian Chen, Tomoya Itakura, Munehiro Inukai, Daiki Umeyama, Hiroyuki Asakura, and Susumu Kitagawa

Chemical Communications, **2014**, *50*, 10241–10243.